OPTICAL AND GAMMA-RAY STUDY OF GAMMA-RAY BINARIES

Itumeleng Monageng

Dec 2017

A dissertation submitted in partial fulfilment of the requirements for the degree Ph.D.

UNIVERSITY OF CAPE TOWN

Supervisors: Dr. Vanessa McBride, Prof. Markus Böttcher and Dr. Shazrene Mohamed

Abstract

X-ray binary stars are fascinating objects that provide an opportunity to study extreme astrophysical conditions. A small population of X-ray binary systems, namely gamma-ray binaries, consisting of only six confirmed sources, exhibits multiwavelength emission observed from the radio to the VHE gamma-ray regime. The focus of this thesis is the optical and gamma-ray emission of gamma-ray binaries.
We present optical spectroscopic analysis of 1FGL J1018−5856 with the Southern African Large Telescope, where we perform radial velocity measurements using blue spectra of the O star in this system. The extensive orbital phase coverage from our observations, together with measurements obtained from literature allows for constraints to be placed on the orbital parameters. We derive, for the first time, the orbital eccentricity of 1FGL J1018−5856 which, along with the other parameters, enables us to decipher the orbital geometry of the system. Furthermore, the mass function obtained allows us to constrain the mass of the compact object. We find that a neutron star is favoured for a large range of allowed orbital inclination angles, in agreement with previous inferences from literature, although a black hole is not completely excluded provided that the inclination angle is very small.
We have also explored long-term variability of the circumstellar disc in LS I +61 303 through the analysis of the Hα emission line. We present analysis of measurements of different features of the Hα line and evaluate these using a semi-analytical model which describes the motions of particles in Keplerian orbits. In this work, we demonstrate that several different parameters describing the geometry of the disc vary on timescales comparable to the superorbital period of the system. The work also shows, for the first time, observational signatures of the Kozai-Lidov mechanism in hydrodynamical discs through the evaluation of eccentricity changes of the disc.

A study of high energy emission processes in gamma-ray binaries is presented. We have explored the Bethe-Heitler mechanism for the production of gamma-ray emission, where energetic protons collide with stellar photons to produce energetic electron-positron pairs which upscatter photons to high energies. We show calcula-

tions of the spectrum and modulated flux in the context of the pulsar wind scenario, with photon-photon absorption and cascading effects taken into account. The effects of the ambient magnetic field around the massive star are shown, which result in quasi-isotropic gamma-ray emission, and the orbital modulation of the flux resulting in photon-photon absorption.

Acknowledgements

The work presented in this thesis could not have been possible without the support and assistance I have received from various people.
I am indebted to Dr. Vanessa McBride for helping me realise my childhood dream of becoming an astronomer. I thank you very much for believing in me and for all the encouragement, patience and support you have shown me throughout my postgrad career. I am grateful to Prof. Markus Böttcher for all the assistance and guidance provided in my PhD work. Thank you to Dr. Shazrene Mohamed for all the advice provided, especially towards the end of my degree.
I sincerely thank the admin staff at the South African Astronomical Observatory for the assistance with the queries that I've come forth to them with. I appreciate the discussions I've had with members of the stellar astrophysics group at SAAO (BANG!) that were useful for various parts of my research.
A very special gratitude goes out to Prof. Atsuo Okazaki and Dr. Yuki Moritani for sharing ideas and being very accommodative in my visits to Japan.
A special thank you to Dr. Marissa Kotze for the random check-ups and helpful conversations. I thank my office mates for the funny conversations we had at the office that proved to be vital for keeping one's sanity in stressful times. Thank you to my friends, Mokhine, Elias and Sulona for all the group chats and social gatherings we had, and useful discussions regarding our career paths. A great thank to my childhood friends, Koketso "Buster" Muller, Celiwe Mpambani and Shorn Monnakgotlha for the encouragement and support they have shown me thoughout my degree. I appreciate the support and motivation from my brothers, Mpho and Tlhware, I love you both dearly! To Atandile Mafanya, I thank you for keeping me sane towards the end of my degree - I love you dearly! I can not express my appreciation enough for my mother and late father for all the sacrifices that they have made to put me in a position that I'm in today, thank you for everything!

Plagiarism Declaration

I, Itumeleng Monageng, know the meaning of plagiarism and declare that all of the work in the document, save for that which is properly acknowledged, is my own.

Contents

List of Figures

List of Tables

Chapter 1

Introduction

X-ray binary stars are composed of a remnant of an evolved star, the compact object, which could be a neutron star (NS), a white dwarf (WD) or a black hole (BH), and a companion star. The X-ray emission in these systems is powered by matter supplied by the companion star and accreted by the compact object, hence authors in this field of research often use the nomenclature "donor" for the normal star and "accretor" for the compact object. The process of accretion can occur via different mechanisms, depending on the nature of the two objects and the orbit. Roche-lobe overflow (RLO) can occur when the donor overfills the volume of space around it within which matter is gravitationally bound to it, where the matter flows through the inner Lagrangian point (L_1). Because the L_1 point is orbiting with the binary, the matter has angular momentum and therefore does not fall directly onto the compact object, but rather moves in orbit around it until it is accreted, causing X-ray emission to be produced (Fig. 1.1a). Wind RLO can occur when the stellar radius is smaller than the Roche lobe but the stellar wind, with speeds that are less than the escape speed of the star, falls into the potential well of the companion as it goes through the L_1 point (Fig. 1.1b; Mohamed & Podsiadlowski 2012, Abate et al. 2013). Stellar wind accretion occurs when the donor star has a significant wind, some of which is captured as the accretor orbits through the outflowing material (Fig. 1.1c). A fourth mode is disc accretion, where the donor star has an equatorial circumstellar disc from which the accretor can capture matter as it passes through it at close passage (Fig. 1.1d).

X-ray binaries are generally divided into high mass X-ray binaries (HMXBs) and low mass X-ray binaries (LMXBs). The classification into the different classes of X-ray binaries is solely dependent on the spectral type of the donor star. Systems with a donor star of spectral type O or B ($M \geq 10 M_\odot$) fall into the HMXB subclass

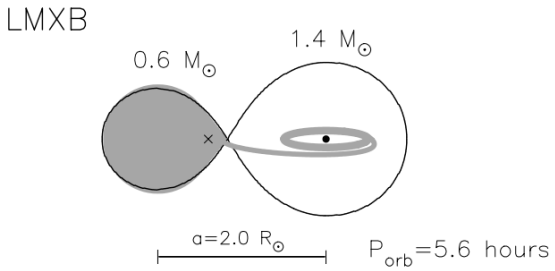

(a) Roche-lobe overflow, where the primary star fills its Roche lobe and mass passes through the L_1 point onto the companion. From Tauris & van den Heuvel (2006).

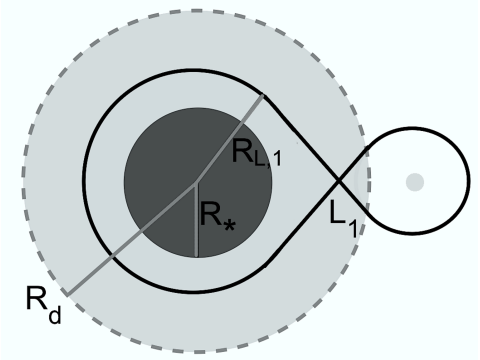

(b) Wind Roche-lobe overflow. The shaded represents the wind acceleration region. R_d is the wind acceleration radius and $R_{L,1}$ is the Roche-lobe radius. From Abate et al. (2013).

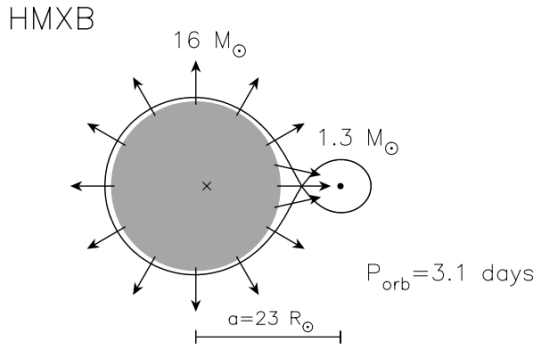

(c) Wind accretion. The companion captures the outflowing wind from the primary along its orbit. From Tauris & van den Heuvel (2006).

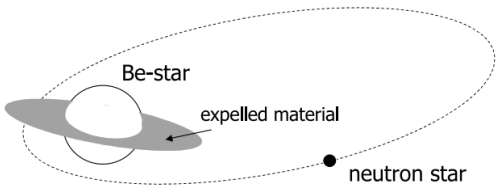

(d) Circumstellar disc accretion. The companion accretes material from the circumstellar disc of the primary. From Tauris & van den Heuvel (2006).

Figure 1.1: Schematics of the different accretion modes in X-ray binaries.

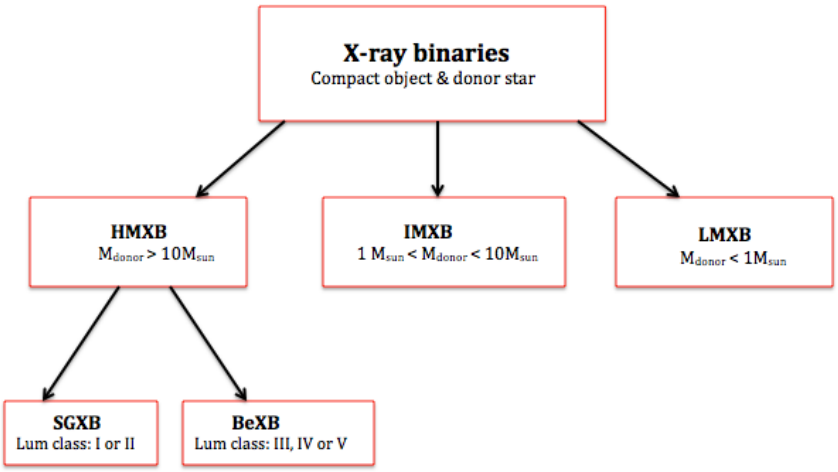

Figure 1.2: Classes and subclasses of X-ray binaries.

Table 1.1: Summary of the different properties of HMXBs and LMXBs (Tauris & van den Heuvel 2006).

Property	HMXB	LMXB
Donor	O or B ($\geq 10M_{\odot}$)	Later than A ($\leq 1M_{\odot}$)
Orbital period	A few to hundreds of days	a few hours to days
X-ray characteristics	Transient and persistent	Transient & persistent
Lifetime	$10^5 - 10^7$ years	$10^7 - 10^9$ years
Accretion mechanism	wind accretion and/or disc accretion	RLO

while those of spectral types later than A ($M \leq 1M_{\odot}$) make up the LMXB subclass. Binary systems with a donor star of mass range $1 \leq M \leq 10M_{\odot}$ fall under the rare subclass of IMXBs (Tauris & van den Heuvel 2006, Reig 2011). Fig. 1.2 shows a tree structure of the different classes and subclasses of X-ray binaries. A summary of the different properties of the two main classes of X-ray binaries is presented in Table 1.1.

1.1 High mass X-ray binaries

The luminosity class of the donor star in HMXBs further divides this population into supergiant X-ray binaries (SGXBs) and Be X-ray binaries (BeXBs). Donor stars of luminosity class I or II fall into the subclass of SGXBs. Donor stars of luminosity class III, IV or V with a fast rotating Be/Oe star fall under BeXBs. In SGXBs, the compact object accretes matter via RLO or through the capture of dense wind ($10^{-6} - 10^{-8} M_{\odot} \mathrm{yr}^{-1}$, Reig 2011) lost from the donor star. The orbits of the NS in SGXB are of typically relatively low eccentricity resulting in persistent

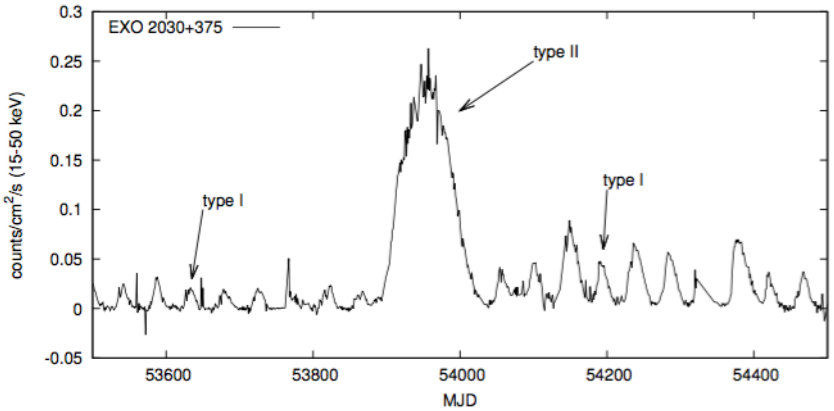

Figure 1.3: *Swift/BAT* X-ray lightcurve of EXO 2030+375 showing the different types of outbursts in BeXBs. From: Itumeleng Monageng, MSc thesis (University of Cape Town).

X-ray emission with luminosities, $L_{\rm X} \sim 10^{35} - 10^{36}$ erg. s^{-1} (Charles & Coe 2006). A subclass of SGXBs exists which exhibits transient X-ray behaviour lasting a few hours ($L_{\rm X} \sim 10^{36} - 10^{37}$ erg. s^{-1}), but are quiescent for a majority of the time ($L_{\rm X} \sim 10^{32} - 10^{33}$ erg. s^{-1}; Sguera et al. 2006, Romano et al. 2016).
BeXBs form the largest subclass of HMXBs, with 49% of the total population made up of these systems (42% are SGXBs and 9% are peculiar HMXBs, Coleiro & Chaty 2013). The compact object, primarily a NS (the first and only BH system known so far, MWC 656, was discovered by Casares et al. 2014), is usually in a relatively wide (up to 300 days) and eccentric ($e \geq 0.3$) orbit (Reig 2011). Although WD systems have been suggested as candidates for BeXB based on their X-ray spectra, no confirmations have been made (Torrejón & Orr 2001). Accretion of matter, resulting in X-ray activity, takes place from the periastron passage of the NS through the disc. The transient X-ray nature of these systems is owed largely to the variable circumstellar disc behaviour. The X-ray behaviour in BeXBs is generally characterised by two types of X-ray outbursts (Fig. 1.3). Type I outbursts, also termed "normal" outbursts are regular and generally associated with the periastron passage of the NS. The X-ray luminosity of these outbursts can reach up to 10^{37}erg. s^{-1} (Stella, White & Rosner 1986). Type II outbursts, also termed "giant" outbursts, occur less frequently and appear to not necessarily be associated with the orbital phase of the NS (e.g. Monageng et al. 2017a). Type II outbursts exhibit larger luminosities ($\geq 10^{37}$erg. s^{-1}, Stella, White & Rosner 1986) and last longer than type I outbursts.

HMXBs containing NS accretors often show pulsed X-ray emission. Young neutron stars in HMXBs harbour strong magnetic fields ($B \sim 1 - 6 \times 10^{12}$ G, Reig 2011) which interact with the matter from the donor. The magnetic fields channel

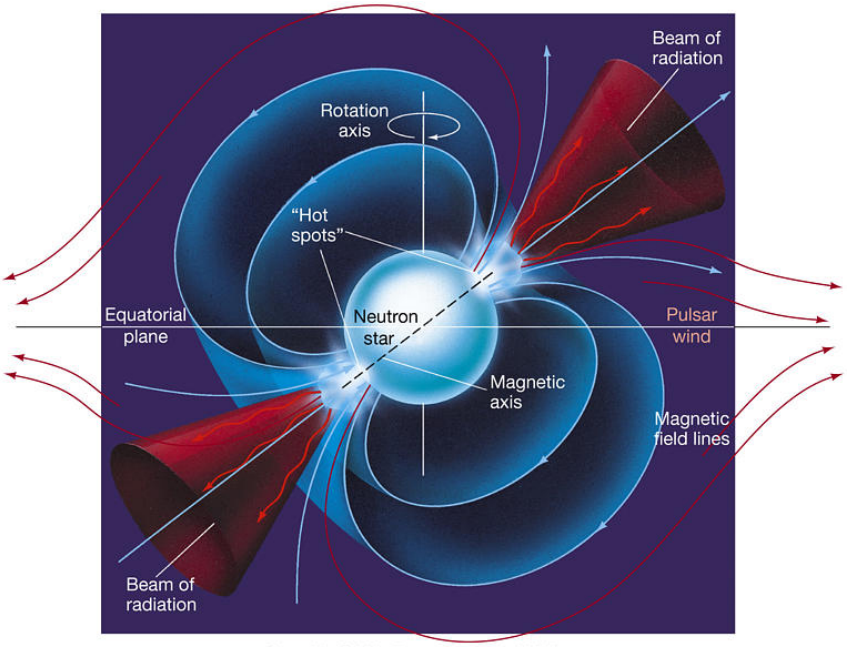

Figure 1.4: Sketch illustrating the misalignment of a NS magnetic axis and spin axis that results in a lighthouse effect. From: Chaisson & McMillan (2005).

the matter (transferred either via RLO, wind accretion or disc accretion) from the donor star to the polar caps where it falls into the large gravitational well of the NS and free-fall motion occurs due to the matter being accelerated. X-ray emission then occurs due to the kinetic energy being converted to thermal energy as it is decelerated near the NS surface. The pulsed X-ray emission results from the misalignment of the spin axis of the NS with the magnetic field axis (Fig. 1.4). The pulse period detected depends on the spin frequency of the NS, with pulsed signals detected when a beam of radiation from one of the poles crosses our line of sight in a lighthouse effect. The pulsed signals may be detected twice per rotation if both poles cross our line of sight.

The Corbet diagram (Fig. 1.5) shows the relationship between the orbital period ($P_{\rm orb}$) and spin period ($P_{\rm spin}$) in these systems. As seen from Fig. 1.5 different classes of X-ray binaries occupy almost distinct regions, displaying different relationships between the two observed quantities. The type of mass transfer process onto the NS is the main determining factor in the location of each system on the Corbet diagram. SGXBs do not show any strong correlation (or anticorrelation) between $P_{\rm orb}$ and $P_{\rm spin}$, while the BeXBs display a correlation between the two quantities. The correlation between $P_{\rm orb}$ and $P_{\rm spin}$ in BeXBs results from the relationship between

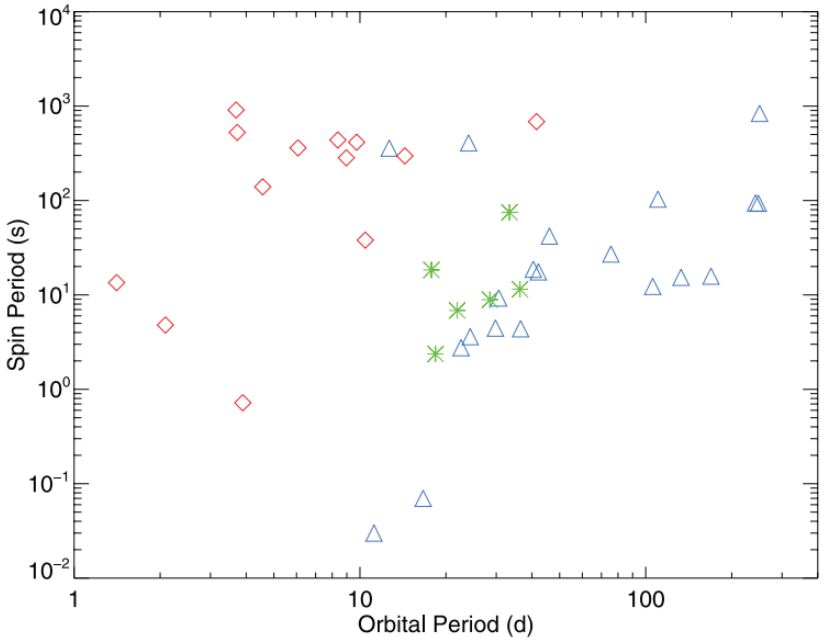

Figure 1.5: Corbet diagram for HMXBs. The red diamonds represent SGXBs, blue triangles represent Galactic BeXBs, green stars represent BeXBs in the Small Magellanic Cloud. From Townsend et al. (2011).

the size of the magnetospheric radius ($R_{\rm mag}$, the equilibrium radius between magnetic field pressure and ram pressure of the accreted material) of the NS and the corotation radius ($R_{\rm cor}$, the radius of rotation of the material at the NS Keplerian period). In a scenario when the magnetic field is very strong ($R_{\rm mag} > R_{\rm cor}$), the material is propelled away. When the magnetic field is relatively weak ($R_{\rm mag} < R_{\rm cor}$), then the material from the donor is accreted. In BeXBs, the NS is spinning close to equilibrium ($R_{\rm mag} \approx R_{\rm cor}$). The equilibrium period in turn is related to the mass flux ($P_{\rm eq} \propto \dot{M}^{-3/7}$), and the mass flux is a function of the size of the orbit (i.e. $P_{\rm orb}$). As follows, the spin period and the orbital period are correlated since the longer the orbital period the smaller the mass flux (and the shorter the orbital period the larger the mass flux; Stella, White & Rosner 1986, Waters & van Kerkwijk 1989).

Evolution of HMXBs

In this subsection I give a brief description of the formation and evolution of HMXBs, since they are the main subject of this thesis. For HMXBs to form, the two original stars in orbit must be of relatively high mass ($\geq 12 M_\odot$, Tauris & van den Heuvel 2006). Because the more massive star (primary star) evolves more rapidly, it will eventually expand and fill its Roche lobe where mass transfer occurs onto the secondary. Once the primary star has used up its hydrogen, helium burning occurs.

At this stage of the evolution the binary system is made up of a helium star and a massive O/B star. For a helium core with mass exceeding a critical threshold for NS formation ($\geq 2.8 M_{\odot}$), nuclear fusion will continue until an iron core remains. Once the core mass exceeds the Chandrasekhar limit, a supernova explosion occurs, leaving a NS with a high velocity kick (mean birth speed of ~ 400 km/s, Hobbs et al. 2005). With the NS orbiting the unexploded companion, a HMXB is formed, with mass transferred onto the NS via the circumstellar disc (BeXB) or RLO and/or radial stellar wind. The O/B star continues nuclear fusion until it eventually reaches the red supergiant phase, where it expands until a common envelope phase is reached. Loss of angular momentum occurs, leading to a decrease in orbital separation between the two stars, as a drag force is created from the motion of the NS through the envelope. The secondary star eventually uses up its hydrogen and also ends up with a helium core. Mass transfer onto the NS now occurs via RLO of the helium star. Nuclear fusion continues until an iron core is left, from which a supernova explosion will occur when the Chandrasekhar limit is reached. The final product of this evolutionary process is a recycled pulsar (originally the primary) and a young pulsar. For orbital separations of the double neutron star product that are short enough, a gravitational wave signal may be produced from the interaction between the two compact objects, and possibly a gamma-ray burst should they merge. Fig. 1.6 shows an illustration of the evolution of HMXBs, with the different stages described above.

HMXB systems with a primary star of mass range $8 - 20$ $M_{\odot}$ can take a different evolutionary route to the one described above. If a binary survives the common envelope and spiraling-in phase, a helium star Roche lobe overflow phase can be initiated (case BB mass transfer). In this scenario, once the hydrogen in the primary star is exhausted, the star evolves into a helium star. When the helium in the core is depleted the star expands and fills its Roche lobe and transfers its material onto the NS. The fate of the system is dependent on the initial mass of the helium star. Mass transfer from a helium star with mass range $1.5 - 2.1$ $M_{\odot}$ will result in a CO white dwarf, while a mass range of $2.1 - 2.5$ $M_{\odot}$ leads to an ONe white dwarf. In scenarios where the helium star is more massive than 2.5 $M_{\odot}$ the result is a double NS system (Delgado & Thomas 1981, Dewi et al. 2002, Tauris & Konar 2003).

1.2 Low mass X-ray binaries

LMXBs comprise a NS or BH compact object in orbit with a low mass star as the donor. The donor star is of spectral type later than A and typically has a mass

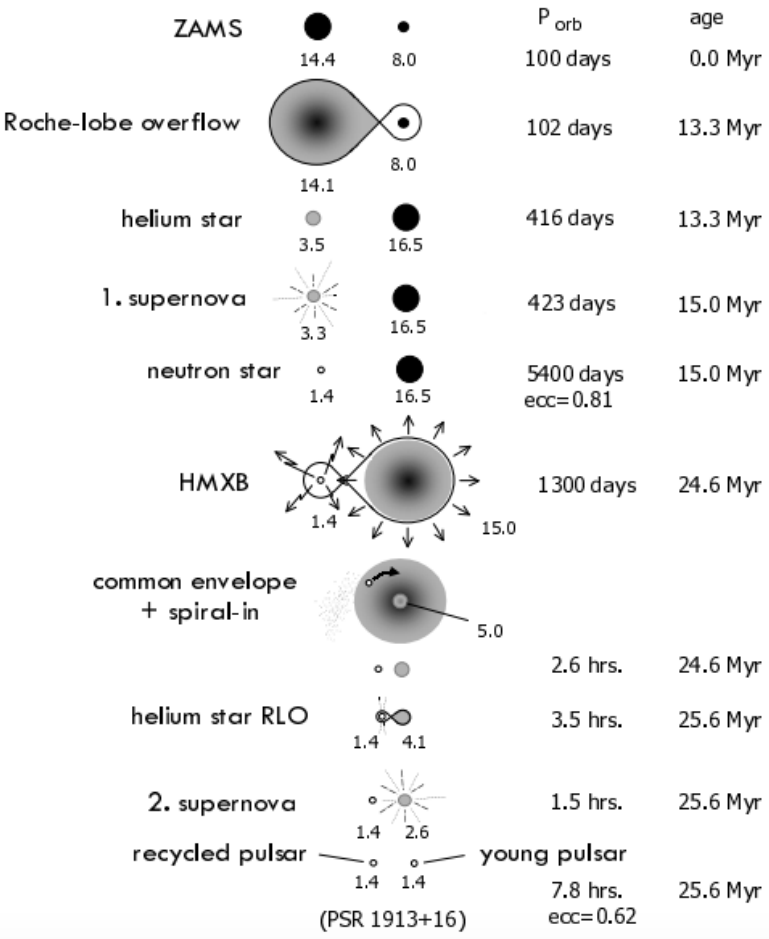

Figure 1.6: Evolution stages of a HMXB system. From Tauris & van den Heuvel (2006).

$\leq 1M_{\odot}$. Because the donor's stellar wind mass-loss rates are low, accretion in these systems takes place via RLO. This, combined with the relative small size of the donor (compared to the Roche lobe) requires the orbital periods in these systems to be short (11 minutes − 17 days, Tauris & van den Heuvel 2006). The matter from the donor passes through the L_1 point and due to the large angular momentum it possesses, it does not fall directly onto the compact object. The stream of matter flows around the compact object and eventually circularises, forming an accretion disc. Any further matter falling onto the compact object from the L_1 point will enter the outer parts of the disc and then flow towards the inner ring through the viscous torque until it is eventually accreted by the compact object (Hellier 2001). LMXBs have long lifetimes ($10^7 - 10^9$ years) and the majority are located in the Galactic bulge and globular clusters (Tauris & van den Heuvel 2006).

1.3 Intermediate mass X-ray binaries

A rare population of X-ray binaries exists with donor masses in between the two extreme cases ($1M_{\odot} \leq M \leq 10M_{\odot}$). It was argued by van den Heuvel (1975) that X-ray binaries with these moderate donor masses must exist but the low observed number of these systems, compared to LMXBs and HMXBs, is due to a selection effect. Unlike HMXBs, the donor stars in IMXBs have weak stellar winds which do not supply sufficient matter to the NS/BH to produce X-ray emission. Furthermore, when the donor evolves off the main sequence and RLO is initiated, the large mass ratio between the two stars results in an X-ray phase that is relatively short (on the order of ∼100 years). Moreover, the dense gas surrounding the NS/BH during this phase may cause the X-ray emission to be absorbed.

1.4 Gamma-ray binary stars

Gamma-ray binaries (GRBis) are a population of binary stars displaying non-thermal emission across the whole electromagnetic spectrum, from radio to gamma-rays. These systems are often defined by the feature in their νF_{ν} spectral energy distribution (SED) which shows a peak in the non-thermal emission above 1 MeV. All the known GRBis host an O/B spectral type star which dominates the optical and infrared (IR) emission and a compact object that is either a NS or BH. The radio, X-ray and gamma-ray emission are due to processes discussed later in this chapter. These objects display a number of puzzling features which vary from system to system. To date, there are only six confirmed GRBis with a wide

range of orbital and observational features, namely PSR B1259−63, LS I +61 303, HESS J0632+057, 1FGL J1018.6−5856, LS 5039 and LMC P3.
The small number of GRBis compared to the total number of HMXBs in the Galaxy is believed to be a consequence of the short evolutionary lifetimes of these systems, in the case of a NS compact object (Dubus 2013). A newborn pulsar has a high enough spindown power and sufficiently strong magnetic field that the pulsar wind prevents matter from the companion star from being accreted. As the pulsar spins down, the spindown power decreases and eventually the accretion of matter via the capture of material from a circumstellar disc (BeXBs) or wind loss from the stellar companion (SGXB) commences. With the pulsar wind "switched off", non-thermal emission originating from the interaction of the two winds is halted, bringing the GRBi phase to an end. This stage marks the beginning of the traditional HMXB phase (BeXB or SGXB). The lifetime of the systems in the GRBi phase is no longer than the spindown timescale of the pulsar (on the order of 10^5 years, Dubus 2013), which is short compared to the lifetime of a binary system ($\sim 25\times10^6$ years, Tauris & van den Heuvel 2006). This would therefore explain the small number of confirmed GRBis. Dubus et al. (2017) used high energy (HE) and very high energy (VHE) data to simulate observations of GRBis in the Galaxy. From this work, the authors predict that the number of Galactic GRBis is 101^{+89}_{-52} systems, and so current surveys (e.g. *Fermi*/LAT 3FGL and HESS Galactic Plane survey) and future surveys (e.g. *Cherenkov Telescope Array* Galactic Plane Survey) promise to increase the population of these systems. While the *Fermi*/LAT survey was expected to contribute as many as 8 new detections, it has only yielded one discovery (LMC P3, Corbet et al. 2016) since its initial launch in 2015.

Compact object

A lot of mysteries surrounding the phenomena in GRBis revolve around the nature of the compact object. One of the main questions that has been puzzling researchers in this field for years has been whether GRBis are accreting sources or non-accreting pulsar wind nebulae. It would seem trivial to provide the answer to this question from observations. A majority of the known HMXBs host a NS which accretes matter from an optical companion. The main piece of evidence to support the NS compact object claim is the detection of X-ray pulsations as a result of the misalignment of the spin and magnetic axes. In PSR B1259−63 pulsations are detected in the radio domain with a period of 47.76 ms (Johnston et al. 1994). This is the only GRBi in which the nature of the compact object is confirmed. In other systems, multiwavelength observations resulted in unsuccessful searches for pulsations. In the systems with short

orbital periods (LS 5039, LS I +61 303, LMC P3 and 1FGL J1018.6−5856) the detection of radio pulsations would be almost impossible, as the free-free absorption is more prominent due to the close proximity to the stellar wind from the companion star (Dubus 2006b, Zdziarski, Neronov & Chernyakova 2010). This is evident in PSR B1259−63 at phases close to periastron, as pulsations disappear ∼20 days before to ∼20 days after periastron due to free-free absorption by the stellar wind and disc environment (Melatos, Johnston & Melrose 1995). Gamma-ray and X-ray pulsations have not been detected in GRBis. This is due to their intrinsic faintness and the requirement of precise knowledge of the orbital parameters. Due to the long integration times at X-ray and gamma-ray bands, the detection of the pulsations at these energies requires orbital demodulation. The uncertainty in the demodulation, however, is dependent on the errors in the orbital parameters determined from radial velocity studies. Thus, the power of the signal calculated is correlated to the precision of the orbital parameters. Currently, the precision in the known orbital of GRBis is insufficient for pulsations to be detected at high energy bands. This is further complicated by the fact that the high energy emission is likely dominated by the contribution from the shock between the two objects in the system for a large portion of the orbit, which is far enough away from the pulsar light cylinder for the emission to be unpulsed (Caliandro, Torres & Rea 2012).
Another means for constraining the nature of the compact object is through optical spectroscopy to derive the dynamical mass. Absorption and emission lines of Hydrogen and Helium atoms from the optical companion can be used to measure radial velocity shifts (see chapter 2). With a known value of the mass of the optical companion (e.g. inferred from the spectral type classification) and an upper limit of the inclination angle, one can derive the mass of the compact object (or a range of allowed masses from the allowed inclination angles). A dynamical mass of >3 $M_{\odot}$ for the compact object would favour a BH. Placing constraints on the mass of the compact object using radial velocity measurements in GRBis is hampered by large uncertainties in the orbital inclination angles, resulting in a wide range of possible masses that includes both the NS and BH. The uncertainty in the nature of the compact object (and therefore the physical processes) in GRBis gives rise to two main scenarios to try to explain the origin of the multiwavelength emission: The microquasar and pulsar wind scenario (Fig. 1.7).

The microquasar scenario

X-ray binaries share many similar properties with Active Galactic Nuclei (AGN), such as an accreting compact object, relativistic jet and an accretion disc. Quasars,

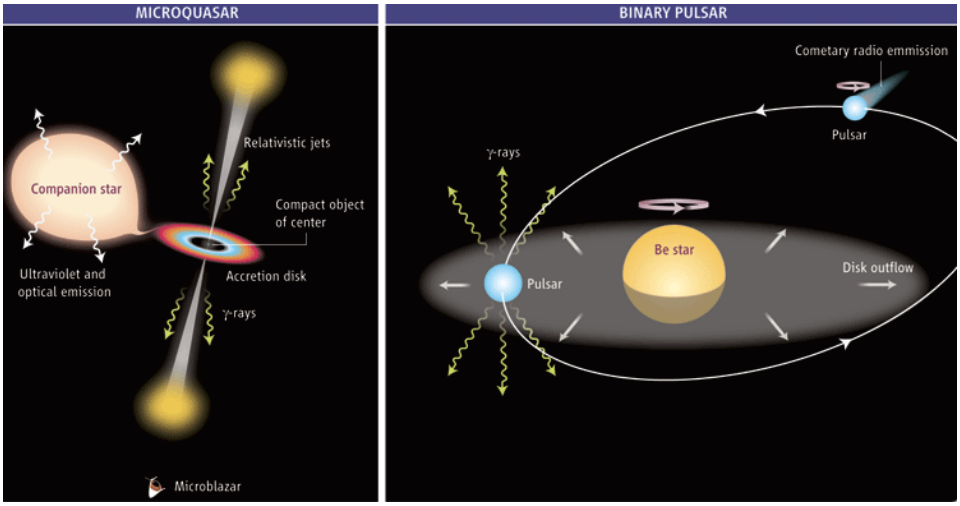

Figure 1.7: The microquasar and pulsar wind model scenarios proposed for gamma-ray binaries. From Mirabel (2006).

a subclass of AGN, are supermassive ($\geq 10^6 M_\odot$) BH which accrete matter from the host galaxy through an accretion disc, a fraction of which is ejected in the form of relativistic jets. X-ray binaries that display these features are given the name microquasars (MQs) since they are essentially scaled-down versions of quasars (Fig. 1.8, Massi 2004).

The idea that GRBis are MQs was suggested based on radio observations of LS 5039 using the Very Large Array (VLA) and Very Long Baseline Array (VLBA). The images displayed extended structures emerging from the core, which were interpreted as jets extending over 6 milliarcsecs in the sky (Fig. 1.9a, Paredes et al. 2000). Additionally, LS I +61 303 was observed with the European VLBI Network (EVN) at milliarcsecond scales and a one-sided extended structure was revealed reaching up to tens of AU. This was interpreted as a Doppler-boosted jet with a velocity of $0.4c$ (Massi et al. 2001). These observations of LS I +61 303 were later extended to larger structures (hundreds of AU) using the Multi-Element Radio-Linked Interferometer Network (MERLIN), where a double-sided structure extending up to 200 AU was observed (Massi et al. 2004). These observational features had striking similarities to some of the well-known MQ systems (e.g. Cygnus X-1 and SS 433). The non-thermal high energy emission in this scenario would then arise due to the interaction of charged energetic particles in the jet with cold photons and particles from the massive companion.

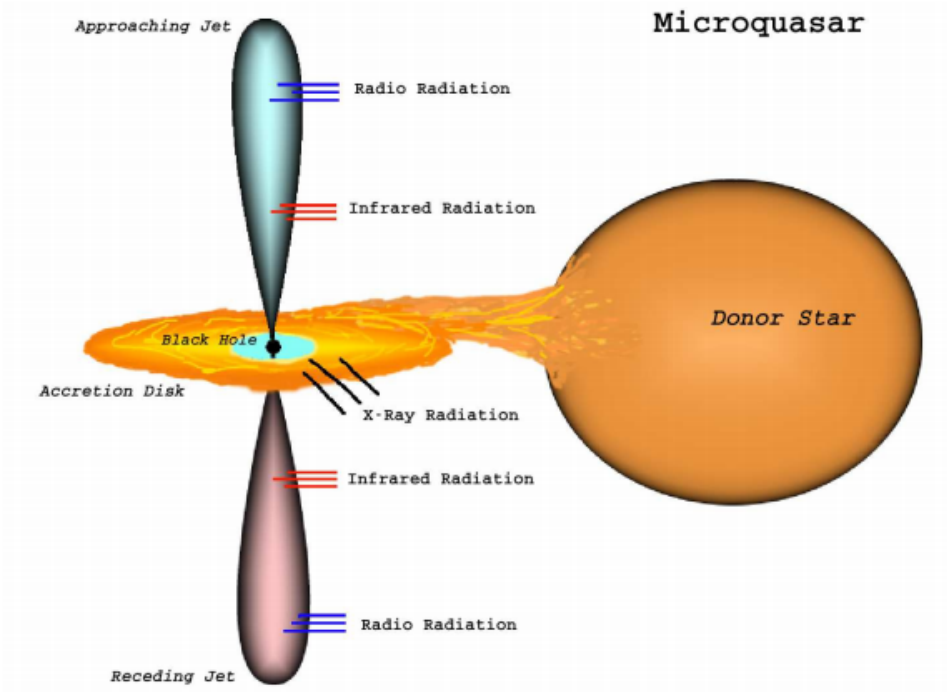

Figure 1.8: Sketch of a microquasar highlighting the main components. From Massi (2004).

Pulsar wind scenario

An alternative scenario to the accretion (MQ) model is the pulsar wind model (PWM). In this scenario, a rapidly rotating young pulsar prevents matter from the massive companion from being accreted. The rapidly rotating pulsar releases a relativistic wind that interacts with the slow-moving wind and/or disc from the massive companion, creating a double shock feature in between the two stars with a contact discontinuity separating the shocked matter from the two regions (Dubus 2013; 2006b). The non-thermal high energy emission then originates from particles accelerated at the shocked region interacting with the massive stellar photons and particles. This is the scenario that takes place in PSR B1259−63. The PWM was already proposed by Maraschi, Treves & Tanzi (1981) for LS I +61 303 where it was suggested that the compact object is a young pulsar of age $10^4 - 10^5$ years.
Tavani & Arons (1997) and Kirk, Ball & Skjæraasen (1999) built on this picture, from a theoretical viewpoint, to explain the origin of the high energy emission. The analysis of VLBA data from observations of LS I +61 303 by Dhawan, Mioduszewski & Rupen (2006) on microarcsecond scales revealed an extended tail-like structure pointing away from the Be star that was interpreted as a pulsar wind nebula (Fig. 3.2). Moreover, the authors measure non-relativistic speeds ($c < 1000$ km/s) for the outflow, further refuting the claims of a powerful jet being the source of particle acceler-

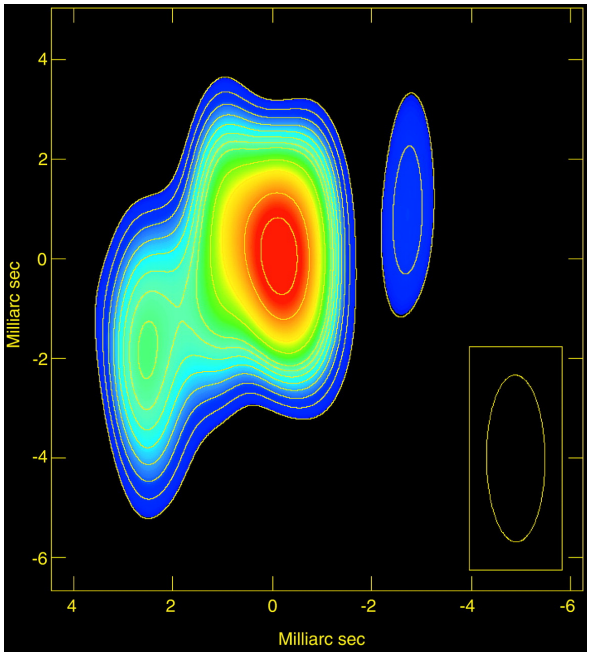

(a) VLBA image of LS 5039 showing extended structures interpreted as jets. From Paredes et al. (2000).

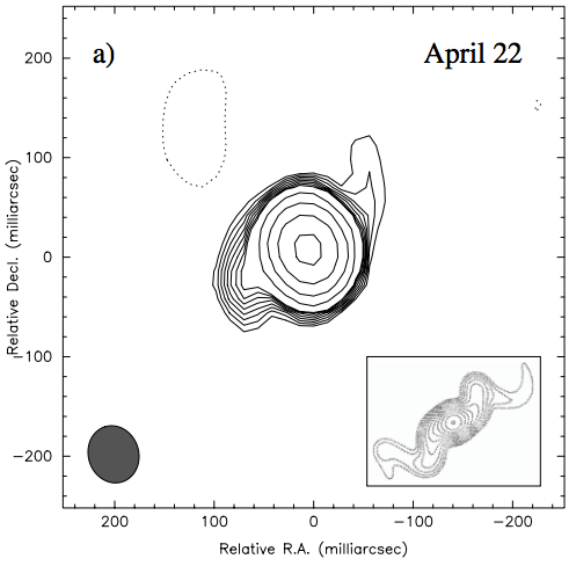

(b) MERLIN image of LS I +61 303 showing a two-sided jet. The small box shows the simulated radio emission of SS 433 for comparison. From Massi et al. (2004).

Figure 1.9: Radio images of LS 5039 and LS I +61 303.

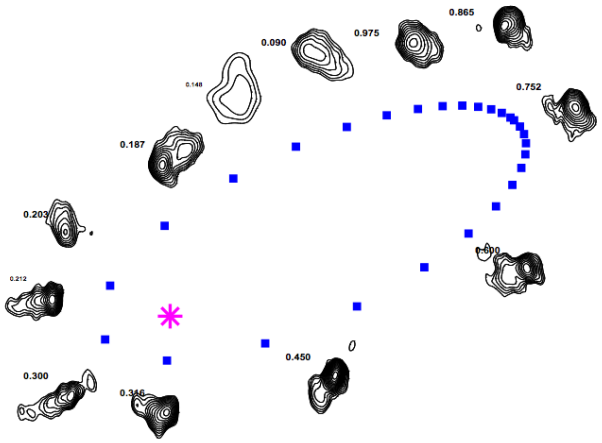

Figure 1.10: Microarcsecond images of LS I +61 303 from VLBA. From Dhawan, Mioduszewski & Rupen (2006).

ation. Dubus (2006b) provides the most compelling argument for the PWM where it was argued that it is possible for the morphology of their radio tails to mimic the jets of MQs. Furthermore, the SEDs of LS 5039, LS I +61 303 and PSR B1259−63 (the only known GRBis at the time) from this work were reproduced in the framework of the PWM. The lack of detection of pulsations in the systems in the PWM can be explained by free-free absorption in the dense stellar wind environment of the massive companion (Dubus 2013; 2006b). In PSR B1259−63 the pulsations vanish near periastron passage as a result of free-free absorption due to the close proximity of the pulsar to the Be star wind and disc. The separation of the pulsar and Be star at periastron passage for PSR B1259−63 ($P_{\rm orb} = 1237$ days) is on the same order of magnitude as the average orbits of the GRBis with tight orbits ($P_{\rm orb} < 30$ days). HESS J0632+057 also has a relatively large orbit ($P_{\rm orb} = 321$ days) and therefore has more promise for the detection of pulsations (if it does indeed operate in the PWM).

1.5 Thesis overview

The small population of GRBis allows for dedicated studies of each source at different wavelengths. Despite the wealth of data analysed and theoretical models produced for each individual source, a lot of the multiwavelength features displayed by these sources remain puzzling. For the more recently discovered objects found at high energies, follow-up observations are required at low energies to put constraints on the orbital parameters. Deciphering the geometry of these systems from the derived orbital parameters is particularly important for modeling the high-energy emission.

While high-energy models have been extensively applied to GRBis by using inverse Compton scattering and pion decay mechanisms, in some instances these mechanisms alone cannot fully account for the observed gamma-ray emission. Although they display many similar features, a number of the multiwavelength characteristics vary from system to system, suggesting different mechanisms to be at work.
Three of the confirmed GRBis contain B spectral-type stars with a circumstellar disc as the massive component of the system. The behaviour of circumstellar discs in Be stars has long been a subject of interest in HMXBs and isolated systems. Although an abundance of data and simulations has been presented in literature to investigate the variability of the discs, a number of the features remains unclear. This is especially true in the case of binary systems, as the interaction of the compact object with the disc presents additional physics that complicates the variability further. This thesis addresses some of the puzzling behaviour of GRBis through three main projects:

The orbit of 1FGL J1018.6−5856 Since its discovery in the GeV regime in 2011, the orbital parameters of 1FGL J1018.6−5856 have been poorly constrained. Previous attempts at deriving the orbital parameters through radial velocity measurements have been frustrated by low signal-to-noise data and poor phase coverage. In chapter 2, we present radial velocity measurements of data obtained with SALT where, for the first time, the orbital geometry of 1FGL J1018.6−5856 is derived. A discussion of the results obtained is provided in the context of the lightcurves at high energies.

Long term spectroscopic study of LS I +61 303 LS I +61 303 has a unique feature that distinguishes it from other members in its class; it has a long term superorbital period. This long term periodicity has been detected across the whole electromagnetic spectrum. There has been a lot of speculation regarding the origin of this superorbital modulation since its detection and this remains an open question. The goal of this project is to understand the long term variability of the Be disc in LS I +61 303 by studying its detailed geometrical changes. This is done through the analysis of long term spectroscopic data in conjunction with a semi-analytical model which describes the motions of test particles in the disc. Chapter 3 begins with a description of the main multiwavelength observational properties of LS I +61 303 and then I provide a background of Be discs from a theoretical and observational viewpoint. I then present the results and give a discussion of the possible implications of them.

The Bethe-Heitler mechanism for high energy emission in GRBis The high energy emission in GRBis has been modelled through invoking leptonic and hadronic processes. In leptonic models, the low energy photons are scattered by energetic electrons accelerated at the shock region (pulsar wind model) or in the jet (microquasar model). Hadronic models explain the origin of gamma-rays through the decay of neutral pions from the collision of energetic protons from the accelerated region with low-energy protons from the donor star/disc. In chapter 4, I present the Bethe-Heitler model which incorporates both leptons and hadrons, whereby energetic protons interact with soft photons to produce electron-positron pairs which then upscatter soft photons to high energies. The modeling of the high energy emission is studied in the context of the PWM, where I perform calculations of the flux and spectrum along the orbital phase.

Chapter 2

The orbit of 1FGL J1018.6−5856

This chapter presents analysis of spectra of 1FGL J1018.6−5658 (J1018 hereafter) collected with the Southern African Large Telescope (SALT). While the system was identified through its orbital modulation at GeV energies, other orbital parameters remain elusive. Radial velocity (RV) measurements are presented, which when combined with published measurements provide wide orbital phase coverage, allowing for the orbital parameters to be derived. Constraining the geometry of J1018 will help improve the interpretation of the high energy variability through analytical modeling of the system. This work has been published in Monageng et al. (2017b).

2.1 Background and observational properties

J1018 was discovered, in a search for periodic modulation of sources in the first Fermi/LAT catalog, when a 16.6 day modulation was detected in the 100 MeV−200 GeV energy band (Corbet et al. 2011). Historical radio and X-ray data of the respective sources within the error circle of Fermi/LAT showed clear orbital modulation at the 16-day period. Spectroscopic optical observations from the South African Astronomical Observatory (SAAO) 1.9 m telescope allowed for an O6V((f)) classification of the spectral type of the massive star to be inferred, while no photometric variability was observed (Fermi LAT Collaboration et al. 2012).

Radio properties Soon after the discovery of J1018 with Fermi, radio observations were performed at two frequencies, 5.5 GHz and 9.0 GHz, with the Australia Telescope Compact Array (ATCA; Fermi LAT Collaboration et al. 2012). The folded radio lightcurve displays clear variability on the orbital period with a sine-wave like feature and amplitude range $\sim 1 - 6$ mJy (Fig. 2.1). The spectral index is seen to vary around 0 with a range, $-0.6 \leq \alpha \leq 0.4$, although no orbital phase dependence

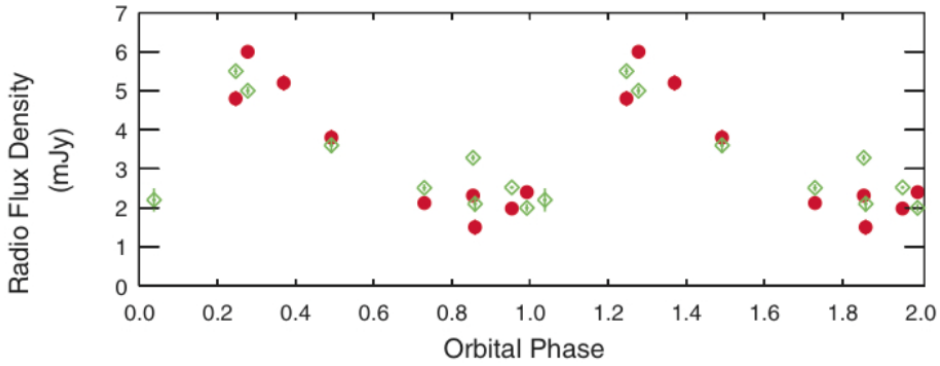

Figure 2.1: ATCA folded radio lightcurve of 1FGL J1018.6−5856 at 5.5 GHz (red points) and 9 GHz (green points). From Corbet et al. (2011).

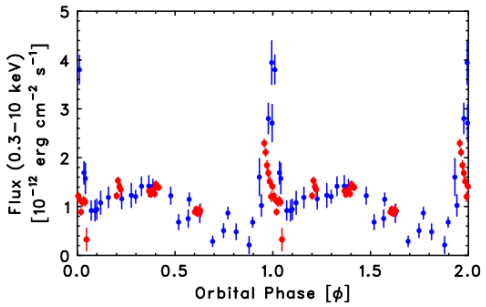

Figure 2.2: Folded X-ra flux of J1018 from Suzaku (red) and Swift (blue). From Tanaka et al. (2014).

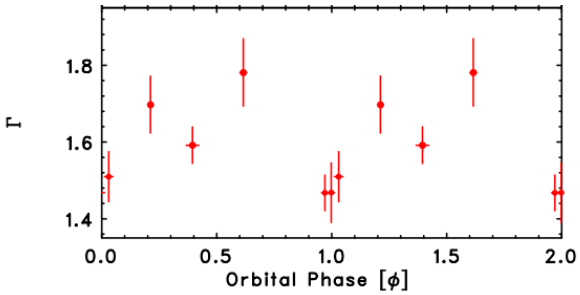

Figure 2.3: Orbital variation of the X-ray photon index of J1018 from Suzaku. From Tanaka et al. (2014).

has been identified yet due to the lack of long-term monitoring in the radio regime (Fermi LAT Collaboration et al. 2012).

X-ray properties The initial observations undertaken with Swift XRT displayed a sharp feature in addition to the broad sinusoidal-like peak in the folded lightcurve (Fig. 2.2; Fermi LAT Collaboration et al. 2012). An et al. (2013) noted that the sharp peak is not persistent, having only been detected in the first ∼100 days of Swift observations. Timing analysis of the Swift data revealed a period of 16.57±0.11 days, in agreement with that obtained from GeV studies. Phase-resolved spectral analysis from Suzaku observations revealed a power-law spectrum with spectral index range $1.47 \leq \Gamma \leq 1.78$ (Fig. 2.3; Tanaka et al. 2014).

Gamma-rays (GeV) The first Fermi/LAT catalogue saw the discovery of J1018 when a 16-day modulation was detected (Corbet et al. 2011). The folded Fermi/LAT lightcurve displays a narrow peak structure at orbital phase, $\phi \sim 0$ and a broad minimum at phase range, $\phi \sim 0.2 - 0.6$ (Fig. 2.4), the behaviour of which is more

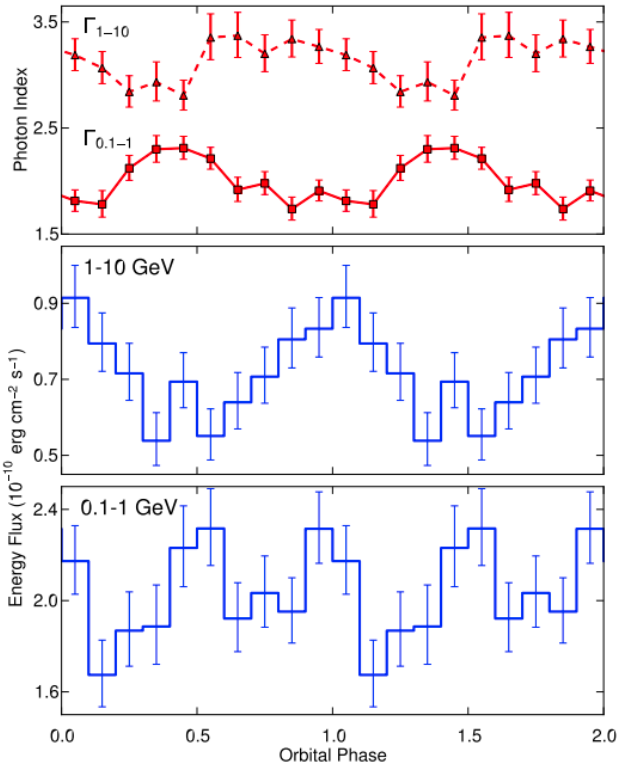

Figure 2.4: Folded Fermi flux (blue) and photon index (red) of J1018 at energy ranges $0.1-1$ GeV and $1-10$ GeV. From Fermi LAT Collaboration et al. (2012).

prominent at higher energies ($0.5-6.4$ GeV) than lower energies ($0.1-0.4$ GeV, An & Romani 2017). The phase-resolved spectrum is described by a power-law with an exponential cutoff and best-fit parameters: $\Gamma = 1.82 \pm 0.02$, $E_{\rm cutoff} = 3.00 \pm 0.19$ GeV for the high flux state ($\phi \sim 0.0-0.3$, $\phi \sim 0.8-1.0$) and $\Gamma = 1.94 \pm 0.01$, $E_{\rm cutoff} = 3.277 \pm 0.175$ GeV for the low flux state ($\phi \sim 0.3-0.8$, Chen et al. 2017).

Gamma-rays (TeV) The detection of J1018 in the TeV domain was established when it was positionally associated with the HESS source HESS J1018−589, which is in the neighbourhood of the supernova remnant SNR G284.3−1.8 (H. E. S. S. Collaboration et al. 2012). Two emission regions in HESS J1018−589 were detected as shown in Fig. 2.5. The position of source A in Fig. 2.5 is consistent with the 95% confidence contour of 1FGL J1018.6−5856 from Fermi/LAT. Confirmation of the association was made when the folded HESS lightcurve showed modulation on the 16.6-day orbital period with behaviour similar to that seen at GeV energies (Fig. 2.6; H. E. S. S. Collaboration et al. 2015). The spectrum is best-fit with a power-law function with a spectral index, $\Gamma = 2.20 \pm 0.14$ (Fig. 2.7; H. E. S. S. Collaboration et al. 2012; 2015).

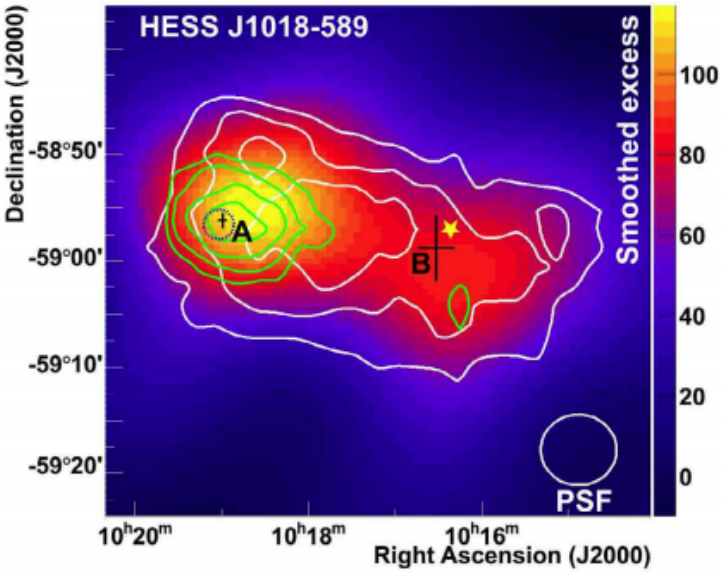

Figure 2.5: Image of the J1018 emission region obtained with HESS. The green and white lines represent significance contours calculated using a an oversampling radius of 0.1° and 0.22°, respectively. From H. E. S. S. Collaboration et al. (2012).

This chapter is written as follows: in Sect. 2.2 we summarise previous RV studies of J1018 and discuss their implications. In Sect. 2.3, we give a description of SALT and describe the observational setup. Sect. 2.4 details the theory of cross-correlation used in the analysis of the data presented here. In Sect. 2.5, we derive the equations that describe the orbital motion in binary systems. In Sect. 2.6 we present the results of the RV measurements and we discuss them in Sect. 2.7. The conclusions of the work are presented in Sect. 2.8.

2.2 Previous radial velocity studies

Waisberg & Romani (2015a) present the first RV study of J1018 using data obtained with the CTIO 1.5 m telescope. In their work, Waisberg & Romani (2015a) used Gaussian fits to absorption lines of He I 5875.65 Å, He II (4686 Å, 5411 Å, 6527 Å) and H I (Hγ, Hβ, Hα) to measure the central wavelengths of the line species and calculate RVs by comparing them to laboratory rest wavelengths. From the average velocities of the He II (4686 Å, 5412 Å) and H I (Hα, Hβ), the fitted Keplerian models resulted in semi-amplitudes of $K = 40$ km/s and $K = 15$ km/s, respectively. Assuming a mass range of the O6V((f)) star of 20.0−26.4 $M_\odot$, as used by Casares et al. (2005b), the maximum allowed semi-amplitude of $K = 40$ km/s from their work results in a compact object mass $M_X > 2.2$ $M_\odot$, supporting a BH as a likely

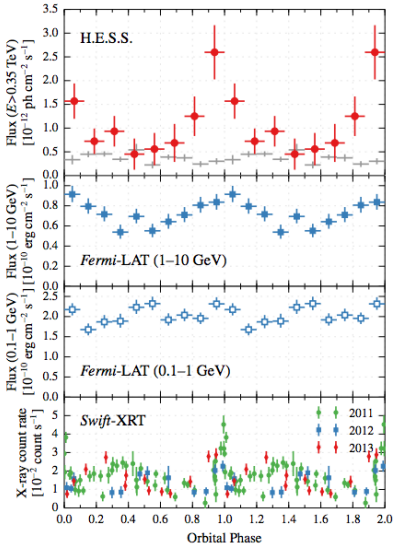

Figure 2.6: Top to bottom: folded lightcurves of J1018 from HESS, Fermi and Swift XRT. From H. E. S. S. Collaboration et al. (2015).

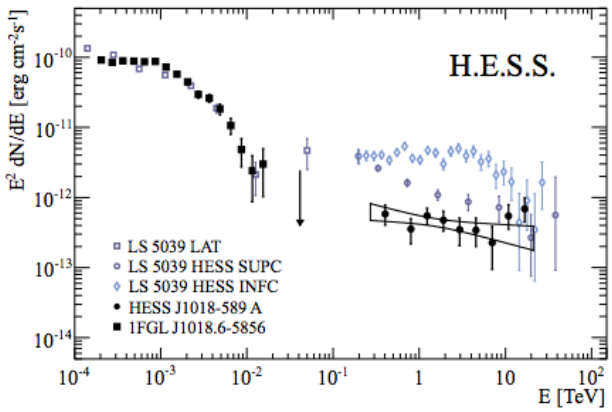

Figure 2.7: Fermi (black squares) and HESS (black circles) spectrum of J1018. The blue symbols are for LS 5039. From H. E. S. S. Collaboration et al. (2015).

candidate for the nature of the compact object. It is noted, however, that the RV measurements from Waisberg & Romani (2015a) are hindered by scatter as a result of continuum calibration imprecision and contamination of the absorption lines by stellar wind line features (Fig. 2.8).

Strader et al. (2015) (S15, hereafter) performed a follow-up RV study of J1018 using data obtained with the Goodman High-Throughput Spectrograph on the SOAR 4.1 m telescope. In their analysis, S15 cross-correlated their spectra against the spectrum of the O6V star, HD 172275, in two regions covering the H γ and He II (4542 Å and 4686 Å) lines separately. RV measurements were performed separately for the two line species. For the two line species, a circular Keplerian fit was performed, which resulted in semi-amplitude values of $K = 11.4 \pm 1.5$ km/s and $K = 12.2 \pm 2.7$ km/s from H γ and He II, respectively. As seen from Fig. 2.9, the fitting of the orbital parameters is limited by the sparse phase coverage. From the mass function obtained and an assumption of the optical companion mass range $20.0 - 26.4$ $M_{\odot}$, a NS as the compact object is allowed for inclination angles ranging between 26° and 64°. For a BH ($M_X \geq 3$ M$\odot$) to be the compact object in J1018, much lower orbital inclination angles ($i < 16°$) are implied for the system.

2.3 SALT

The Southern African Large Telescope (SALT, Fig. 2.10) is a 10-m class telescope located at the South African Astronomical Observatory (SAAO) observing station in Sutherland. The telescope is made up of 91 hexagonal segments which are arranged to form a primary mirror of dimensions 11 m × 10 m (Fig. 2.11, Buckley 2005, Buckley et al. 2006).

The fixed elevation primary mirror directs incoming light to a moving tracker at the prime focus which is equipped with a spherical aberration corrector (Buckley 2005). The declination range of the telescope is restricted to a range, $10° \leq \delta \leq -75°$, setting the track time of the object of interest to the time it takes to transit the annulus illustrated in Fig. 2.12.

SALT has a list of instruments currently in operation working in different modes, making the telescope versatile for different scientific goals:

- Robert Stobie Spectrograph (RSS): formerly known as the Prime Focus Imaging Spectrograph (PFIS), the RSS is an imaging spectrograph that has been the main workhorse for SALT. RSS has a wide range of capabilities, as it operates in different modes: long-slit spectroscopy, narrow-band imaging, Fabry-

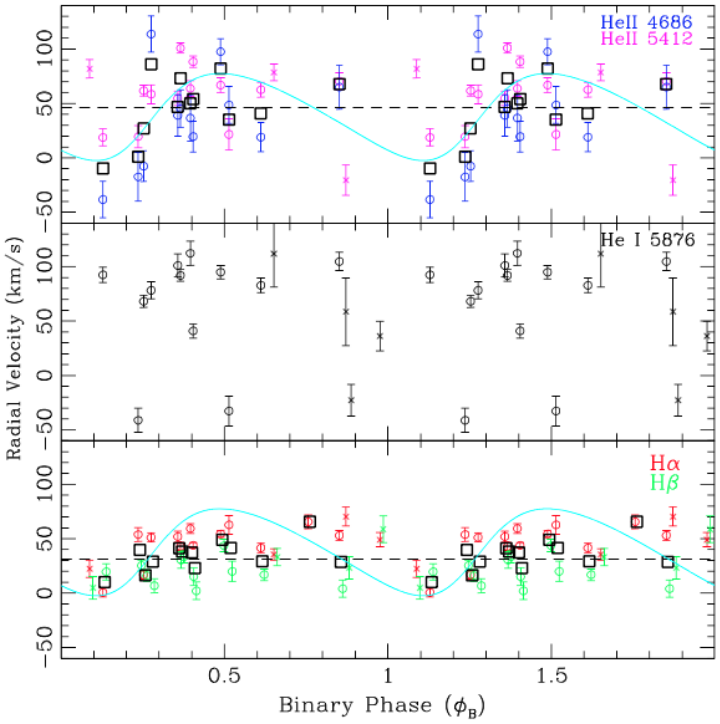

Figure 2.8: Radial velocity fits to He II, He I and H I (top to bottom). The black open squares show the mean velocity of the strongest lines from each species. From Waisberg & Romani (2015a).

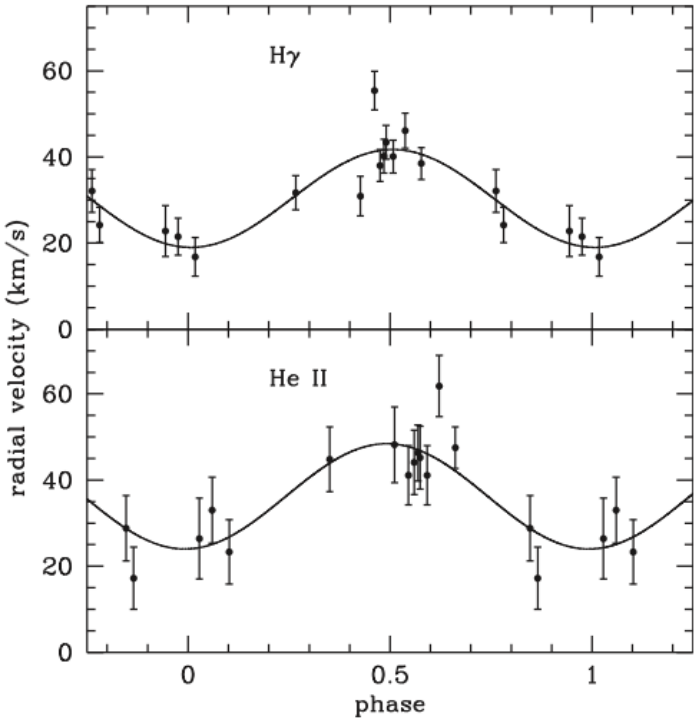

Figure 2.9: Orbital fits to the radial velocities of 1FGL J1018.6−5856 derived from Hγ (top) and He II (bottom) lines. From Strader et al. (2015)

Figure 2.10: Southern African Large Telescope located in Sutherland, South Africa. From Southern African Large Telescope official Facebook page (`https://www.facebook.com/SATelescope/photos/a.1468732880070346.1073741825.1468732113403756/1468937386716562/?type=3&theater`).

Figure 2.11: The primary mirror on SALT formed by 91 hexagonal segments. From Buckley et al. (2006).

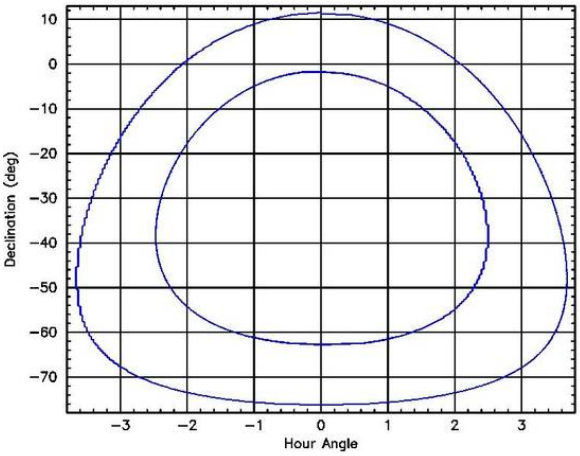

Figure 2.12: SALT viewing annulus. From www.salt.ac.za

Perot imaging spectroscopy, high time-resolution spectroscopy and long-slit spectropolarimetry (Buckley 2005).

- SALTICAM: this is an imaging and acquisition camera operating from UV to visible wavelengths ($3200 - 9000$ Å). SALTICAM can be used in several modes, namely frame transfer, normal imaging and slot mode (O'Donoghue et al. 2006).

- Berkeley Visible Image Tube Camera (BVIT)*: an imaging, photon-counting camera originally designed to perform high time-resolution astronomy in the visible and near-UV bands (McPhate et al. 2011). While currently not able to achieve high-precision absolute photometry, BVIT can obtain a flux intensity relative precision of ∼5% by observing nearby standard stars†. Observations with BVIT can be performed using a range of filters: B, V, R or Hα‡ (McPhate et al. 2011).

- High Resolution Spectrograph (HRS): a fibre-fed Échelle spectrograph with refractive cameras. HRS has a dual-beam with the blue and red arms operating at wavelength ranges, $3700 - 5500$ Å and $5500 - 8900$ Å, respectively. The instrument can be operated in three different modes at different resolutions: low resolution (LR, $R \sim 14000$), medium resolution (MR, $R \sim 40000$) and high resolution (HR, $R \sim 65000$, Barnes et al. 2008, Bramall et al. 2012).

For our programme, J1018 was observed with SALT using HRS in MR mode on

*BVIT is a visitor instrument.
†`http://pysalt.salt.ac.za/proposal_calls/current/ProposalCall.html#h.bh5n0br19jgk`
‡http://bvit.ssl.berkeley.edu/

8 epochs between 06 December 2015 and 20 December 2015. The primary reductions for all the data were performed with the SALT data reduction pipeline which executes the overscan correction, bias subtraction and gain correction (Crawford 2015). The remainder of the data reduction is performed using the MIDAS FEROS and ECHELLE packages (Stahl, Kaufer & Tubbesing 1999, Ballester 1992) and the steps are summarised as follows (Kniazev, Gvaramadze & Berdnikov 2016):

- The spectral orders were first located from the flat frames. The background, originating from offsets due to electronics, was then subtracted from the flat and science frames, after which the spectral orders were extracted using the task EXTRACT/FEROS.

- The efficiency of the spectrograph is not uniform along each order, as a result of the blaze effect* of the echelon grating. To correct for this, the object frames are divided by the flat frame using FLAT/FEROS (Fig. 2.13).

- Wavelength calibration is then applied by first extracting orders from the arc frame, a process which involves interactive identification of lines in each order by comparing with a reference arc list with known pixel position as a function of wavelength using the task IDENTIFY/FEROS.

- Finally, once the spectra are blaze-corrected and wavelength-calibrated, the individual orders are merged using the task MERGE/ECHELLE, where a weighted average of the overlapping regions of the adjacent orders is computed. Fig. 2.14 and 2.15 show examples of final blue and red spectra, respectively.

  Table 2.1 lists the observations and S/N measured. We measured the S/N using different regions of the continuum and recorded the average. Exposure times of 1400 s were used for all observations. All the spectra were normalised using IRAF task CONTINUUM. To correct for the Earth's motion around the Sun, the spectra were corrected for the heliocenter using IRAF tasks RVCORRECT and DOPCOR.

*An instrumental modulation of the flux in each order which causes the intensity to rise from one end, reach a peak towards the centre and drop at the other end

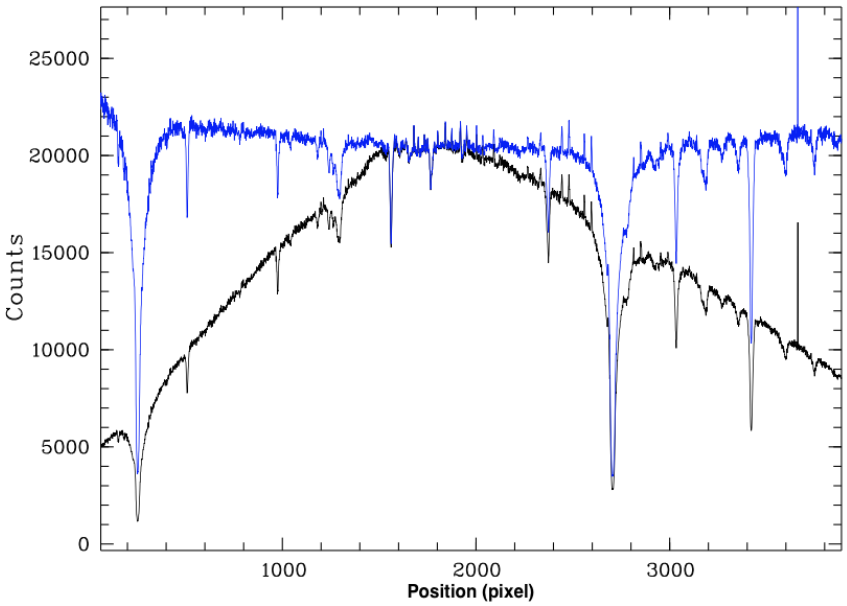

Figure 2.13: An example of flat-fielding performed by the MIDAS pipeline. The blue and black-coloured lines denote flat-fielded and non flat-fielded spectra, respectively.

Table 2.1: Log of observations of 1FGL J1018.6−5856 from SALT with S/N ratio of the blue spectra.

BJD (days)	orbital phase	S/N
2457362.53488	0.360	40
2457363.55958	0.422	43
2457365.55890	0.543	35
2457367.52029	0.661	50
2457371.52145	0.903	40
2457373.53962	0.025	40
2457375.50240	0.144	35
2457377.49907	0.264	15

2.4 Cross-correlation

The measurement of RVs in this work is performed using a mathematical technique called cross-correlation. In basic terms, cross-correlation gives a measure of similarity between two signals at different lag positions. Mathematically, the cross-correlation function (CCF) of an independent variable, x, has the expression (Hilditch 2001):

$$c(x) = \int_{-\infty}^{\infty} f(k)g(k-x)dk, \tag{2.1}$$

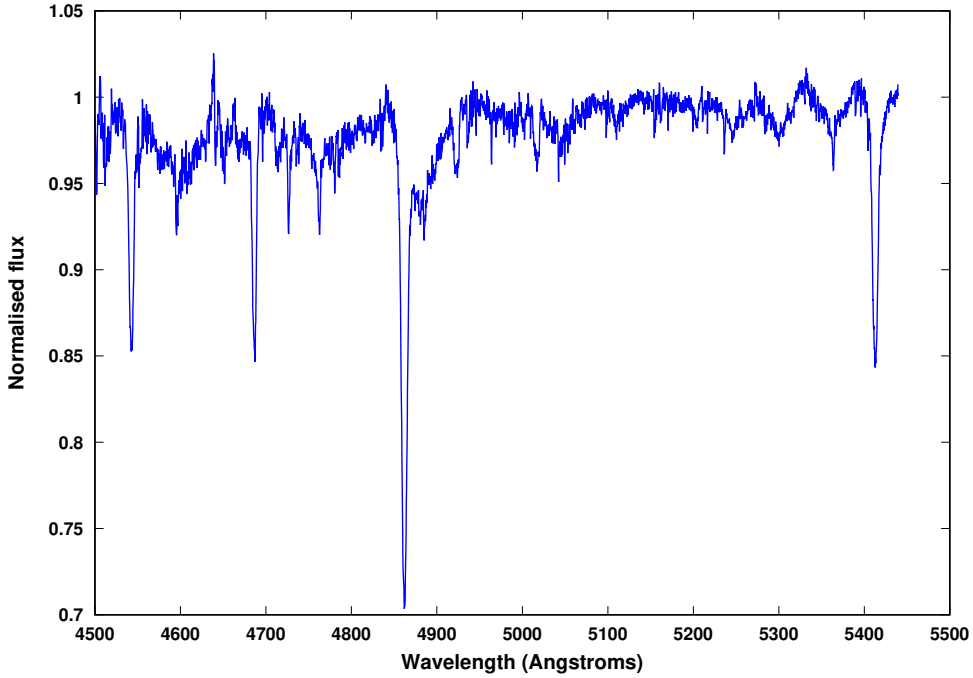

Figure 2.14: Example of a final wavelength-calibrated and stitched blue spectrum for J1018.

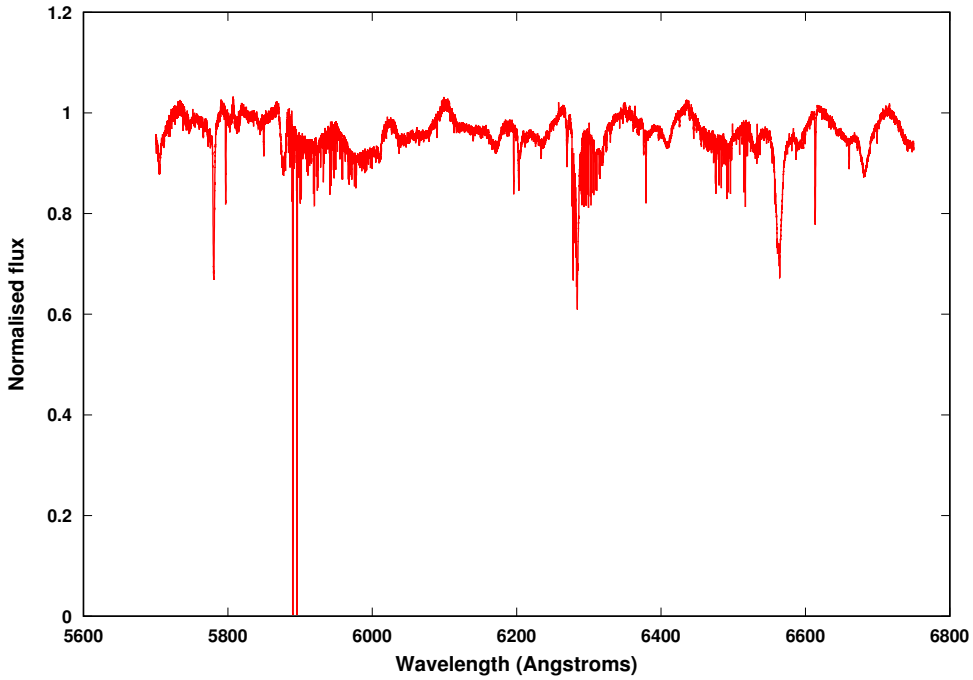

Figure 2.15: Example of a final wavelength-calibrated and stitched red spectrum for J1018.

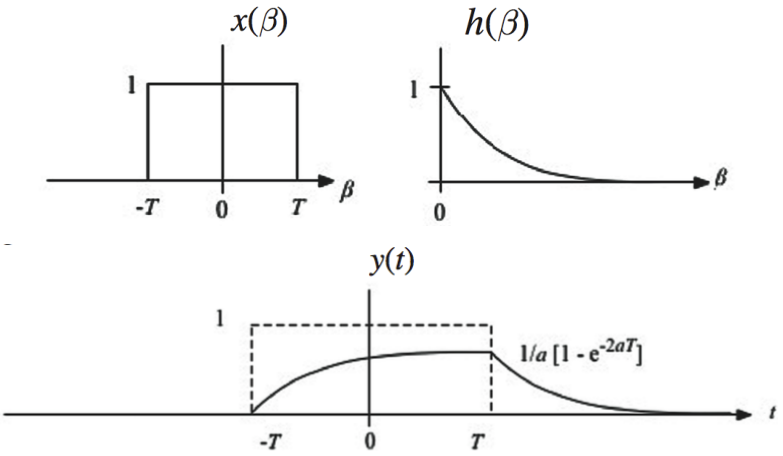

Figure 2.16: Example of cross-correlation of two functions x and h. From Yarlagadda (2009).

where $f(k)$ and $g(k)$ are two functions of the independent variable, k. The two functions, $f(k)$ and $g(k)$, are convolved and the CCF is calculated for a range of x values. Fig. 2.16 is an illustration of the convolution of two simple functions, f and g, with the resultant CCF shown. Below is a summary of the theory of cross-correlation as explained by Tonry & Davis (1979) in their application to RVs of galaxies.

Suppose the spectrum of the star we are interested in is represented by $si(n)$ and that of a template star with a known RV be represented by $st(n)$, where n is the bin number defined by $n = A \ln \lambda + B$. The spectra are sampled into N bins and binned at equal intervals in $\ln \lambda$. The CCF of the two stars is

$$c(x) = \int_{-\infty}^{\infty} si(n) st(n - x) dn. \tag{2.2}$$

The normalised CCF can then be written as

$$c(x) = \frac{1}{N \sigma_{\rm si} \sigma_{\rm st}} \sum_{n=1}^{N} si(n) st(n - x), \tag{2.3}$$

where the $\sigma_{\rm si}$ and $\sigma_{\rm st}$ represent the root-mean-square uncertainties of $si(n)$ and $st(n)$, respectively. Suppose $SI(k)$ and $ST(k)$ are Fourier transforms of $si(n)$ and $st(n)$, respectively, one can calculate the CCF more effeciently, where the Fourier transform of $c(x)$ takes the form:

$$C(k) = \frac{1}{N \sigma_{\rm si} \sigma_{\rm st}} SI(k) ST^*(k), \tag{2.4}$$

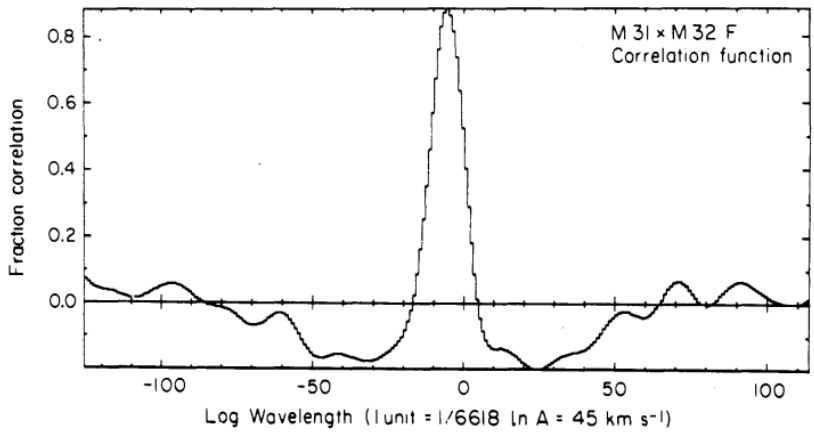

Figure 2.17: Example of a CCF of the galaxy M31 correlated against M32. From Tonry & Davis (1979).

where

$$SI(k) = \sum_{n=1}^{N} si(n)\exp\left[\frac{2\pi ikn}{N}\right], \tag{2.5}$$

and

$$ST(k) = \sum_{n=1}^{N} st(n)\exp\left[\frac{2\pi ikn}{N}\right]. \tag{2.6}$$

ST^* is the complex conjugate of ST. Fig. 2.17 shows an example of a CCF from the result of cross-correlation of the galaxy M31 with M32.

The half-FWHM, μ, of the peak of the CCF is given by:

$$\mu^2 = 2\tau^2 + \sigma^2, \tag{2.7}$$

where τ is the intrinsic half-width of the spectral lines of the template spectrum and σ is the observed half-width of the lines of the object spectrum. The error of the velocity measurements obtained from cross-correlation is then given by the expression:

$$error = \frac{3w}{[8(1+r)]}, \tag{2.8}$$

where w is the FWHM of the correlation peak and r is defined as the ratio of the true correlation peak height to the average peak.

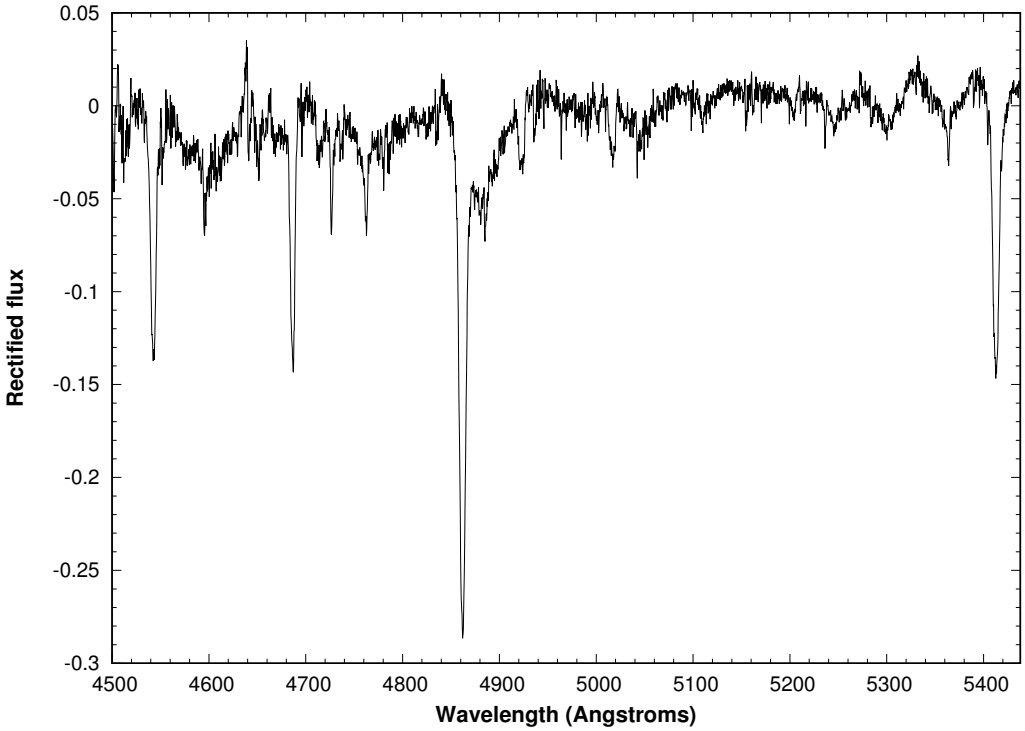

Figure 2.18: Final template used for cross-correlation.

2.4.1 Cross-correlation application

To perform cross-correlation analysis on J1018 spectra obtained with SALT, the IRAF task XCSAO was used. An iterative process described by Foellmi, Moffat & Guerrero (2003) and Manick, Miszalski & McBride (2015) was used to generate a high signal-noise ratio (SNR) zero velocity template. First, individual spectra were rectified and the continuum level subtracted. Each spectrum was then converted to a logarithmic wavelength scale and the spectra were grouped according to SNR (highest to lowest). The RV shifts of each spectrum relative to the spectrum with the highest SNR were measured. Individual spectra were then shifted to the same rest wavelength as the high SNR template using VELSET, from the results of the first cross-correlation iteration, and a mean spectrum was created by combining all the shifted spectra using SCOMBINE (Fig. 2.18). This became the final template spectrum, which was then used to compute the RV shifts (Fig. 2.19).

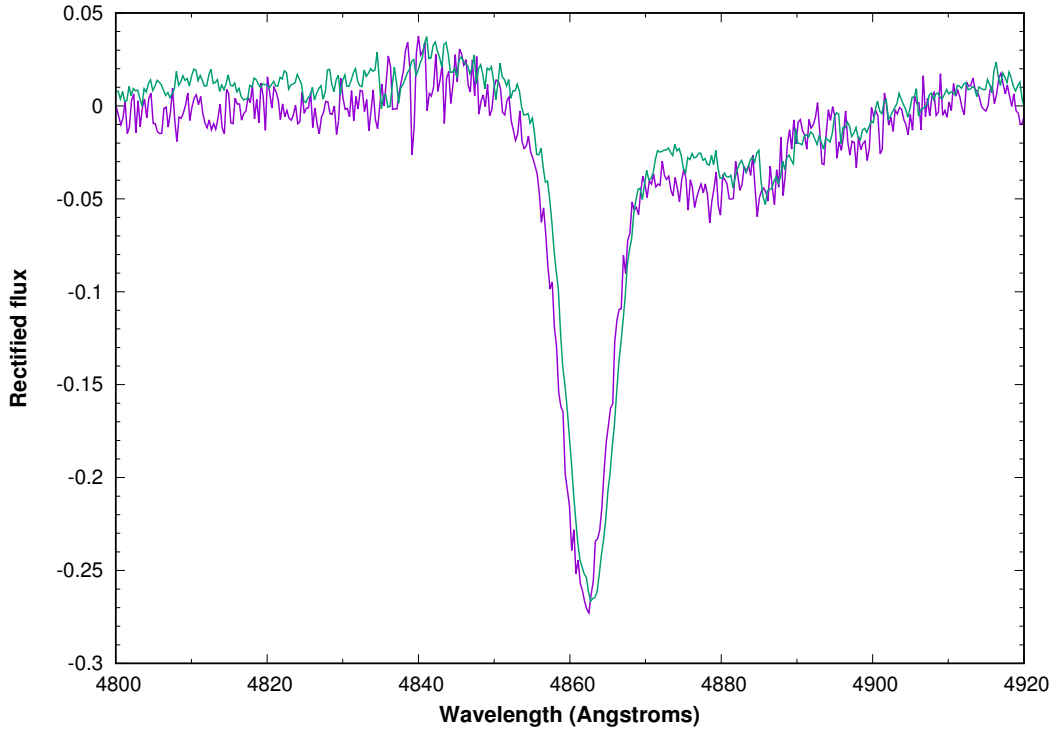

Figure 2.19: Example of a cross-correlation shift of the Hβ line between the object spectrum (purple) and template spectrum (green).

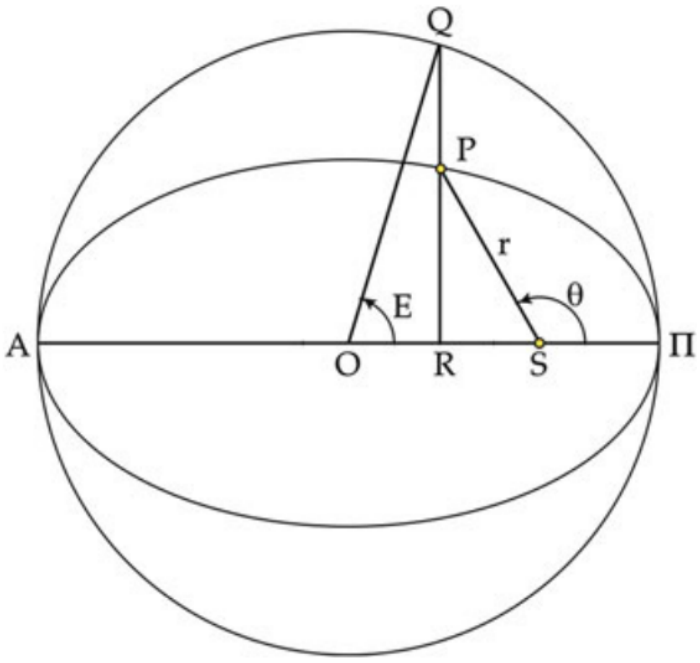

Figure 2.20: Illustration of an eccentric orbit. From Benacquista (2013).

2.5 Kepler's equation and orbital parameters

The following is a summary of the derivation of expressions of the orbital parameters based on notation used by Hilditch (2001) and Benacquista (2013). Fig. 2.20 illustrates different properties of an ellipse, where the centre of the ellipse is denoted by O. Periastron and apastron are marked by Π and A, respectively. With the location of the center of mass being orbited denoted by S, the periastron and apastron distances are given by

$$S\Pi = a(1-e) \tag{2.9}$$

and

$$SA = a(1+e), \tag{2.10}$$

where e is the eccentricity of the orbit and $a = O\Pi = OA$ is the semi-major axis. Suppose the orbiting body is at position P after some time t, then the true anomaly of the source is given by $\theta = \Pi SP$. Another angular parameter is the eccentric anomaly, given by the expression $E = QOR$. From Fig. 2.20 it can be seen that

$$RS = r\cos(180^\circ - \theta), \tag{2.11}$$

and since $\cos(180^\circ - \theta) = -\cos\theta$, it follows that $RS = -r\cos\theta$. Since also

$$RS = -r\cos\theta = OS - OR, OS = ae \text{ and } OR = a\cos E, \tag{2.12}$$

it follows that

$$r\cos\theta = a(\cos E - e). \tag{2.13}$$

From the figure, we see that $PR = r\sin\theta$ and $QR = a\sin E$. This gives

$$r = (r^2\cos^2\theta + r^2\sin^2\theta)^{1/2} = a(1 - e\cos E). \tag{2.14}$$

From eq. 2.13, 2.12 and 2.14, we get

$$\sin\theta = \frac{b\sin E}{a(1-e\cos E)} \tag{2.15}$$

and

$$\cos\theta = \frac{a(\cos E - e)}{a(1 - e\cos E)}, \tag{2.16}$$

where the semi-minor axis is defined by $b = a(1-e^2)^{1/2}$. Taking the derivative of eq. 2.15, we get $\cos\theta d\theta = \frac{b(\cos E - e)dE}{a(1-e\cos E)^2}$. Substituting eq. 2.16 in to this, we get

$$d\theta = \frac{bdE}{a(1 - e\cos E)}. \tag{2.17}$$

With the angular momentum given by $L = [Ma(1-e^2)]^{1/2}$, the specific angular-momentum equation is given by $r^2 d\theta = Ldt$ and substituting eq. 2.17 into this, we get

$$(1 - e\cos E)dE = \frac{Ldt}{ab} \tag{2.18}$$

Integrating the left and right-hand side of eq. 2.18, this gives

$$E - e\sin E = \frac{Lt}{ab} + k \tag{2.19}$$

Setting the initial conditions to the time of periastron, $t = T_p$, when $\theta = 0$ and $E = 0$, we find $k = -(L/ab)T_p$. From Kepler's third law, $M = \frac{4\pi^2 a^3}{P^2}$, we get

$$\frac{L}{ab} = \left[\frac{M}{a^3}\right]^{1/2} = \frac{2\pi}{P} \tag{2.20}$$

Substituting this into eq. 2.19, we get

$$E - e\sin E = \frac{2\pi}{P}(t - T_p) \tag{2.21}$$

Eq. 2.21 is known as Kepler's equation and it describes the position of an orbiting body as a function of time, subject to gravitational influence from a central source.

Fig. 2.21 shows an elliptical orbit of a particle, m_2, in space presented in three dimensions. The observer's line-of-sight is along the z-axis and is perpendicular to the tangent plane of the sky ($xy-$plane). Three angles describe the orbit of the particle: θ, Ω and ω represent the true anomaly, longitude of ascending node and longitude of periastron, respectively. The orbit is inclined relative to the plane of the sky by an angle i ($i = 0°$ means that the orbit is face-on and $i = 90°$ means an edge-on orbit). The position of the particle projected onto

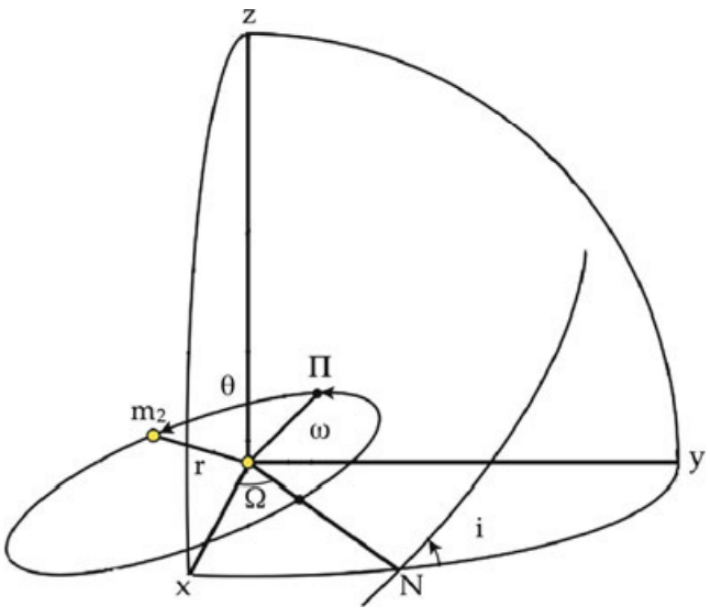

Figure 2.21: Illustration of an eccentric orbit in three-dimensional space. In this figure, i is the inclination angle, Ω is the longitude of the ascending node, ω is the longitude of periastron, m_2 is the particle in orbit, N is the ascending node, θ is the true anomaly, Π is the location of periastron passage of the orbiting particle. From Benacquista (2013).

the line-of-sight along the orbit can be described by the equation

$$z = r\sin(\theta+\omega)\sin i \tag{2.22}$$

The RV of the particle can be obtained taking the derivative of eq. 2.22 with respect to time:

$$\dot{z} = \sin i[\sin(\theta+\omega)\dot{r} + r\cos(\theta+\omega)\dot{\theta}]. \tag{2.23}$$

Using polar equations for an ellipse and Kepler's second law

$$r = \frac{a(1-e^2)}{(1+e\cos\theta)} \text{ and } \dot{r} = \frac{e\sin\theta r\dot{\theta}}{(1+e\cos\theta)}, \tag{2.24}$$

$$r^2\dot{\theta} = \frac{2\pi a^2(1-e^2)^{1/2}}{P}. \tag{2.25}$$

Substituting eq. 2.24 and eq. 2.25 into eq. 2.23, this gives

$$\dot{z} = \frac{2\pi a\sin i}{P(1-e^2)^{1/2}}[\cos(\theta+\omega) + e\cos\omega]. \tag{2.26}$$

The semi-amplitude of the velocity curve is written as

$$K = \frac{2\pi a \sin i}{P(1-e^2)^{1/2}}, \tag{2.27}$$

and so the final expression for the observed RV is

$$v_{\rm rad} = \dot{z} = K[\cos(\theta+\omega) + e\cos\omega] + \gamma, \tag{2.28}$$

where γ is the systemic velocity. From spectroscopic observations, one can calculate RVs, v, at times t and using eq. 2.28 the orbital parameters K, e, ω, T_p, P, and γ can be derived.

Mass function

In a single-lined binary system*, the mass function relates the masses of the components of the binary to the derived orbital parameters from the Keplerian fit of the RV curve. In the following, we will present a derivation of the mass function. In a binary system with components of masses m_1 and m_2, the semi-amplitude of the visible components (suppose it is m_1) is given by

$$K_1 = \frac{2\pi a_2 \sin i}{P\sqrt{1-e^2}}. \tag{2.29}$$

Rearranging this and taking the cube on both sides, we find

$$a_2^3 = \frac{(1-e^2)^{3/2}}{8\pi^3 \sin^3 i} K_1^3 P^3. \tag{2.30}$$

From Kepler's third law, we have $G(m_1+m_2) = \frac{4\pi^2}{P^2}a^3$, where $a = a_1 + a_2$. This can be rearranged as $a^3 = a_2^3(1+a_1/a_2)^3$. Substituting this into Kepler's third law and using the $m_1 a_1 = m_2 a_2$, we get,

$$G(m_1+m_2) = \frac{4\pi^2}{P^2} a_2^3 \left(1 + \frac{m_2}{m_1}\right)^3. \tag{2.31}$$

Substituting equation 2.30 into equation 2.31, we get the final expression for the mass function:

$$f(M) = \frac{(m_2 \sin i)^3}{(m_1+m_2)^2} = \frac{P K_1^3}{2\pi G}(1-e^2)^{3/2}. \tag{2.32}$$

*A binary system in which the spectrum of only one component of the binary is visible.

Using the mass function, one can obtain an estimate of the mass m_2 as a function of inclination angle, given a known value of m_1 determined from other techniques (e.g. mass inferred from determination of the spectral type).

2.6 Results: Radial velocity measurements

The red spectra are complicated by prominent Diffuse Interstellar Band (DIB)* features. Furthermore, there are few absorption lines available for use for the measurement of RVs on the red end, some of which are at the edge of the orders. The combined effect of this causes the merging of the orders to be challenging, as seen in Fig. 2.15, with extended bumps along the continuum. The difficulty in defining the continuum results in large error bars and a large scatter in the measured RVs. The blue spectra were used in the final analysis, covering a wavelength range, 4500−5500 Å. To check the effects of order-merging along the wavelength range, different combinations of the absorption line species were considered for RV measurements, as labelled in Fig. 2.22. As seen in Fig. 2.23, no significant differences are seen between the different wavelength regions considered. The whole wavelength range (region 1) was used for the final RV values, listed in Table 2.2. The relatively large error bars in the RVs could have resulted from the imperfect blaze function removal. Any slight differences in the position of the orders between the flat field spectrum and object spectrum can result in intensity jumps at the overlapping regions of adjacent orders. This results in periodic bumps in the merged 1D spectra which can have an influence of the RV derived from cross-correlation (Fig. 2.24). Moreover, for the absorption lines that lie close to the edges of the orders, this effect could result in slight shifts in the central position of the line when merging the orders. This can be mitigated in late-type stars which contain a sufficient number of narrow lines for cross-correlation to be performed per order. In early-type stars, such as the one studied in this work, cross-correlation per order is impossible due to the low density of absorption lines available for use in each order (at most, there is one line per order).

To obtain a more densely covered phase sampling, the data obtained from the SALT programme was combined with that published by S15. The measurements from Waisberg & Romani (2015a) were not considered since their RV

*absorption features that arise due to interstellar medium (Geballe 2016).

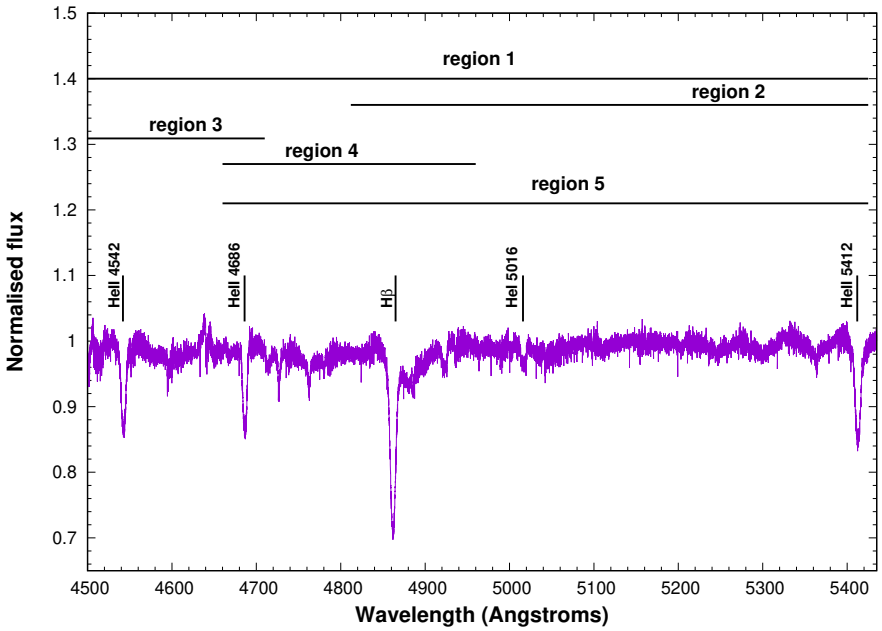

Figure 2.22: Normalized average blue spectrum for the wavelength range used for 1FGL J1018.6−5856, with the strongest lines used for cross-correlation labelled. The different wavelength regions considered for RV measurements are labelled.

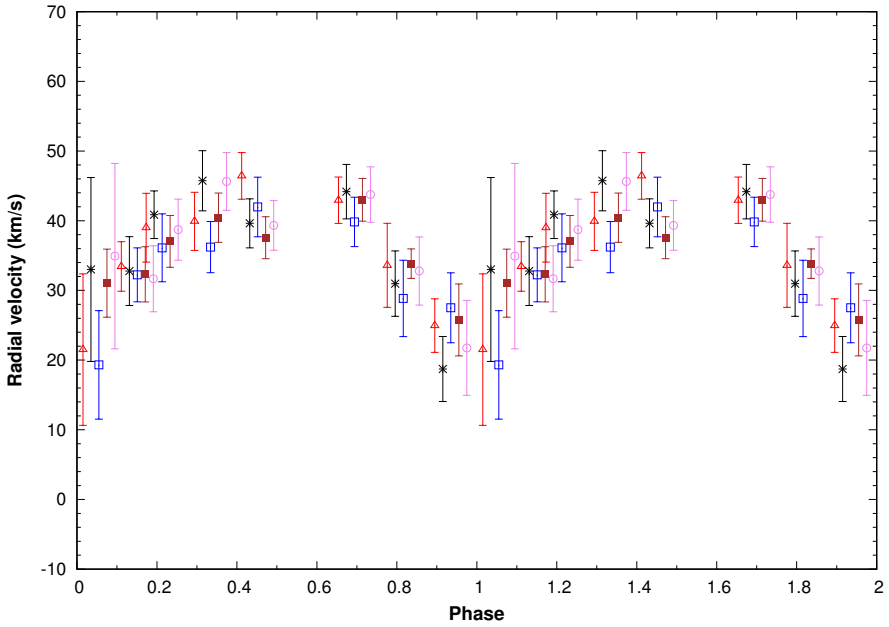

Figure 2.23: Radial velocities from SALT data obtained by considering different line species combinations labelled in Fig. 2.22 with slight horizontal shifts for clarity: red triangles (region 1), black asterisks (region 2), blue open squares (region 3), brown filled squares (region 4) and violet circles (region 5).

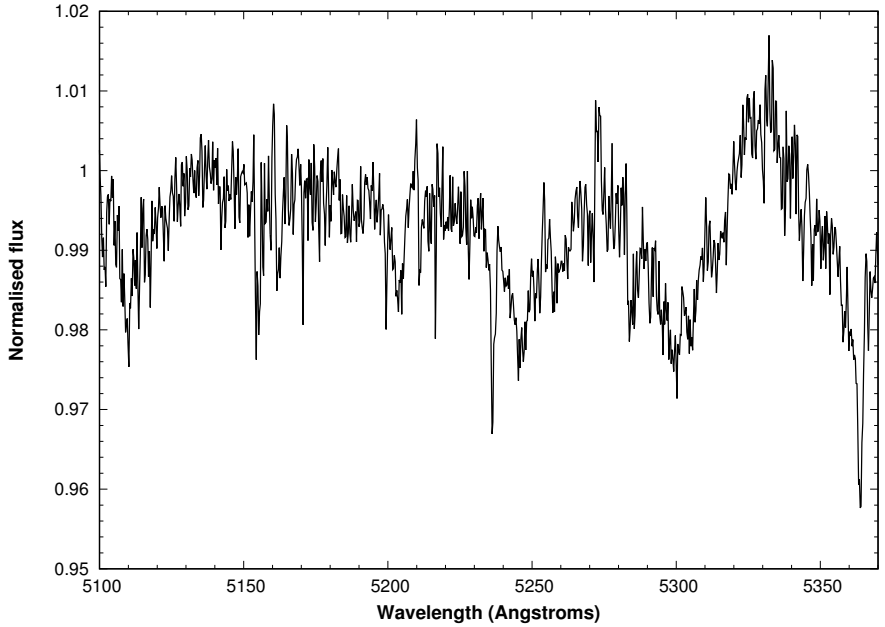

Figure 2.24: Illustration of the intensity jumps along the continuum as a result of imperfect blaze function removal.

curve has a large scatter due to systematic errors related to continuum calibration. S15 measured the RVs by considering the He II (4542 Å and 4686 Å) and Hγ lines separately. The consideration of the different line species separately in measuring RVs of O stars in gamma-ray binaries was undertaken by Casares et al. (2005b) and Sarty et al. (2011) in the case of LS 5039. For both studies, systemic offsets in velocity were observed in the HI, He I and He II lines, and it was noted that the HI are systematically more blue-shifted than the He lines. In a study of mass-loss and wind momentum rates of O stars, Puls et al. (1996) used analytical line-formation techniques to demonstrate that the HI and He I lines are more contaminated by wind emission than the higher excitation He II lines. Casares et al. (2005b) and Sarty et al. (2011) therefore conclude that the He II lines provide more reliable RV measurements. For this reason the RV measurements from SALT are combined with those of He II measurements from S15 for the final analysis of this study. The RV measurements from this work show a systematic difference of 9.3 km/s (from the systemic velocity, γ) to those from S15, and so we corrected for this by adding this value to our measurements. Such systematic differences between combined RV datasets from independent studies have been reported for LS 5039 and LS I +61 303 (e.g. Casares et al. 2012, Grundstrom et al. 2007, Aragona et al. 2009).

Table 2.2: Radial velocities of 1FGL J1018.6−5856 from SALT corrected for the systematic difference of values from S15. Phase zero is chosen to co-incide with MJD55403.3 (phase of INFC; Corbet et al. 2011).

BJD (days)	Orbital phase	Velocity (km/s)
2457362.53488	0.360	31.4 ± 3.6
2457363.55958	0.422	36.9 ± 4.9
2457365.55890	0.543	37.9 ± 4.2
2457367.52029	0.661	44.4 ± 3.4
2457371.52145	0.903	40.9 ± 3.3
2457373.53962	0.025	31.6 ± 6.0
2457375.50240	0.144	22.9 ± 3.9
2457377.49907	0.264	19.5 ± 10.9

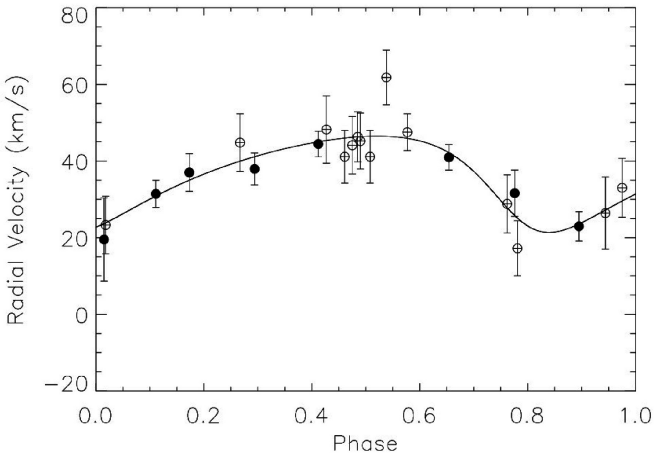

Figure 2.25: Best-fit curve to the radial velocities of the HeII lines. The unfilled circles are from Strader et al. (2015) and the filled circles are from this work.

Fig. 2.25 shows the folded RV curve with a Keplerian model fitted onto it. To perform the fit to the RVs and obtain the orbital parameters, we used the IDL package RVLIN, developed by Wright & Howard (2009). RVLIN employs the Levenberg-Marquardt method (Levenberg 1944, Marquardt 1963) that uses non-linear least squares techniques by minimising the χ^2. The uncertainties in the orbital parameters were obtained using the BOOTTRAN package supplied by Wang et al. (2012). BOOTTRAN uses bootstrapping techniques, where the main idea is to perform re-sampling from the original input data to create a bootstrap sample (with 1000 bootstrap replicates). The orbital parameters are then derived for each sample from the bootstrap sample, where the standard deviation of each of the orbital parameter collection provides the standard error of that parameter.

Table 2.3: Orbital elements of 1FGL J1018.6−5856

Parameter	Value
$P_{\rm orb}$ (days)	16.544 (fixed)
$T_{\rm p}$ (JD)	2457256.0 ± 1.2
e	0.31 ± 0.16
$\omega(^\circ)$	89 ± 30
K (km/s)	12.3 ± 1.9
γ (km/s)	35.5 ± 1.3
RMS of fit (km/s)	5.85

We fixed the period of the fit to that obtained from X-ray analysis of the source (P = 16.544 days, An et al. 2015). For a Keplerian fit with the period as a free parameter, a period of $P = 16.583 \pm 0.042$ days is obtained, in excellent agreement with the period derived from X-ray and GeV data ($P = 16.549 \pm 0.007$ days from *Fermi/LAT* GeV data). The derived orbital parameters are summarised in Table 2.3. From the derived orbital parameters, we obtained a mass function of $f(M_{\rm X}) = 0.0027 \pm 0.0013$ M$_\odot$. Using this value for the mass function we made a mass-mass plot, as shown in Fig. 2.26, to show the relationship between the mass of the compact object vs. optical companion as a function of inclination angle of the orbit. We used a canonical mass range of $M_{\rm o} = 20 - 26.4$ M$_\odot$ for the optical companion, as used by Casares et al. (2005b), Strader et al. (2015), Waisberg & Romani (2015b), given the spectral class of O6V((f)). A canonical neutron star mass range of $1.4 - 2.5$ M$_\odot$ implies an inclination angle range of $i \approx 50 - 26^\circ$ for the lower limit mass of the optical companion ($M_{\rm o} = 20$ M$_\odot$). An inclination angle range of $i \approx 70 - 32^\circ$ is implied for the upper limit mass of the optical companion ($M_{\rm o} = 26.4$ M$_\odot$). Antoniadis et al. (2013) report a mass of $M = 2.01 \pm 0.04$ M$_\odot$ for PSR J0348+0432, a pulsar in a binary orbit with a possible low-mass white dwarf. This makes this the most massive neutron star currently known, and for this mass value, inclination angles of $i = 33^\circ$ and $i = 41^\circ$ are obtained for $M_{\rm o} = 20$ M$_\odot$ and $M_{\rm o} = 26.4$ M$_\odot$, respectively. A BH ($M_{\rm x} \geq 3.0$ M$_\odot$) implies lower inclination angles of $i \leq 22^\circ$ and $i \leq 26^\circ$ for $M_{\rm o} = 20$ M$_\odot$ and $M_{\rm o} = 26.4$ M$_\odot$.

2.7 Discussion

The value of the mass function obtained from this study agrees with that found by S15 to within the errors. For the mass range of the companion star

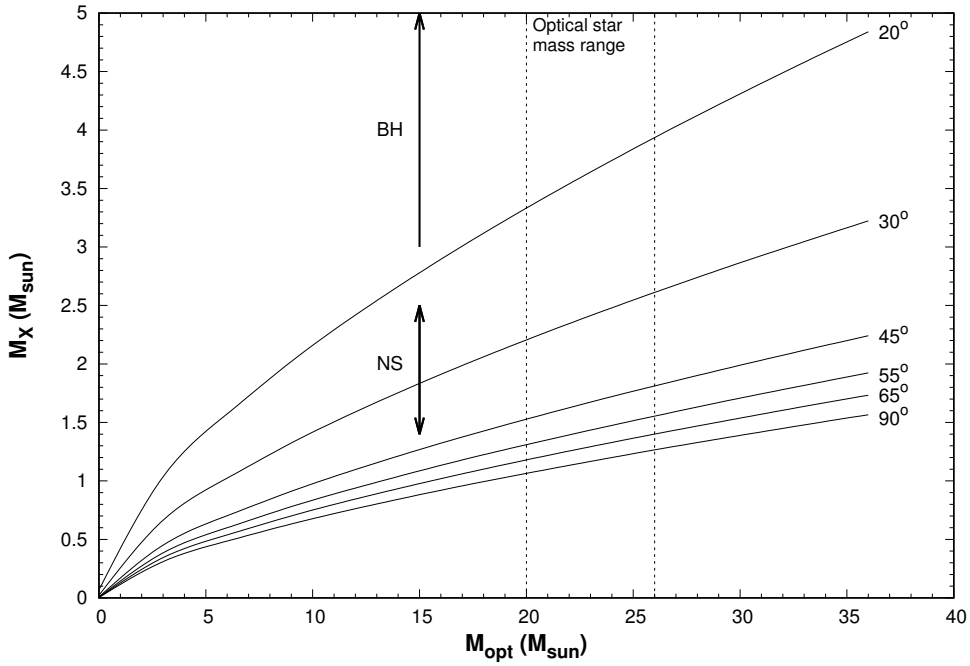

Figure 2.26: Mass constraints for the two stars in 1FGL J1018.6−5856 for different inclination angles. The two vertical lines show the mass range for the optical star.

considered, similar values for the allowed inclination angles for different masses of the compact object are found (Fig. 2.26). A best-fit Keplerian model with eccentricity $e = 0.31 \pm 0.16$ is obtained. The probability of this model, given the data in this study, is $P(\chi^2 > 11.05)$ ∼85% (a circular fit results in a probability ∼50%).

High energy studies

Fig. 2.27 shows the phasograms of the X-ray, HE and VHE emission of J1018. As seen in Fig. 2.27, the lightcurves at the different wavelengths are roughly correlated, with maxima occurring close to $\phi = 0$ (the X-ray lightcurve shows a second sinusoidal peak at $\phi \sim 0.3$). In other GRBis, the VHE and X-ray flux are correlated, while the GeV flux is anti-correlated with the VHE and X-ray flux (Dubus 2013). Whatever the nature of the compact object, if the gamma-rays are produced by anisotropic Compton scattering of star-light photons, (see chapter 4), the HE emission is expected to occur at phases when the compact object is behind the optical companion relative to our line-of-sight (superior conjunction, SUPC), while the VHE emission is expected to occur around inferior conjunction (INFC, since $\gamma - \gamma$ absorption peaks at SUPC). The peculiar

feature of the similar orbital modulation of VHE and HE lightcurves of J1018 could possibly be explained by a low orbital inclination (H. E. S. S. Collaboration et al. 2015). Moreover, the relatively low amplitude modulation ($\sim 25\%$) observed from GeV data implies a low eccentricity and inclination of the orbit ($i \leq 50°$; Fermi LAT Collaboration et al. 2012, H. E. S. S. Collaboration et al. 2015, Chen et al. 2017). An & Romani (2017) model the X-ray and gamma-ray light curves and SED of J1018, where the spike in the modulated X-ray light curve is modelled and fitted by an orbital eccentricity of $e = 0.35$ and inclination angle of $i \sim 50°$. The geometric orientation required for the model proposed by An & Romani (2017), however, uses a longitude of periastron that is at odds with the one obtained from this work. The value of the longitude of periastron passage obtained in our work has a large error bar and future observations with smaller error bars in the RVs will be crucial in constraining this. These inferences of the inclination angle and eccentricity of the orbit from high energy observations and modelling of J1018 suggest a low-mass compact object ($M_{\rm X} < 2.0$ M$_\odot$, Fig. 2.26), favouring a NS.

Optical companion

Donor stars in HMXBs have been shown to exhibit different properties to their isolated counterparts of similar spectral types (Conti 1978, Rappaport & Joss 1983, Kaper 2001). As a result of the interaction with the compact object, massive stars in binary systems undergo different evolutionary paths compared to isolated stars, resulting in undermassive and undersized optical companions in HMXBs for a given spectral type. As follows, the mass estimates used for the O star in this study could be lower by up to 3 M$_\odot$ (e.g. Coe et al. 2015, Rajoelimanana et al. 2017), which would make the NS even more likely.

Orbit geometry

Fig. 2.28 shows the relative orbit of the compact object with mass, $M_{\rm X} = 1.4$ M$_\odot$, around an optical companion of mass and radius, $M_{\rm O} = 22.9$ M$_\odot$ and $R_{\rm O} = 9.3$ R$_\odot$ (Casares et al. 2005b), respectively. As seen from the orbital geometry, periastron passage occurs close to phases when the compact object is at INFC. The derived orbital geometry as illustrated in Fig. 2.28 was suggested by S15 as a possible solution to the high energy emission (X-ray, HE and VHE)

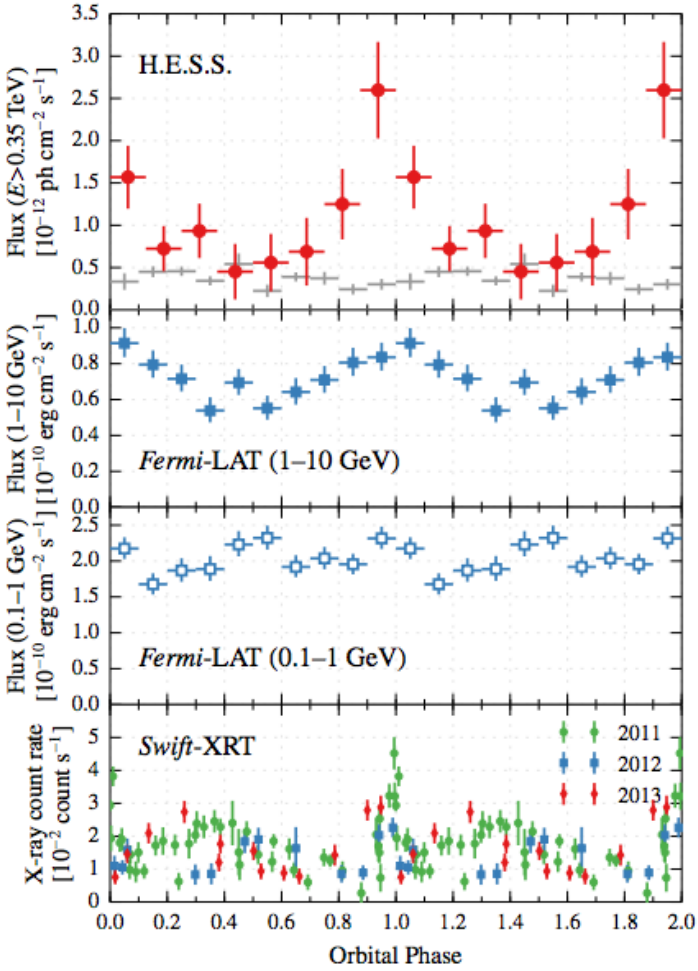

Figure 2.27: Folded lightcurves of J1018 (top to bottom): $HESS$, $Fermi(1-10$ GeV), $Fermi(0.1-1$ GeV), $Swift-XRT$. From H. E. S. S. Collaboration et al. (2015).

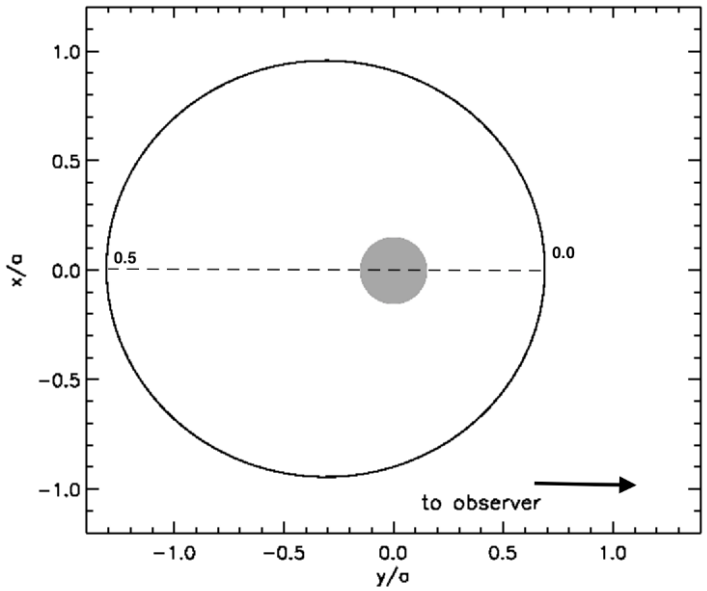

Figure 2.28: The orbit of the compact object around the optical companion (shaded circle) in J1018 as seen from above the orbital plane. Periastron and apastron phases are indicated in the plot. The coordinates are in units of the semimajor axis.

maxima occurring at the same phase (INFC) in a model where the mechanism responsible for the emission is anisotropic inverse Compton scattering.

Period vs. eccentricity

We plot the orbital period and eccentricity of J1018 alongside those of other HMXBs, following the work of Townsend et al. (2011) (Fig 2.29). As seen in the plot, J1018 lies roughly around the transition region between supergiant and Be X-ray binary systems. Another notable feature is the correlation between eccentricity and orbital period for the five GRBis with known orbital parameters, which was first discussed by Casares et al. (2012). A linear least-squared fit for GRBis is included in the plot and is represented by the relation:

$$e = 0.276 \log P + 0.070. \tag{2.33}$$

Casares et al. (2012) speculated that the correlation between P and e in GRBis is due to the requirement of the two bodies to be close enough for efficient VHE emission to be triggered, which for long period systems requires large eccentricities. The limited sample of GRBis exhibit similar behaviour as the traditional accreting HMXBs, supporting the notion that GRBis are progeni-

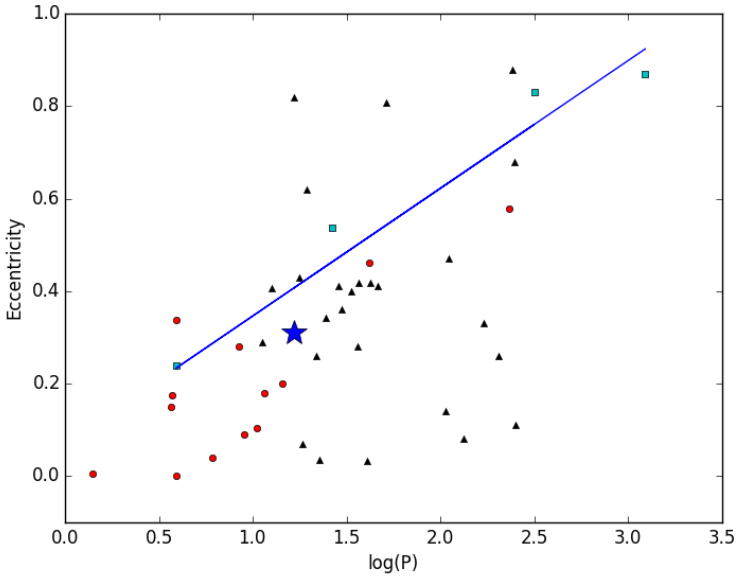

Figure 2.29: Updated orbital period against eccentricity for HMXBs from Townsend et al. (2011) for supergiant (red circles), Be X-ray (black triangles) and GRBi (cyan squares) systems. The blue star represents J1018. The blue curve represents a best-fit curve to the GRBis.

tors of HMXBs.

2.8 Conclusion

J1018 was observed using SALT and the RV measurements obtained are combined with those from S15 to attain a wider and more densely sampled phase coverage. A Keplerian fit to the RV measurements results in an eccentricity of $e = 0.31 \pm 0.16$ and a mass function of $f(M_{\rm x}) = 0.0027 \pm 0.0013$ $M_{\odot}$. The value of the eccentricity obtained agrees, to within errors, with estimates inferred from the analysis of high energy data and theoretical modelling. Using a mass range of $20 - 26.4$ $M_{\odot}$ for the optical companion, the resultant mass function implies masses for the compact object which favour a NS. From the orbital parameters obtained, a BH as the compact object in J1018 is possible only for very low inclination angles of $i \leq 26°$.

In this work, a NS is favoured for the compact object, supporting the PWM scenario for J1018. McSwain et al. (2011) present radio pulsar search results for LS I +61 303 and LS 5039, where they report upper limits of flux density between 4.1 μJy to 14.5 μJy. They postulate that the lack of detection of pulsation in the two systems is due to free-free absorption by the dense stellar

wind environment. They speculate, however, that there is hope for detection at higher frequencies ($\geq$9 GHz) if the contact discontinuity shelters the pulsar from the stellar wind (LS 5039) or at certain favourable orbital phases when the circumstellar disc has minimal absorption effects (LS I +61 303). Indeed, the pulsations in PSR B1259−63 are seen to disappear from $\sim$20 days before to $\sim$20 days after periastron passage when the pulsar is in the vicinity of the high free-free opacity (Johnston et al. 2005, Moldón et al. 2011). The relatively tight orbit of J1018 could be the reason for the lack of pulsations, as the free-free absorption is too high due to the pulsar being in constant close proximity to the dense stellar wind.

Future observations will be important to reduce the error bars of the derived orbital parameters. More specifically, the constraint on the longitude of periastron, and therefore the geometry of the system, is more crucial for high-energy modeling of J1018 to explain the puzzling occurrence of HE and VHE peaks and troughs at a similar orbital phase.

Chapter 3

Be disc variability of LS I +61 303

LS I +61 303 is one of the most extensively monitored HMXBs which has displayed enigmatic behaviour, both on long and short timescales, across the whole electromagnetic spectrum. This chapter presents analysis of long-term optical data of LS I +61 303 (LSI hereafter) obtained with the Liverpool Telescope, the 188 cm reflector telescope at the Okayama Astrophysical Observatory, the Subaru telescope and the Canada France Hawaii Telescope. The data is analysed in conjunction with a semi-analytical model developed by Prof. Atsuo Okazaki presented in Appendix A to study detailed long-term geometric disc variability through the analysis of different properties of the Hα emission line. The results presented here will be published in Monageng et al. (2018, in prep.).

This chapter is written as follows: In section 3.1 we give an introduction to LSI, where a brief multiwavelength picture of the source is provided. We then describe the main properties of Be discs, where we discuss the literature on the Be phenomenon, as well as detail the observational features of Be discs and the measurement of Be disc sizes (section 3.2). Section 3.3 gives a description of the Kozai-Lidov mechanism, where the effect on test particles and hydrodynamical discs is explained. This effect is discussed as a way of putting into context some of the interpretation of the results in this chapter. The background and observational setup of The Liverpool Telescope is provided in section 3.4, as this was used as the main workhorse for the data collected for LSI. In section 3.5 we discuss the results for LSI where we present measurements of different properties of the Hα line and interpret these to explain the long term variability

of the disc.

3.1 Background and observational properties

LSI was discovered as a highly variable radio source during a survey of the Galactic plane and was found to coincide in position with the gamma-ray source CG 135+1 (Gregory & Taylor 1978). Radio observations performed with the NRAO 91 m transit telescope revealed a period of 26.5 days with a possible optical counterpart of B-spectral type identified (Gregory & Taylor 1981). Using spectra obtained with the Dominion Astrophysical Observatory (DAO) 1.8 m telescope, Hutchings & Crampton (1981) confirmed the optical companion as a rapidly rotating B0 Ve star, as the spectra revealed broad Balmer (Hα and Hβ) and HeI emission lines.

LSI has also been studied extensively at radio wavelengths with a wealth of data collected, dating back to the 1970s. The best known ephemeris for LSI is from Bayesian analysis of radio data performed by Gregory (2002):

$$\begin{aligned} P_{\rm orb} &= 26.4960 \pm 0.0028 \text{ days}, \\ P_{\rm SO} &= 1667 \pm 8 \text{ days}, \\ T_0 &= JD2443366.775, \end{aligned}$$

where $P_{\rm orb}$ is the orbital period, $P_{\rm SO}$ is the superorbital period and T_0 is the epoch of zero orbital phase. As with other members of its class (PSR B1259−63 excluded), the nature of the compact object in LSI has been argued to be either a NS or BH. This makes the debate between the MQ and the PWM as the physical scenario for LSI ongoing. Observations performed with the European very-long-baseline interferometry Network (EVN) revealed an elongated structure which was interpreted as a Doppler-boosted jet with a lower limit $0.4c$ for the velocity (Massi et al. 2001). Moreover, observations obtained with the Multi-Element Radio-Linked Interferometer (MERLIN) over two consecutive days revealed hints of a fast-precessing, jet-like structure which was likened to that of the well-known precessing jet of SS 433 (Fig. 3.1; Massi et al. 2004). These results supported the MQ scenario for LSI. Micro-arcsecond images obtained with the Very Long Baseline Array (VLBA) covering the full orbit, however, revealed an elongated structure with non-relativistic speeds which was interpreted as a pulsar wind nebula shaped by the anisotropic environment (Fig. 3.2; Dhawan, Mioduszewski & Rupen 2006). This suggested that

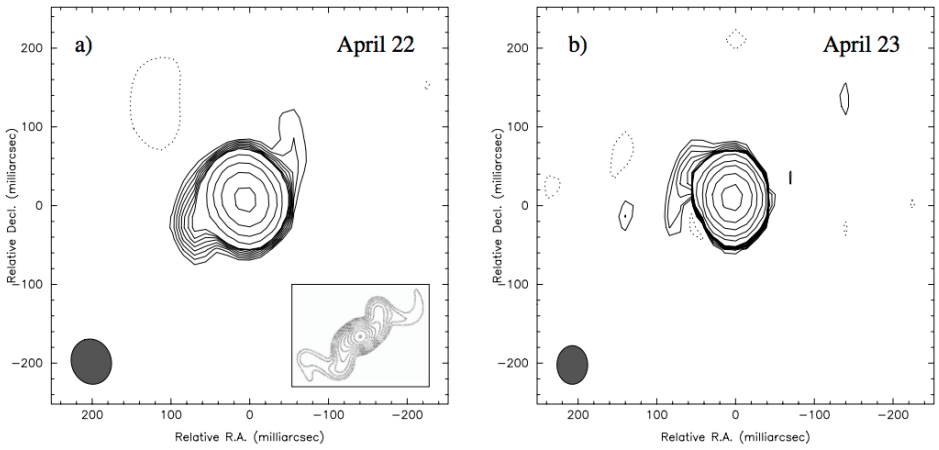

Figure 3.1: MERLIN images of LSI showing precessing, jet-like features similar to those seen in SS 433 (insert in the left image). From Massi et al. (2004).

the PWM in LSI cannot be ruled out. These results were brought into question, however, when Massi, Ros & Zimmermann (2012) re-analysed the VLBA data, improving the dynamic range of the images, and found several images with a double-sided structure. The change from a double-sided to a one-sided structure cannot be explained by the PWM, however, in a MQ scenario a precessing jet can explain this morphology in terms of variable Doppler boosting.

At optical wavelengths, spectroscopic observations revealed double-peaked emission lines from the Balmer series and the HeI 5870 Å line (Zamanov et al. 1999). The strength of the Hα emission has been seen to vary in the range $-8 \leq EW_{H\alpha} \leq -18$ Å (Fig. 3.3; Zamanov et al. 1999; 2013; 2014, Grundstrom et al. 2007). Using the Hα peak separation, Zamanov et al. (2016) estimated the long-term disc size variability and it was found that the disc is truncated at the 2:1 resonance for a majority of the time (assuming Be star and compact object masses of 15 $M_\odot$ and 1.4 $M_\odot$, respectively). It was also noted that the compact object only interacts with the outer parts of the disc and does not penetrate deep into the disc.

In the X-ray domain, LSI was first detected with the Einstein Observatory Imaging Proportional Counter (IPC) and High Resolution Imaging camera (HRI) at $0.15 - 3$ keV and $0.4 - 4$ keV energies, respectively (Bignami et al. 1981). For a long time the direct determination of the orbital period at X-ray energies was elusive, with data collected with different instruments being sporadic and the monitoring periods too short to cover a full orbit and hence perform comprehensive timing analysis (e.g. Chernyakova, Neronov & Walter 2006, Taylor et al. 1996, Goldoni & Mereghetti 1995). The first power

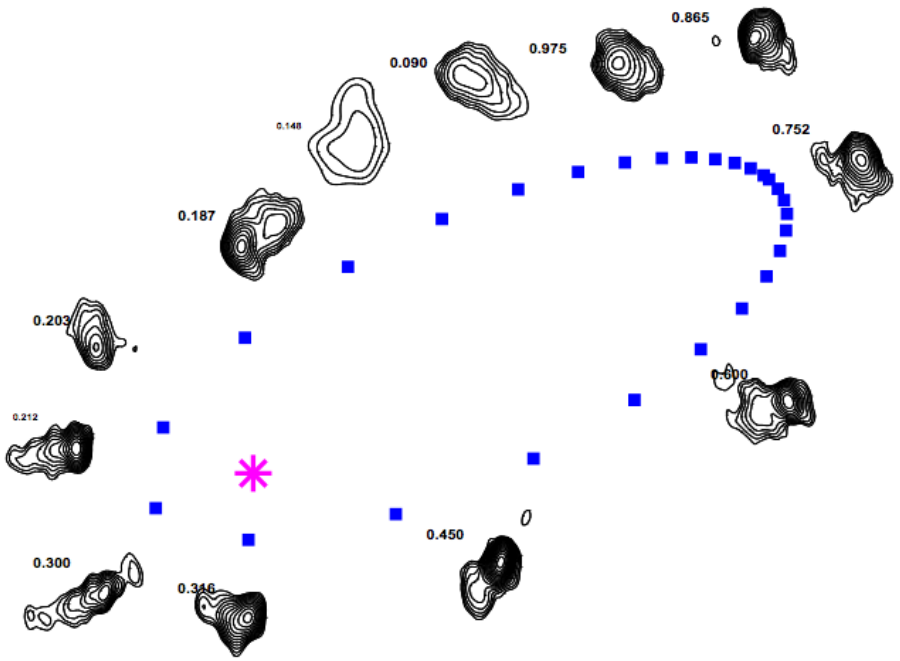

Figure 3.2: VLBA images of LSI showing a pulsar wind nebula changing shape along the orbit. The image has a resolution of 3×2.2 AU. From Dhawan, Mioduszewski & Rupen (2006).

spectrum analysis was performed on hard X-ray ($20 - 60$ keV) data from INTEGRAL/ISGRI where a signal at 27 ± 4 days was detected (Fig. 3.4; Zhang et al. 2010).

The first detection of an orbital modulation in LSI at GeV energies was done with Fermi/LAT at 20 MeV – 100 GeV using data spanning ∼7 months (Abdo et al. 2009). The observations served to confirm the association of the COS B source, 2CG 135+01 with LSI. Timing analysis of the LAT lightcurves revealed the orbital period of 26.6 ± 0.5 days. The folded lightcurve displays a peak just after periastron passage (Fig. 3.5).

The first detection of LSI at VHE was obtained with the Major Atmospheric Gamma Imaging Cherenkov (MAGIC) telescope with detections made at similar orbital phases ($\phi_{\rm orb} \approx 0.4 - 0.7$) over six orbital cycles (Albert et al. 2006). This detection was confirmed with follow-up observations performed using both MAGIC (Albert et al. 2008; 2009) and the Very Energetic Radiation Imaging Telescope Array System (VERITAS, Acciari et al. 2008; 2009; 2011). Periodicity on the orbital timescale was obtained from data observed with MAGIC, where a period of 26.8 ± 0.2 days was detected (Fig. 3.6; Albert et al. 2009).

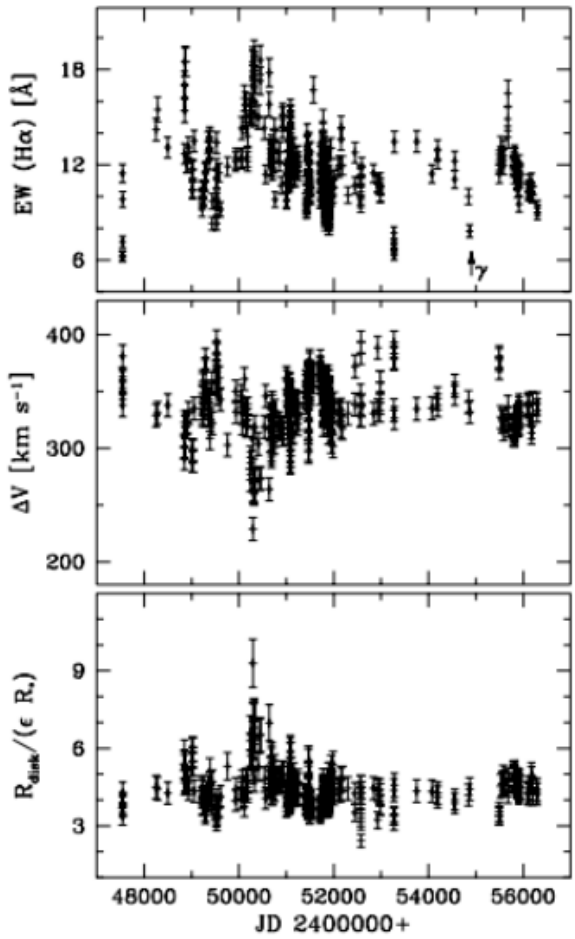

Figure 3.3: Spectroscopic variability of different properties of the Hα emission line in LS I . From top to bottom: Equivalent width, peak separation and disc radius. From Zamanov et al. (2013).

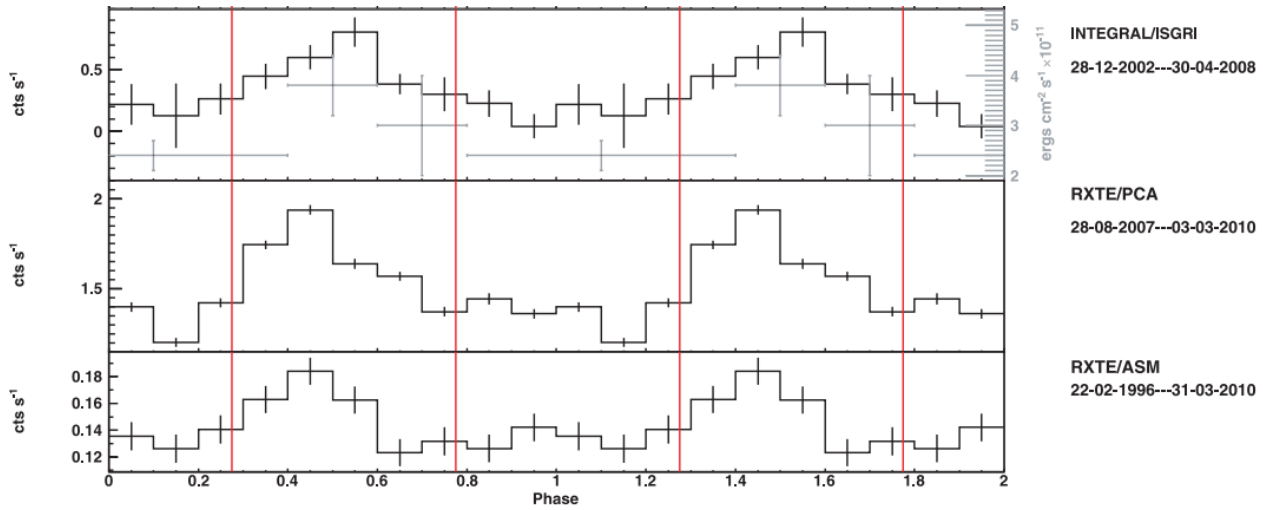

Figure 3.4: Folded X-ray flux variability in LS I. From top to bottom: INTEGRAL/ISGRI, RXTE/PCA AND RXTE/ASM. The red vertical lines represent periastron (phase = 0.23) and apastron (phase = 0.775) passages. From Zhang et al. (2010).

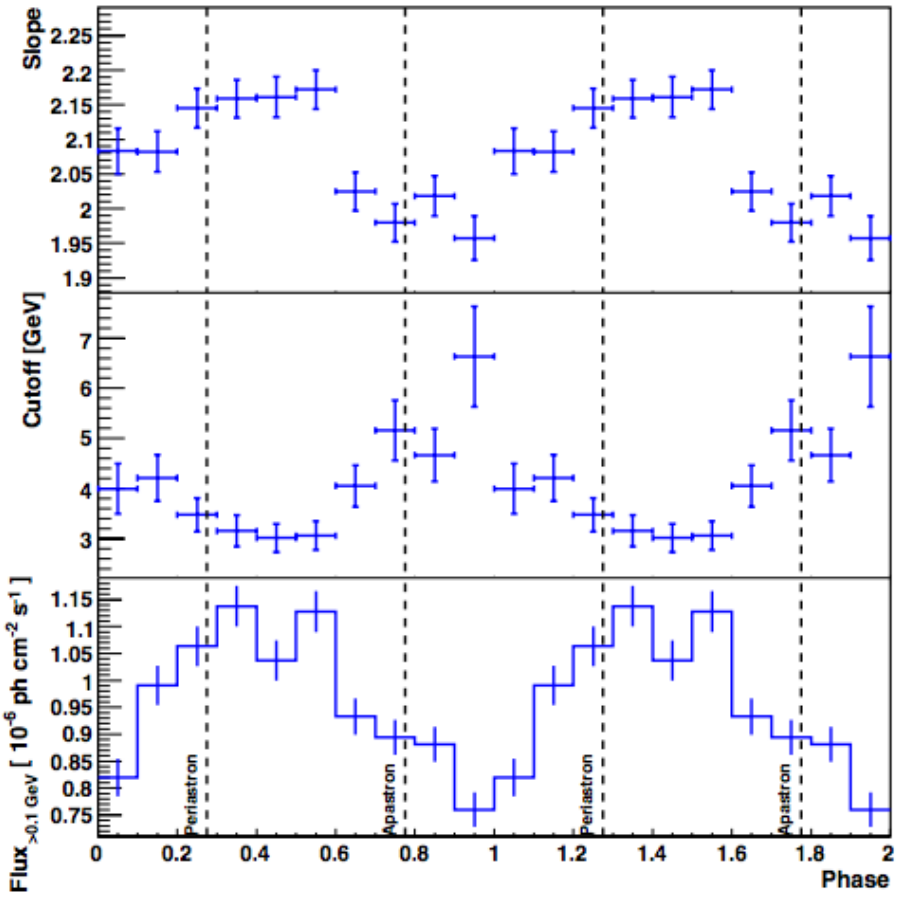

Figure 3.5: Variability of the Fermi spectral parameters in LSI. From top to bottom: Spectral index, cutoff energy and flux modulation. From Hadasch et al. (2012).

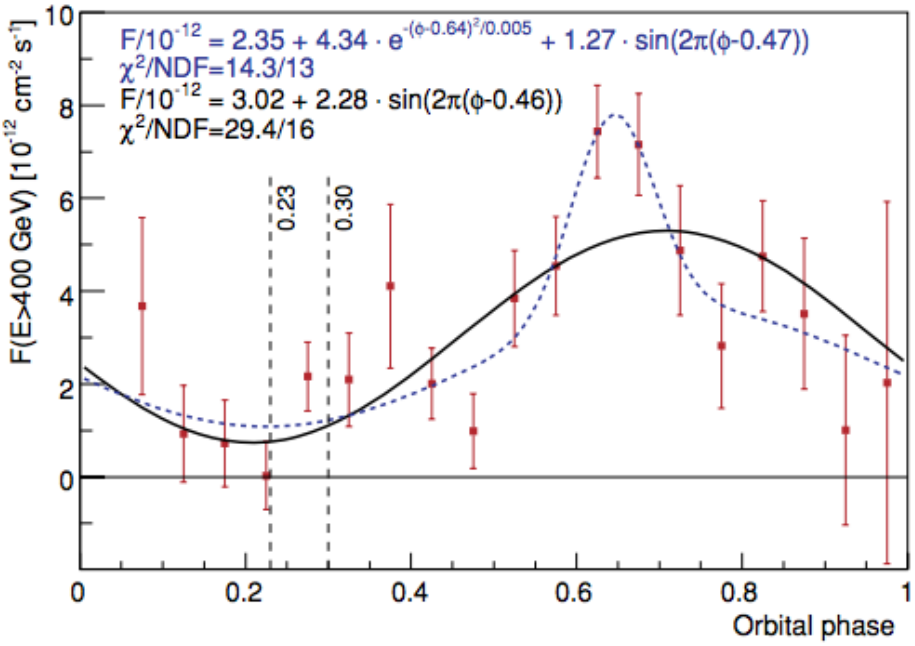

Figure 3.6: Folded MAGIC lightcurve of LS I fitted with a sinusoidal curve (solid black line) and sinusoidal plus Gaussian function (blue, dashed line). From Albert et al. (2009).

Superorbital modulation

What sets LSI apart from other GRBis is that in addition to the orbital period, a longer superorbital period has been observed at all wavelengths. This long-term periodicity was first detected at radio wavelengths when ten years of data from the National Radio Astronomy Observatory (NRAO) 91 m telescope revealed a 4-year modulation (Gregory, Peracaula & Taylor 1999). The authors of that work suggested two possible explanations for this: variable beaming from a precessing relativistic jet and variable accretion due to quasi-cyclic Be star envelope variability. Paredes, Estalella & Rius (1990) confirmed the presence of the superorbital period using data from the NASA Deep Space Network (DSN) and obtained an improved estimate of the period of 1476 days in the radio peak flux density (Fig. 3.7).

Zamanov et al. (1999) first hinted at the presence of the superorbital modulation at optical wavelengths when variability of the Hα equivalent width (EW) was seen on the long timescale. Zamanov et al. (2013) confirmed the presence of the superorbital modulation, where timing analysis of the Hα EW variability revealed a period of 4.86 years (Fig. 3.8b). Optical photometric data also revealed superorbital periodicity when a positive orbital phase shift was seen

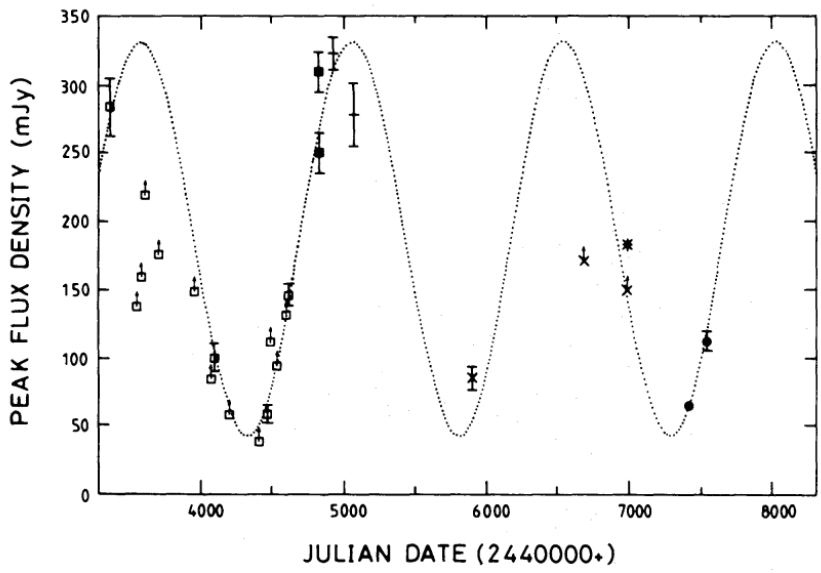

Figure 3.7: Long term evolution of the radio outburst peak flux of LSI fitted with a sine curve of best-fit period $P = 1476$ days. From Paredes, Estalella & Rius (1990).

in data obtained over two seasons (1 year apart), similar to the behaviour at radio wavelengths (Fig. 3.8a; Paredes-Fortuny et al. 2015).

In the X-rays, the superorbital modulation was observed through the analysis of Rossi X-ray Timing Explorer (RXTE) data when Chernyakova et al. (2012) noted that the peak X-ray emission drifts in the orbital phase range $\sim 0.35 - 0.75$ within one cycle of the superorbital period. In an independent analysis of RXTE data, Li et al. (2012) also detected evidence of the superorbital modulation when the peak X-ray flux was seen to be modulated on a period of 1667 days (Fig. 3.9).

At GeV energies, Ackermann et al. (2013) analysed Fermi/LAT data where the data is binned in tenths of the orbital phase and the superorbital period is seen to be more prominent in data obtained at phases near apastron. The final regime in which the superorbital modulation in LSI was detected is at TeV energies, with folded flux from MAGIC and VERITAS on the superorbital period fitted with a sinusoidal curve (Fig. 3.10b; Ahnen et al. 2016).

The origin of the superorbital modulation has been a subject debate since it was first detected, with a few scenarios proposed. On the one hand the superorbital modulation is attributed to changes in the Be star/disc system. In this scenario, quasi-cyclic changes in the Be star envelope result in variable accretion which is modulated on the superorbital period (Gregory et al. 1989, Zamanov et al. 1999; 2013). Alternatively, a precessing jet model has been proposed, where

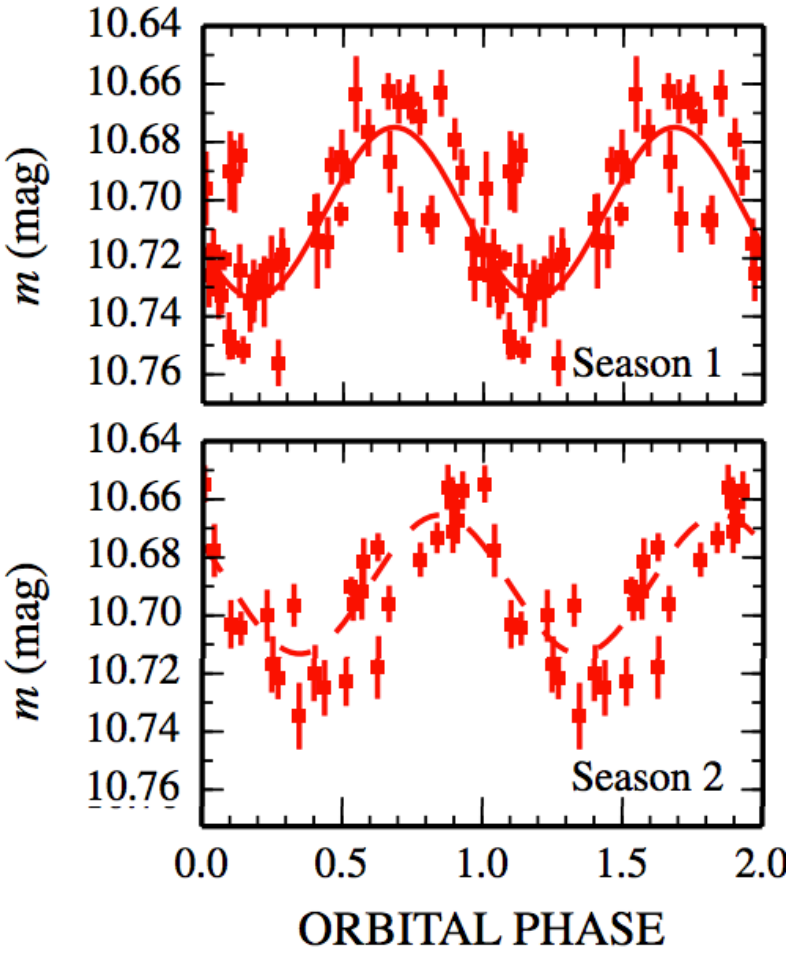

(a) Folded photometric variability of LSI displaying a phase shift over two seasons. From Paredes-Fortuny et al. (2015).

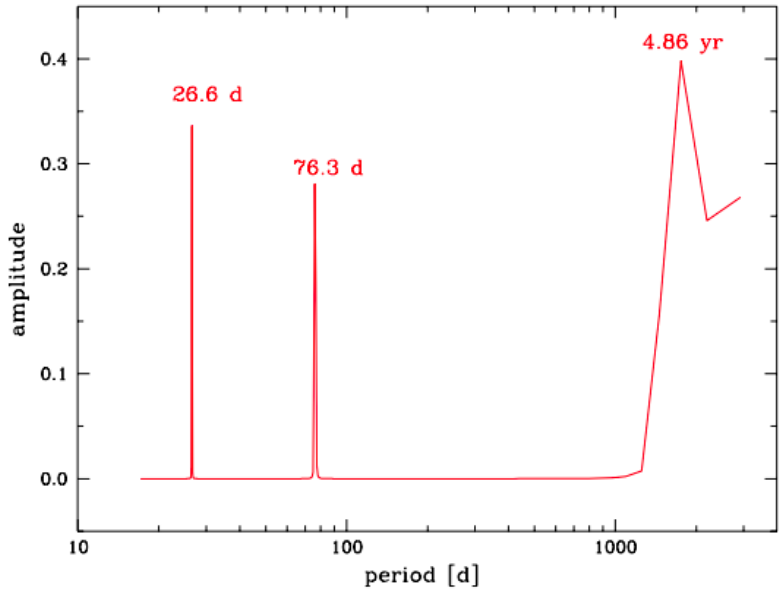

(b) Periodogram of the EW variability in LSI. From Zamanov et al. (2013).

Figure 3.8: Superorbital modulation at optical wavelengths.

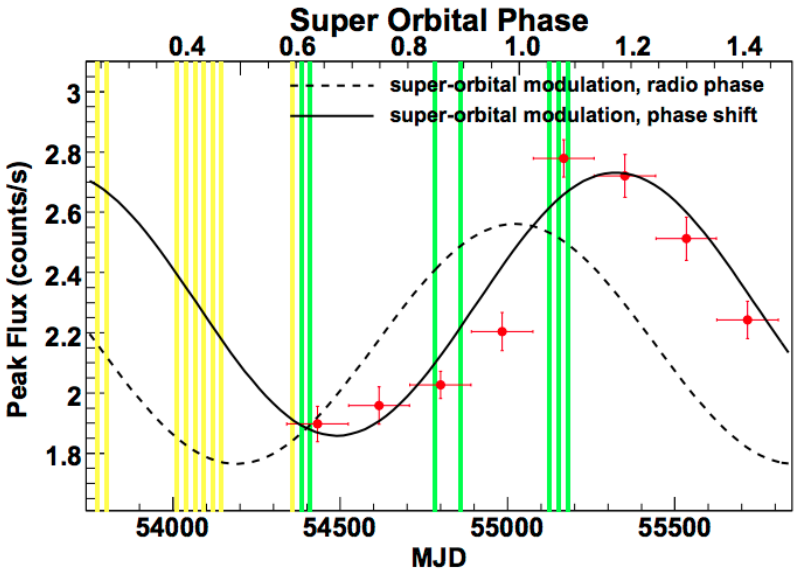

Figure 3.9: Peak X-ray flux modulated on the superorbital period. The green lines represent epochs of low TeV states and the yellow lines represent epochs of high TeV states. From Li et al. (2012).

the superorbital modulation is suggested to be due to beating between the orbital period and the precession period of the jet ($P_{\rm prec} = 26.935$ days; Massi & Torricelli-Ciamponi 2014; 2016).

3.2 Properties of Be discs

Among the population of GRBis, LSI is one of three systems that contain a B-type star with a circumstellar disc (HESS J0632+057 and PSR B1259−63 are the other two). In this chapter we begin with some background literature on theoretical and observational properties of Be discs. Section 3.2.1 discusses the models that have been proposed for the Be phenomenon; the main observational properties of Be stars are then discussed in 3.2.2 and a discussion on the measurement of disc sizes follows in section 3.2.3.

3.2.1 Be disc formation

For a long time the formation of the circumstellar disc (Be phenomenon) has been a subject of debate. A key question is how close the stellar rotational velocity is to the critical, break-up velocity needed for the material to be expelled at the equator to form a disc. The critical velocity of rotation for a star

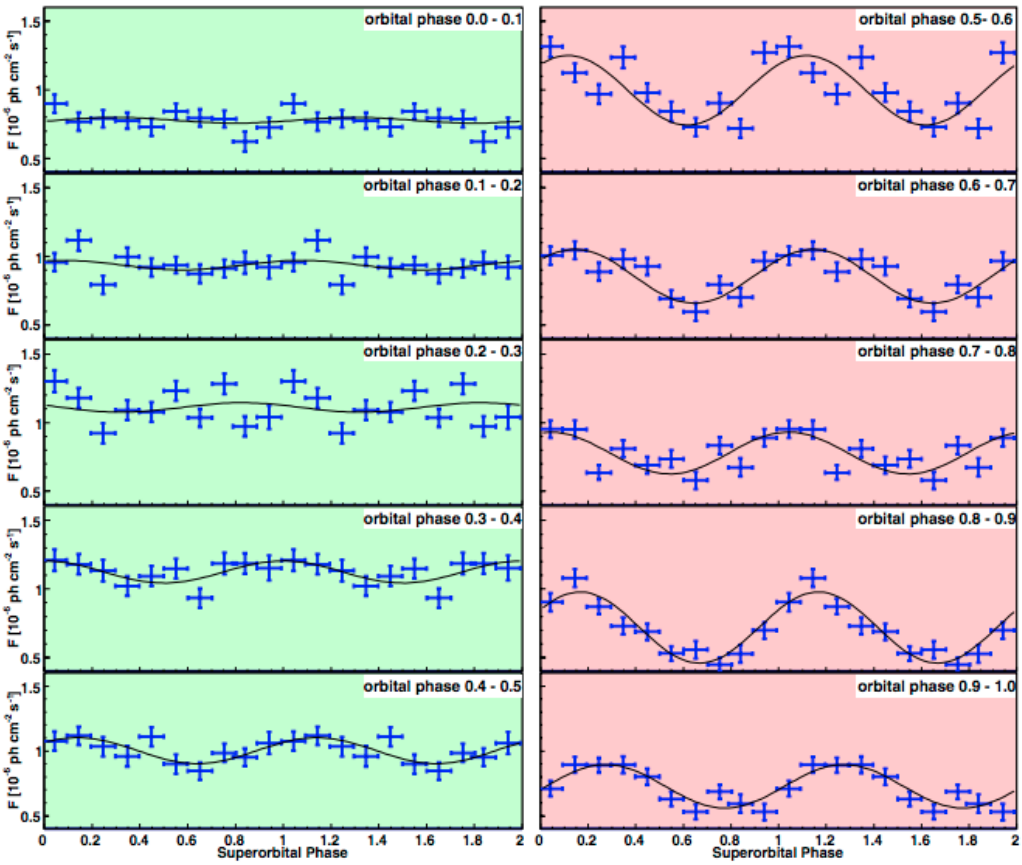

(a) Fermi/LAT flux folded on the superorbital modulation for data obtained at different orbital phase ranges. From Ackermann et al. (2013).

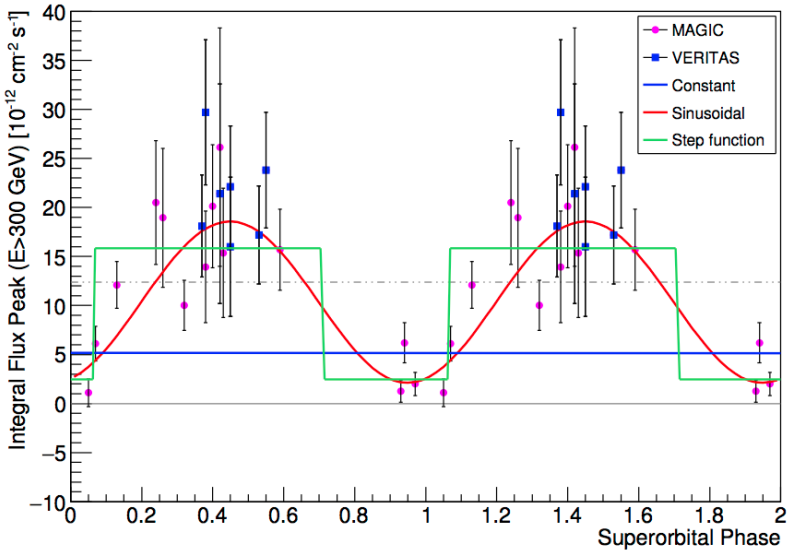

(b) MAGIC and VERITAS flux folded on the superorbital period. From Ahnen et al. (2016).

Figure 3.10: Superorbital modulation at gamma-ray energies.

is reached when the rotational velocity at the equator ($v_{\rm rot}$) is equal to the escape velocity ($v_{\rm e}$). This is defined quantitatively as:

$$v_{\rm crit} = \sqrt{\frac{2GM_*}{3R_{\rm pole}}}, \tag{3.1}$$

where M_* is the mass of the Be star and $R_{\rm pole}$ is the radius of the star at the poles. The factor of 2/3 takes into account the fact that the critically rotating star becomes oblate, with the radius at the equator ($R_{\rm eq}$) increasing, while $R_{\rm pole}$ remains roughly constant (Maeder 2009). An important effect which must be taken into account in the determination of the rotational velocity of the Be stars is gravity darkening. In rotating stars, gravity darkening is a consequence of the local flux being proportional to the local surface gravity, thereby causing the poles to appear brighter than the equatorial regions (e.g. Townsend, Owocki & Howarth 2004).

A number of independent statistical studies have been undertaken to obtain a consensus on the rotational velocities of samples of isolated Be stars (Townsend, Owocki & Howarth 2004, Cranmer 2005, Rivinius, Štefl & Baade 2006, Ekström et al. 2008, Huang, Gies & McSwain 2010). The results from these studies suggest that the Be nature of these stars requires $v_{\rm rot} \geq 0.7\ v_{\rm crit}$. However, the efficiency of the disc formation depends on the spectral subclass, with early types requiring lower velocities than later types (e.g., $v_{\rm rot}$ as high as $0.93\ v_{\rm crit}$ has been observed without a disc; Huang, Gies & McSwain 2010). Additional mechanism(s) are required for the Be phenomenon to occur, since a majority of the observed Be stars rotate below $v_{\rm crit}$. Additional velocities of order 100 km/s are required for stellar particles to achieve Keplerian orbit for $v_{\rm rot} \approx 0.75\ v_{\rm crit}$ (Rivinius et al. 2013).

The wind compressed disc (WCD) model was initially suggested to be responsible for the formation of the circumstellar disc (Bjorkman & Cassinelli 1993). In the WCD model, gas expelled by the photosphere of the star is channelled by wind streamlines from each hemisphere which intercept at the equator, forming a shock which eventually produces a disc (Fig. 3.11). The viability of the WCD model was brought into question with the inclusion of the non-radial line-driving force which decreases the wind rotation velocity significantly, making it difficult for a disc to form. Moreover, the predicted infrared excess of

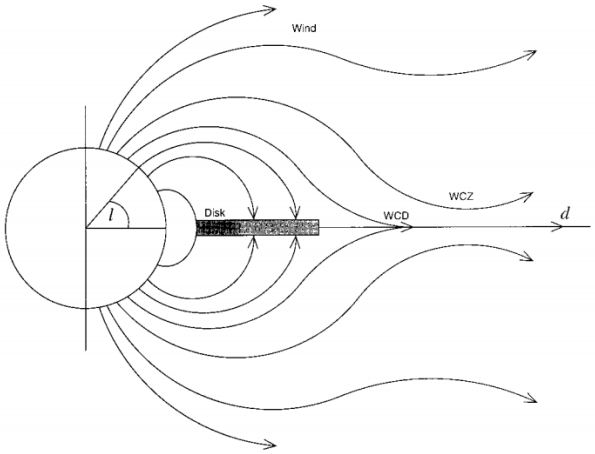

Figure 3.11: A schematic showing the WCD model for disc formation. The arrows represent wind streamlines which channel material from the star leaving at latitude l to the equatorial distance d. From: Cassinelli et al. (2002).

Be stars from the WCD model does not match that from observations (Porter 1997).

A variation of the WCD model is the magnetically torqued disc (MTD) model (Cassinelli et al. 2002). The main idea behind this model is that the matter from the stellar photosphere is channeled by magnetic field lines from each hemisphere which then meet at the equator, forming a shock and eventually a disc (Fig. 3.12). The validity of the MTD model was assessed by Owocki & Ud-Doula (2003) using magneto-hydrodynamic simulations to study the effect of different magnetic field strengths on disc formation. It was demonstrated that for strong magnetic field strengths (i.e. magnetospheric radius larger than the stellar escape radius) the material flows along the field lines and then breaks out upon meeting at the equator. For weak magnetic field strengths (magnetospheric radius smaller than the Keplerian radius) the material falls back onto the star after travelling along the field lines. In the case of intermediate magnetic field strengths, a combination of the two effects is seen (i.e. both falling-in and breaking-out of material).

A binary companion has been suggested to be the possible cause of the Be phenomenon (e.g. Harmanec et al. 2002, Bisikalo et al. 2006). In this case, the effective gravity in the equatorial regions of the Be star is lowered enough by the tidal force due to the companion, that the matter is expelled outwards.

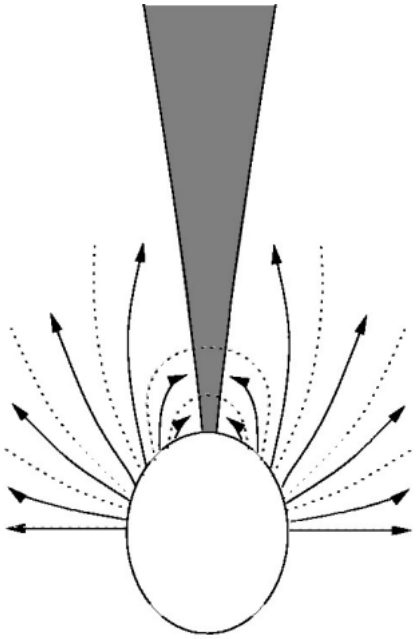

Figure 3.12: A schematic showing the MTD model for disc formation. The dotted lines represent magnetic field lines that channel the material from the stellar photosphere to the equatorial regions, where a disc eventually forms. From: Porter & Rivinius (2003).

A challenge to this model, however, was demonstrated using gas-dynamical simulations, where the results require very high rotational velocites which are close to $v_{\rm crit}$ (Harmanec et al. 2002).

An alternative model for the formation of the Be disc involves non-radial pulsations (Baade 1988, Cranmer 2009). In this scenario, non-radial pulsations from the star add enough angular momentum into the stellar atmosphere to spin up a Keplerian disc. The velocities of the pulsations, however, are too low for matter to be ejected (restricted to sound velocity, $v_{\rm puls} \approx 20$ km/s), unless there is beating of different modes (l, m, n) which would give sufficient amplitudes for ejection of matter (Rivinius et al. 2013).

3.2.2 Observational properties of Be discs

The optical emission in BeXBs comes mainly from the Be star/disc system. The spectra are characterised by emission lines originating from the circumstellar disc as a result of recombination (Woolf, Stein & Strittmatter 1970, Gehrz, Hackwell & Jones 1974). The most common of these are those of H I, He I, Fe II, Si II and Mg II. The Hα line originates from an extended re-

gion and is often used as a tracer of the state of the circumstellar disc. The emission lines are typically double-peaked due to the Keplerian distribution of matter, with a blue-shifted (V) and red-shifted (R) peak. The variability of the strength of the V and R peaks is termed V/R variability. It was proposed that the cause of the V/R variability is the precession of one-armed density waves in the Keplerian disc (Okazaki 1991, Papaloizou, Savonije & Henrichs 1992, Savonije & Heemskerk 1993). Observational evidence of the precession of an enhanced-density region in the disc was presented by Telting et al. (1994) from long term monitoring of the Be star, β Mon. In their work, Telting et al. (1994) demonstrated that the precession is prograde and follows the sequence (Fig. 3.13):

- $V/R > 1$: The region with increased density moves towards the observer.
- $V/R = 1$: The region with increased density is in front of the star, giving maximum shell absorption (shell profile).
- $V/R < 1$: The region with increased density is moving away from the observer.
- $V/R = 1$: The region with increased density is behind the star relative to the observer.

For the stars that show cyclic behaviour in the V/R variability, the period is typically much longer than the rotation period of the circumstellar disc particles, and ranges from a few years for BeXBs, to a decade for isolated Be stars (Okazaki 1997).
For an optically thick disc, the equivalent width (EW) of the Hα line is used as a measure of the size of the Be disc (see section 3.2.3). The EW of an emission (or absorption) line gives a measure of the strength of the line. Referring to Fig. 3.14, the EW is defined as the width of a box reaching up to the continuum level with the same area as the spectral line. With F_c and F_λ representing the flux at the continuum and flux across the line as a function of wavelength (λ), respectively, the EW can be defined quantitively as (Carroll & Ostlie 2006):

$$EW = \int \frac{F_c - F_\lambda}{F_c} d\lambda. \tag{3.2}$$

Another observational feature of Be stars is the excess in infrared (IR) light observed compared to the photospheric flux expected for the star. This is due to free-free radiation from proton-electron scattering in the disc material (Woolf,

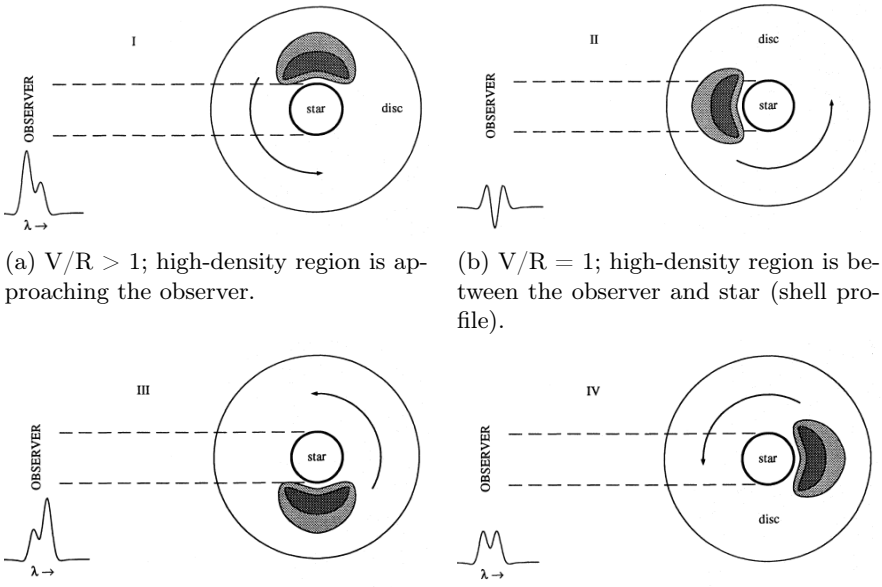

(a) V/R $>$ 1; high-density region is approaching the observer.

(b) V/R $=$ 1; high-density region is between the observer and star (shell profile).

(c) V/R $<$ 1; high-density region is moving away from the observer.

(d) V/R $=$ 1; high-density region is behind the star.

Figure 3.13: Illustration of the prograde revolution of the enhanced-density portion of the disc in β Mon giving rise to cyclic V/R variability of the Hα line. From Telting et al. (1994).

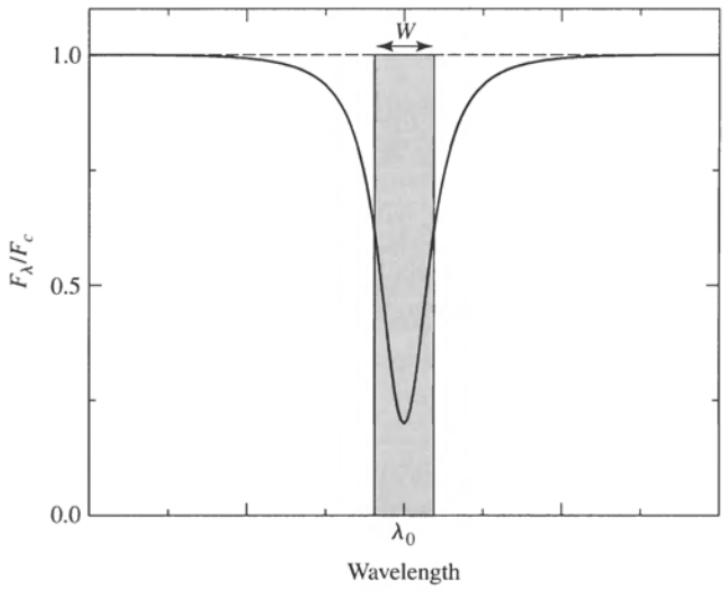

Figure 3.14: A schematic illustrating the equivalent width (W) of an absorption line. From: Carroll & Ostlie (2006).

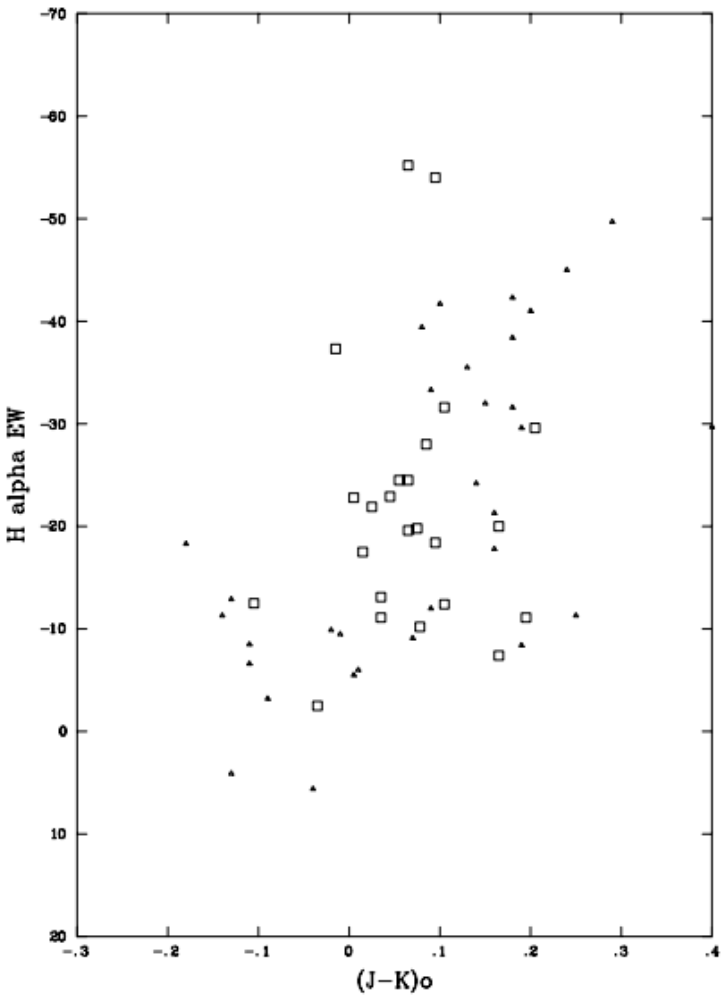

Figure 3.15: Correlation between the Hα EW and IR colour $(J-K)$ for BeXBs (square symbols) and isolated Be stars (triangle symbols). From Coe et al. (2005).

Stein & Strittmatter 1970, Gehrz, Hackwell & Jones 1974, Waters 1986). A correlation exists between the optical and IR light from Be stars through the measurements of the Hα EW and IR colour $(J-K)$ which was first reported for isolated Be stars (Dachs & Wamsteker 1982, Neto & de Freitas-Pacheco 1982) and later extended to binary systems (Fig. 3.15; Coe et al. 2005). This suggests that both the optical and IR radiation originate from the same region, i.e. the circumstellar disc. Gies et al. (2007) demonstrated, however, that the size of the emission region in the disc of the optical and IR emission is different. Through long-baseline interferometric observations of a sample of isolated Be stars, Gies et al. (2007) showed that the angular size of the K-band emission is smaller than that of the Hα emission.

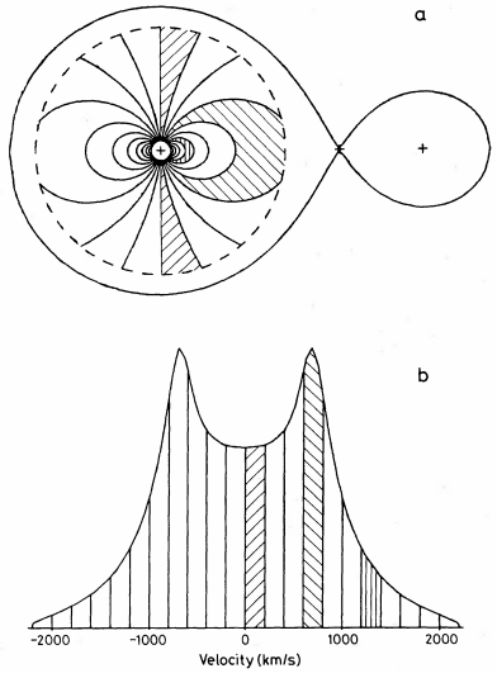

Figure 3.16: A schematic illustrating a face-on view of a Keplerian circumstellar disc (top). The bottom panel shows the resultant double-peaked Hα emission line with the shaded regions matching those in the disc, where the peak separation of the line can then be used to obtain an estimate of the disc size. From: Horne & Marsh (1986).

3.2.3 Be disc sizes

The peak separation in the double-peaked profiles of the Hα emission line can be used to obtain estimates of the disc size (Fig. 3.16). Using Kepler's laws, Huang (1972) showed that the size of the disc can be expressed as:

$$R = \frac{GM \sin^2 i}{(0.5\Delta V)^2}, \tag{3.3}$$

where M is the mass of the Be star, G is the gravitational constant, i is the inclination angle with respect to the plane of the sky and ΔV is the peak separation.

In the case when the Hα line is single-peaked and no direct information on the peak separation can be obtained, an empirical relationship between the EW and ΔV from systems where both parameters can be measured is used (Hanuschik 1989):

$$\log\left(\frac{\Delta V}{2v \sin i}\right) = -a \log\left(\frac{-EW}{\text{Å}}\right) + b, \tag{3.4}$$

where $v \sin i$ is the projected rotational velocity of the star. A fit to $\log(\Delta V/2v \sin i)$ vs. $\log(-EW)$ gives the parameters a and b. The parameter a is related to the rotational distribution of the disc, while b is related to the electron density (Hanuschik 1989). The disc radius estimates from the measurement of the peak separation of the Hα line provides more reliable estimates compared to those obtained from the empirical relationship between the EW and ΔV, as the measurements from the latter method result in large error bars ($50 - 70\%$ the size of the radius, compared to $10 - 15\%$ from direct measurements of the peak separation; Monageng et al. 2017a). This is due to the large scatter in the distribution of $\log(\Delta V/2v \sin i)$ and $\log(-EW)$.

It was demonstrated that in BeXBs there exists a correlation between the orbital period of the NS and the maximum Hα EW ever recorded for each source (Fig. 3.17, Reig, Fabregat & Coe 1997; Fig. 9 from Haberl & Sturm 2016). This was interpreted as an indication of truncation of the circumstellar disc by the NS. Follow-up work on this, from a theoretical point of view, was done to demonstrate the interaction between the disc and the NS in the viscous decretion disc model (Okazaki & Negueruela 2001, Negueruela et al. 2001, Negueruela & Okazaki 2001). In the decretion disc model, the Be star provides angular momentum to the inner regions of the disc and increases its angular velocity to Keplerian (Lee, Osaki & Saio 1991). The material in the disc gets transported outwards via viscosity until the resonant torque applied by the NS in its orbit becomes dominant over the viscous torque. At this point the disc gets truncated, which only happens at particular radii where the ratio between the angular frequency of the NS and that of the disc rotation is an integer, represented by $n : 1$ (e.g. Fig 3.18). In a comparative study between isolated Be stars and BeXBs, Zamanov et al. (2001) showed, from measured values of the Hα EW and ΔV, that on average the discs in BeXBs are twice as dense as those in isolated Be stars. This further validates, from an observational viewpoint, the effect of the NS through truncation (Zamanov et al. 2001, Reig et al. 2016).

3.3 Kozai-Lidov mechanism

One of the effects discussed in the interpretation of the results presented in this chapter is the Kozai-Lidov mechanism (KLM). In the following section I describe the main properties of this effect, broken up into two parts: a brief history of KLM and the effect in test particles (Section 3.3.1); and KLM in

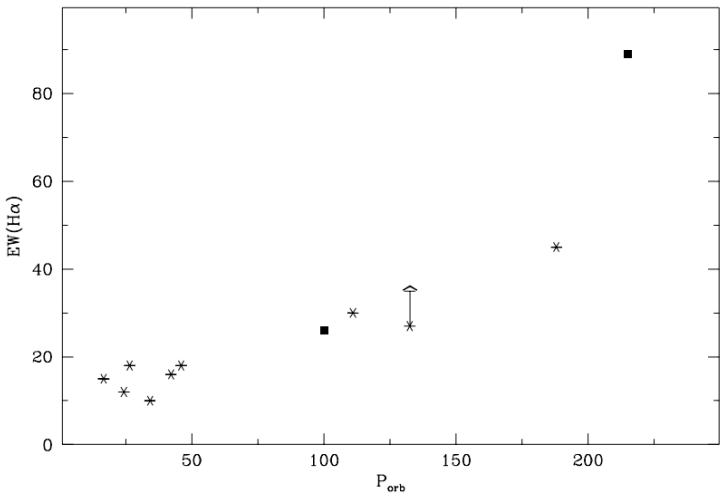

Figure 3.17: Correlation between maximum $EW(H_\alpha)$ and orbital period in BeXBs to demonstrate disc truncation. The two square symbols represent systems in which the orbital period was derived from $P_{\rm spin} - P_{\rm orb}$ relationship. The arrow represents a lower limit for the EW. From: Reig, Fabregat & Coe (1997).

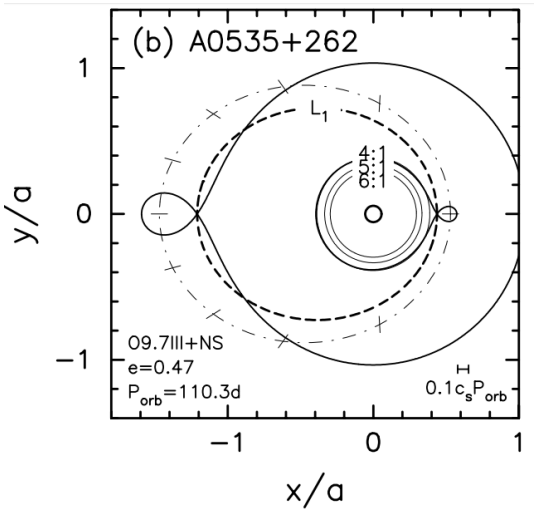

Figure 3.18: The proposed orbital model for A 0535+262. The truncation resonances are indicated in the plot. The dashed, dashed-dotted and thick solid lines represent the first Lagrangian point, NS orbit and critical lobe radii of the stars, respectively. The Be star is located at the origin. From: Negueruela & Okazaki (2001).

hydrodynamical discs (Section 3.3.2).

3.3.1 KLM with test particles

Astronomical objects in three-body systems have been observed for a long time. In our Solar System in particular, sources (asteroids and comets) whose orbits are highly inclined relative to the invariable plane* have long been subjects of interest due to their peculiar orbits. It was not until soon after the beginning of the Space Age (the late 1950s) that theoretical work that focused on the understanding of the orbits of such systems was seriously considered (Lidov 1962, Kozai 1962). The *Luna 3* mission was originally launched in 1959 with the goal of obtaining close-up images of the far side of the moon. The space probe made its way back to Earth upon completion of its mission and orbited the planet. After several orbits around the Earth, the probe's perigee entered the Earth's atmosphere and it is believed to have burned up after signal was lost† (Shevchenko 2017). Unknown at the time, this was the first man-made example of the exchange between eccentricity and orbital inclination. Soon after that, Russian physicist Mikhail Lidov derived equations describing the evolution of the orbits of artificial satellites around Earth as they are perturbed by the Moon (Lidov 1962). The work was able to explain, for the first time, the disappearance of *Luna 3*. It was demonstrated that for a satellite on an initially circular orbit with an inclination angle relative to the Earth-Moon orbit of at least $i_{\rm crit} = \arccos(\sqrt{\frac{3}{5}}) \approx 39.2°$ (the critical angle for Kozai-Lidov oscillations to be initiated) the eccentricity will oscillate between its initial state and a maximum given by $e_{\rm max} = \sqrt{1 - \frac{5}{3}\cos^2 i}$. In so doing, there will be a periodic exchange between the eccentricity and inclination angle. Throughout the process of this exchange between the two parameters the perpendicular component of the angular momentum (relative to the Earth-Moon orbit) of the satellite is conserved and is quantified as:

$$\sqrt{1 - e^2}\cos(i) \approx const. \tag{3.5}$$

*the plane passing through the barycentre of the Solar System that is perpendicular to its total angular momentum vector (Souami & Souchay 2012).

†https://nssdc.gsfc.nasa.gov/nmc/spacecraftDisplay.do?id=1959-008A

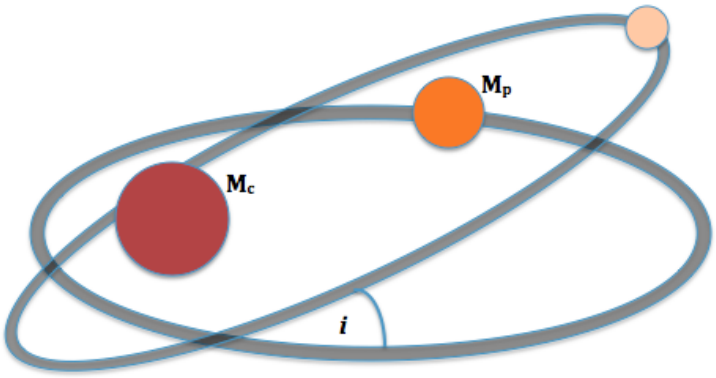

Figure 3.19: Illustration of the KLM for test particles. The orbit of the particle undergoing Kozai-Lidov oscillations is inclined relative to the orbit of the main binary ($M_{\rm p}$ and $M_{\rm c}$) with angle, i.

The analytical expression for the period of the oscillations, $P_{\rm KL}$, is given by (Innanen et al. 1997, Kiseleva, Eggleton & Mikkola 1998):

$$\frac{P_{\rm KL}}{P_{\rm b}} \approx \frac{M_{\rm c}+M_{\rm p}}{M_{\rm p}}\frac{P_{\rm b}}{P}(1-e_{\rm b}^2)^{3/2}, \tag{3.6}$$

where $P_{\rm b}$ is the orbital period of the binary, $M_{\rm c}$ is the mass of the central object, $M_{\rm p}$ is the mass of the perturbing object, P is the orbital period of the object undergoing oscillations, $e_{\rm b}$ is the eccentricity of the binary. The equations are derived under the assumption that the mass of the object undergoing the oscillations is negligible relative to the masses of the perturber and the central object (mass of the *Luna 3* relative to the masses of the Sun and Moon in the example above; Fig 3.19).

In an independent study, Japanese astrophysicist, Yoshihide Kozai, investigated this phenomenon by analysing the orbits of asteroids around the Sun as they are perturbed by Jupiter (Kozai 1962). With the work from the two scientists published around the same time, this phenomenon is widely referred to as the Kozai-Lidov mechanism (although some authors use Lidov-Kozai mechanism in recognition of the Lidov's work being published slightly earlier). Hierarchical triple systems appear frequently in the Universe and so the KLM has many applications, as seen by the recent increase in citations of the two original papers in Fig 3.20, including those in studies of the Solar System (comets, e.g. Sekhar et al. 2017), exoplanets (e.g. Takeda & Rasio 2005), stellar systems (e.g. Naoz & Fabrycky 2014) and X-ray binaries (e.g. Martin et al. 2014b).

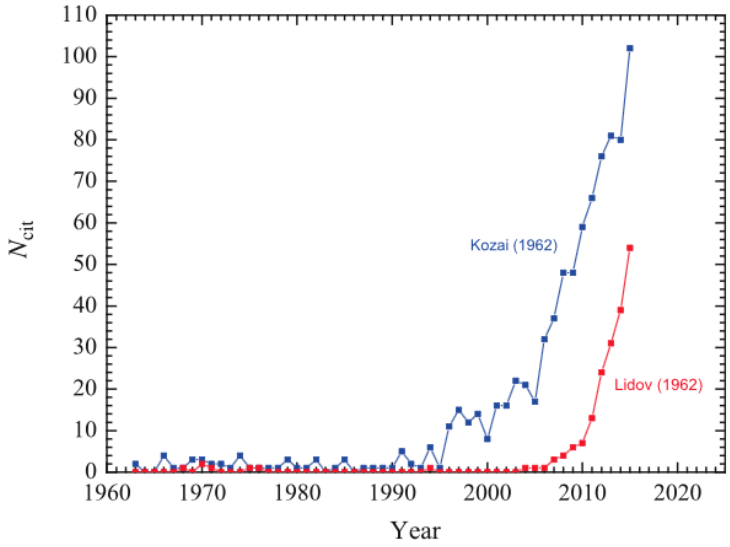

Figure 3.20: A demonstration of the recent increase in citations per year (N_{crit}) of the two original articles of the KLM. From: Shevchenko (2017).

3.3.2 KLM in HMXBs

The effect of periodic exchange between eccentricity and inclination angle is not limited to test particles. A circumstellar disc around one component of a binary that is significantly misaligned relative to the binary plane can also undergo Kozai-Lidov oscillations (Fig. 3.21). Martin et al. (2014a) used 3D smoothed particle hydrodynamics (SPH) simulations to model the evolution of circumstellar discs in BeXBs. In their work, it was established that for a circular disc that is initially misaligned by an angle $\gtrsim 60°$ relative to the binary orbit, the disc becomes eccentric after several orbits. Moreover, the results showed that type *II* outbursts occur due to accretion of a large reservoir of matter from the eccentric disc. At the time of publication, the authors were unaware that this was the first demonstration of the KLM involving a hydrodynamical disc. Soon after that, follow-up work was performed from a theoretical viewpoint through SPH simulations in a series of papers: Martin et al. (2014b), Fu, Lubow & Martin (2015a;b).

Martin, Tout & Pringle (2009) postulated that the supernova explosion that forms the NS in BeXBs may give a large-enough velocity kick that the spin axis of the unexploded star is left highly misaligned relative to the orbit. Since the decretion disc forms in the equatorial regions of the Be star, this will result in a misaligned disc-orbit situation. If the misalignment angle is sufficient, Kozai-Lidov oscillations will occur. SPH disc simulations performed with an initially

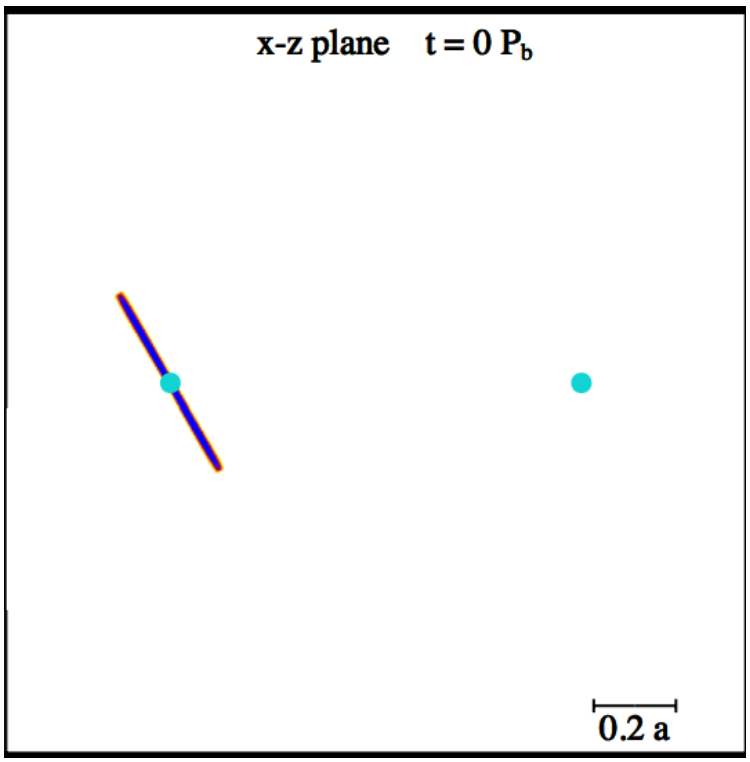

Figure 3.21: An example of a snapshot from simulations showing a misaligned disc relative to the binary orbit (the horizontal plane). The two cyan circles represent stars in a binary orbit. From: Martin et al. (2014b).

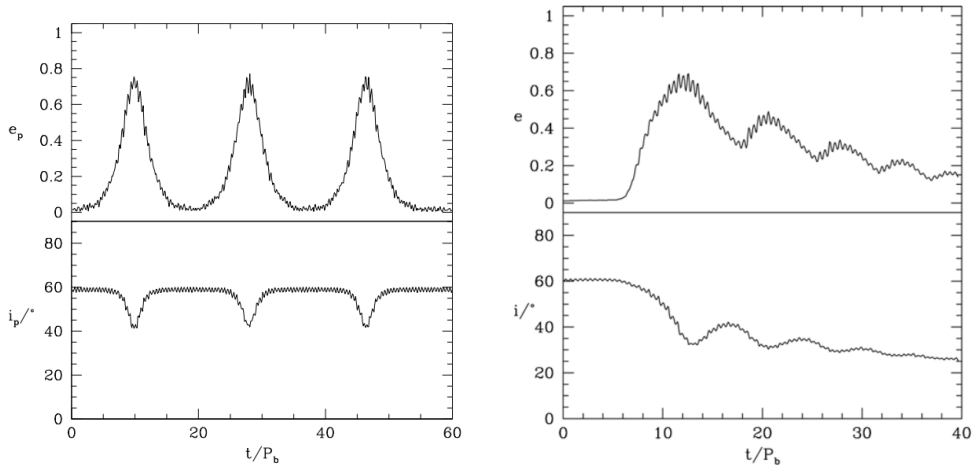

(a) Eccentricity and inclination as a function of time for a test particle.

(b) Eccentricity and inclination as a function of time for a hydrodynamical disc.

Figure 3.22: SPH simulation results demonstrating the evolution of eccentricity and inclination in the cases of a test particle and a hydrodynamical disc. From Martin et al. (2014b).

circular disc inclined by an angle $i = 60°$ with respect to the orbital plane result in the periodic exchange between the disc eccentricity and inclination angle (Fig. 3.22). As seen in Fig. 3.22, the oscillations are damped after a few cycles, unlike the case of test particles, due to viscosity in the disc. The other noticeable difference between the disc and test particle is that in the case of the disc, the eccentricity never drops to zero and after complete damping of the oscillations the disc is left with a residual eccentricity of $e \approx 0.2$.

The simulations of the test particles show a period-dependence on the initial inclination angle which is not included in equation 3.6, and thus this expression for the period of the oscillations generally gives estimates that differ from those obtained from simulations by a few factors. For a hydrodynamical disc, the expression for the period of the global Kozai-Lidov oscillations, $\langle \tau_{\rm KL} \rangle$, is given by (Martin et al. 2014b):

$$\frac{\langle \tau_{\rm KL} \rangle}{P_{\rm b}} \approx \frac{(4-p)}{(5/2-p)} \frac{\sqrt{M_1 M}}{M_2} \left(\frac{a}{R_{\rm out}} \right)^{3/2}, \tag{3.7}$$

where M_1 and M_2 are the masses of the objects in the main binary, M is the sum of those masses, $R_{\rm out}$ is the initial disc outer radius and p is from the power-law dependence in radius of the surface density.

Follow-up work of Martin et al. (2014b) presented by Fu, Lubow & Martin (2015a) studied the effects of binary and disc parameters and the results are summarised as follows:

- Changing initial inclination angle: for initial angles in the range $45° < i < 60°$, the Kozai-Lidov cycles occur earlier for larger angles (i.e. eccentricity peaks faster at $i = 60°$). It is also noted that at $i = 45°$ the Kozai-Lidov cycles do not occur, and thus the critical angle required for the oscillations to commence in hydrodynamical discs is larger than in the case of the test particle.
- Disc surface density power-law indices: for a range of indices, $0.5 < p < 1.5$, there is little difference in the results of the evolution of the eccentricity and inclination angle.
- Disc inner radius: for different values of the inner radius of the disc the results show that the smaller the inner radius, the longer the cycle period. This is possibly due to weaker global perturbations since for a smaller inner radius the disc material is further away from the companion star (closer to the central star).
- Disc outer radius: for a smaller disc outer radius the onset of the Kozai-Lidov cycles is delayed due to the weaker perturbations by the companion. The initial Kozai-Lidov period is also longer for a smaller initial disc outer radius.
- Mass ratio of the two stars ($M_\mathrm{p}/M_\mathrm{c}$): smaller $M_\mathrm{p}/M_\mathrm{c}$ results in a delayed onset of Kozai-Lidov cycles. Moreover, the period of the cycles decreases with increasing mass ratio.
- Binary orbital eccentricity (e_b): the effect of varying e_b results in a faster onset of Kozai-Lidov cycles for larger values of orbital eccentricity. The Kozai-Lidov period remains roughly equal for different values of e_b.

The effects of self-gravity and disc mass were studied by Fu, Lubow & Martin (2015b). For the simulations performed without self-gravity, varying the mass of the disc results in no difference in the period and amplitude of the oscillations. The inclusion of self-gravity does not significantly affect the disc orbital elements for small values of the disc mass ($\mathrm{M}_d \leq 0.01M$, where M is the mass of the star), while for larger disc mass ($\mathrm{M}_d \geq 0.01M$), the amplitude of the oscillations is significantly reduced. By the end of the simulations, the disc has lost more than 50% of its initial mass, a majority of which is accreted by the central star and some of it ending up in the vicinity of the companion star.
The KLM in HMXBs has so far only been studied theoretically, from the works described above using SPH simulations. One of the main goals of the work presented here is to obtain, for the first time, observational signatures of this effect

in hydrodynamical discs. As a starting point, we analyse optical data of LSI obtained primarily with The Liverpool Telescope to study the long term variability of the disc using the Hα emission line features described in Section 3.2.

3.4 The Liverpool Telescope

Located at the Observatorio del Roque de Los Muchachos on La Palma, Spain, The Liverpool Telescope (LT) is a 2 m altitude-azimuth telescope. The telescope is fully robotic and is operated by the Astrophysics Research Institute of Liverpool John Moores University (Barnsley, Smith & Steele 2012). The original scientific objectives of the telescope include follow-up observations of transients, monitoring of variable sources and monitoring targets in conjunction with other telescopes (Steele 2001, Gomboc et al. 2003, Steele 2004). Since operations on the LT commenced in April 2004, a number of instruments have been employed* (Barnsley, Smith & Steele 2012):

- Infrared-optical instruments (IO:O, IO:I and the now-decommissioned IO:THOR).
- RISE - fast-readout camera for measurements of transiting exoplanet timing.
- RINGO - a series of optical imaging polarimeters (RINGO3 and the now-decommissioned RINGO and RINGO2).
- SPRAT - low resolution spectrograph for rapid acquisition of transients.
- LOTUS - low resolution optical-near UV spectrograph.
- FRODOSpec - integral field unit spectrograph.
- SkyCam - a series of wide-field cameras.
- Meaburn (decommissioned) - low dispersion spectrograph.
- RATCam (decommissioned) - optical CCD camera.
- SupIRCam (decommissioned) - near-infrared camera.

3.4.1 FRODOSpec

The integral field unit (IFU) spectrograph FRODOSpec succeeded the Meaburn spectrograph and has been the spectroscopic workhorse of the telescope since

*http://telescope.livjm.ac.uk/TelInst/Inst/index.php

Figure 3.23: The Liverpool Telescope. From: Liverpool Telescope Facebook page.

Table 3.1: Specifications of the dispersive elements on FRODOSpec.

	VPH	diffraction grating
Blue wavelength range (Å)	3900−5100	3900−5700
Red wavelength range (Å)	5900−8000	5800−9400
Blue resolving power	5500	2600
Red resolving power	5300	2200

February 2010 (Barnsley, Smith & Steele 2012). The system consists of optical fibres which are organised in a two-dimensional matrix to form a 12 × 12 IFU. A pseudo-slit is formed from the rearrangement of the fibres to form an aperture. The IFU system gives a total field-of-view of the sky of 10" × 10" (Morales-Rueda et al. 2004, Barnsley, Smith & Steele 2012). A dichroic beamsplitter serves to separate the incoming light into two optical arms (blue and red) until it eventually gets focused onto the CCDs (Fig. 3.24). The spectrograph employs two dispersive elements in each arm which operate at different resolutions: a higher resolution Volume Phase Holographic (VPH) grating and a low resolution diffraction grating. A summary of the different properties of the two gratings is presented in Table 3.1.

The raw data is reduced using a fully autonomous pipeline which operates in two stages: L1 and L2. The L1 pipeline performs primary tasks of bias subtraction, overscan trimming and flat-fielding. A brief description of the L2 pipeline is given below (Barnsley, Smith & Steele 2012):

The L2 pipeline first generates a fibre tramline map which describes how the flux from the fibres propagates along the CCD axes. This is performed in three

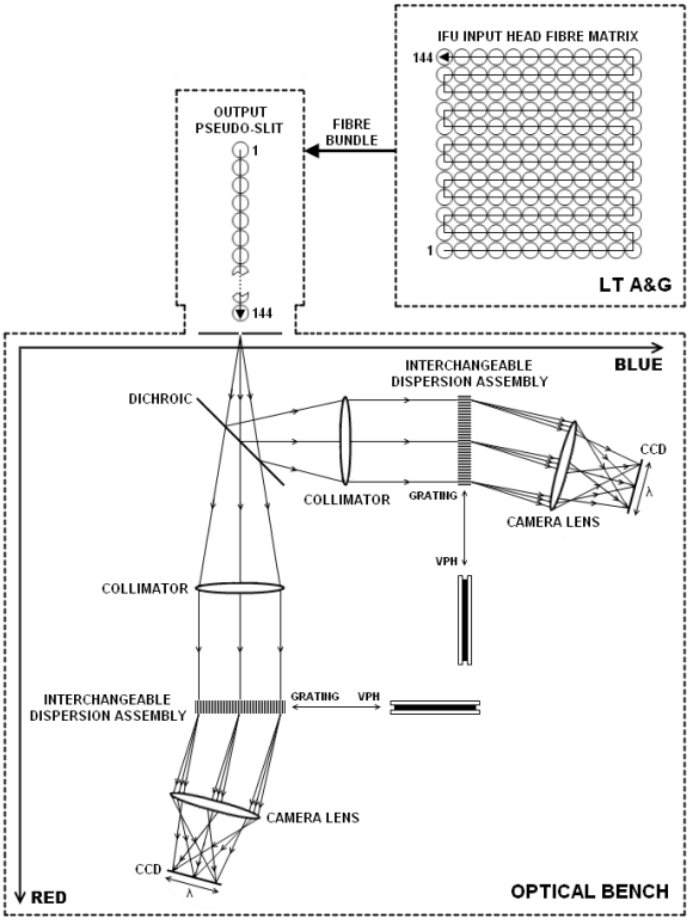

Figure 3.24: The optical system of FRODOSpec. From: Barnsley, Smith & Steele (2012).

stages, the first of which is to find fibre profile peaks by reading in the rows of the CCD output. Next, the removal of spurious rows which have poorly-determined locations is performed. The criteria for the removal are set by calculating the distance between the location of the peak and the average location for that peak number, which must be smaller than a pre-determined maximum. Finally, polynomials are fitted to the fibre profile peaks.

Flux extraction is then performed from each fibre in all frames (target, continuum and arc) using the maps generated from the previous task. The pipeline then fits arc lines by checking candidate lines from the target frames against a reference arc line list, in which the wavelength and corresponding pixel position is known.

The throughput in the pseudo-slit varies from fibre to fibre as a result of misalignments and fibre defects. This is accounted for by normalising the target row stacked spectra (RSS) frames with the continuum RSS frame. Spectral rebinning is then performed, where the flux is first rebinned along the dispersion axis for spectra in the target RSS frame and the rebinned flux value calculated by interpolating the flux between neighbouring wavelength values.

The final task of the pipeline is to perform sky-subtraction. The sky-subtraction routine identifies sky-only fibres and subtracts the median flux at each wavelength from the target spectra (Fig. 3.25). An example of the final product from the L2 FRODOSpec pipeline is illustrated in Fig. 3.26. LSI was observed using FRODOSpec between January 2010 and January 2014 with the red and blue VPH with exposure times of 600 s. The data from LT were supplemented with high-dispersion spectra (HR henceforth) from three instruments: the High Dispersion Echelle Spectrograph (HIDES) on the 188 cm reflector telescope at the Okayama Astrophysical Observatory (OAO), High Dispersion Spectrograph (HDS) on the 8.2 m Subaru telescope and the ESPaDOnS echelle spectrograph spectropolarimeter on the Canada France Hawaii Telescope (CFHT).

A model stellar photosphere was generated from the templates of Lanz & Hubeny (2003), using the stellar parameters of Casares et al. (2005a) as a starting point. These parameters were varied, and the resulting model spectra were fit to one of the high resolution spectra from CFHT in the wavelength range 4000 - 5000 Angstroms. To check for the continuum variability in the wavelength range used to generate the template, we calculated the root-mean-squared error of the continuum using spectra from different epochs, which gave values below 5%. The parameters that provided the best fit were T = 27500 K, log g = 4.5 with a rotational velocity of 113 km/s (Table 3.2). The spectra were

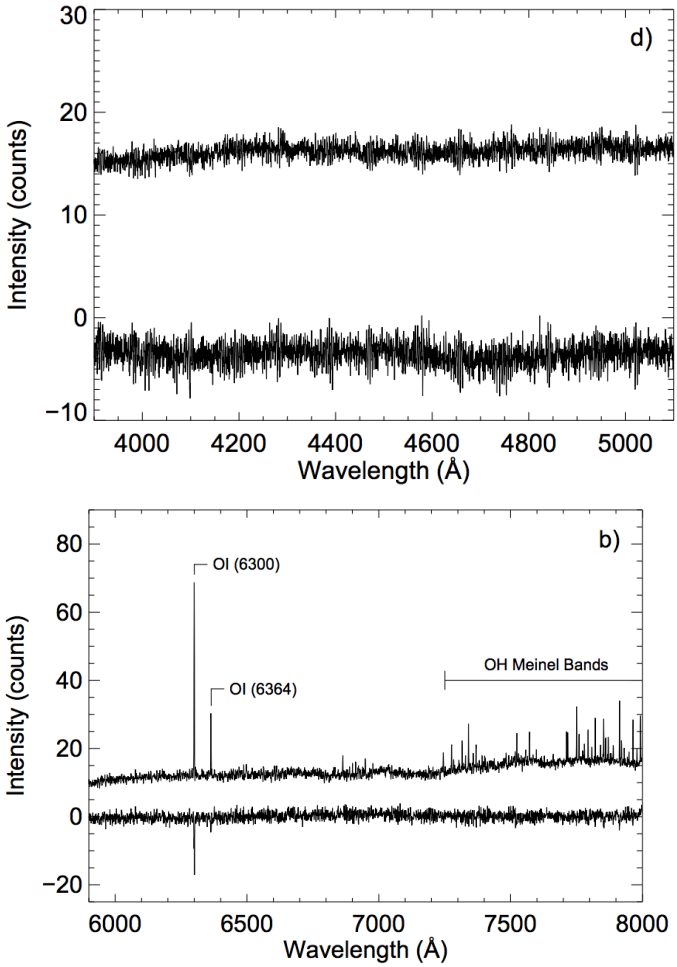

Figure 3.25: An example of sky subtraction from the L2 pipeline from the blue (top) and red (bottom) VPH. The top and bottom plots in each panel shows the non sky-subtracted and sky-subtracted spectra, respectively. From Barnsley, Smith & Steele (2012).

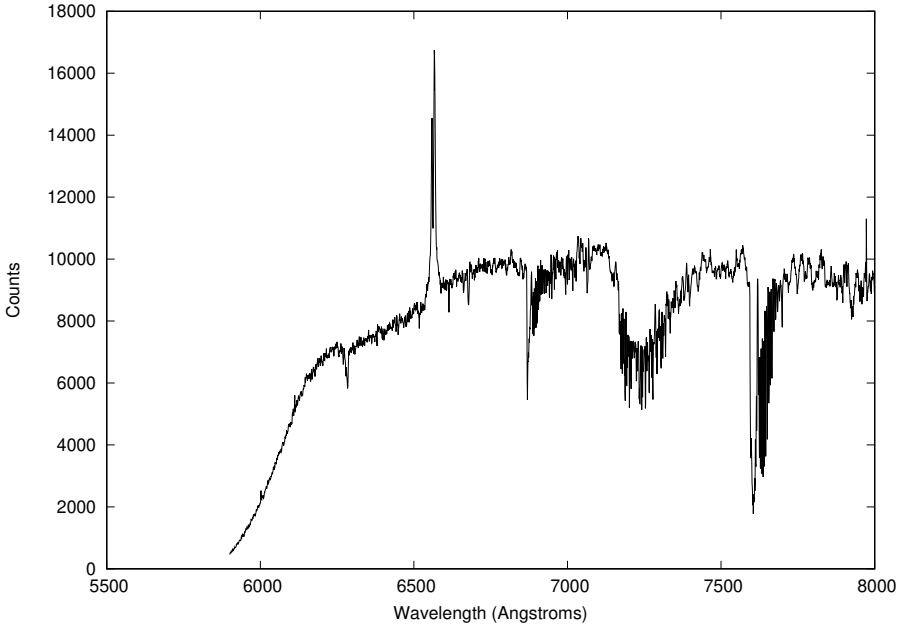

Figure 3.26: An example spectrum of LSI produced by the L2 pipeline.

normalised using the IRAF task CONTINUUM. The normalised spectra were corrected for the photospheric contribution from the Be star by subtracting the model template (Fig. 3.27). The input parameters of the template were varied, where a temperature range 27500 K $<$ T $<$ 32500 K and surface gravity range 4.00 $<$ log g $<$ 4.25 were used. The measured EW values acquired from the spectra obtained by subtracting the templates in the temperature and surface gravity ranges varies to within 12%. The spectra were also corrected for the systemic velocity ($v_{\rm sys}$ = −40.2 km/s, Casares et al. 2005a), heliocentric velocity and orbital velocity to account for the effect of the orbital motion using IRAF tasks RVCORRECT and DOPCOR.

Table 3.2: B0 V stellar parameters. (Casares et al. 2005a)

Spectral type	B0 V
Effective temparature	28 000 K
$\log g$	4.5
$v \sin i$	113 km/s

The peaks and central dip of the Hα double-peaked lines were measured by fitting Gaussian profiles. The mean value and standard deviation of the mean of the measurements of each of the peaks and central dip were used for the final analysis (Fig. 3.28). The EW of the blue peak was estimated by calculating the area under the curve of the normalised spectra by selecting a region on

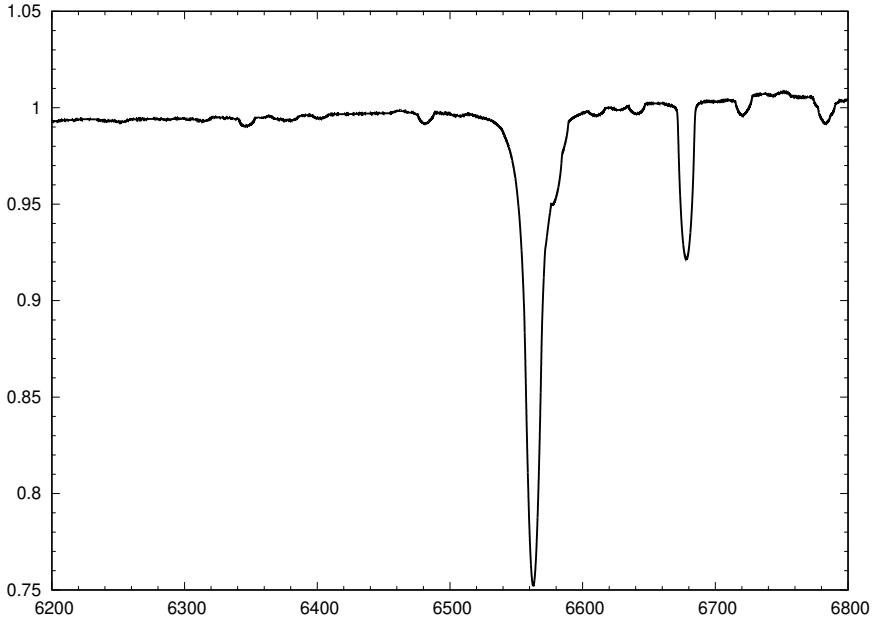

Figure 3.27: Template spectrum used for LSI to account for the photospheric contribution from the Be star around the Hα line.

the continuum as an initial point (on the blue end) and integrating until the position of the central dip. A similar procedure was followed for measuring the area under the red peak, with the integration performed from the central dip to the continuum (Fig. 3.29). The measured parameters used in this chapter are displayed in Appendix B.

3.5 Results: Be disc variability in LSI

3.5.1 Blue and red peak velocity variation

Fig. 3.30 shows the long-term evolution of the blue and red peak velocities of the Hα emission line. The red and blue peak velocities are represented by red and blue colours, respectively. The circles and triangles represent data from LT and HR, respectively. An interesting feature in the evolution of the velocities is the parallel shift in the red and blue peaks. This is presented more clearly in Fig. 3.31, where a correlation between the red and blue peak velocities is observed and is overplotted with a best-fit correlation line with a slope of 0.94 and an intercept of -319.18 km/s.

To understand this correlation, consider a circular, Keplerian disc around a Be

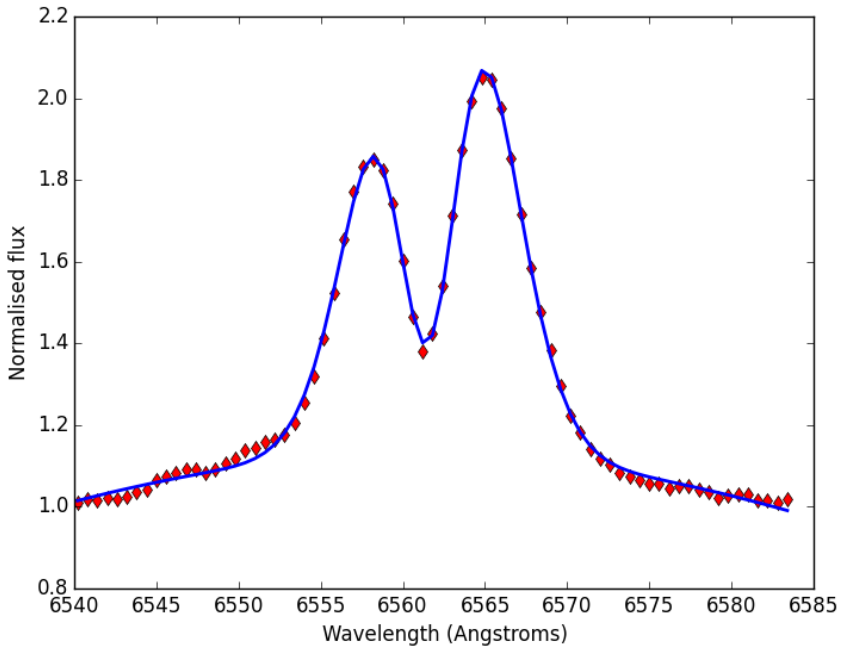

Figure 3.28: Example of Gaussian fitting on the blue peak, central dip and red peak. The red points show the Hα emission line and the blue curve is the fit to the line.

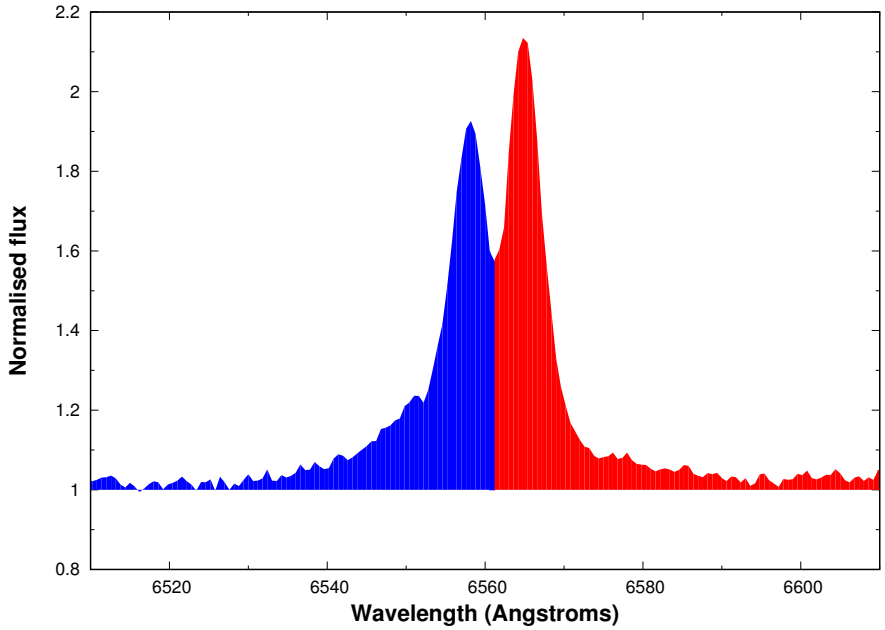

Figure 3.29: Example of an Hα line profile demonstrating the red and blue area measurements.

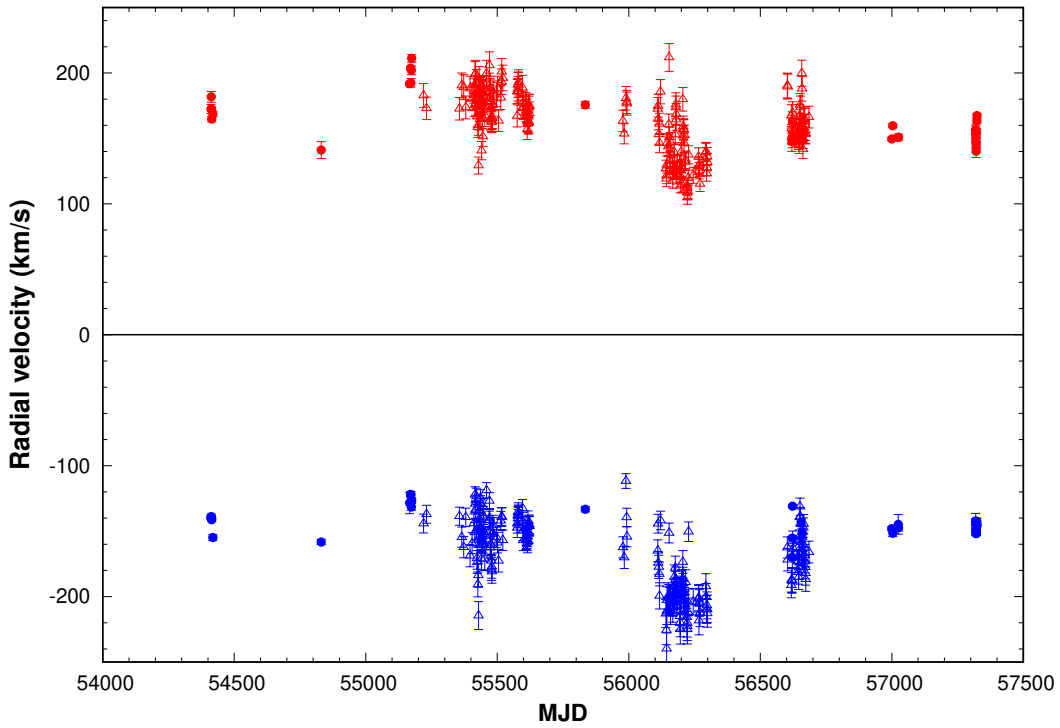

Figure 3.30: Evolution of the red and blue peak velocities of the Hα emission line in LSI. The triangles and circle symbols represent data from LT and HR, respectively.

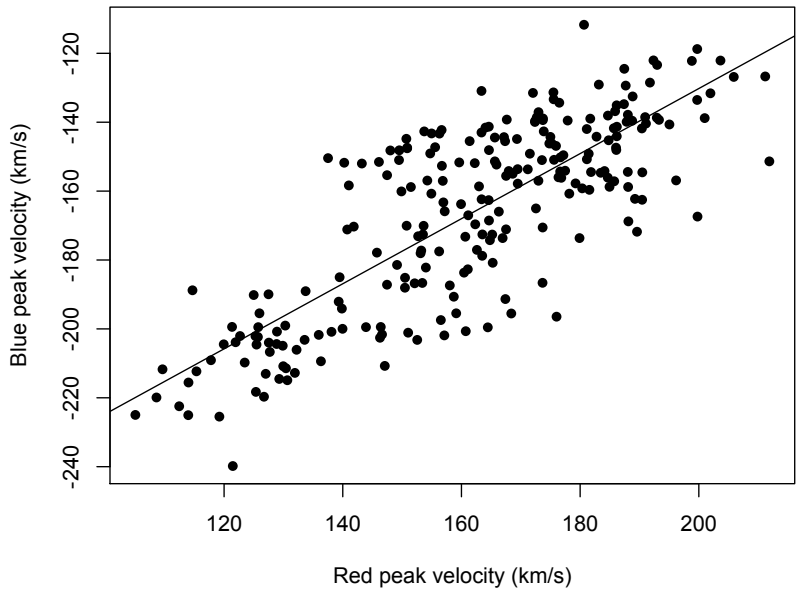

Figure 3.31: Correlation between the red and blue peak velocities of the Hα line with the best-fit line in LSI.

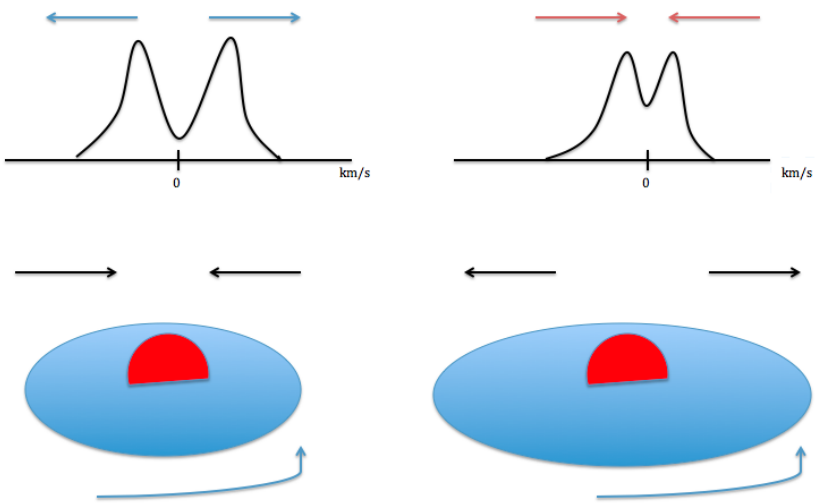

Figure 3.32: Illustration of axisymmetric decline (a) and growth (b) of a Be disc with the resultant change in the Hα line profile.

star. If the disc grows axisymmetrically, one expects the peaks to shift towards each other, i.e. towards smaller velocities, right panel of Fig. 3.32, with the situation reversed for axisymmetric decline in size (left panel of Fig 3.32). The parallel shifts in the peak velocities would be expected in a disc that is undergoing elliptical changes: for counterclockwise rotation of a disc with respect to our line of sight and elongation on the red side of the disc, the blue peak of the Hα line profile is expected to drift towards higher negative velocities while the red peak is expected to shift to lower velocities (left panel of Fig. 3.33). For elongation on the blue end of the disc, the blue peak is expected to shift to lower negative velocities and the red peak towards higher velocities (right panel of Fig. 3.33).

To study this in a more quantitative way, we apply a particle disc model described in Appendix A to the measured parameters. Fig. 3.34 is a sketch illustrating the model with the important parameters used in the equations for variability of the disc geometry. From the parameters defined in Fig. 3.34 we can analyse the motion of an orbiting particle in the disc plane and derive the relationship between the disc eccentricity (e_p) and the argument of pericentre (ω), given by (the full derivation is included in Appendix A):

$$e_p = \frac{v_{\rm red} + v_{\rm blue}}{v_{\rm red} - v_{\rm blue}} \sec \omega, \tag{3.8}$$

where $v_{\rm blue}$ and $v_{\rm red}$ are the measured blue and red peak velocities, respectively, of the Hα line.

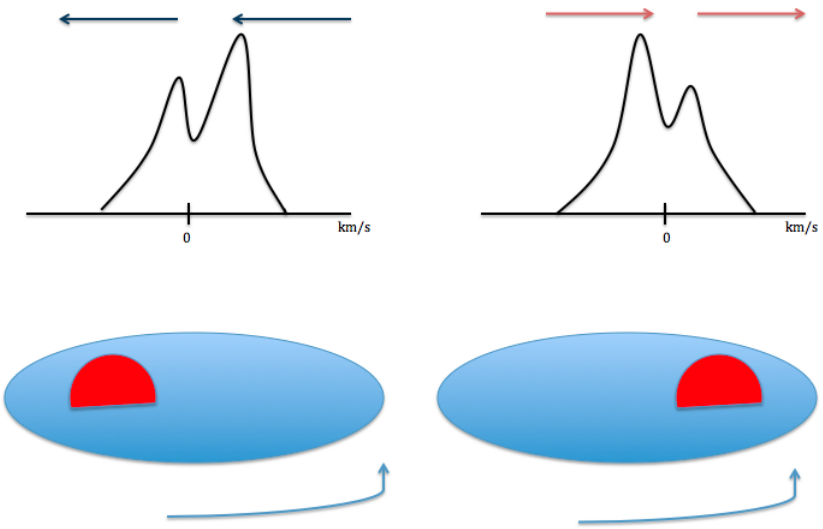

Figure 3.33: Illustration of elliptical changes in the Be disc with the resultant change in the Hα line profile.

The relationship between e_p and ω is represented graphically in Fig. 3.35, where the blue curves show data from LT and red curves from HR. Fig. 3.35a shows the relationship between e and ω using all the data, while Fig. 3.35b shows it for data averaged per orbital cycle to take into account day-to-day fluctuations. In order to study the variability of either e_p or ω, one must fix one of the variables in eq. 3.8. We can then overplot a model over the distribution of the two parameters over time.

From Fig. 3.35, there are several possibilities for disc variability. Vertical variability translates to the disc eccentricity varying while ω remains roughly constant (i.e. Kozai-Lidov mechanism). The horizontal variability means ω varies significantly, with the eccentricity remaining roughly constant (disc precession). In the following analysis, we consider the following possibilities for disc variability:

- Varying argument of pericentre with constant eccentricity.
- Varying eccentricity with constant argument of pericentre.
- Simultaneous variability of both e and ω.

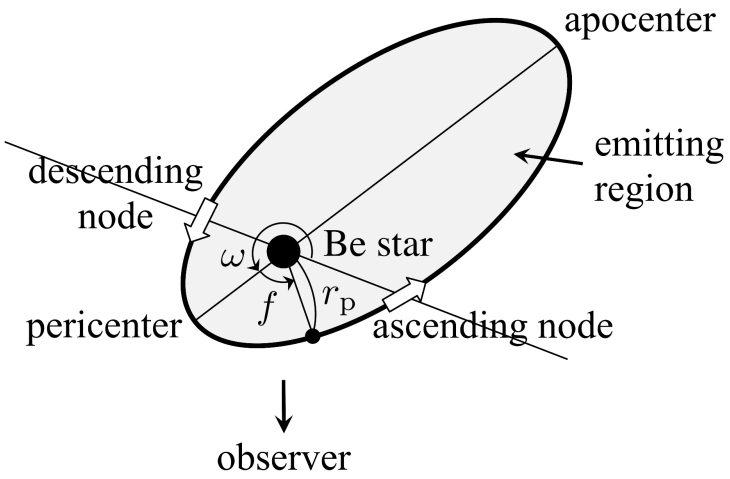

Figure 3.34: A schematic diagram of the elliptical orbit of a particle orbiting along the limb of a line emitting region. The orbit has the semi-major axis a_p and eccentricity e_p, and the radius and true anomaly of the particle at a time, t, is r_p and f, respectively. The orbital plane is inclined to the tangent plane of the sky by an angle i_p, which is not labeled in the figure. The pericentre is at the angle ω measured from the ascending node within the orbital plane. The observer views the orbit from below the figure. The shaded area denotes the line-emitting region.

3.5.2 Argument of pericentre variability with constant eccentricity

Fig. 3.36 shows the long-term variability of the argument of pericentre, where the eccentricity is fixed at $e = 0.4$ (maximum possible value of eccentricity, as seen in Fig. 3.35). The diagonal lines in Fig. 3.36 show the best-fit distribution of ω, given by the relationship:

$$\omega = \pm \frac{MJD - MJD_0}{P_0} \times 360^\circ, \tag{3.9}$$

where the best-fit parameters are $MJD_0 = 55747$ and $P_0 = 1282$ days. The positive sign represents prograde precession, while the negative sign represents retrograde precession. As seen in Fig. 3.36, there are two values for ω for a particular date, that are symmetric about the line $\omega = 180^\circ$. This follows from Eq. 3.8 that gives two solutions for ω. From the distribution of ω, a best-fit period of 1282 days for precession in the disc plane with a constant eccentricity is obtained. Fig. 3.37 is a schematic representing the scenario described above.

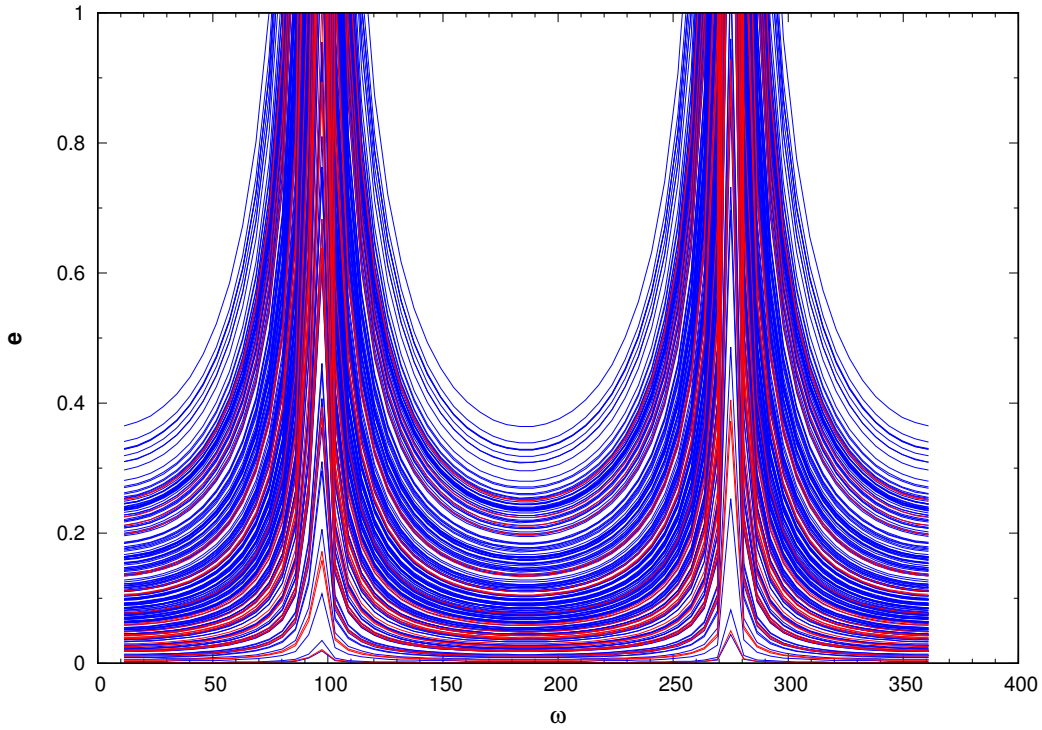

(a) Non-averaged velocities.

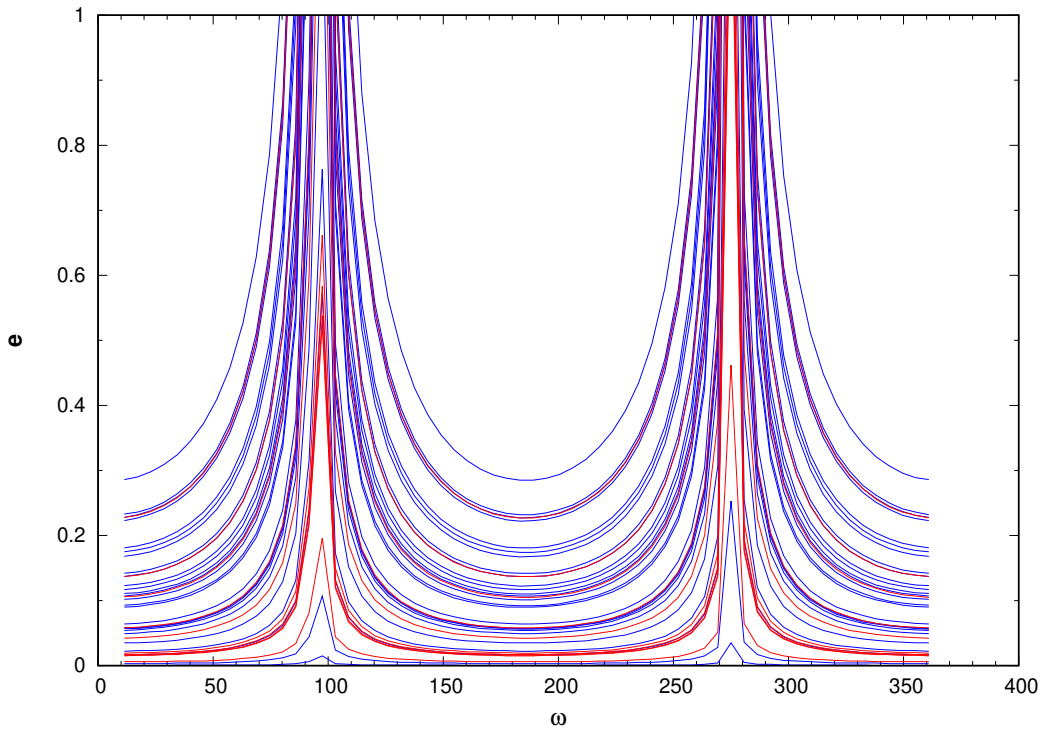

(b) Velocities averaged per orbital cycle.

Figure 3.35: Eccentricity (e) as a function of the argument of pericentre (ω) from measurements of the red and blue peak velocities from LT (blue curves) and HR (red curves). (a) shows the relationship between e and ω for all measured red and blue peak velocities and (b) shows the relationship for velocities averaged per orbital cycle.

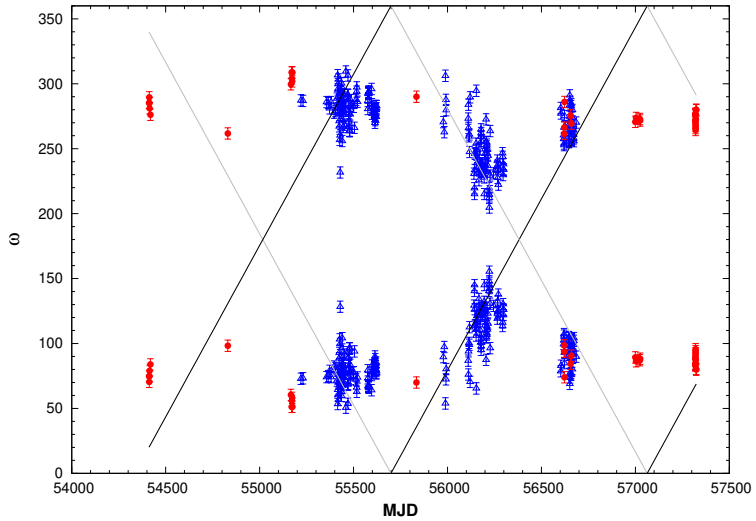

(a)

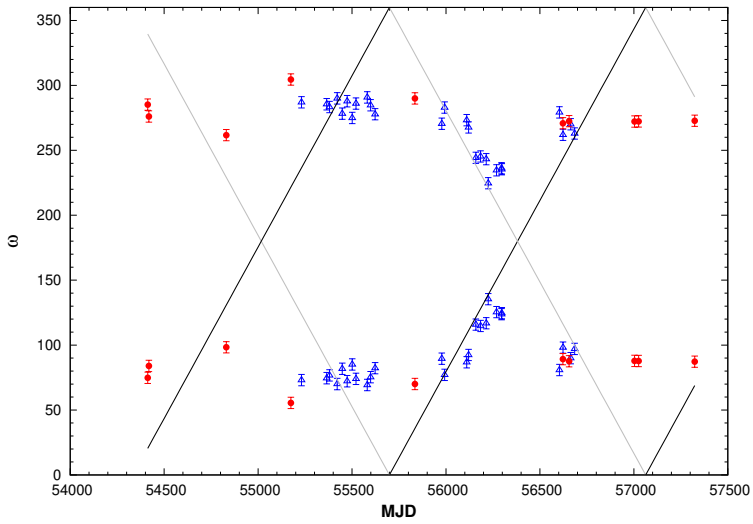

(b)

Figure 3.36: Evolution of the argument of pericentre for a fixed eccentricity of $e = 0.4$ from (a) all the measured peak velocities and (b) the peak velocities averaged per orbital cycle.

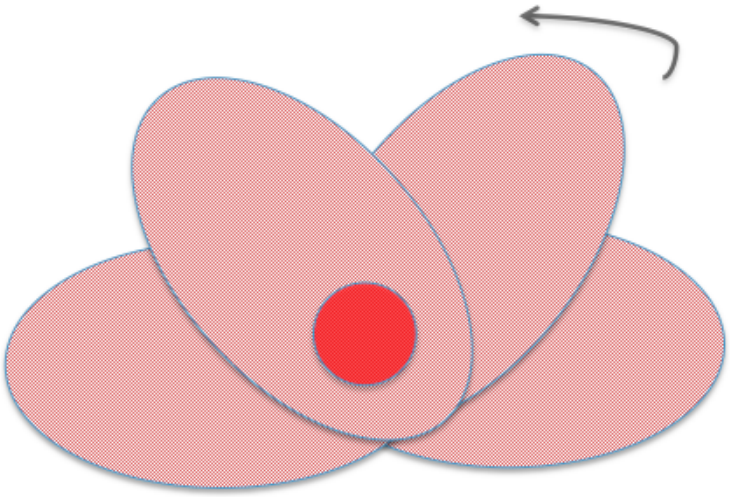

Figure 3.37: Schematic illustrating a precessing disc with a constant eccentricity.

3.5.3 Eccentricity variability with constant argument of pericentre

The scenario for disc eccentricity mainly varying while the argument of pericentre remains roughly constant is presented in Fig. 3.38. The argument of pericentre is fixed to $\omega = 0°$, where the eccentricity is least sensitive to ω (Fig. 3.35). From Eq. 3.8, $\omega = 180°$ produces negative values for the eccentricity, which is equivalent to the reversal of the side of pericentre of the disc. In Fig. 3.38 the eccentricity distribution is fit with a sinusoidal curve represented by

$$e = e_A \sin[(MJD - MJD_0)/P_0] - e_\phi, \tag{3.10}$$

with best-fit parameters $e_A = 0.145$, $MJD_0 = 55216$, $P_0 = 1419$ and $e_\phi = 0.0369$. In this scenario, the periodic variability in the eccentricity can be attributed to the KLM. While the KLM itself does not cause reversal of the pericentre (unless the disc precesses simultaneously), the behaviour shown in Fig. 3.38 could be due to external processes not included in the model (see Section 3.6).

3.5.4 Simultaneous variability in e and ω

In the following scenario, the precession rate is assumed to be constant, with a period equal to the superorbital period and varying in a limited range (librat-

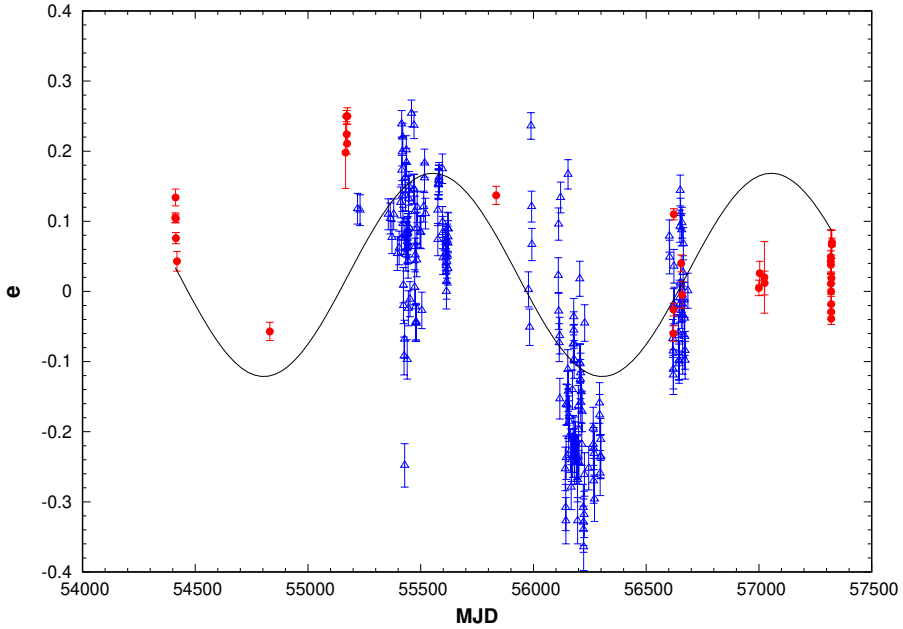

(a)

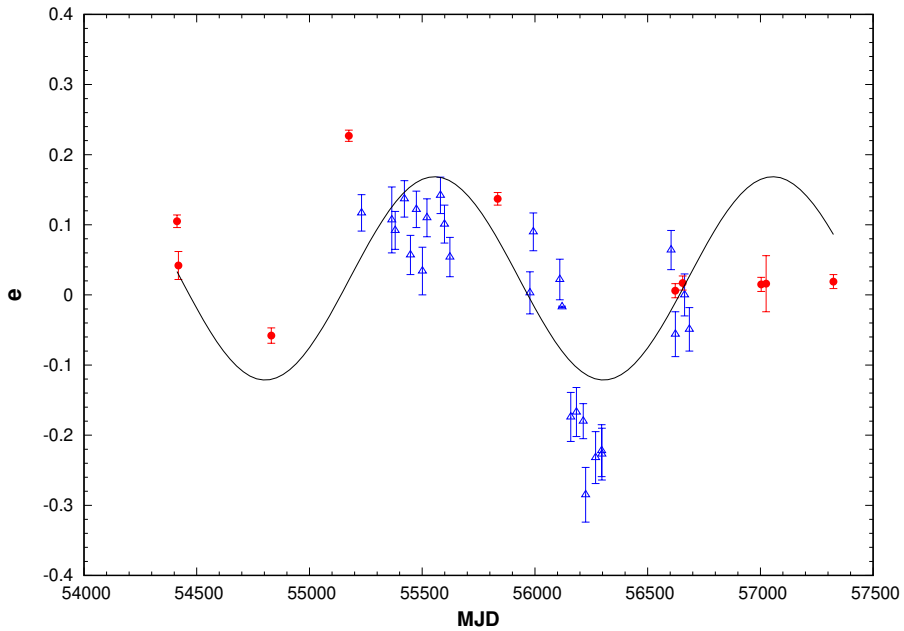

(b)

Figure 3.38: Evolution of the eccentricity for a fixed argument of pericentre of $\omega = 0^{\circ}$ from (a) all the measured peak velocities and (b) the peak velocities averaged per orbital cycle.

ing) taking the form:

$$\omega = \pm 90^\circ \sin\left[360^\circ (t - 55700)/1667\right] \pm 90^\circ. \quad (3.11)$$

Fig. 3.39 and 3.40 (top panel) is the resultant plot, where there are two solutions for ω from Eq. 3.8 for each set of measured peak velocities as seen with the distribution of ω being symmetric about 0°. The eccentricity can then be derived from ω values and the measured peak velocities, as shown in Fig 3.39 and 3.40 (bottom panel) where it is fitted to the function:

$$e = 0.18 \sin\left[360^\circ (t - 56200)/1667\right] + 0.18. \quad (3.12)$$

This scenario is equivalent to the idea of the disc precessing at a constant rate (in the disc plane or the binary orbit axis), and the disc eccentricity varying due to the KLM (the disc is initially inclined relative to the binary orbit axis).

In an alternative scenario, the eccentricity is assumed to vary in a positive range, taking the form (Fig 3.41 and 3.42 top panel):

$$e = 0.2 \sin\left[360^\circ (t - 56000)/1667\right] + 0.2. \quad (3.13)$$

The resulting ω distribution is then fitted to the function (Fig. 3.41 and 3.42 bottom panel):

$$\omega = \pm 25^\circ \sin\left[360^\circ (t - 56000)/1667\right] \pm 90^\circ. \quad (3.14)$$

The simple models overplotted to the eccentricity and argument of pericentre distributions in Figs. 3.36−3.42 for the different scenarios show a relatively large scatter. This is especially the case for the variation in eccentricity, where the scatter is approximately as large as the half-amplitude of the model. The effect is less pronounced in the variability of the argument of pericentre, more notably for the data averaged over the orbital period. The relatively poor agreement between the calculated e and ω parameters with the models applied could be a result of the degeneracy between the two parameters, as well as the basic assumption of sinusoidal variability in the parameters. The simple assumptions adopted of the particle model where the external effects due to the interaction of the Be star/disc with the compact object could also account for the scatter (see section 3.6).

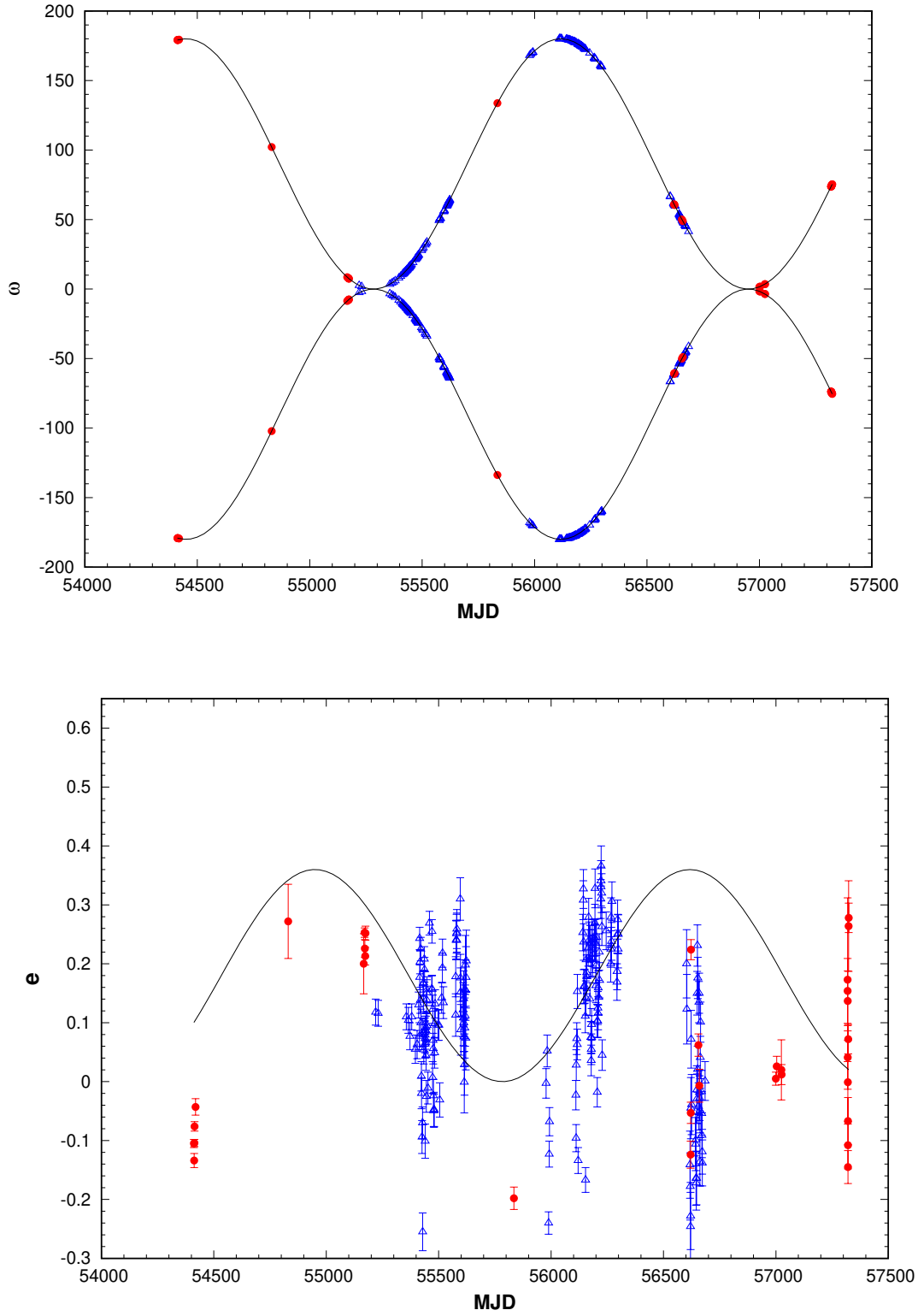

Figure 3.39: Top: Argument of pericentre as a function of time from the assumption of constant precession rate. Bottom: Resultant distribution of the eccentricity as a function of time using LT (blue) and HR (red) data.

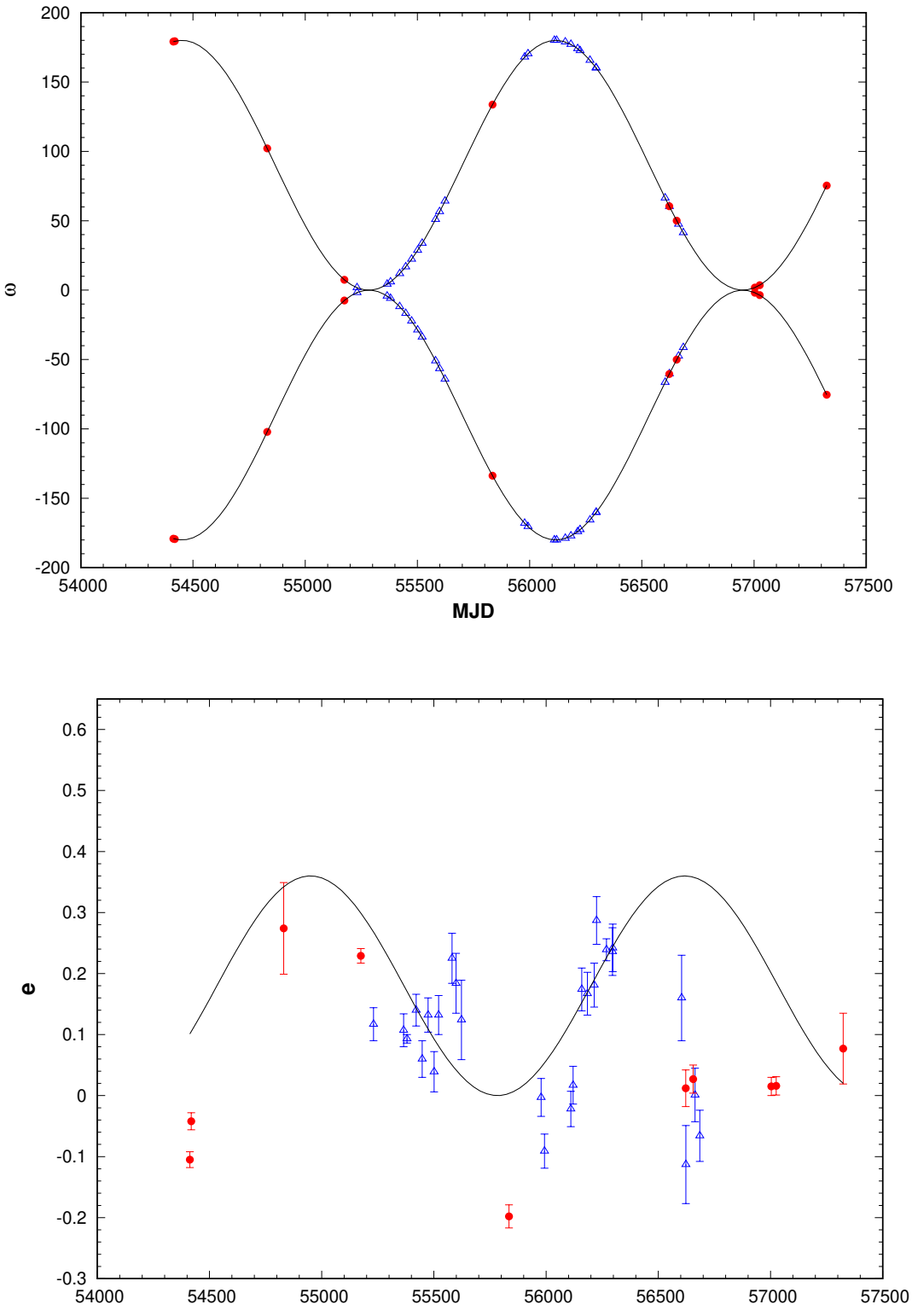

Figure 3.40: Same as Fig. 3.39, but for velocities averaged per orbital cycle.

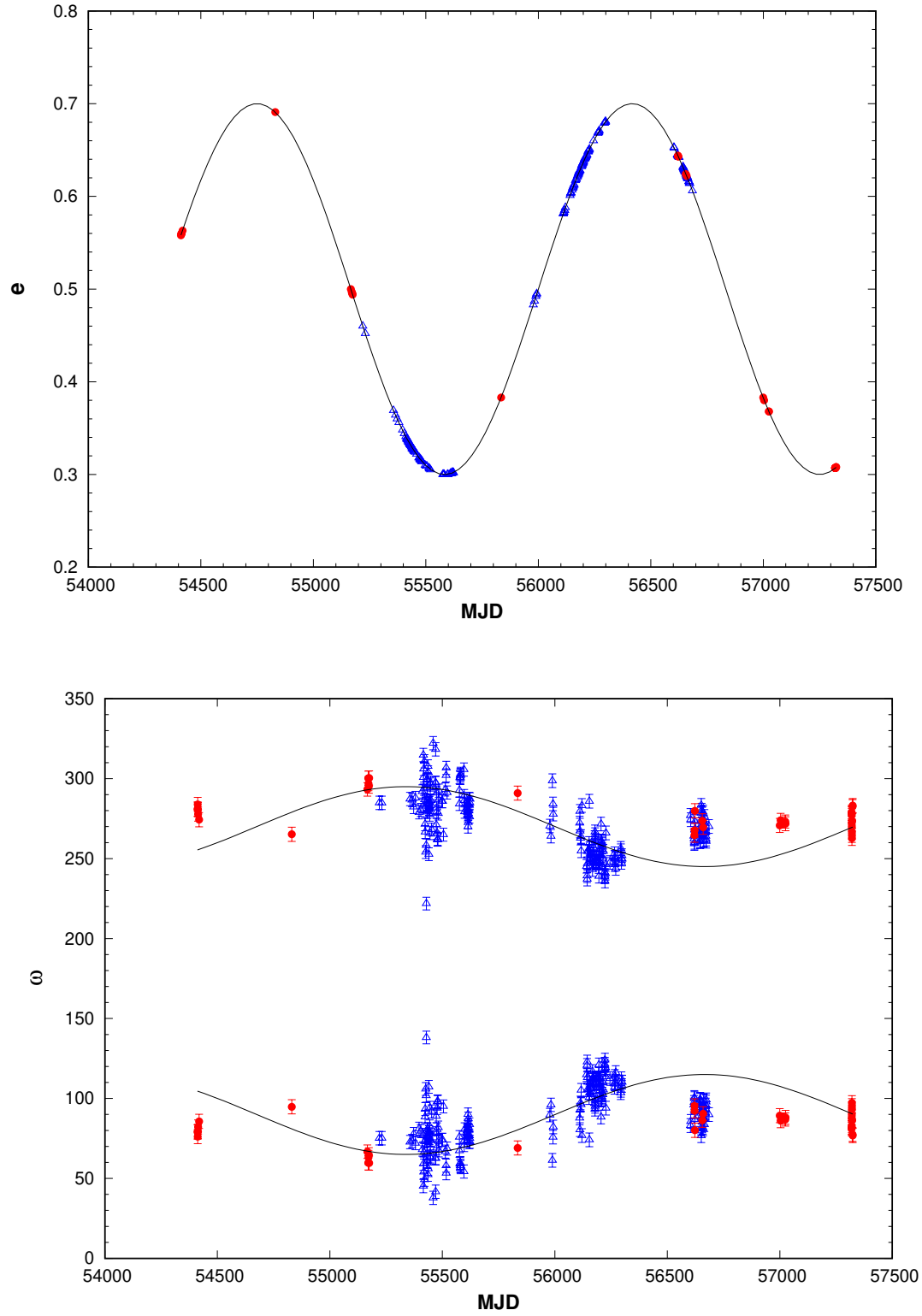

Figure 3.41: Top: Eccentricity as a function of time from the assumption of constant rate of variability. Bottom: Resultant fit to the argument of pericentre as a function of time using LT (blue) and HR (red) data.

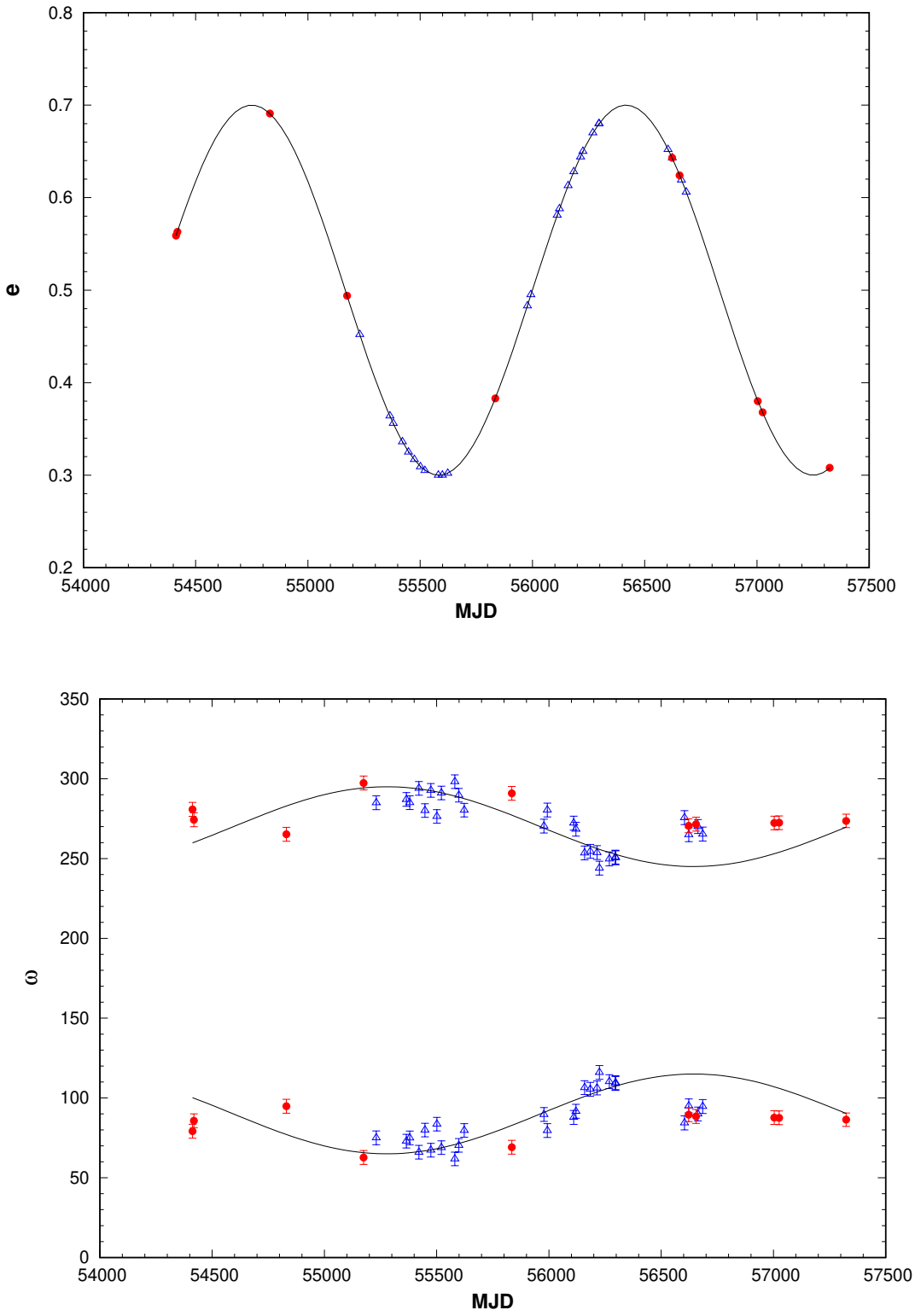

Figure 3.42: Same as Fig. 3.41, but using velocities averaged every orbital cycle.

3.5.5 Semi-major axis variability

The semi-major axis, $a_{\rm p}$, is given by

$$\frac{a_p}{R_1} = \frac{4v_{\rm crit}\sin^2 i}{(v_{\rm red}-v_{\rm blue})^2 - (v_{\rm red}-v_{\rm blue})^2\sec\omega}, \tag{3.15}$$

$$\frac{a_p}{R_1} = \left(\frac{2v_{\rm crit}}{v_{\rm red}-v_{\rm blue}}\right)^2 \frac{\sin^2 i}{1-e_p^2}, \tag{3.16}$$

where R_1 is the stellar radius, $v_{\rm crit}$ is the critical velocity and i is the inclination angle of the disc relative to the line of sight. The relationship in eq 3.15 is similar to the well-known relation from Huang (1972) that is widely used to obtain the estimates of the Be disc size from the measured peak separation of the Hα emission line. The relationship from Huang (1972), however, underestimates the size of the disc by a factor of $(1-e^2)$, if the disc is eccentric. Fig. 3.43 shows the semi-major axis as a function of inclination angle, with the eccentricity fixed to $e = 0.4$ (as in Fig. 3.36). The black and purple horizontal lines indicate the size of the Roche lobe of the Be star and the separation of the binary at periastron passage, respectively. The relatively low X-ray activity in LSI implies that the size of the disc is smaller than the periastron distance. From this, the inclination angle of the disc relative to the line of sight can be constrained to $27^\circ \leq i \leq 37^\circ$ (Fig. 3.43).

Fig. 3.44 and 3.45 show the evolution of the semi-major axis for $i = 27^\circ$ and $i = 37^\circ$, respectively. For the case of $i = 37^\circ$, the disc shows sizes significantly larger than the binary separation at periastron and the Roche lobe radius, while for $i = 27^\circ$ the disc sizes are comparable to the binary separation at periastron and the Roche lobe radius.

3.5.6 EW and V/R vs. surface area and iso-velocity contours

From the particle model, the areas of the blue-shifted ($S_{\rm blue}$) and red-shifted ($S_{\rm red}$) regions of the disc are represented by

$$S_{\rm blue} = \frac{1}{2}(a_p^2 - a_{\rm in}^2)(1-e_p^2)\cos i \int_{f_{0,1}}^{f_{0,2}} \frac{df}{(1+e_p\cos f)^2}, \tag{3.17}$$

$$S_{\rm red} = \frac{1}{2}(a_p^2 - a_{\rm in}^2)(1-e_p^2)\cos i \int_{f_{0,1+2\pi}}^{f_{0,2}} \frac{df}{(1+e_p\cos f)^2}, \tag{3.18}$$

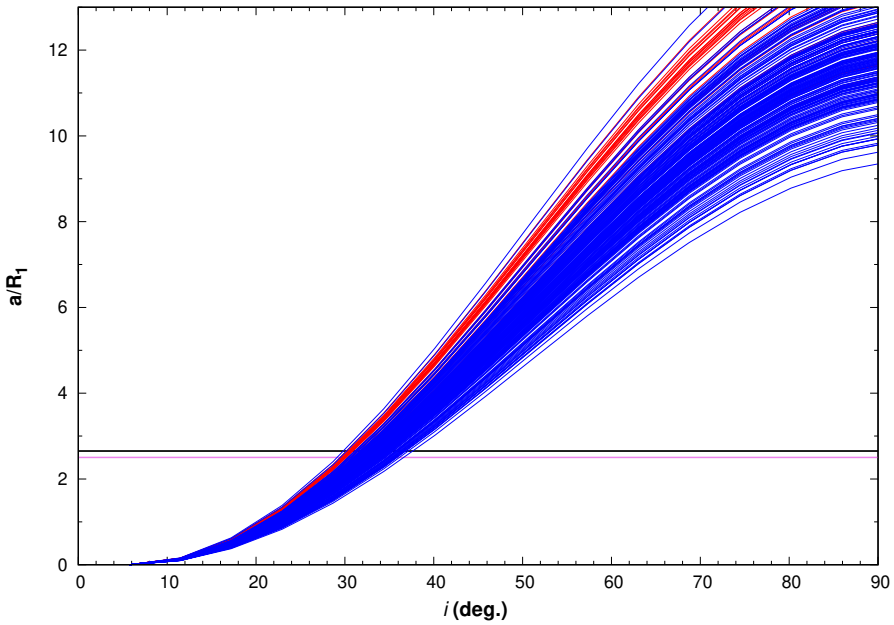

(a) Non-averaged velocities.

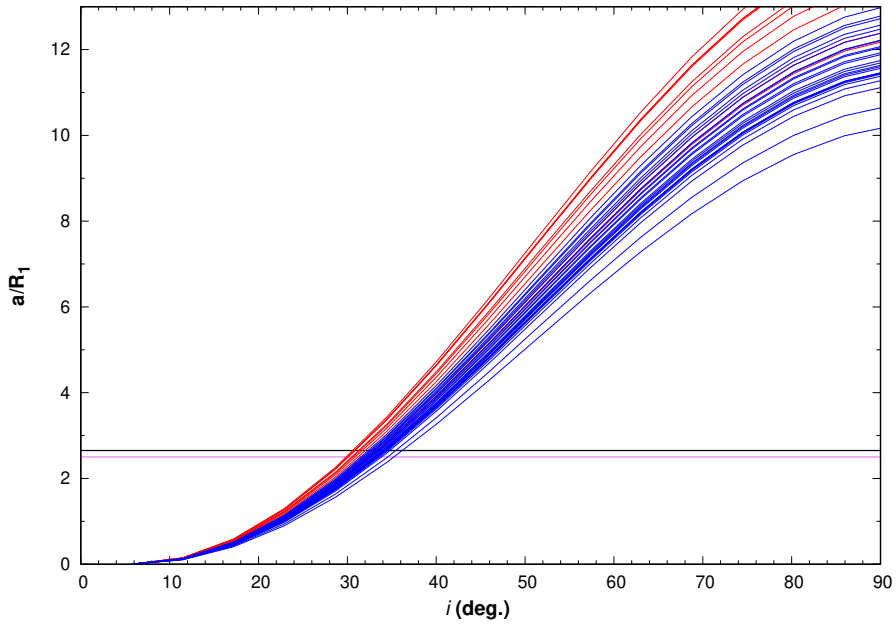

(b) Velocities averaged per orbital cycle.

Figure 3.43: Semi-major axis of the emitting region as a function of inclination angle with the eccentricity fixed at $e = 0.4$, using all the measured velocities (a) and velocities averaged for every orbital cycle (b). The black and purple lines represent the size of the Roche lobe of the Be star and the separation of the binary at periastron passage, respectively.

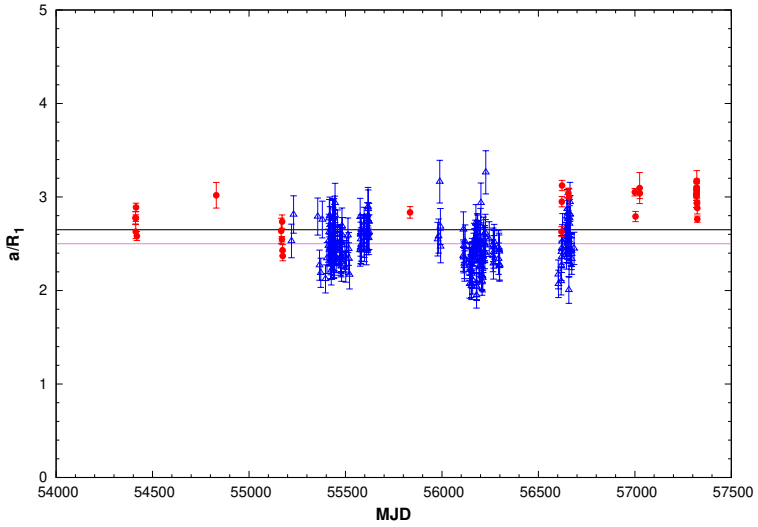

(a) Non-averaged velocities.

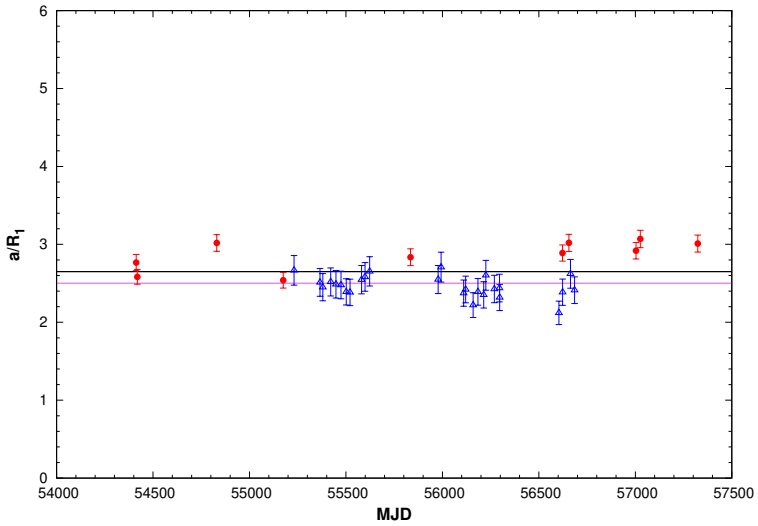

(b) Velocities averaged per orbital cycle.

Figure 3.44: The evolution of the semi-major axis of the emitting region with the eccentricity fixed at $e = 0.4$ and disc inclination with respect to the line of sight of $i = 27°$, using all the measured velocities (a) and velocities averaged every orbital cycle (b). The black and purple lines represent the size of the Roche lobe of the Be star and the separation of the binary at periastron passage, respectively.

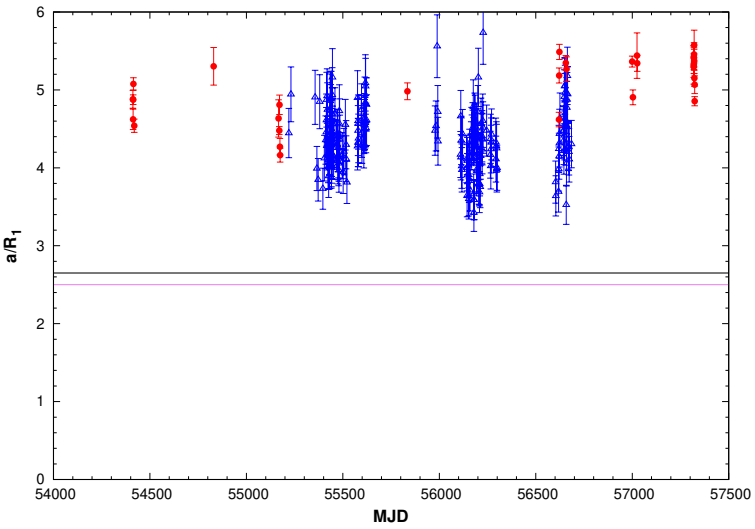

(a) Non-averaged velocities.

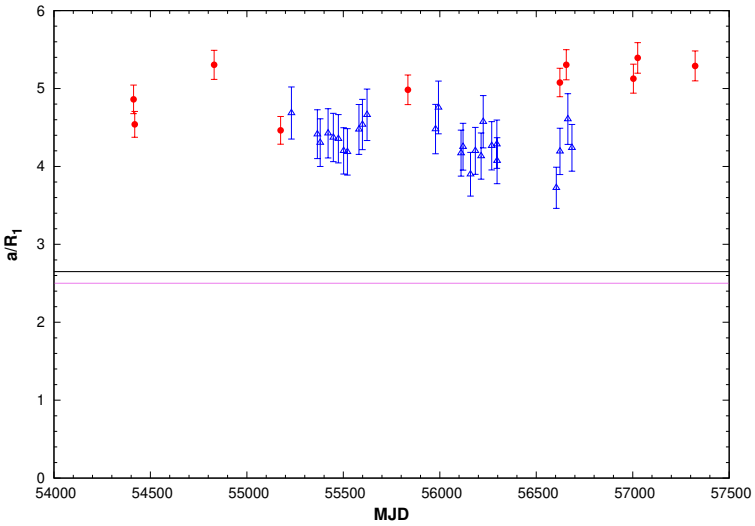

(b) Velocities averaged per orbital cycle.

Figure 3.45: The evolution of the semi-major axis of the emitting region with the eccentricity fixed at $e = 0.4$ and disc inclination with respect to the line of sight of $i = 37°$, using all the measured velocities (a) and velocities averaged every orbital cycle (b). The black and purple lines represent the size of the Roche lobe of the Be star and the separation of the binary at periastron passage, respectively.

where $a_{\rm in}$ is the semi-major axis at the innermost orbit, the $f_{0,1}$ and $f_{0,2}$ represent the true anomalies of an orbiting particle at the contour of the zero radial velocity. Eqs. 3.17 and 3.18 can be compared with the measured EWs. Fig. 3.46 shows the evolution of the ratio between the blue-shifted and red-shifted EW (EW_b/EW_r) with the ratio of the blue-shifted and red-shifted areas from the particle model overplotted shown in the violet and brown symbols, respectively. The model is systematically larger than the EW, which is especially seen in the epoch between MJD55350 and MJD55620. The possible reasons for the discrepancies between the model predictions and the EW are discussed in section 3.6.

From the assumption made about uniform emissivity of the disc (Appendix A), the blue and red peak intensities are proportional to the lengths of the iso-velocity contours $v_{\rm blue}$ and $v_{\rm red}$. The lengths of the iso-velocity contours at the blue and red peak velocities are represented by

$$\begin{aligned}\ell_{\rm blue}, \ell_{\rm red} &= (1-e_{\rm p}^2)\int_{a_{\rm in}}^{a_{\rm p}} da \\ &\times \left\{ \frac{1}{1+e_{\rm p}\cos f_{\mp,1}} \sqrt{1+\frac{a\left(\mp 1+e_{\rm p}\cos\omega\right)^2}{4a_{\rm p}\sin^2(\omega+f_{\mp,1})}} \right. \\ &\left. + \frac{1}{1+e_{\rm p}\cos f_{\mp,2}} \sqrt{1+\frac{a\left(\mp 1+e_{\rm p}\cos\omega\right)^2}{4a_{\rm p}\sin^2(\omega+f_{\mp,2})}} \right\}. \end{aligned} \tag{3.19}$$

$\ell_{\rm blue}$ and $\ell_{\rm red}$ from Eq. 3.19 can be compared with the peak intensities of the Hα line. Fig. 3.47 is a comparison of the V/R ratio with the ratio of iso-velocities from the model predictions. Again, the violet symbols represent the measured parameters while the brown symbols are the model predictions. As with the evolution of the EW, the model generally shows a comparable global trend compared to the V/R ratios, with model being systematically larger.

3.6 Discussion

3.6.1 Discrepancies in EW and V/R measurements

From the particle model, the ratio of the blue and red surface area can be compared to the ratio of the EW of the red and blue peaks of the Hα emission line. From a qualitative viewpoint, the model approximately follows the general trend of the changes in the emission line. The model, however, produces

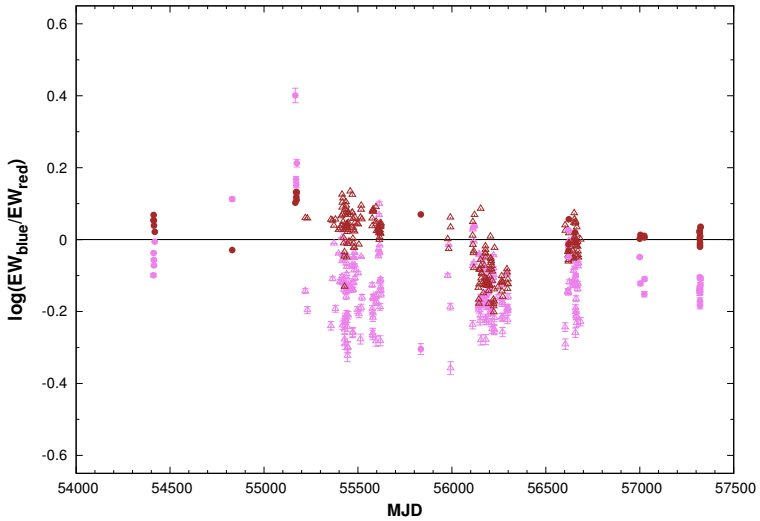

(a) Non-averaged velocities.

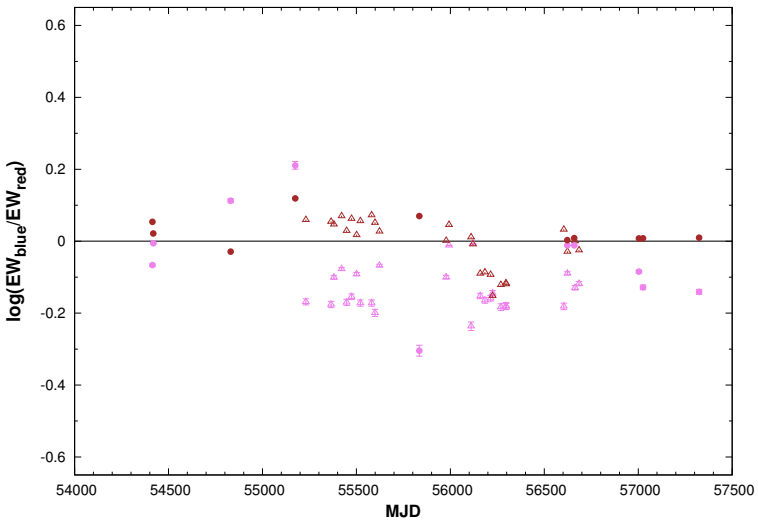

(b) Velocities averaged per orbital cycle.

Figure 3.46: Evolution of the measured equivalent width ratio (violet symbols) from LT (triangles) and HR (circles) compared to model surface area (brown symbols).

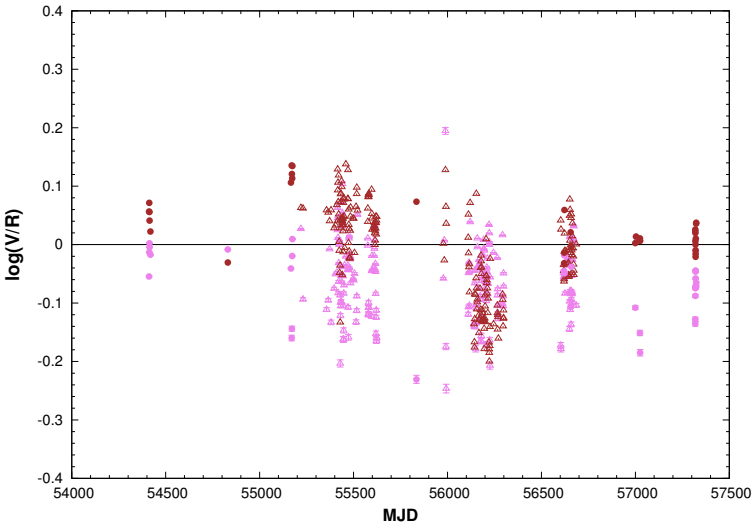

(a) Non-averaged velocities.

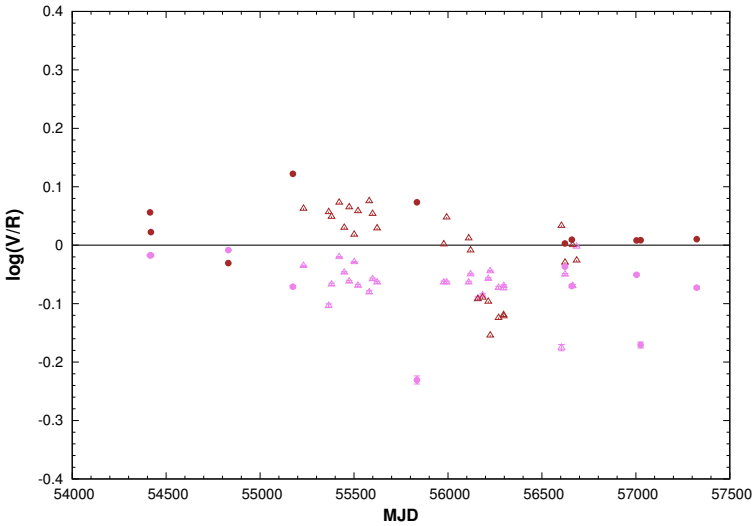

(b) Velocities averaged per orbital cycle.

Figure 3.47: Evolution of the V/R ratio (violet symbols) from LT (triangles) and HR (circles) compared to lengths of the iso-velocity contours from model predictions (brown symbols).

systematically larger values of the surface area ratio. A similar trend is observed in the behaviour of the ratio of the iso-velocity lengths from the model in comparison to the ratio of the measured blue and red intensities.
There are several possible explanations for the discrepancy between model predictions and the measured EW and V/R. The model assumes particles orbit in Keplerian fashion in a flat disc. Be discs in binary systems, however, can undergo warping as has been speculated to take place on a few occasions in the BeXBs 4U 0115+634 (Negueruela et al. 2001, Reig et al. 2007) and A 0535+262 (Moritani et al. 2011) suggested through the analysis of Hα line shape changes. In a warped disc, the particles' kinematics may temporarily depart from Keplerian motion. Another possible reason for the slight deviation between model predictions and measured parameters is because the model does not take into account external effects arising from the interaction of the Be star/disc system with the compact object. If LSI operates in the PWM scenario, then the pulsar wind may have an influence on the motions of the disc particles, and hence the disc geometry. In the following, a calculation is performed to quantify the effect of the pulsar wind as it interacts with the Be wind. Matching the ram pressures of the pulsar and the stellar winds:

$$P_{\rm pw} = \frac{\dot{E}}{4\pi d_{\rm s}^2 c} = P_{\rm SW} = \rho_{\rm W} v_{\rm W}^2 = \frac{\dot{M}_{\rm W}}{4\pi (d - d_{\rm s})^2 v_{\rm W}}, \tag{3.20}$$

with

- $\dot{E}$ - spin down energy of pulsar,
- $d_{\rm s}$ - distance from the shock discontinuity to pulsar,
- d - orbital separation,
- $v_{\rm W}$ - stellar wind outflow velocity,
- $\dot{M}_{\rm W}$ - stellar mass-loss rate.

So we have

$$\frac{d_{\rm s}}{d} = \frac{\eta^{1/2}}{1 + \eta^{1/2}}, \tag{3.21}$$

where

$$\eta \approx 0.05 \left(\frac{\dot{E}}{10^{36} {\rm erg.s^{-1}}} \right) \left(\frac{10^{-7} {\rm M_\odot} yr^{-1}}{\dot{M}_{\rm W}} \right) \left(\frac{1000 {\rm kms^{-1}}}{v_{\rm W}} \right). \tag{3.22}$$

With $v_W \sim 1000$ km s^{-1}, $\dot{M}_W \sim 10^{-8} {\rm M_\odot yr^{-1}}$ and $\dot{E} \sim 80 \times 10^{34}$ erg. s^{-1}

(similar to PSR B1259-63), we get

$$\eta \approx 0.4 \tag{3.23}$$

At periastron (Casares et al. 2005a parameters) the orbital separation is:

$$d_{\rm peri} \approx 25 \ {\rm R}_{\odot}. \tag{3.24}$$

And so,

$$d_{\rm s} = (25) \left(\frac{(0.4)^{1/2}}{1 + (0.4)^{1/2}} \right) \ {\rm R}_{\odot} \approx 9.7 \ {\rm R}_{\odot} \tag{3.25}$$

Thus, the distance between the shock discontinuity and the Be star at periastron is

$$d_{\rm Be} = d_{\rm peri} - d_{\rm s} \approx 15.3 \ {\rm R}_{\odot} \tag{3.26}$$

Estimating the size of the disc to the size of the Roche lobe radius of the Be star:

$$R_{\rm L} = \frac{0.49 q^{2/3}}{0.6 q^{2/3} + \ln(1 + q^{1/3})}, \tag{3.27}$$

where $q = M_{\rm x}/M_{\rm O}$. Using $M_{\rm X} = 1.4$ M$_{\odot}$ for the pulsar mass and $M_{\rm O} = 12.5$ M$_{\odot}$ (Casares et al. 2005a), this is

$$R_{\rm L} \approx 25.5 \ {\rm R}_{\odot}. \tag{3.28}$$

From the above calculation, the disc size is larger than the separation between the contact discontinuity and Be star. As follows, the pulsar wind can affect the shape of the disc, as well as possibly suppress the emission of the blue component of the disc (Fig. 3.48). Furthermore, tidal interaction of the compact object with the disc, particularly close to periastron passage, can excite spiral density waves in the disc which could cause the disc to temporarily diverge from Keplerian motion (Okazaki et al. 2002, Martin et al. 2014a). These effects may also account for the relatively poor agreement between the models fitted to the distribution of eccentricity and argument of pericentre.

From the orbital geometry shown in Fig. 3.49 derived by Casares et al. (2005a) and the fact that the Hα profile shows the red peak being dominant for a large majority of the time (Fig. 3.50), the disc is expected to be elongated towards phases of apastron for prograde precession. It follows that in the epochs when the model prediction overestimates emission from the blue side of the disc, as also seen in the reversal of the side of pericentre from the eccentricity distri-

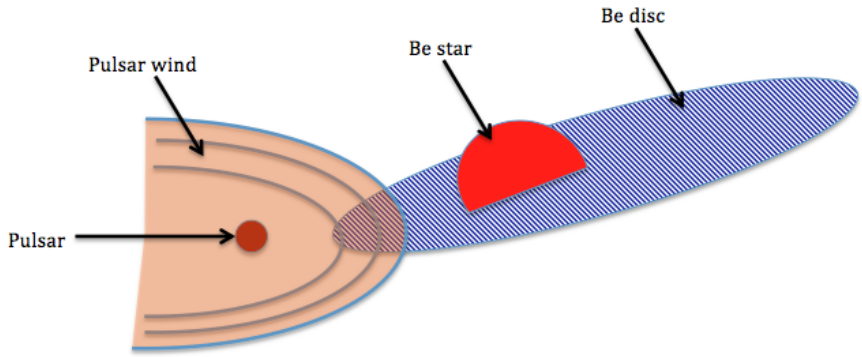

Figure 3.48: Illustration of the effect of the pulsar wind suppressing emission of the blue component of the disc at periastron passage.

bution, this could be due to the external effects being excluded. Nonetheless, the particle model gives a reasonable first approximation for interpreting the long-term observational parameters of the Be disc.

3.6.2 Precessing eccentric disc picture

A scenario analogous to the one presented here of the disc with a constant eccentricity and precessing on the superorbital period (subsection 3.5.2) is discussed by Xing, Wang & Takata (2017), where they bin the GeV data into tenths of the orbit and fold the lightcurves on the superorbital period. The folded, binned lightcurves show different amplitudes for the different orbital phase bins, and also the peaks (and troughs) shift in superorbital phase. The authors interpret this as the precession of an elliptical disc. In their scenario, the semi-major axis rotates at the superorbital period and is elongated towards periastron at superorbital phases $0.6 - 0.7$, causing the synchrotron emission to be reduced significantly at these phases (the compact object is embedded in the disc here, Fig. 3.51). The trough in the superorbital modulation is attributed to the compact object being surrounded by high-density matter (i.e. at periastron), with this matter gradually changing location as the eccentric disc precesses.

3.6.3 Relative disc inclination angle

While we can study the eccentricity as a function of time from the analysis of the Hα line properties with the particle model, we do not have a proxy of

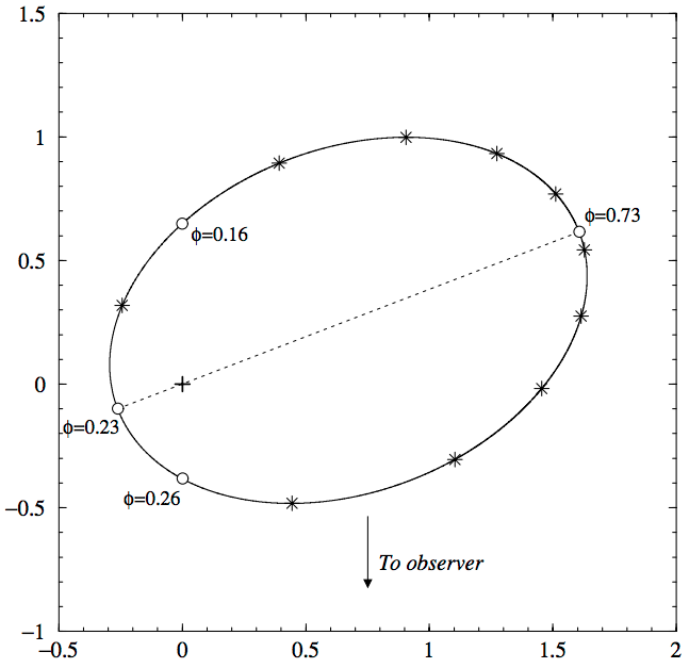

Figure 3.49: The orbital geometry of LSI as seen from above the orbital plane. From: Casares et al. (2005a)

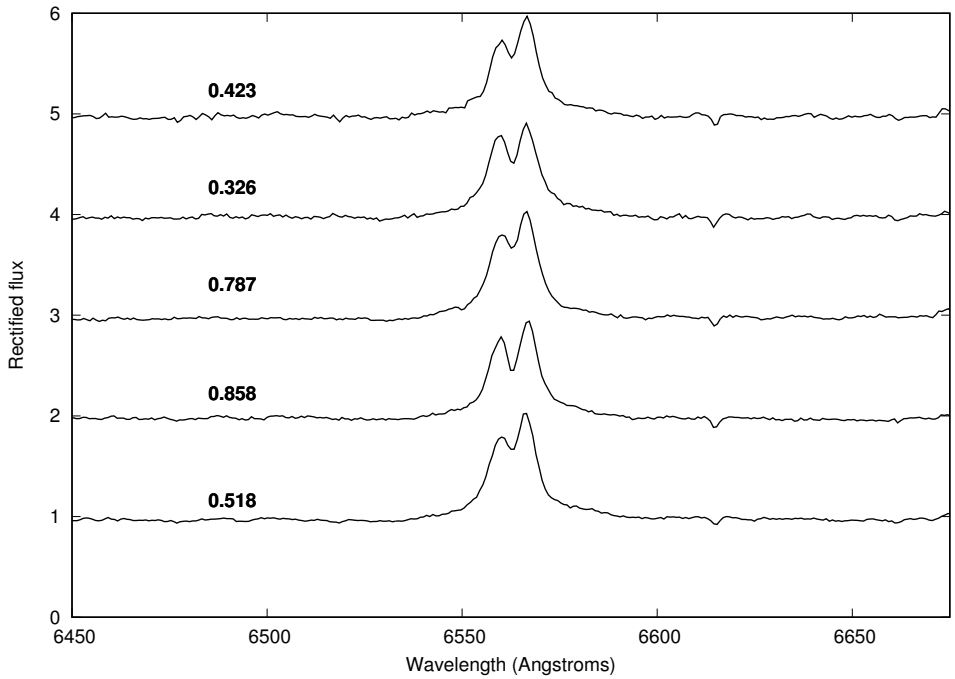

Figure 3.50: Example profiles of the Hα emission line of LSI showing the red peak being dominant. The orbital phases are indicated in the figure.

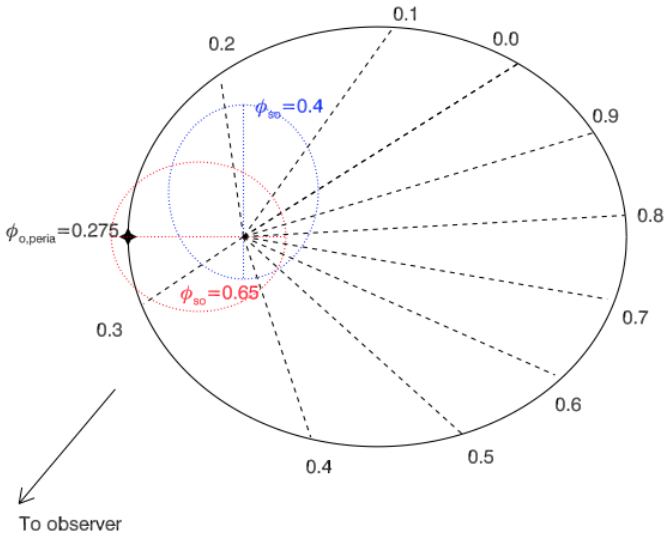

Figure 3.51: Schematic diagram illustrating precession of an eccentric disc in LSI. From: Xing, Wang & Takata (2017).

simultaneously getting a measure of the disc inclination variability. Zamanov et al. (2013) estimate the inclination angle of the disc by using intensities of the Hα line from the relationship between the central depression and the peaks, as described by Hanuschik (1996). The ratio between the mean peak intensity and the central depression, $I_p/I_{CD}(\mathrm{H}_\alpha) = 1.16 - 1.70$ (mean value of 1.40), is argued to imply an inclination angle $\approx 70°$. In a follow-up study, Zamanov et al. (2016) estimate the inclination angle of the orbit using the orbital parameters of Aragona et al. (2009) and assuming $M_1 = 15$ M$_\odot$ and $M_2 = 1.4$ M$_\odot$ for the Be and neutron star, respectively, they obtain an estimate of the orbital inclination angle in the range, $i_{\mathrm{orb}} = 67 - 73°$. From this result, Zamanov et al. (2016) argue that the misalignment between the disc plane and the orbital plane relative to the line of sight is insignificant. Despite this inference, however, the disc could still be significantly misaligned, as the azimuth of tilt of the disc and the orbital plane could be significantly different (Fig. 3.52).

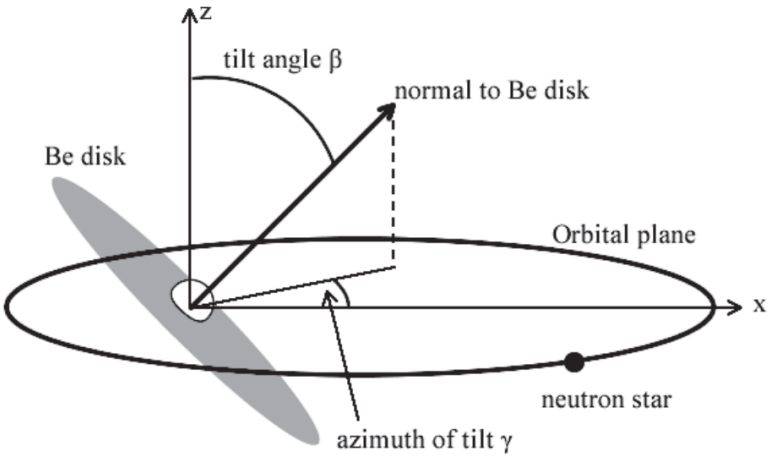

Figure 3.52: Illustration of a misaligned Be disc relative to the orbital plane. Even if the relative inclination angle of the disc relative to the orbit (tilt angle, β, in this schematic) is small, the azimuth of tilt (γ) could still be significantly large. From Okazaki, Hayasaki & Moritani (2013).

3.6.4 KLM timescale

Below is an analytical calculation of the KLM timescale from Martin et al. (2014b), Eq. 3.7 in this manuscript:

$$\begin{aligned} \frac{\tau_{\rm KLM}}{P_{\rm orb}} &\approx \frac{(4-p)}{(5/2-p)} \frac{\sqrt{M_1 M}}{M_2} \left(\frac{a}{R_{\rm out}}\right)^{3/2} \\ \frac{\tau_{\rm KLM}}{P_{\rm orb}} &\approx 122 \\ \tau_{\rm KLM} &\approx 3240 \text{ days.} \end{aligned} \tag{3.29}$$

The above timescale was calculated with the following assumptions: $M_{Be} = 12.5$ M$_\odot$ for the mass of the Be star, $M_{\rm NS} = 1.4$ M$_\odot$ for the mass of the pulsar, $p \sim 1.5$ for the surface density power-law index (Martin et al. 2014b), $R_{\rm out}$ is the initial disc radius (approximated to the average Roche lobe radius, 0.29 a). The calculated period of the KL oscillations is roughly twice the superorbital period of LSI. It should be noted, however, that the value obtained from the expression used above for the period has a large uncertainty, as it does not take into account the relative inclination angle between the disc and orbit of the compact object. As discussed by Fu, Lubow & Martin (2015a), the effect of a large relative inclination angle results in a faster onset and a smaller amplitude of the oscillations. In a comparison of the period timescales obtained from simulations and those obtained analytically, Fu, Lubow & Martin (2015a) show that Eq. 3.7 is valid to a factor of about 2. Moreover, although the viscosity of the disc will have an effect on the damping of the oscillations, its effect on the

timescale is uncertain, but could be signficant (Fu, Lubow & Martin 2015a).

3.7 Summary

We have analysed measured parameters of the Hα emission line in LSI, together with a disc model using particles orbiting the Be star which mimic a circumstellar disc, to analyse the long-term behaviour of the disc. Using the measured peak velocities, the variability of the disc eccentricity, e_p, as a function of the disc argument of pericentre, ω, is examined. We have systematically studied various possibilities for the disc behaviour in the framework of the disc model: in the one case, the precession of the disc about an axis, with the assumption that e_p simultaneously varies, is considered. Alternatively, the variability of the eccentricity is examined for a uniform variation (libration) of ω. The two other scenarios examined are those of variability of either of the two quantities, e and ω, while the other remains constant. We have shown that for the different scenarios for the variability in e_p and ω the timescales for variability in the two parameters is roughly on the order of the superorbital period for LSI. Based on the fits to the eccentricity and argument of pericentre, it is difficult to distinguish which mechanism is dominant in the long-term variability of the Be disc in LSI. Furthermore, in analysing the motions of the particles in the disc with the current model, it is challenging to study simultaneous variability between the eccentricity and disc inclination relative to our line of sight. Nonetheless, the analysis of the measured disc parameters in conjunction with the particle model provides a way to investigate the KLM from an observational viewpoint through the variability of the disc eccentricity.

As noted in the results presented for LSI in the comparison between measured EW and V/R with the predictions made from the particle model, there are epochs which display slight discrepancies for these quantities due to the limitations of the model. In its current state, the model does not take into account the external effects of the compact object. Moreover, Be discs can occasionally be deformed, resulting in warping and/or spiral density waves. Despite this, the analysis presented in this chapter provides, as zeroth order approximation, a way of quantitatively investigating several properties of Be discs. Our future efforts will be directed towards improving our analysis by including these effects directly.

Chapter 4

The Bethe-Heitler mechanism for high energy emission in gamma-ray binaries

This chapter discusses the mechanisms for producing high energy emission in GRBis. Gamma-ray emission involves the interaction of accelerated charged particles (electrons and protons) with target cold photons, charged particles and magnetic fields. We first give a description of the main gamma-ray production and absorption mechanisms relevant for GRBis. The derivations of the various quantities presented here are based on the notation used by Longair (2011), Rybicki & Lightman (1986) and Blumenthal & Gould (1970). We then present the Bethe-Heitler mechanism for gamma-ray production in GRBis in the framework of the pulsar wind model (PWM). We calculate the gamma-ray spectrum and lightcurves, accounting for the effects of absorption and cascading. We also show the effect of the magnetic field on the gamma-rays produced and demonstrate the orbital phase modulation due to absorption, as well as show the effects of electromagnetic cascading.

4.1 Particle acceleration

The detection of high energy photons from astrophysical sources implies that energetic particles that aided in creating them are accelerated by some physical mechanism. The most prevalent mechanism that has been discussed across several fields of research is diffusive shock acceleration, sometimes referred to as

first-order Fermi acceleration (Axford, Leer & Skadron 1977, Bell 1978, Baring 1997). To explain this, let us imagine a non-relativistic shock that moves at a speed U through a gaseous medium with charged particles present on either side of the shock, as illustrated in Fig. 4.1(a). In the reference frame where the shock is at rest, the matter ahead of the shock ("upstream") moves towards the shock at a speed, $v_1 = U$. From the equation of continuity, the parameters on either side of the shock can be related as:

$$\rho_1 v_1 = \rho_2 v_2, \tag{4.1}$$

where ρ_1 and ρ_2 is the density of the gas on the upstream and downstream medium, respectively, and v_2 is the velocity of the downstream medium. The ratio of the densities can be written in terms of the ratio of the specific heat capacities, γ, as:

$$\frac{\rho_2}{\rho_1} = \frac{\gamma + 1}{\gamma - 1} = \frac{v_1}{v_2}. \tag{4.2}$$

In a monatomic gas, $\gamma = 5/3$, so that $v_1 = 4v_2$. So, in the reference frame where the shock is at rest the downstream gas moves away from the shock at a speed of $v_2 = 1/4U$. If we consider the reference frame in which the upstream gas is at rest, the shock is approaching at a speed U and the downstream gas in that frame is seen to be approaching at a speed $3/4U$ (Fig. 4.1(c)). As the particles cross the shock from the upstream gas to the downstream gas they are accelerated to a mean speed of $3/4U$ as seen from the upstream frame of reference. The particles scatter off turbulent magnetic fields and cross the shock once more from the downstream gas to upstream gas. The particles are again accelerated by a speed of $3/4U$ as seen from the downstream gas. This back and forth crossing of particles continues and leads to an increase in speed upon each crossing, resulting in significant acceleration of the particles.

A consequence of diffusive shock acceleration is a power-law energy distribution of the accelerated particles. Suppose β is a factor in the relation $E = \beta E_0$, representing the average energy of a particle after one collision, and P the probability of the particle remaining in the accelerating region after each shock-crossing. The average energy of the particle initially at E_0 after k shock-crossings is $E = \beta^k E_0$, while the number of particles is $N = N_0 P^k$. Taking logarithms of these expressions and making k the subject of the formulae, one obtains:

$$\frac{\ln(N/N_0)}{\ln(E/E_0)} = \frac{\ln P}{\ln \beta}, \tag{4.3}$$

which rearranges to

$$\frac{N}{N_0} = \left(\frac{E}{E_0}\right)^{\ln P/\ln \beta}. \tag{4.4}$$

The differential energy spectrum from this works out to be

$$N(E)dE = constant \times E^{-1+(\ln P/\ln \beta)}dE. \tag{4.5}$$

For a particle moving from upstream to downstream, the Lorentz transformation of the particle's energy is given by

$$E^{'} = \gamma_V(E + pV\cos\theta), \tag{4.6}$$

where θ is the angle between the initial velocity vector of the particle and the normal to the shock and γ_V is the Lorentz factor of the shock. Since the shock is non-relativistic, $\gamma_V \approx 1$. The energy of the particle is given by $E = pc$. So, from eq. 4.6 it follows that

$$\Delta E = pV\cos\theta, \tag{4.7}$$

and

$$\frac{\Delta E}{E} = \frac{V}{c}\cos\theta. \tag{4.8}$$

The particle's probability of crossing the shock within angles θ to $\theta + d\theta$ is given by

$$p(\theta) = 2\sin\theta\cos\theta d\theta, \tag{4.9}$$

and so, the average energy gain of the particle when crossing the shock is

$$\left\langle \frac{\Delta E}{E} \right\rangle = \frac{V}{c}\int_0^{\pi/2} 2\cos^2\theta\sin\theta d\theta = \frac{2}{3}\frac{V}{c}. \tag{4.10}$$

The particle gains an energy of $2V/3c$ when crossing back to the upstream gas, therefore the total energy gained for a complete to-and-fro journey is

$$\left\langle \frac{\Delta E}{E} \right\rangle = \frac{4}{3}\frac{V}{c}. \tag{4.11}$$

Therefore

$$\beta = \frac{E}{E_0} = 1 + \frac{4}{3}\frac{V}{c}, \tag{4.12}$$

and

$$\ln\beta = \ln\left(1 + \frac{4}{3}\frac{V}{c}\right) = \frac{4}{3}\frac{V}{c} = \frac{U}{c}. \tag{4.13}$$

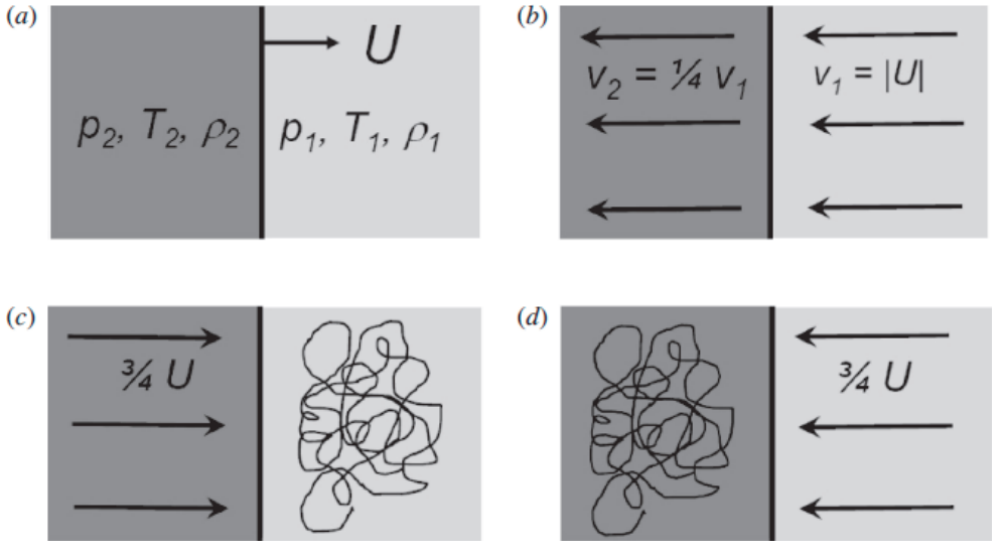

Figure 4.1: Illustration of the motion of energetic particles in a shock region along upstream (subscript 1) and downstream medium (subscript 2). The shock moves through gaseous medium with respect to the observer at a speed of U, as shown in (a). The motions of the gas medium in the rest reference frame of the shock is shown in (b). Motion of gas in the rest reference frame of the upstream gas material where the velocity distribution of the particles is isotropic is shown in (c). Motion of gas in the rest reference frame of the downstream gas material where the velocity distribution of the particles is isotropic, as shown in (d). From: Longair (2011).

Bell (1978) demonstrates, by considering classical kinetic theory arguments, that the fraction of particles lost is U/c. So, $P = 1 - (U/c)$ and

$$\ln P = \ln(1 - U/c) = -U/c. \tag{4.14}$$

From eq. 4.3, $\frac{\ln P}{\ln \beta} = -1$. Substituting this into eq. 4.5 we have

$$N(E)dE = constant \times E^{-2}dE. \tag{4.15}$$

The description of diffusive shock acceleration above is only valid for non-relativistic shocks and the treatment of magnetic fields is not included. Analytic and simulation work on diffusive shock acceleration for relativistic shocks with the effects of the magnetic field taken into account at different orientations (parallel, perpendicular and oblique to the shock normal) results in a range of spectral indices for particle distribution from hard (spectral index $\sigma \approx 1$) to softer power laws ($\sigma \approx 4$; e.g. Kirk & Heavens 1989, Ostrowski 1991, Bednarz & Ostrowski 1998, Summerlin & Baring 2012).

4.2 Inverse Compton scattering

The process in which energetic electrons upscatter low energy photons is referred to as inverse Compton (IC) scattering. In this mechanism, the electrons lose energy which is gained by the photons. IC scattering is important in high energy astrophysics and has numerous applications, e.g. X-ray binaries, active galactic nuclei and galaxy clusters. The basic reaction describing IC scattering is represented by:

$$e^- + \gamma_{\rm LE} \rightarrow e^- + \gamma_{\rm HE}. \tag{4.16}$$

Suppose we have electrons of energy E_e scattering soft photons of initial energy ϵ_*. For photons with number density $n_{\rm ph}$, the spectrum of photons formed is given by (Jones 1968, Blumenthal & Gould 1970, Lefa, Kelner & Aharonian 2012):

$$\frac{dN_\gamma}{dtdE_*} = \int_0^\infty \int_{E_{min}}^\infty G(E_e, \epsilon_*, E_*) n_{\rm ph} n_e(E_e) dE_e d\epsilon_*, \tag{4.17}$$

where the total scattering probability, $G(E_e, \epsilon_*, E_*)$, is given by

$$G(E_e, \epsilon_*, E_*) = \frac{8\pi r_e^2 c}{E_e \eta}\left[2q\ln q + (1-q)(1+2q) + (1-q)\frac{\eta^2 q^2}{2(1+\eta q)}\right], \tag{4.18}$$

and

$$\eta = \frac{4\epsilon_* E_e}{m^2c^4}\ ,\ q = \frac{E_*}{\eta(E_e - E_*)}. \tag{4.19}$$

$n_e(E_e)$ is the energy distribution of the electrons and E_* is the energy of photons after scattering. The scattering of the photons by the electrons can occur in the Thomson or the Klein-Nishina regime, depending on the parameter η. In the case where $\eta << 1$, scattering takes place in the Thomson regime while for $\eta >> 1$ the Klein-Nishina regime applies. In the Thomson regime, the photons gain an average energy of $\gamma^2 E_*$ after a scattering, while in the Klein-Nishina regime the energy gained is γE_*.

4.3 Pion production and decay

4.3.1 Proton-proton interaction

Gamma-rays can also be produced via hadronic processes through the decay of neutral pions. Energetic protons interacting with low-energy protons can

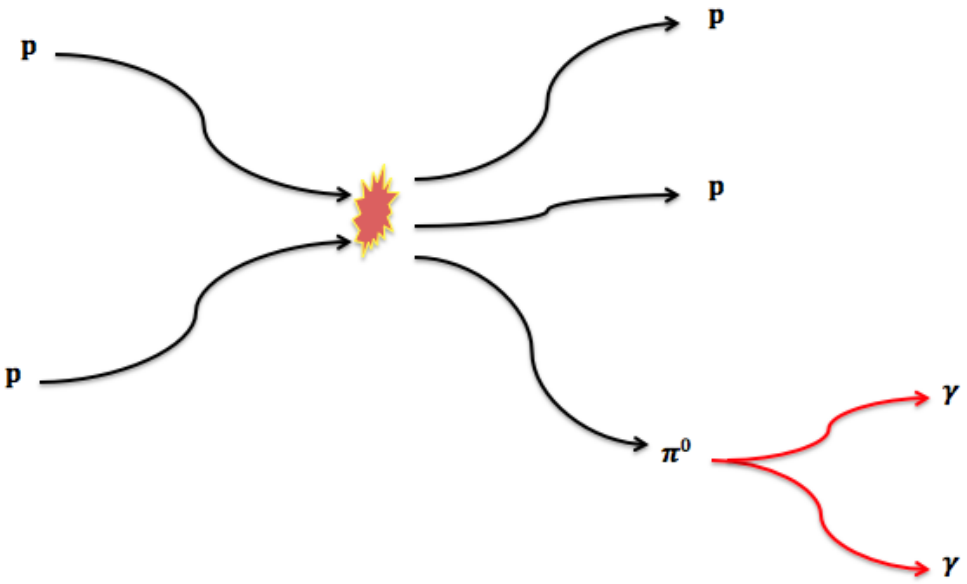

Figure 4.2: Neutral pion production from collision of two protons and the subsequent decay of the pion into two gamma-rays.

produce pions through several possible reactions:

$$p + p \rightarrow p + p + \xi_{\pi^0}\pi^0 + \xi_{\pi^\pm}(\pi^+ + \pi^-) \tag{4.20}$$

$$p + p \rightarrow p + n + \pi^+ + \xi_{\pi^0}\pi^0 + \xi_{\pi^\pm}(\pi^+ + \pi^-) \tag{4.21}$$

$$p + p \rightarrow n + n + 2\pi^+ + \xi_{\pi^\pm}(\pi^+ + \pi^-), \tag{4.22}$$

where n is a neutron, the π terms represent the pions and the ξ terms represent the multiplicities of the respective products. The charged products undergo a further series of reactions via these decay processes into muons (μ), neutrinos (ν) and antineutrinos ($\bar{\nu}$) (Longair 2011):

$$\pi^+ \rightarrow \mu^+ + \nu_\mu \tag{4.23}$$

$$\pi^- \rightarrow \mu^- + \bar{\nu}_\mu \text{ , mean lifetime } = 2.551 \times 10^{-8} \text{ s} \tag{4.24}$$

and the muons

$$\mu^+ \rightarrow e^+ + \nu_e + \nu_\mu \tag{4.25}$$

$$\mu^- \rightarrow e^- + \nu_e + \bar{\nu}_\mu \text{ , mean lifetime } = 2.2001 \times 10^{-6} \text{ s.} \tag{4.26}$$

The neutral pions, on the other hand, have a mean lifetime of 1.78×10^{-16} s and decay to two gamma-rays with a probability of 0.988 (Fig. 4.2). Each of the

two gamma-rays produced from this decay process has energy, $E = \frac{1}{2}m_\pi c^2 \approx$ 67.5 MeV.

4.3.2 Proton-photon interaction

Pion production can also occur from the interaction of high-energy protons from the acceleration site with soft stellar photons via the reactions:

$$p + \gamma \rightarrow p + \xi_{\pi^0}\pi^0 + \xi_{\pi^\pm}(\pi^+ + \pi^-) \tag{4.27}$$

$$p + \gamma \rightarrow n + \pi^+ + \xi_{\pi^0}\pi^0 + \xi_{\pi^\pm}(\pi^+ + \pi^-), \tag{4.28}$$

where the pions decay as demonstrated in 4.3.1. In the following, I derive the threshold energy of the proton for pion production. Suppose the momentum four-vectors of the proton and photon before and after the interaction are given by:

Before

$$\vec{P_p} = \gamma_p m_p c[1, \vec{\beta_p}] \ , \ \vec{P_*} = \frac{E_*}{c}[1, \hat{i}]. \tag{4.29}$$

After

$$\vec{P_p'} = m_p c[1, \vec{0}] \ , \ \vec{P_\pi} = m_\pi c[1, \vec{0}]. \tag{4.30}$$

The conservation of four-momentum requires:

$$\vec{P_p} + \vec{P_*} = \vec{P_p'} + \vec{P_\pi}. \tag{4.31}$$

Squaring both sides, we get

$$\vec{P_p} \cdot \vec{P_p} + 2\vec{P_p} \cdot \vec{P_*} + \vec{P_*} \cdot \vec{P_*} = \vec{P_p'} \cdot \vec{P_p'} + 2\vec{P_p'} \cdot \vec{P_\pi} + \vec{P_\pi} \cdot \vec{P_\pi}. \tag{4.32}$$

For each of the terms in eq. 4.32:

$$\vec{P_p} \cdot \vec{P_p} = \vec{P_p'} \cdot \vec{P_p'} = (m_p c)^2 \ , \ \vec{P_*} \cdot \vec{P_*} = 0 \tag{4.33}$$

$$\vec{P_p} \cdot \vec{P_*} = \gamma_p m_p E_* - \gamma_p m_p E_* \beta_p \cos\theta \tag{4.34}$$

$$\vec{P_p'} \cdot \vec{P_\pi} = m_p m_\pi c^2. \tag{4.35}$$

So, eq. 4.32 becomes

$$2\gamma_p m_p E_* (1 - \beta_p \cos\theta) = 2m_p m_\pi c^2 + m_\pi^2 c^2, \tag{4.36}$$

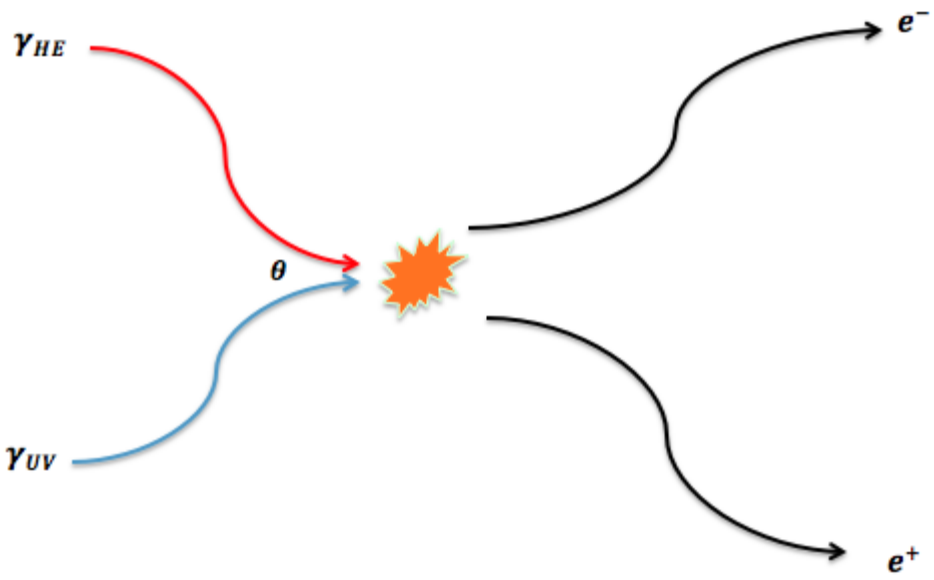

Figure 4.3: Illustration of photon-photon absorption.

and so the threshold Lorentz factor for the proton to produce a neutral pion is

$$\gamma_p = \frac{m_\pi c^2}{E_*(1-\beta_p \cos\theta)}\left(1+\frac{m_\pi}{2m_p}\right) \tag{4.37}$$

4.4 Photon-photon absorption

High energy photons (γ_{HE}) interact with the soft photons (γ_{UV}) from the massive stellar radiation field. The interaction produces an electron-positron pair, with the reaction:

$$\gamma_{HE} + \gamma_{UV} \rightarrow e^- + e^+ \tag{4.38}$$

Fig. 4.3 illustrates this process, where an energetic photon propagates at an angle θ relative to the low-energy photon. In the following, I will derive the threshold energy for an electron-positron pair to form. With $\vec{P_{*,HE}}$ and $\vec{P_{*,UV}}$ representing the momentum four-vectors of the photons, and $\vec{P_{e^-}}$ and $\vec{P_{e^+}}$ the momentum four-vectors of the electron-positron pair, conservation of four-momentum states:

$$\vec{P_{*,HE}} + \vec{P_{*,UV}} = \vec{P_{e^-}} + \vec{P_{e^+}}. \tag{4.39}$$

If we square both sides of Eq. 4.39, we get

$$\vec{P_{*,HE}} \cdot \vec{P_{*,HE}} + 2\vec{P_{*,HE}} \cdot \vec{P_{*,UV}} + \vec{P_{*,UV}} \cdot \vec{P_{*,UV}} = \vec{P_{e^-}} \cdot \vec{P_{e^-}} + 2\vec{P_{e^-}} \cdot \vec{P_{e^+}} + \vec{P_{e^+}} \cdot \vec{P_{e^+}} \tag{4.40}$$

Using the properties of momentum four-vectors at the threshold (particles created are at rest) of the electron/positron and photon

$$\vec{P_{*,HE}} \cdot \vec{P_{*,HE}} = \vec{P_{*,UV}} \cdot \vec{P_{*,UV}} = 0, \tag{4.41}$$

$$\vec{P_{e^-}} \cdot \vec{P_{e^-}} = \vec{P_{e^+}} \cdot \vec{P_{e^+}} = \vec{P_{e^-}} \cdot \vec{P_{e^+}} = m_e^2 c^2, \tag{4.42}$$

for $\vec{P_{*,HE}} = [\frac{E_{*,HE}}{c}, (\frac{E_{*,HE}}{c})\hat{i}]$, $\vec{P_{*,UV}} = [\frac{E_{*,UV}}{c}, (\frac{E_{*,UV}}{c})\hat{i}]$, $\vec{P_{e^-}} = \vec{P_{e^+}} = [m_e c, \vec{0}]$. Therefore, Eq. 4.40 reduces to

$$2\left(\frac{E_{*,HE}E_{*,UV}}{c^2} - \frac{E_{*,HE}E_{*,UV}}{c^2}\cos\theta\right) = 4m_e^2c^2, \tag{4.43}$$

rearranging this, we find the threshold energy of the high energy photon to produce an electron-positron pair is given by

$$E_{*,HE} = \frac{2m_e^2c^4}{E_{*,UV}(1-\cos\theta)}. \tag{4.44}$$

The cross-section for the photon-photon absorption process is given by (Jauch & Rohrlich 1976):

$$\sigma_{\gamma\gamma} = \frac{\pi r_e^2}{2}(1-\lambda^2)\left[2\lambda(\lambda^2-2) + (3-\lambda^4)\ln\left(\frac{1+\lambda}{1-\lambda}\right)\right], \tag{4.45}$$

where r_e is the classical electron radius, $\lambda = \sqrt{1-\frac{1}{s}}$ and $s = \frac{E_{*,UV}E_{*,HE}(1-\cos\theta)}{2m^2c^4}$. The differential optical depth of a high-energy photon ($E_{*,HE}$) travelling a distance l interacting with a low-energy photon ($E_{*,UV}$) in a radiation field with a number density $n_{E_{*,UV}}$ is then given by (Gould & Schréder 1967):

$$\mathrm{d}\tau_{\gamma\gamma} = (1-\cos\theta)n_{E_{*,UV}}\sigma_{\gamma\gamma}\mathrm{d}E_{*,UV}\mathrm{d}\Omega\mathrm{d}l. \tag{4.46}$$

Eq. 4.46 can then be integrated over all energies (from $E_{\min}$ to $E_{\max}$) and solid angles, Ω, to obtain the total opacity:

$$\tau_{\gamma\gamma} = \int_0^\infty \mathrm{d}l \int_0^{4\pi} \mathrm{d}\Omega \int_{E_{\min}}^{E_{max}} \frac{\mathrm{d}\tau_{\gamma\gamma}}{\mathrm{d}E_{*,UV}\mathrm{d}\Omega\mathrm{d}l}. \tag{4.47}$$

Photon-photon absorption of energetic photons has the effect of modifying the VHE flux emitted in GRBis. As a result of the angular-dependence of the interacting photons, the VHE flux will be modulated on the orbital phase, with the effect being more prominent for larger inclination angles of the orbit relative to the observer. At inferior conjunction (INFC), the interaction between the VHE gamma-rays and the soft photons from the stellar radiation field occurs at low angles ($\theta \sim 0^{\circ}$), resulting in minimal absorption since the threshold for absorption to take place becomes high (Eq. 4.44). It follows from this that VHE flux is expected to be at maximum at INFC. Similarly, a trough in the modulated VHE flux is expected at superior conjunction (SUPC) since the absorption is a maximum at this orbital phase (Fig. 4.4a). Absorption of the VHE gamma-rays also alters the shape of the spectra, characterised by the phase and energy-dependent opacity which causes an attenuation of the flux (Fig. 4.4b).

Cascades

The electron-positron pairs produced from photon-photon absorption contain the same energy as the high-energy photon that produced them. In a scenario where the magnetic field strength is low-enough that synchrotron losses are not dominant, i.e. when the inverse Compton timescale is less than the timescale for synchrotron losses, then the electron-positron pairs created will upscatter the low-energy photons to higher energies (though at lower energies than the original gamma-ray). A second generation of electron-positron pairs will be produced through the absorption of these newly-created high-energy photons. This process of electromagnetic cascading will continue until the energy of the photons falls below the threshold for pair-production (Fig. 4.5; Bednarek 2007, Bosch-Ramon, Khangulyan & Aharonian 2008).

4.5 The Bethe-Heitler model

All the GRBi sources have been detected at VHE gamma rays (γ-rays, > 100 GeV) using Imaging Atmospheric Cherenkov Telescopes (IACTs). As mentioned in chapter 1, the high energy emission in GRBis has been modelled by invoking leptonic processes (inverse Compton scattering) and hadronic processes (neutral pion decay).

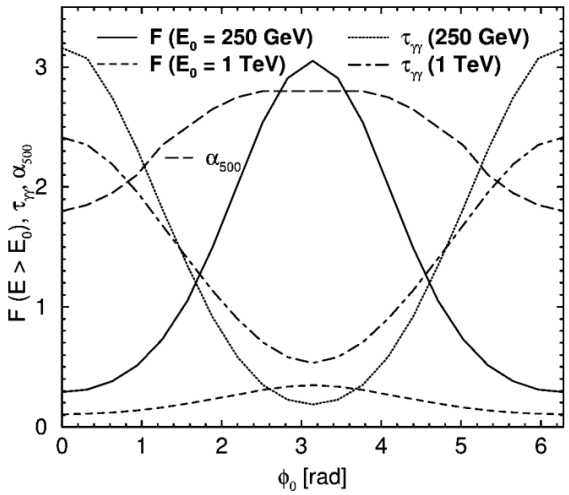

(a) Orbital phase modulated flux at energies 250 GeV (solid line) and 1 TeV (short-dashed line). The plot also shows the photon-photon optical depth at 250 GeV (dotted line) and 1 TeV (dot-dashed line), as well as the local photon spectral index at 500 GeV (long-dashed line). INFC is at $\phi = 0$ and SUPC is at $\phi = \pi$. From Böttcher & Dermer (2005).

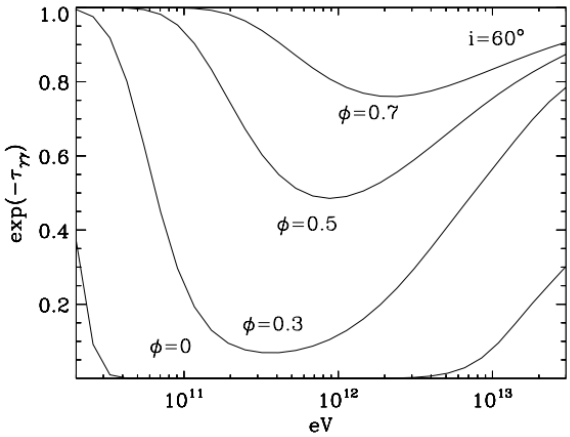

(b) Gamma-ray absorption spectrum of LS 5039 at different orbital phases viewed at an inclination angle of 60°. From Dubus (2006a).

Figure 4.4: Examples of the effect of photon-photon absorption in GRBis.

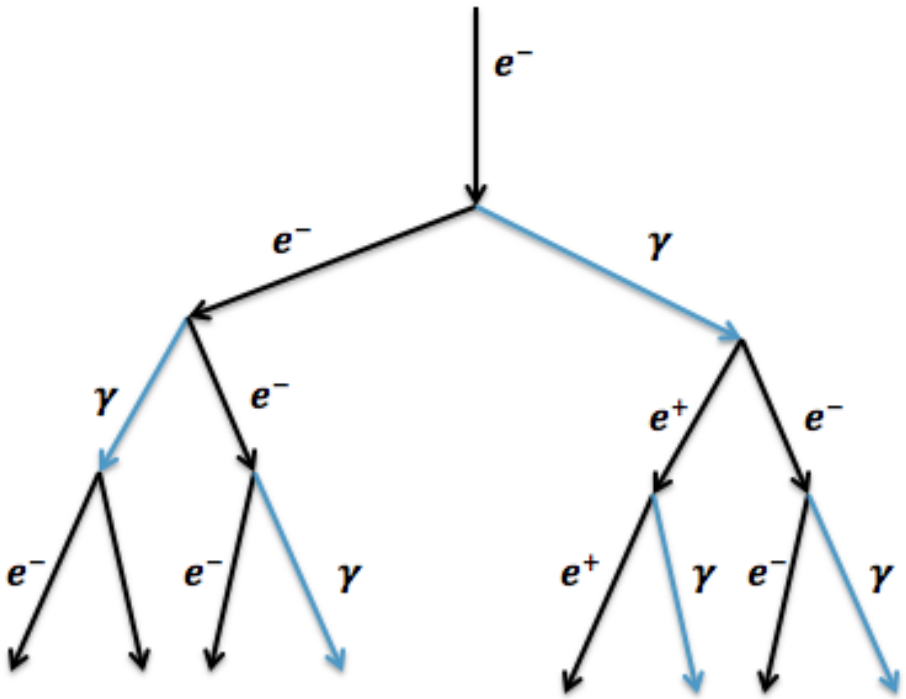

Figure 4.5: An illustration of an electromagnetic cascade.

The hadronic pion-production processes have been demonstrated to be inefficient in the production of VHE photons in GRBis, primarily because the Larmor radii for the protons would be larger than the shock size (Dubus 2013). However, lower-energy protons may still exceed the threshold for photo-pair production, known as the Bethe-Heitler process. That process is typically neglected in hadronic emission models in which photo-pion production occurs due to the much larger radiative efficiency of pion production processes (m_π/m_p for pion production vs. $2m_e/m_p$ for Bethe-Heitler pair production). However, in an intermediate regime in which Bethe-Heitler pair production occurs, but not pion production, pairs produced through the Bethe-Heitler process may dominate the radiative output.

As we will demonstrate below, given realistic magnetic fields, protons can plausibly be accelerated to exceed the energy threshold for Bethe-Heitler pair production. Therefore, in this work we investigate the Bethe-Heitler mechanism for the production of VHE emission in GRBis. The work is presented in the context of the PWM, where the protons are accelerated at the wind collision region and interact with the stellar photons to produce energetic electron-positron pairs via the Bethe-Heitler process. The pairs then upscatter the stel-

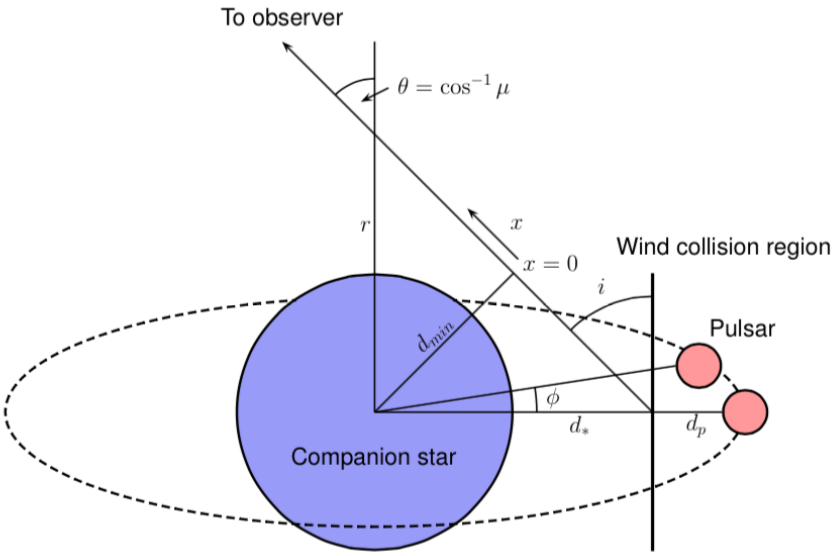

Figure 4.6: Geometry of the pulsar wind model. The different symbols indicated on the diagram are described in the text.

lar photons to high energies. We present the calculations to derive the flux and νF_ν spectrum, and study the variability with respect to the inclination angle and orbital phase. The VHE emission produced is subject to $\gamma - \gamma$ absorption from the stellar photons and cascading, the effects of which are included.

4.6 Model description

Figure 4.6 is a sketch illustrating the geometry of the PWM of a GRBi. The system is inclined with respect to the observer by an inclination angle i. The orbital separation of the system is defined by $d_{\rm orb}$. The distances from the pulsar and massive star to the wind collision region, S, where particle acceleration takes place are defined by $d_{\rm p}$ and d_*, respectively. The accelerated protons travel a distance x before interacting with a stellar photon at a distance $r = \sqrt{d_{\rm min}^2 + x^2}$ away from the star, where $d_{\rm min}$ is the distance of closest approach to the star. The phase angle, ϕ, is defined such that $\phi = 0$ at SUPC (where the pulsar is located behind the companion star relative to the observer). In order to develop a generic model (not tailored to any specific source), we introduce the following simplifying assumptions:

1. The neutron star is in a circular orbit around the massive companion.

Table 4.1: Parameters used in the model

Parameter	Value
Spindown pulsar luminosity, $L_{\rm pw}$ (erg. s^{-1})	10^{36}
Stellar outflow velocity, $v_{\rm w}$ (km. s^{-1})	10^{3}
Stellar mass-loss rate, $\dot{M}$ (M$_\odot$ yr^{-1})	10^{-7}
Orbital separation, d$_{\rm orb}$ (cm)	2×10^{12}
Stellar luminosity, L_* (erg. s^{-1})	10^{38}
Stellar photon energy, E_* (eV)	10
Proton acceleration efficiency, ξ	0.1
Magnetic field at the shock, B$_{\rm sh}$ (G)	1
Distance to the source, $d_{\rm obj}$ (kph)	1
Fraction of shock power, f_{sh}	$\sim$1

2. The photon spectrum of the companion star is approximated as a delta function in energy at E_*.

3. The massive companion does not have a decretion disc in its equatorial regions, and is assumed to radiate isotropically (neglecting possible effects of heating from the neutron star/pulsar).

The basic reactions for the processes studied here are:

$\rm p + \gamma \rightarrow e^+ + e^- + p'$ (Bethe-Heitler),
$\rm e^\pm + \gamma_{LE} \rightarrow e^\pm + \gamma_{VHE}$ (inverse Compton scattering),
$\gamma_{\rm VHE/HE} + \gamma_{\rm O/UV} \rightarrow e^- + e^+$ ($\gamma - \gamma$ absorption).

In the following we derive the energy threshold of Bethe-Heitler pairs. The momentum four-vectors of the proton, photon and electron-positron pairs before and after the interaction are given by:
Before

$$\vec{P_p} = \gamma_p m_p c[1, \vec{\beta_p}] \ , \ \vec{P_*} = \frac{E_*}{c}[1, \hat{i}]. \tag{4.48}$$

After

$$\vec{P_p'} = m_p c[1, \vec{0}] \ , \ \vec{P_e} = m_e c[1, \vec{0}]. \tag{4.49}$$

The conservation of four-momentum requires:

$$\vec{P_p} + \vec{P_*} = \vec{P_p'} + 2\vec{P_e}. \tag{4.50}$$

Squaring both sides, we get

$$\vec{P_p} \cdot \vec{P_p} + 2\vec{P_p} \cdot \vec{P_*} + \vec{P_*} \cdot \vec{P_*} = \vec{P_p'} \cdot \vec{P_p'} + 4\vec{P_p'} \cdot \vec{P_e} + 4\vec{P_e} \cdot \vec{P_e}. \tag{4.51}$$

So, eq. 4.51 becomes

$$(m_p c)^2 + 2\gamma_p m_p E_* (1 - \beta \cos\theta) = (m_p c)^2 + 4(m_e c)^2 + 4 m_e m_p c^2, \tag{4.52}$$

where θ is the angle of incidence between the photon and proton. Here $\gamma_{\rm p}$ is the Lorentz factor of the proton and $\beta_{\rm p} \sim 1$ is its velocity normalized to the speed of light.
Therefore, the minimum proton Lorentz factor for the production of pairs is

$$\gamma_{\rm p}^{\rm thr,BH} \approx \frac{1 \times 10^5}{(1 - \cos\theta)} E_{*,10}^{-1}, \tag{4.53}$$

where $E_{*,10}$ is the stellar photon energy in units of 10 eV (typical for a massive early type star). This can be compared to the much higher threshold for photo-pion production:

$$\gamma_{\rm p}^{\rm thr,\pi} = \frac{m_\pi c^2}{E_* \, (1 - \cos\theta)} \left(1 + \frac{m_\pi}{2 m_{\rm p}}\right) \approx 1 \times 10^7 \, E_{*,10}^{-1}. \tag{4.54}$$

4.7 Conditions at the shock

The power released at the shock, $L_{\rm sh}$, can be approximated by summing the contributions from the pulsar and the massive companion:

$$L_{\rm sh} \simeq \left(\frac{L_{\rm pw}}{2} + \frac{L_{\rm SW}}{2}\right) f_{sh}, \tag{4.55}$$

where $f_{sh} \leq 1$ is the fraction of the power that goes into the shock, $L_{\rm SW} = \frac{1}{2}\dot{M} v_{\rm w}^2$ is the stellar wind luminosity of the companion star, expressed in terms of mass-loss rate $\dot{M} = 10^{-7} \, \dot{M}_{-7} \, M_\odot \ {\rm yr}^{-1}$ and terminal outflow velocity, $v_{\rm w} = 10^3 \, v_{\rm w,3}$ km s^{-1}:

$$L_{\rm SW} \approx 3 \times 10^{34} \dot{M}_{-7} v_{\rm w,3}^2 \ {\rm erg. \ s}^{-1}. \tag{4.56}$$

$L_{\rm pw}$ is the spindown luminosity of the pulsar, which can be parameterised as $L_{\rm pw} = 10^{36} L_{\rm pw,36}$ erg. s^{-1} (e.g. Dubus 2006b, Romero et al. 2007). So the

luminosity emitted at the shock is estimated as

$$L_{\rm sh} \approx \left(\frac{L_{\rm pw}}{2}\right) f_{sh} \approx 5\times10^{35} L_{\rm pw,36}\, f_{sh} \ \text{ erg. s}^{-1}. \tag{4.57}$$

The luminosity emitted in the form of relativistic protons can be estimated as a fraction, ξ, of the total luminosity emitted by the shock:

$$L_{\rm p} \simeq \xi L_{\rm sh} \approx \xi \left(\frac{L_{\rm pw}}{2}\right) f_{sh} \approx 5\times10^{35} L_{\rm pw,36}\, f_{sh}\, \xi \ \text{ erg. s}^{-1}, \tag{4.58}$$

where ξ is the proton acceleration efficiency. The power carried by the protons with energy spectrum $\dot{N}(\gamma)$ is given by:

$$L_{\rm p} = \int_1^\infty m_{\rm p} c^2 \dot{N}(\gamma)\gamma d\gamma. \tag{4.59}$$

A plausible value for a high-energy cut-off of the proton spectrum, $\gamma_{\rm max}$ can be constrained by the condition that the Larmor radius of the particles is still smaller than the size of the shock:

$$\gamma_{\rm max} = \frac{eBr_{\rm sh}}{m_{\rm p}c^2} \approx 3\times10^5 B_{\rm sh,G} r_{\rm sh,12} \approx 10^5 \gamma_{\rm max,5}, \tag{4.60}$$

where $r_{\rm sh,12}$ is the size $r_{\rm sh}$ of the shocked wind interaction region in units of 10^{12} cm and $B_{\rm sh,G}$ is the magnetic field in the shock region in units of Gauss. Thus, for reasonable magnetic fields of a few to a few tens of Gauss, protons can easily be accelerated beyond the Bethe-Heitler pair production threshold, but not up to the pion production threshold (see Eqs. 4.53 and 4.54). The synchrotron cooling timescale for protons is given by

$$t_{\rm sync} = \frac{6\pi m_{\rm p}^4 c^3}{\sigma_{\rm T} m_{\rm e}^2 E_{\rm p} B^2} \approx 4.77\times10^{18} \gamma_{\rm p}^{-1} B^{-2} \text{ s}, \tag{4.61}$$

while the Bethe-Heitler timescale, $t_{\rm BH}$, can be approximated using (Begelman, Rudak & Sikora 1990):

$$t_{\rm BH} = \frac{kT_*}{m_e c^2 n_{ph} \mathscr{B}} \approx 55 r_{12}^2 E_{*,10} L_{*,38}^{-1} \text{ s}, \tag{4.62}$$

where $\mathscr{B} = 2.18\times10^{-20}$ is the cooling function, k is the Boltzmann constant, $T_* = 39000$ K is the stellar temperature, and the stellar photon density, $n_{\rm ph}$, can be estimated as:

$$n_{\rm ph} = \frac{L_*}{4\pi r^2 c E_*} \approx 1.656 \times 10^{13} r_{12}^{-2} E_{*,10}^{-1} L_{*,38}\ {\rm cm}^{-3}, \tag{4.63}$$

where $L_* = 10^{38} L_{*,38}$ erg s^{-1} is the stellar photon luminosity (not to be confused with the stellar wind luminosity, $L_{\rm SW}$) and $r = \sqrt{d_{\rm min}^2 + x^2} \approx 10^{12}\, r_{12}$ cm. The most general form of the acceleration time for the protons is given by

$$t_{\rm acc} = \frac{\eta_{\rm acc} r_L}{c}, \tag{4.64}$$

where $r_L = E/eB$ is the Larmor radius and $\eta_{\rm acc}$ characterizes the acceleration efficiency. This gives $t_{\rm acc} \approx 1.04 \times 10^{-4} \eta_{\rm acc} \gamma B_G^{-1}$s. The maximum allowed Lorentz factor by synchrotron losses ($t_{\rm acc} = t_{\rm sync}$):

$$\gamma_{\rm max,sync} \approx 2 \times 10^{11} \eta_{\rm acc}^{-1/2} B_G^{-1/2}, \eta_{\rm acc} > 1 \tag{4.65}$$

For magnetic fields of $10^2 - 10^3$ G ($B_{\rm OB}$) around O and B stars (Hubrig et al. 2011; 2013), this gives

$$\gamma_{\rm max,sync} \approx (20 - 7) \times 10^9 \eta_{\rm acc}^{-1/2} B_{\rm OB}^{-1/2}. \tag{4.66}$$

For the same range of magnetic field values, the maximum allowed Lorentz factor by Bethe-Heitler losses ($t_{\rm acc} = t_{\rm BH}$) in comparison is

$$\gamma_{\rm max,BH} \approx (53 - 5.3) \times 10^7 r_{12}^{-2} E_*^{-1} L_* B_{\rm OB}. \tag{4.67}$$

Since both of these values of $\gamma_{\rm max}$ are much larger than the one from Eq. 4.60, the maximum energy is set by the condition that the Larmor radius of the protons is smaller than the shock size.

4.8 Spectrum formation

The distribution of the protons is assumed to be of an exponentially cut-off power-law, given by

$$\dot{N}(\gamma) = \dot{N}_0 \gamma^{-p} e^{-\gamma/\gamma_{\rm max}}, \tag{4.68}$$

and so, from eq. 4.59 we have

$$L_{\rm p} = \dot{N}_0 m_{\rm p} c^2 \int_1^\infty \gamma^{1-p}\, e^{-\gamma/\gamma_{\rm max}}\, d\gamma, \tag{4.69}$$

which, for the canonical $p = 2$, becomes

$$L_{\rm p} \approx \dot{N}_0 m_{\rm p} c^2 \ln(\gamma_{\rm max}) \tag{4.70}$$

rearranging this, we find the proton spectrum normalisation :

$$\dot{N}_0 = \frac{L_{\rm p}}{m_{\rm p} c^2 \ln(\gamma_{\rm max})} \approx \frac{(3.3 \times 10^{38}) f_{sh} \xi}{\ln(\gamma_{\rm max,5}) + 5\ln(10)} L_{\rm pw,36}\ {\rm s}^{-1}. \tag{4.71}$$

As a quick sanity check, we calculate the predicted flux of cosmic rays (CRs) from such a proton accelerator in the most optimistic case in which protons could propagate directly to Earth unmodulated. Due to the hard production spectrum, the highest contribution to the CR flux would be expected near the knee of the CR spectrum at $E_{\rm p} \sim 10^{15}$ eV, where a CR flux of $\Phi_E^{\rm obs} \sim 10^{-11}$ m^{-2} s^{-1} GeV^{-1} is measured by various instruments (e.g. Longair 2011, p. 494). Our proton-acceleration normalization yields a typical CR flux at that energy of $\Phi_E^{\rm binary} \sim 6 \times 10^{-15}\, d_{\rm obj,kpc}^{-2}$ m^{-2} s^{-1} GeV^{-1} for typical parameters as used above and a distance to the source of $d_{\rm obj} = 1\, d_{\rm obj,kpc}$ kpc. Thus our proton acceleration scenario proposed here is not in conflict with the observed CR flux at Earth.

The optical depth for protons to create e^+e^- pairs from the interaction with the stellar photons:

$$\tau_{\pm} = \int_{x_0}^{\infty} n_{\rm ph}(x) \sigma_{\rm BH}(\epsilon_0)(1-\mu) dx. \tag{4.72}$$

Referring to figure 4.6, $\mu = \cos\theta = \frac{x}{r}$, where θ is the angle between the photon and proton momenta, $\epsilon_0 = E_0/m_{\rm e}c^2$ is the normalized stellar photon energy in the proton rest frame, with $E_0 = E_*\, \gamma_{\rm p}\, (1 - \beta_{\rm p}\mu)$, and where $x_0 = -(\cos\phi)\sqrt{d_*^2 - d_{\rm min}^2}$, and $d_{\rm min} = d_* \sqrt{1 - \sin^2(i)\cos^2(\phi)}$. The distance from the massive companion to the shock, d_*, can be obtained by matching the ram pressures from the pulsar wind and the stellar wind:

$$\frac{L_{\rm pw}}{4\pi d_{\rm p}^2 c} = \rho_{\rm w} v_{\rm w}^2 = \frac{\dot{M} v_{\rm w}}{4\pi (d_{\rm orb} - d_{\rm p})^2}. \tag{4.73}$$

The ratio of the wind momentum fluxes can be written as:

$$\eta = \frac{L_{\rm pw}/c}{\dot{M}_{\rm w} v_{\rm w}} \approx 0.05 L_{\rm pw,36} \dot{M}_{-7}^{-1} v_{\rm w,3}^{-1}\ , \tag{4.74}$$

where $L_{\rm pw,36} = L_{\rm pw}/10^{36}$ erg s^{-1}. This gives

$$\frac{d_{\rm p}}{d_{\rm orb}} = \frac{\eta^{1/2}}{1+\eta^{1/2}}, \tag{4.75}$$

and so:

$$d_* = d_{\rm orb} - d_{\rm p} = d_{\rm orb}\left(\frac{1}{1+\eta^{1/2}}\right), \tag{4.76}$$

which can be parametized by $d_* = 10^{12} d_{*,12}$ cm.

The opacity then becomes

$$\tau_{\pm} \approx 1.656 \times 10^{11} E_{*,10}^{-1} L_{*,38} \int_{x_0}^{\infty} \left(\frac{1}{x^2+d_{\rm min}^2} - \frac{x}{(x^2+d_{\rm min}^2)^{3/2}}\right) \sigma_{\rm BH,-26} dx. \tag{4.77}$$

In Equation 4.77, the total Bethe-Heitler (Bethe & Heitler 1934) cross-section is given by:

$$\begin{aligned}\sigma_{\rm BH} &= 10^{-26}\,\sigma_{\rm BH,-26}\,{\rm cm}^2 \\ &= 2\pi r_0^2 \left[\frac{1+\epsilon_0}{\epsilon_0^3}\frac{2\epsilon_0(1+\epsilon_0)}{1+2\epsilon_0} - \ln(1+2\epsilon_0) + \frac{1}{2\epsilon_0}\ln(1+2\epsilon_0) - \frac{1+3\epsilon_0}{(1+2\epsilon_0)^2}\right],\end{aligned} \tag{4.78}$$

where r_0 is the classical electron radius. Given that the integral in Equation 4.77 is dominated by contributions near the star, where $\mu \sim 0$, we simplify the integral by assuming that $\epsilon_0 \approx \epsilon_* \gamma_{\rm p}$ (where ϵ_* is the normalised photon energy from the massive star in the photon rest frame), independent of x so that $\sigma_{\rm BH}$ can be excluded from the integral, which can then be solved analytically:

$$\begin{aligned}\int_{x_0}^{\infty} \left(\frac{1}{x^2+d_{\rm min}^2} - \frac{x}{(x^2+d_{\rm min}^2)^{3/2}}\right) dx &= \frac{1}{d_{\rm min}}\left[\frac{\pi}{2} - \arctan\left(\frac{x_0}{d_{\rm min}}\right)\right] \\ &\quad - \frac{1}{\sqrt{x_0^2+d_{\rm min}^2}} \\ &= \frac{f_{\rm a}(i,\phi)}{d_*},\end{aligned} \tag{4.79}$$

where the factor

$$\begin{aligned}f_{\rm a}(i,\phi) = &\frac{1}{\sqrt{1-\sin^2 i\cos^2\phi}}\left(\frac{\pi}{2} - \arctan\left[\frac{-(\cos\phi)\,|\sin i\cos\phi|}{\sqrt{1-\sin^2 i\cos^2\phi}}\right]\right) \\ &- \frac{1}{\sqrt{\sin^2 i\cos^4\phi - \sin^2 i\cos^2\phi + 1}}\end{aligned} \tag{4.80}$$

encompasses the entire inclination-angle and phase dependence. Thus,

$$\tau_{\pm} \approx 0.2 E_{*,10}^{-1} L_{*,38}\, \sigma_{\mathrm{BH},-26}\, d_{*,12}^{-1} f_{\mathrm{a}}(i,\phi). \tag{4.81}$$

Given that the total momentum in the Bethe-Heitler pair production process is strongly dominated by the proton momentum, both the electron and positron will move essentially in the direction of the incident proton momentum in the rest frame of the binary system, and have Lorentz factors $\gamma_{\pm} \sim \gamma_{\mathrm{p}} > \gamma^{\mathrm{thr,BH}}$ in that frame. For electron/positron pairs with energies larger than $(m_{\mathrm{e}}c^2)^2/E_* \sim 25$ GeV (i.e., $\gamma_{\pm} \geq 5 \times 10^4/E_{*,10}$), the scattering of the stellar photons occurs in the Klein-Nishina regime. As this is expected to be the case for all secondary Bethe-Heitler pairs, the scattered photons take all the energy from the electrons/positrons scattering them, with each electron/positron scattering at most one photon. Considering Compton scattering in the Klein-Nishina limit, with

$$\sigma_{\mathrm{KN}} \approx \frac{3}{8} \frac{\sigma_{\mathrm{T}}}{\epsilon_* \gamma_{\pm}} \left(\ln[\epsilon_* \gamma_{\pm}] + \frac{1}{2} \right), \tag{4.82}$$

we can evaluate the average Compton scattering optical depth τ_{C} of the stellar photon field for the newly produced electrons/positrons as

$$\tau_{\mathrm{C}} = \int_{x_0}^{\infty} dx\, n_{\mathrm{ph}}(x)\, \sigma_{\mathrm{KN}}\, (1-\mu) \geq 3.1\, L_{*,38}\, f_{\mathrm{a}}\, d_{\mathrm{min},12}^{-1}\, E_{*,10}^{-2}\, B_{\mathrm{sh,G}}^{-1}\, r_{\mathrm{sh},12}^{-1}, \tag{4.83}$$

for electron/positron pairs produced with the maximum proton Lorentz factor as given in Eq. 4.60. Thus, in the following we assume that every Bethe-Heitler electron/positron has a probability of one to scatter a stellar photon in the Klein-Nishina regime. We first consider the strength of the magnetic field at the point where the Bethe-Heitler interactions occur and its effect on the direction of the γ-ray photons. Comparing the Larmor radius of relativistic electrons,

$$r_{\mathrm{L}} = \frac{\gamma\, m_{\mathrm{e}}\, v}{e\, B_{\mathrm{BH}}} \sim 5 \times 10^8\, B_{\mathrm{BH,G}}^{-1} B_{\mathrm{sh,G}}\, r_{\mathrm{sh},12}\ \mathrm{cm}, \tag{4.84}$$

with the Compton scattering mean-free path,

$$\lambda_{\mathrm{C}} = \frac{1}{n_{\mathrm{ph}}\, \sigma_{\mathrm{KN}}} \sim 6 \times 10^{11}\, r_{12}^2\, E_{10}^2\, L_{*,38}^{-1}\, B_{\mathrm{sh,G}}\, r_{\mathrm{sh},12}\ \mathrm{cm}, \tag{4.85}$$

we find a critical magnetic field strength at the Bethe-Heitler interaction point

at

$$B_{\rm BH,crit} \sim 8.5 \times 10^{-4}\, r_{12}^{-2}\, E_{10}^{-2}\, L_{*,38}\ {\rm G}. \tag{4.86}$$

If the magnetic field is too weak ($B_{\rm BH} \ll B_{\rm BH,crit}$) to cause a significant deflection and with the assumption that the Compton scattered photon (of energy $E_\gamma \approx E_\pm = \gamma_\pm\, m_{\rm e}c^2$) travels in the direction of the primary proton, the flux and spectrum of the accelerated protons can be directly translated into the spectrum of the Bethe-Heitler produced electrons/positrons and thus also the photons generated per unit time per unit area as

$$\frac{dN}{dtd\epsilon dA} \equiv \phi_\epsilon = \frac{2\dot{N}_0 \epsilon^{-p} \tau_\pm e^{-\epsilon/\gamma_{\rm max}}}{4\pi d_{\rm obj}^2}, \tag{4.87}$$

where $\epsilon = E_{\rm ph}/m_{\rm e}c^2$ is the normalized energy of the produced γ-ray photon. Thus,

$$\begin{aligned} \phi_\epsilon \approx \frac{1\times10^{-6}}{\ln\gamma_{\rm max,5} + 5\ln 10}\, f_{sh}\xi L_{\rm pw,36}\, E_{*,10}^{-1} L_{*,38}\ \times \\ \sigma_{\rm BH,-26}\, \epsilon^{-2}\, d_{\rm obj,kpc}^{-2}\, d_{*,12}^{-1}\, f_a(i,\phi)\, e^{-\epsilon/\gamma_{\rm max}}\ {\rm s}^{-1}\ {\rm cm}^{-2}. \end{aligned} \tag{4.88}$$

The νF_ν spectrum resulting from the scattered stellar radiation is ($p = 2$):

$$\nu F_\nu = \epsilon^2 m_{\rm e}c^2 \phi_\epsilon. \tag{4.89}$$

The Bethe-Heitler pair production events will occur in regions where the magnetic field is large enough ($B_{\rm BH} \gg B_{\rm BH,crit}$) that the electrons and positrons produced are deflected by large angles (and, thus, effectively rendered isotropic) before Compton scattering a stellar photon in the Klein-Nishina regime. Compton gamma-rays produced in those regions are expected to produce an isotropic background level of γ-ray emission that will be visible for all inclinations and at all phases, but may still be affected by viewing-angle and orbital-phase dependent $\gamma - \gamma$ absorption (Böttcher & Dermer 2005).

In order to develop a simple expression for this quasi-isotropic background, we average the angle-dependent photon fluxes from Eq. 4.88 over all viewing angles and orbital phases. Considering the symmetry of the system, this yields

$$\nu F_\nu^{\rm iso} \approx \frac{1}{\pi} \int_0^1 d\cos i \int_0^\pi d\phi\, \nu F_\nu(i,\phi). \tag{4.90}$$

The angle integration over the angular function $f_{\rm a}$ is solved numerically to yield

$$\int_0^1 d\cos i \int_0^\pi d\phi\, f_{\rm a}(i,\phi) = 5.69, \tag{4.91}$$

so that the unabsorbed, isotropic γ-ray spectrum is given by:

$$\begin{aligned} \nu F_\nu \approx & \frac{(5.3\times10^{-13})}{\ln(\gamma_{\rm max,5}) + 5\ln(10)}\, f_{sh}\xi L_{\rm pw,36}\, E_{*,10}^{-1} L_{*,38} \times \\ & \sigma_{\rm BH,-26}\; d_{\rm obj,kpc}^{-2}\, d_{*,12}^{-1}\, e^{-\epsilon/\gamma_{\rm max}} \text{ erg. s}^{-1}\text{cm}^{-2}. \end{aligned} \tag{4.92}$$

Fig. 4.7 shows the Bethe-Heitler γ-ray spectrum. In order to estimate the effect of $\gamma-\gamma$ absorption on this quasi-isotropic γ-ray emission component, we realize that most of the Bethe-Heitler pair production processes will occur in a rather concentrated region near the mid-point between the shock and the star, at a distance $d_{\rm BH} = d_*/2$ from the shock. Thus, the effect of $\gamma-\gamma$ absorption on the BH Compton γ-ray spectrum may be roughly approximated by assuming that the entire unabsorbed flux from Eq. 4.92 is produced at that mid-point between the companion star and the shock. The orbitally modulated $\gamma-\gamma$ opacity evaluated according to Böttcher & Dermer (2005) for γ-rays produced at that point is then applied to the unabsorbed γ-ray spectrum.

4.9 Gamma-gamma absorption and cascading

The threshold for pair production for typical energies of the stellar photons on the order ∼10 eV for head-on collisions ($\theta_{\gamma\gamma} = \pi$) is $E_\gamma \geq 30\, E_{*,10}^{-1}$ GeV. The effect of $\gamma-\gamma$ absorption in GRBis has been studied before (e.g., Böttcher & Dermer 2005 and Dubus 2006). The $\gamma-\gamma$ opacity for a VHE photon with energy, ϵ_γ, traveling a distance, l_1, is given by (Böttcher & Dermer 2005)

$$\tau_{\gamma\gamma} = \int_0^{l_1} dl(1-\cos\theta_{\gamma\gamma}) \int_0^\infty d\epsilon \sigma_{\gamma\gamma}(\epsilon_\gamma, \epsilon, \cos\theta_{\gamma\gamma}) n_{\rm ph}(\epsilon), \tag{4.93}$$

where $n_{\rm ph}(\epsilon)$ is the stellar photon number density and $\sigma_{\gamma\gamma}$ is the pair-production cross-section. Böttcher & Dermer (2005) performed calculations of the $\gamma-\gamma$

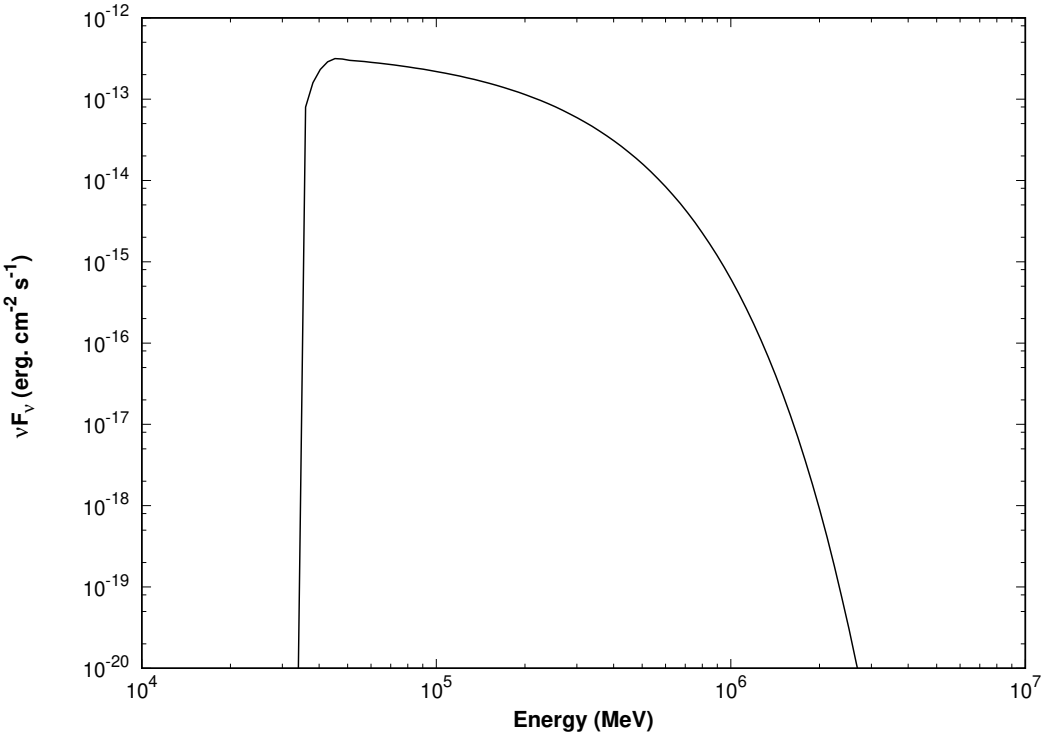

Figure 4.7: The unabsorbed Bethe-Heitler spectrum. The parameters used are listed in Table 4.1.

absorption opacity for LS 5039 for an inclination angle $i = 25°$ in the context of the MQ model, where the $\gamma-$ray photons are produced in the jet region above the compact object which is in a circular orbit around its massive companion. The code of Böttcher & Dermer (2005), with appropriate adjustment for the slightly different geometry, has been adopted here to evaluate $\gamma - \gamma$ opacity effects. Although the physical scenarios studied are different (PWM vs MQ), the orbital phase variations of the opacity will be the same. Taking into account $\gamma - \gamma$ absorption and following from the radiative transfer equation, the νF_ν spectrum becomes:

$$\nu F_\nu^{abs} = \nu F_\nu \frac{(1 - e^{-\tau_{\gamma\gamma}})}{\tau_{\gamma\gamma}}, \tag{4.94}$$

The opacity for $\gamma-\gamma$ absorption is a maximum at superior conjunction (SUPC, $\phi = 0$) resulting in minimum VHE emission at this phase, as shown in Figs. 4.8 and 4.9. Fig. 4.8 shows the phase-dependent flux obtained from the Bethe-Heitler process, with absorption taken into account, as a function of inclination angle at 100 GeV. The expected optical depth at various orbital phases as a function of energy is shown in Fig. 4.9 for an inclination angle of 25°.

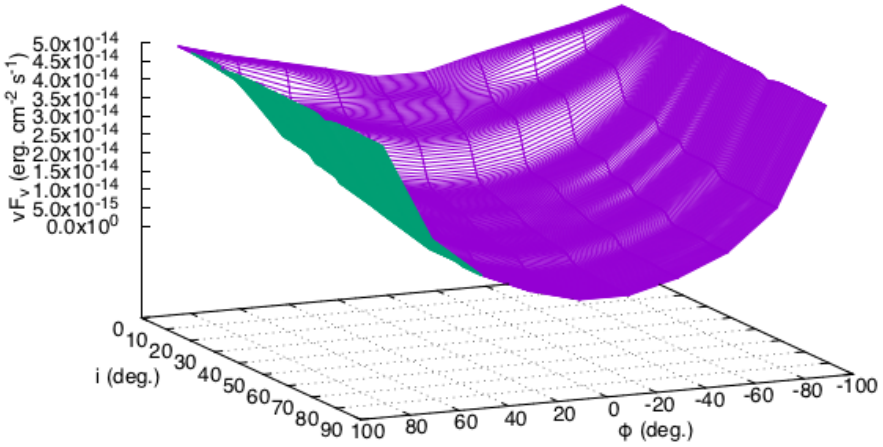

Figure 4.8: The phase-dependent, absorbed Bethe-Heitler flux for different inclination angles at 100 GeV. The parameters used are listed in Table 4.1.

4.9.1 Cascades

An electromagnetic cascade can be initiated, as the $\gamma-$ray production takes place around the massive companion where the stellar photon density is relatively high and the pairs produced from absorption upscatter the photons to energies above the threshold for pair production. In order to compute the electromagnetic cascade we have used a semi-analytical model, the details of which are presented in Appendix C. The Bethe-Heitler spectrum with cascading taken into account is shown in Fig. 4.10.

4.10 Discussion

The predicted $\gamma-$ray flux from the Bethe-Heitler process is presented using the PWM scenario for gamma-ray binaries. Due to the large magnetic field at the site of Bethe-Heitler pair production, the electrons and positrons produced are deflected by large angles so that their distribution is isotropic. The isotropic $\gamma-$ray emission produced is modulated on the orbital phase due to $\gamma - \gamma$ absorption. The unabsorbed spectrum shows a cut-off in the TeV range, reflecting the primary proton energy cut-off. Because of the close proximity of the γ-rays produced to the companion star, $\gamma - \gamma$ absorption plays an important role. Absorption is strongly dependent on the orbital phase, and the flux phasogram

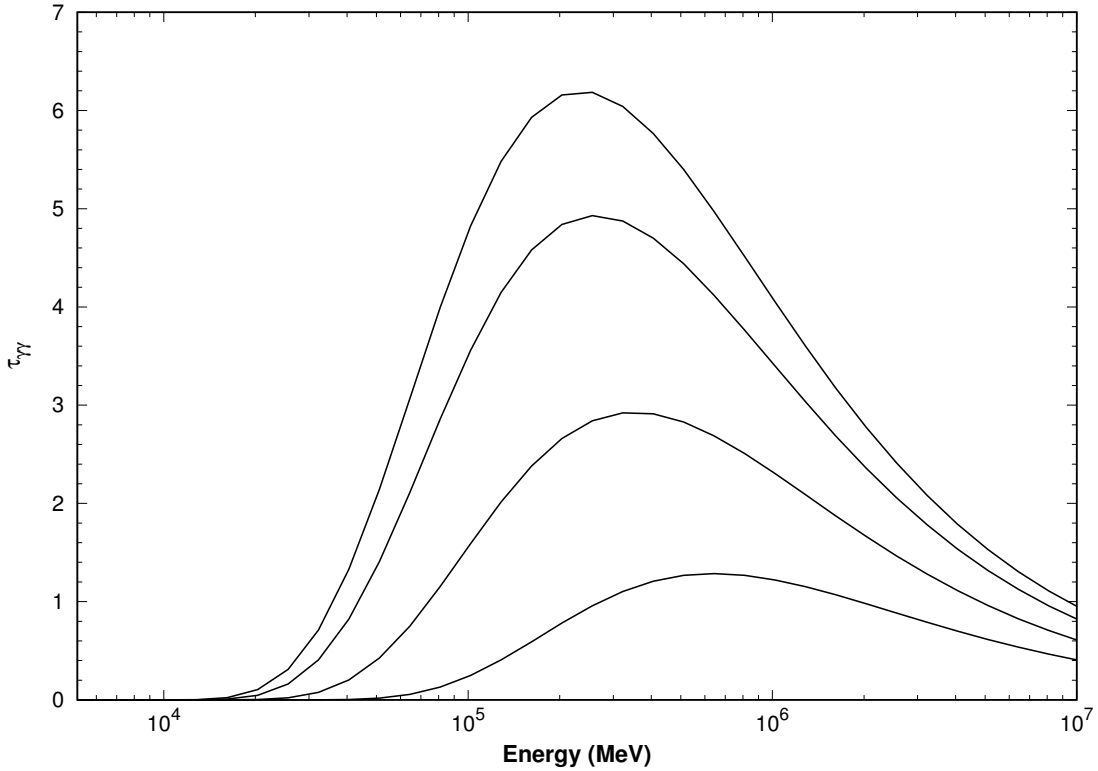

Figure 4.9: Plot of $\gamma - \gamma$ opacity for an inclination of 25° at different orbital phase angles, top to bottom: $\phi = 0°, 45°, 90°, 180°$.

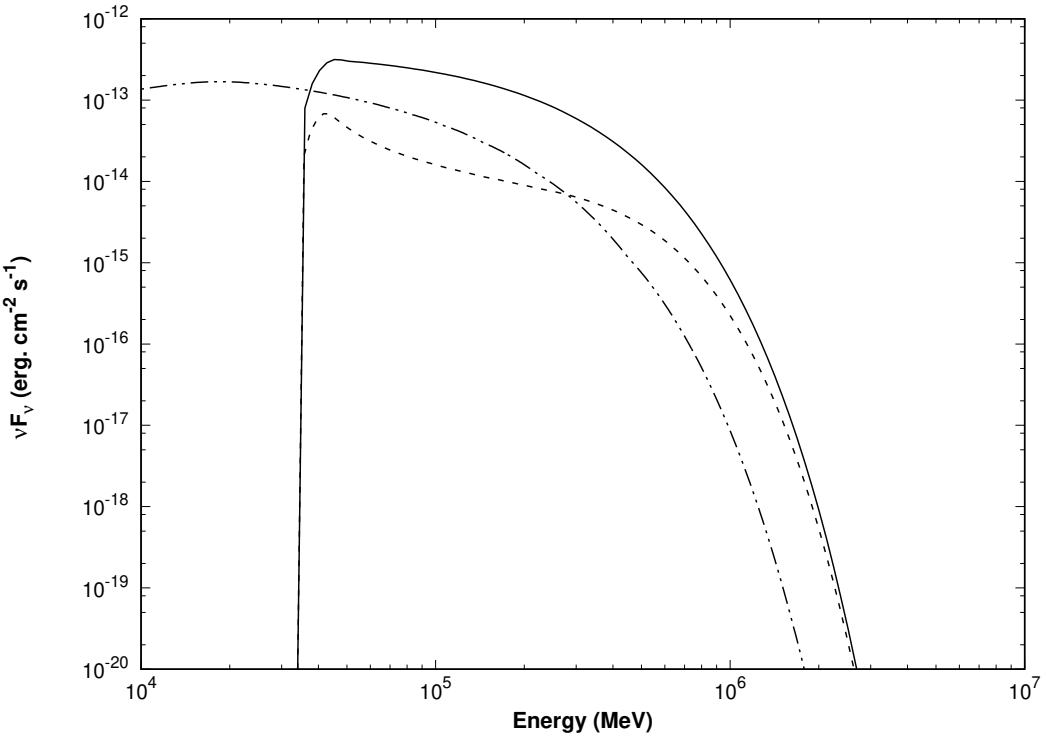

Figure 4.10: The unabsorbed (solid line) and absorbed (dashed line) Bethe-Heitler spectrum (for an orbital phase angle of 0° and an inclination angle of 25°). Contributions from cascades are shown with the dashed-dotted line. The parameters used are listed in Table 4.1.

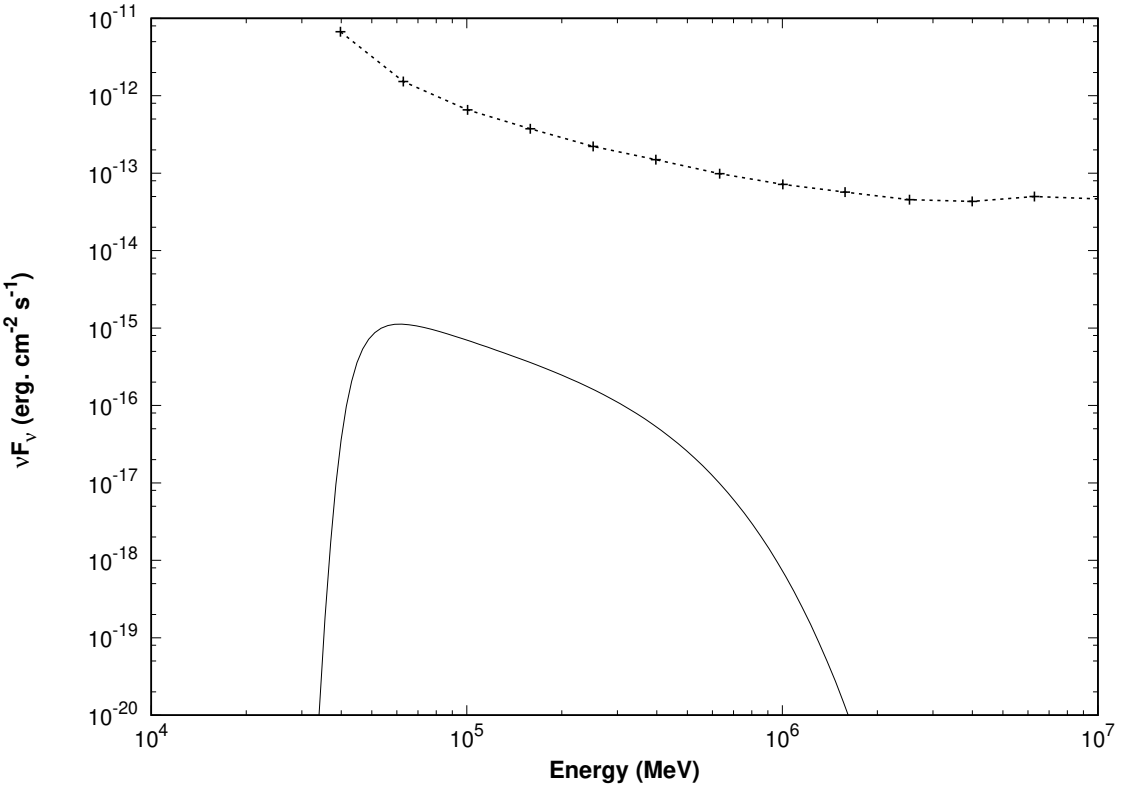

Figure 4.11: The Bethe-Heitler spectrum using distance and orbital parameters of LS 5039 with absorption taken into account (bottom curve) and differential sensitivity for CTA South from a 50-hour scan for a 5-standard-deviation detection of a point-like source (top curve; from https://www.cta-observatory.org/science/cta-performance/).

(Fig. 4.8) with absorption taken into account shows a trough at SUPC, since the opacity for $\gamma - \gamma$ absorption peaks at this phase. Due to $\gamma - \gamma$ absorption by the stellar photon field and cascading, we expect a significant low-energy cut-off in the gamma-ray spectrum around 10 - 30 GeV. Fig. 4.11 shows the Bethe-Heitler spectrum calculated using distance and orbital parameters (at periastron) for LS 5039 (the system whose parameters gives the highest flux) with absorption taken into account. From Fig. 4.11, the Bethe-Heitler component is just below the detection threshold for Cherenkov Telescope Array (CTA) for a 50-hour scan. While the spectral feature of the Bethe-Heitler component may be difficult to detect using CTA telescopes, there may still be contribution to the leptonic models in the total observed flux.

4.11 Conclusion

In this work, we have presented the Bethe-Heitler model for the production of gamma-rays in GRBis. Our calculation of the νF_ν spectrum and flux is done in the framework of the wind collision scenario, where protons are accelerated at the shock region and interact with stellar photons to produce energetic pairs through the Bethe-Heitler process. Gamma-rays then result from the scattering of the low-energy photons by the energetic pairs. The Bethe-Heitler mechanism for $\gamma-$ray production presented in this work in GRBis is complementary to purely leptonic mechanisms, rather than opposed to them. The Bethe-Heitler component peaks in the $10 - 100$ GeV range. While the gamma-ray emission from the known GRBis might be larger than that predicted by the Bethe-Heitler mechanism in this energy range, it can peak at INFC, for example in the case of LS 5039. In contrast, our unabsorbed Bethe-Heitler component in the weak-field case ($B_{\rm BH} \ll B_{\rm BH,crit}$) peaks at SUPC and so may be dominant at this orbital phase. In the strong-field case ($B_{\rm BH} \gg B_{\rm BH,crit}$), where the Bethe-Heitler pairs will predominantly occur, the pairs produced are deflected by large angles, resulting in an isotropic γ-ray emission from Compton scattered stellar photons. This γ-ray emission is affected by $\gamma - \gamma$ absorption and is modulated on the orbital phase. The flux predictions at 100 GeV show a minimum at SUPC, while the spectrum is attenuated in the GeV energy range. The flux from the Bethe-Heitler is less than the typical flux observed from GRBis by about an order of magnitude for the energy range considered. Thus, we have shown that the Bethe-Heitler mechanism for gamma-ray production at these energies may not be dominant, but could contribute to the purely leptonic

models in the total observed flux.

Chapter 5

Summary and future work

5.1 Summary

In this thesis we have studied different theoretical and observational aspects of gamma-ray binaries. We have analysed Échelle spectra of 1FGL J1018.6−5856 obtained from SALT using the HRS with the aim of improving our knowledge of the orbital parameters of this system (presented in Chapter 2). The cadence of our observations of 1FGL J1018.6−5856 provides a wide orbital phase coverage, which when combined with radial velocity measurements from literature allows for the geometry and mass function to be obtained. We find that a neutron star is favoured as the compact object, with a black hole only allowed for very low inclination angles of the orbit relative to our line of sight. With a neutron star favoured in 1FGL J1018.6−5856, this supports a picture similar to that of PSR B1259−63 of a young rotation-powered pulsar interacting with a massive companion. Radial velocity measurements of the recently discovered gamma-ray binary, LMC P3, also favour a neutron star as the compact object for a large parameter space (Corbet et al. 2016). Recently, preliminary results from MAGIC and VERITAS have reported a detection of VHE gamma-rays from a gamma-ray binary candidate, PSR J2032+4127, around periastron passage (Mirzoyan & Mukherjee 2017). PSR J2032+4127 is a binary system comprising a gamma-ray/radio pulsar and a Be star. Confirmation of these detections will make PSR J2032+4127 a new member of the gamma-ray binary population and the second system, alongside PSR B1259−63, with a confirmed compact object. For the other known gamma-ray binaries, the distinction between a neutron star and a black hole is less certain from the inference of the mass of the compact object from radial velocity studies. The pulsar wind model sce-

nario in gamma-ray binaries is supported, indirectly, through multiwavelength observations. This is seen from the similarity in the spectral features of all systems, which implies that as in PSR B1259−63, the source of power originates from a rotating pulsar. Repeated orbital phase-dependent radio morphological features seen in LS I +61 303 interpreted as a one-sided cometary tail are also a natural property of a pulsar wind nebula. The pulsar wind model scenario for gamma-ray binaries is also consistent with the idea that these systems are progenitors of accreting high mass X-ray binaries, where the gamma-ray binary phase represents the pulsar at a young stage of its evolution when the spin down power and large magnetic field prevents accretion of matter from the companion.

We have also analysed long term properties of the Hα line of LS I +61 303 with the aim of studying the circumstellar disc variability. We have studied long-term geometrical changes in LS I +61 303, where various quantities, such as the disc eccentricity and the argument of pericenter may vary on timescales comparable to the superorbital period of LS I +61 303. The origin of the superorbital modulation in LS I +61 303 remains an open question, with its detection across the electromagnetic spectrum resulting in a number of speculations. The detection of the superorbital period at optical wavelengths through spectroscopy and photometry might suggest that its origin is associated with the variability of the Be disc (Zamanov et al. 2013, Paredes-Fortuny et al. 2015). The interaction of the disc with the compact object would then in turn result in the modulation at other wavelengths from non-thermal processes. Variability on superorbital timescales is not unique to LS I +61 303, as they have been observed in other BeXBs and have been proposed to be due to the variation of the Be disc size (Alcock et al. 2001, Rajoelimanana, Charles & Udalski 2011, Rajoelimanana et al. 2017). The exact manner and mechanism(s) responsible for the disc variability on the superorbital timescale in not known. In this work, we have suggested several possible long term geometric changes of the disc variability. Furthermore, we have compared predictions of the EW and V/R ratio from the model with those from measurements which, from a qualitative viewpoint, are in agreement. Chapter 3 shows the results of the analysis of the data, which is presented in conjunction with a semi-analytical model to interpret the motions of test particles in Keplerian orbits. Discrepancies arise at certain epochs, where the model overestimates emission from the blue-shifted region of the disc. We have provided a quantitative discussion of how external effects can result in such discrepancies by demonstrating the possible

effect of the pulsar wind. A significant contribution from the work presented in chapter 3 is that we have developed metrics for investigating observational signatures of the Kozai-Lidov mechanism in hydrodynamical discs, through studying eccentricity variability, which has so far only been presented theoretically in literature.

The final project in the thesis is that which examines high energy emission in gamma-ray binaries. In chapter 4 we have studied the Bethe-Heitler mechanism for the production of high energy emission in the context of the pulsar wind model. In this model, energetic protons interact with cold photons from the radiation field of the massive companion producing electron/positron pairs. The pairs then upscatter the stellar photons to produce gamma-rays. We present calculations of the gamma-ray flux and spectrum, where we have taken the effects of photon-photon absorption and electromagnetic cascading into account. The gamma-ray emission produced is quasi-isotropic due to the relatively strong magnetic field at the site where the Bethe-Heitler interaction occurs, with the orbital modulation occurring due to photon-photon absorption. The flux predicted by the Bethe-Heitler mechanism is lower than that typically observed in gamma-ray binaries by about an order of magnitude. We point out that our Bethe-Heitler model presented here is complementary to purely leptonic models, instead of opposed to them, as this may not be the dominant process at the energy range considered but will contribute to the total observed flux. The high sensitivity of future CTA telescopes may be able to detect the spectral shape and orbital modulation of the Bethe-Heitler component.

5.2 Future prospects

Long-term variability of discs in BeXBs The particle model presented in the analysis of the Hα emission line properties of LS I +61 303 provides a way to analyse detailed geometrical changes in circumstellar discs, despite its simplicity. Future work will involve improving this by including the external effects of the compact object, such as the pulsar wind and the tidal force. We will apply similar analysis to a sample of Galactic BeXBs for which we have long-term on-going programmes with LT and SALT, as well as archival data from various telescopes. The analysis of the Hα emission line properties in conjunction with X-ray lightcurves will be performed to look at elliptical

changes in the disc, particularly around the epochs of X-ray activity to evaluate any correlations between disc-shape changes and type II outbursts, as predicted from SPH simulations by Martin et al. (2014a).

Bethe-Heitler mechanism in the microquasar scenario The calculation of the gamma-ray emission through the Bethe-Heitler mechanism was performed in the context of the pulsar wind model in this thesis. In future, we will perform detailed Monte-Carlo simulations of the three-dimensional cascade development with realistic magnetic fields. With these, one can make realistic predictions for the orbital modulation, which might be used to diagnose the magnetic field in the region where the Bethe-Heitler process dominates. Furthermore, we will apply the model in the framework of the microquasar scenario, where the site for particle acceleration is located closer to the compact object, i.e. in the jet. The energetic protons in this scenario originate in the jet and travel through the radiation field of the massive star where energetic pairs are produced and upscatter the surrounding photons to gamma-ray energies.

As discussed in this thesis, gamma-ray binaries are intriguing members of the X-ray binary population in which a wide range of astrophysical processes can be explored across the whole electromagnetic spectrum. In addition to this, they allow us to explore a short phase in the evolution of high mass X-ray binaries. Of the many baffling aspects of gamma-ray binaries, we have considered and investigated a few. These include understanding the nature of the compact object, the physics involving the interaction between the Be disc and compact object, and the origin of high energy emission. Some of the methods used here are not exclusive to gamma-ray binaries and are applicable to other classes of binary stars to address some of the key issues. The uniqueness of various physical and observational features of each of the systems in this small, but growing population provides an opportunity for testing and understanding a wide range of physical phenomena.

Appendix A

Be disc particle model

This appendix provides a derivation of the equations used in the analysis of the data presented in this chapter. The formulation presented here was derived by Atsuo Okazaki and will be presented in another paper analysing the Be disc properties of the BeXB A 0535−262 (Okazaki et al. 2018, in prep.).

In order to estimate the geometry of the emitting region, we need equations that relate it to the observed quantities characterizing an emission line profile. For this purpose, we analyze the motion of a particle orbiting in the disk plane along the limb of an emitting region, which is generally inclined to the tangent plane of the sky. The orbit is given by

$$r_{\rm p} = \frac{a_{\rm p}\left(1-e_{\rm p}^2\right)}{1+e_{\rm p}\cos f}, \tag{A.1}$$

where $r_{\rm p}$ is the radius, f is the true anomaly, the angle measured from the pericenter, $a_{\rm p}$ is the semi-major axis, and $e_{\rm p}$ is the eccentricity. Along the orbit, the specific relative angular momentum $h_{\rm p}$ is conserved:

$$h_{\rm p} = r_{\rm p}^2\dot{f} = \sqrt{GM_1 a_{\rm p}(1-e_{\rm p}^2)}, \tag{A.2}$$

where M_1 is the mass of the Be star.

The distance of the particle from the tangent plane of the sky along the line of sight, $z_{\rm p}$, is written as

$$z_{\rm p} = r_{\rm p}\sin(\omega+f)\sin i, \tag{A.3}$$

where ω is the argument of pericenter and i is the inclination angle, i.e., the angle between the orbital axis and the line of sight. Note that the observer is

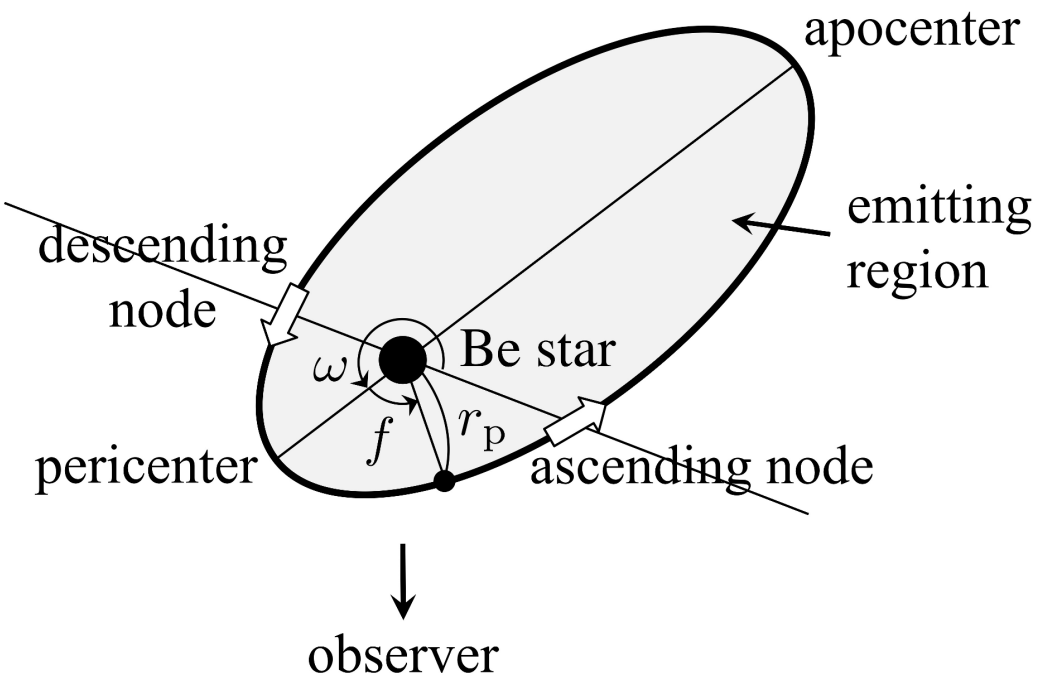

Figure A.1: A schematic diagram of the elliptical orbit of a particle orbiting along the limb of a line emitting region. The orbit has the semi-major axis $a_{\rm p}$ and eccentricity $e_{\rm p}$, and the radius and true anomaly of the particle at a time is $r_{\rm p}$ and f, respectively. The orbital plane is inclined to the tangent plane of the sky by an angle $i_{\rm p}$, which is not labeled in the figure. The intersection between these two planes is the line of nodes connecting the ascending node, where the particle moves away from the observer most rapidly, and the descending node, where the particle approaches the observer most rapidly. The pericenter is at the angle ω measured from the ascending node within the orbital plane. The observer views the orbit from below the figure. The shaded area denotes the line-emitting region.

at the $-z$-direction (see Fig. A.1). Then, the time derivative of $z_{\rm p}$ gives the radial velocity $v_{\rm rad}$, i.e.,

$$\begin{aligned} v_{\rm rad} &= \dot{z}_{\rm p} \\ &= \left[\dot{r}_{\rm p}\sin(\omega+f) + r_{\rm p}\dot{f}\cos(\omega+f)\right]\sin i. \end{aligned} \tag{A.4}$$

From Eq. (A.1),

$$\dot{r}_{\rm p} = \frac{a_{\rm p}e_{\rm p}(1-e_{\rm p}^2)\sin f\cdot\dot{f}}{(1+e_{\rm p}\cos f)^2}, \tag{A.5}$$

and from Eq. (A.2),

$$\dot{f} = \sqrt{\frac{GM_1}{a_{\rm p}^3(1-e_{\rm p}^2)^3}}(1+e_{\rm p}\cos f)^2. \tag{A.6}$$

Substituting Eq. (A.6) into Eq. (A.5), we rewrite $\dot{r}_{\rm p}$ as

$$\dot{r}_{\rm p} = \sqrt{\frac{GM_1}{a_{\rm p}(1-e_{\rm p}^2)}}e_{\rm p}\sin f. \tag{A.7}$$

Using Eqs. (A.6) and (A.7), we have the radial velocity in the form

$$v_{\rm rad} = \sqrt{\frac{GM_1}{a_{\rm p}(1-e_{\rm p}^2)}}\sin i\left[\cos(\omega+f)+e_{\rm p}\cos\omega\right]. \tag{A.8}$$

Note that the radial velocity due to the orbital motion of the particle oscillates around $\sqrt{GM_1/[a_{\rm p}(1-e_{\rm p}^2)]}\,e_{\rm p}\cos\omega\sin i$, which can be positive or negative depending on the argument of pericenter, with the semi-amplitude of $\sqrt{GM_1/[a_{\rm p}(1-e_{\rm p}^2)]}\sin i$. The minimum and maximum values occur at the descending and ascending nodes, respectively. Eq. (A.8) is a well known formula in the binary motion study (except that Eq. (A.8) has no systemic velocity term) (e.g., Hilditch 2001, p.42).

For mathematical simplicity, we assume that the disk has a uniform emissivity, and so do the individual gas particles in the disk. Then, the minimum values of the radial velocity of particles at the outer boundary of the line emitting region is equal to the blue-peak velocity, $v_{\rm blue}$, of the line, while the maximum radial velocity of the particle is equal to the red-peak velocity, $v_{\rm red}$, i.e.,

$$v_{\rm blue} = \sqrt{\frac{GM_1}{a_{\rm p}(1-e_{\rm p}^2)}}(-1+e_{\rm p}\cos\omega)\sin i \tag{A.9}$$

and

$$v_{\rm red} = \sqrt{\frac{GM_1}{a_{\rm p}(1-e_{\rm p}^2)}}(1+e_{\rm p}\cos\omega)\sin i. \tag{A.10}$$

For $\cos\omega \neq 0$, we can derive the relations between $a_{\rm p}$ and $e_{\rm p}$ of the limb-particle orbit, which defines the shape of the emitting region and the velocities along the line of sight, by using Eqs (A.9) and (A.10). Dividing Eq. (A.9) by Eq. (A.10), we have

$$e_{\rm p} = \frac{v_{\rm red}+v_{\rm blue}}{v_{\rm red}-v_{\rm blue}}\sec\omega. \tag{A.11}$$

Since $|e_{\rm p}| < 1$, Eq. (A.11) can be used to constrain the argument of pericenter, ω, using the observed peak velocities:

$$|\cos\omega| > \frac{|v_{\rm red}+v_{\rm blue}|}{v_{\rm red}-v_{\rm blue}}. \tag{A.12}$$

The semi-major axis of the emitting region, $a_{\rm p}$, can also be constrained by the observed peak velocities. Subtracting Eq. (A.9) from Eq. (A.10) gives

$$a_{\rm p} = \frac{4GM_1\sin^2 i}{(v_{\rm red}-v_{\rm blue})^2(1-e_{\rm p}^2)}, \tag{A.13}$$

which is not very useful, because GM_1 has to be calculated to evaluate the right hand side. It is more convenient and useful to rewrite Eq. (A.13) to a non-dimensional form,

$$\frac{a_{\rm p}}{R_1} = \left(\frac{2v_{\rm crit}}{v_{\rm red}-v_{\rm blue}}\right)^2\frac{\sin^2 i}{1-e_{\rm p}^2}, \tag{A.14}$$

where R_1 is the radius of the Be star and $v_{\rm crit} = \sqrt{GM_1/R_1}$ is the critical velocity.*

Eq. (A.14) can also be written in a form without $e_{\rm p}$. By substituting Eq. (A.11) into Eq. (A.14), we have another form of $a_{\rm p}$ as,

$$\frac{a_{\rm p}}{R_1} = \frac{4v_{\rm crit}^2\sin^2 i}{(v_{\rm red}-v_{\rm blue})^2-(v_{\rm red}+v_{\rm blue})^2\sec^2\omega}. \tag{A.15}$$

Note that for $\cos\omega = 0$ neither $a_{\rm p}$ nor $e_{\rm p}$ can be determined from the observed

*Eq. (A.14) gives a general relation between the semi-major axis and the peak separation, $v_{\rm red} - v_{\rm blue}$, for an elliptical disk. It should be noted that, for an elliptical disk with eccentricity e, Huang (1972)'s equation, which is often used to estimate the disk size from the peak separation, underestimates the disk size by a factor of $1-e^2$.

peak velocities. Note also that the unique determination of these orbital elements requires additional information about the argument of pericenter, ω, and the disk inclination angle, i. However, even without such information, we can constrain the (time-dependent) ranges of a_p and e_p (and even those of ω and i as we will see later), which will help us understand the observed long-term behavior of the system.

It is also important to note that, for given distributions of e_p and ω with respect to the semi-major axis, a_p, and a given distribution of the emissivity over the disk, the model allows us to calculate the intensities of blue and red peaks, as well as the EWs of the blueshifted and redshifted regions, both of which can be directly compared to the observation and hence can be used as a sanity check of the model.

For this reason and since full radiation transfer calculations to obtain those distributions is beyond the scope of this work, we make, as zeroth order approximation, another simplified assumption that all particles with different semi-major axes have the same eccentricity, e_p, and argument of pericenter, ω, in addition to the assumption that the emissivity is uniform over the disk, as mentioned before.

By this assumption, the contour of the zero radial velocity becomes two straight lines of constant true anomalies given by

$$f_{0,1}, f_{0,2} = \cos^{-1}(-e_\mathrm{p}\cos\omega) - \omega \tag{A.16}$$

($0 < f_{0,1} < f_{0,2} < 2\pi$) [see Eq. (A.8)], from which the surface areas of blueshifted and redshifted regions, S_blue and S_red, are calculated as

$$S_\mathrm{blue} = \frac{1}{2}(a_\mathrm{p}^2 - a_\mathrm{in}^2)(1-e_\mathrm{p}^2)\cos i \int_{f_{0,1}}^{f_{0,2}} \frac{df}{(1+e_\mathrm{p}\cos f)^2}, \tag{A.17}$$

and

$$S_\mathrm{red} = \frac{1}{2}(a_\mathrm{p}^2 - a_\mathrm{in}^2)(1-e_\mathrm{p}^2)\cos i \int_{f_{0,2}}^{f_{0,1}+2\pi} \frac{df}{(1+e_\mathrm{p}\cos f)^2}, \tag{A.18}$$

respectively. Here, a_in is the semi-major axis of the particle at the innermost orbit. In what follows, we assume that the innermost orbit is tangential to the stellar surface at pericenter, i.e., $a_\mathrm{in} = R_1/(1-e_\mathrm{p})$. The assumption of uniform emissivity enables us to directly compare Eqs. (A.17) and (A.18) with the observed EWs on the blue and red sides, respectively.

Moreover, with these assumptions, the intensities of the blue and red peaks are respectively proportional to the lengths of the iso-velocity contours at $v_{\rm blue}$ and $v_{\rm red}$, $\ell_{\rm blue}$ and $\ell_{\rm red}$, respectively, which are calculated as follows: along the iso-velocity contours, $v_{\rm rad} = v_{\rm blue}$ and $v_{\rm rad} = v_{\rm red}$, the true anomaly, f, is related to the semi-major axis, a ($a_{\rm in} \leq a \leq a_{\rm p}$) as

$$\cos(\omega + f_{\mp}) + e_{\rm p}\cos\omega = \left(\frac{a}{a_{\rm p}}\right)^{1/2} (\mp 1 + e_{\rm p}\cos\omega), \tag{A.19}$$

where the $-$ and $+$ signs correspond to the iso-velocity contours at $v_{\rm blue}$ and $v_{\rm red}$, respectively. Eq. (A.19) has two solutions given by

$$\begin{aligned} f_{\mp,1}, f_{\mp,2} \quad &= \cos^{-1}\left\{ \mp \left(\frac{a}{a_{\rm p}}\right)^{1/2} \right. \\ &\quad \left. - \left[1 - \left(\frac{a}{a_{\rm p}}\right)^{1/2}\right] e_{\rm p}\cos\omega \right\} - \omega. \end{aligned} \tag{A.20}$$

Since the line elements $d\ell_{\mp}$ along the iso-velocity contours, $v_{\rm rad} = v_{\rm blue}$ and $v_{\rm rad} = v_{\rm red}$, are given by

$$d\ell_{\mp} = \sqrt{\left(\frac{\partial r}{\partial a}\right)^2 da^2 + r^2 df_{\mp}^2}, \tag{A.21}$$

with $\partial r/\partial a$ and $df_{\mp}$ being given by

$$\frac{\partial r}{\partial a} = \frac{\left(1 - e_{\rm p}^2\right)}{1 + e_{\rm p}\cos f_{\mp}}, \tag{A.22}$$

and

$$\begin{aligned} \sin(\omega + f_{\mp}) df \quad &= \quad \frac{1}{2a_{\rm p}} \left(\frac{a}{a_{\rm p}}\right)^{-1/2} \\ &\quad \times (\mp 1 + e_{\rm p}\cos\omega)\, da, \end{aligned} \tag{A.23}$$

respectively, we have the following expressions for $\ell_{\rm blue}$ and $\ell_{\rm red}$,

$$\ell_{\rm blue}, \ell_{\rm red} = (1 - e_{\rm p}^2) \int_{a_{\rm in}}^{a_{\rm p}} da \times \left\{ \frac{1}{1 + e_{\rm p} \cos f_{\mp,1}} \sqrt{1 + \frac{a \left(\mp 1 + e_{\rm p} \cos\omega\right)^2}{4 a_{\rm p} \sin^2(\omega + f_{\mp,1})}} + \frac{1}{1 + e_{\rm p} \cos f_{\mp,2}} \sqrt{1 + \frac{a \left(\mp 1 + e_{\rm p} \cos\omega\right)^2}{4 a_{\rm p} \sin^2(\omega + f_{\mp,2})}} \right\}, \tag{A.24}$$

where $\ell_{\rm blue}$ takes the $-$ signs and $\ell_{\rm red}$ the $+$ signs. From Eqs. (A.20) and (A.24), the ratio $\ell_{\rm blue}/\ell_{\rm red}$ can be evaluated and compared to the observed V/R ratio.

Appendix B

Measured Hα properties of LS I +61 303

Table B.1: Measured properties of the Hα emission line of LS I +61 303

MJD	$\mathbf{V_{blue}}$**(km. s^{-1})**	$\mathbf{V_{red}}$**(km. s^{-1})**	$-\mathbf{EW_{blue}}$ (Å)	$-\mathbf{EW_{red}}$ (Å)	**V/R**
54411.4580	-139.6 ± 1.1	172.5 ± 3.5	4.45 ± 0.22	5.59 ± 0.28	0.882 ± 0.004
54412.4030	-138.9 ± 2.0	181.8 ± 4.1	4.34 ± 0.22	4.73 ± 0.24	0.970 ± 0.005
54413.4610	-139.9 ± 1.0	172.4 ± 1.7	4.62 ± 0.23	5.26 ± 0.26	1.005 ± 0.004
54414.4530	-141.3 ± 1.3	164.7 ± 2.0	4.30 ± 0.22	5.08 ± 0.25	0.990 ± 0.005
54418.6680	-154.9 ± 2.2	168.7 ± 2.1	4.45 ± 0.22	4.51 ± 0.23	0.961 ± 0.005
54830.4860	-158.3 ± 2.0	141.1 ± 6.5	4.38 ± 0.22	3.38 ± 0.17	0.981 ± 0.009
55166.5110	-128.5 ± 8.1	191.8 ± 1.6	5.62 ± 0.28	2.23 ± 0.11	0.910 ± 0.008
55170.5120	-122.1 ± 1.3	203.7 ± 1.3	4.05 ± 0.20	2.75 ± 0.14	0.692 ± 0.002
55171.6010	-122.0 ± 2.4	192.4 ± 3.3	4.23 ± 0.21	2.98 ± 0.15	0.718 ± 0.002
55173.5280	-131.6 ± 2.5	202.0 ± 3.3	4.39 ± 0.22	3.29 ± 0.16	0.956 ± 0.004
55174.5860	-126.7 ± 2.0	211.2 ± 3.0	4.55 ± 0.23	2.79 ± 0.14	1.022 ± 0.003
55219.8280	-144.2 ± 7.2	182.8 ± 9.1	4.87 ± 0.15	6.76 ± 0.14	1.064 ± 0.044
55230.8410	-137.1 ± 6.9	173.0 ± 8.6	4.38 ± 0.17	6.88 ± 0.11	0.806 ± 0.046
55356.2013	-138.6 ± 6.9	172.7 ± 8.6	4.30 ± 0.09	7.46 ± 0.11	0.774 ± 0.021
55365.1982	-154.6 ± 7.7	190.5 ± 9.5	4.71 ± 0.08	6.06 ± 0.14	0.803 ± 0.033
55372.1578	-162.3 ± 8.1	189.2 ± 9.5	5.22 ± 0.07	5.35 ± 0.16	0.982 ± 0.058
55380.1592	-139.4 ± 7.0	173.7 ± 8.7	4.16 ± 0.06	6.48 ± 0.20	0.736 ± 0.031
55396.2380	-168.8 ± 8.4	188.1 ± 9.4	4.83 ± 0.02	5.28 ± 0.11	0.841 ± 0.027
55404.1095	-159.2 ± 8.0	180.3 ± 9.0	4.68 ± 0.07	6.12 ± 0.07	0.890 ± 0.029

Continued on next page

Table B.1 – continued from previous page

MJD	V_{blue}(km. s^{-1})	V_{red}(km. s^{-1})	$-EW_{blue}$ (Å)	$-EW_{red}$ (Å)	V/R
55411.1915	-144.1 ± 7.2	186.2 ± 9.3	4.75 ± 0.10	6.23 ± 0.12	0.896 ± 0.044
55414.1258	-150.9 ± 7.5	175.6 ± 8.8	3.94 ± 0.06	3.89 ± 0.22	1.059 ± 0.030
55415.1516	-122.2 ± 6.1	198.8 ± 9.9	4.99 ± 0.11	6.31 ± 0.09	1.156 ± 0.034
55416.1231	-129.1 ± 6.5	183.2 ± 9.2	4.42 ± 0.04	5.07 ± 0.17	1.110 ± 0.038
55417.1449	-133.5 ± 6.7	199.7 ± 10.0	4.84 ± 0.07	6.29 ± 0.09	1.027 ± 0.022
55418.0737	-134.3 ± 6.7	176.5 ± 8.8	4.43 ± 0.04	7.68 ± 0.13	0.826 ± 0.054
55420.2157	-123.4 ± 6.2	193.0 ± 9.6	5.29 ± 0.09	5.83 ± 0.21	0.864 ± 0.070
55421.0763	-149.2 ± 7.5	181.4 ± 9.1	9.63 ± 0.40	9.07 ± 0.29	0.930 ± 0.030
55423.1302	-170.6 ± 8.5	173.7 ± 8.7	5.07 ± 0.11	6.55 ± 0.11	0.999 ± 0.025
55424.0910	-173.6 ± 8.7	166.9 ± 8.3	4.93 ± 0.07	6.52 ± 0.16	1.016 ± 0.030
55426.1954	-190.7 ± 9.5	158.7 ± 7.9	4.41 ± 0.07	6.06 ± 0.12	1.011 ± 0.032
55428.0492	-183.7 ± 9.2	160.4 ± 8.0	3.98 ± 0.12	6.79 ± 0.04	0.819 ± 0.013
55429.0303	-214.5 ± 10.7	129.3 ± 6.5	3.68 ± 0.05	6.97 ± 0.17	0.626 ± 0.035
55430.0452	-154.5 ± 7.7	181.8 ± 9.1	3.53 ± 0.05	6.26 ± 0.20	0.756 ± 0.015
55431.0248	-140.7 ± 7.0	195.0 ± 9.8	3.54 ± 0.09	6.92 ± 0.09	0.796 ± 0.015
55432.0348	-141.3 ± 7.1	186.2 ± 9.3	3.98 ± 0.11	6.53 ± 0.11	0.785 ± 0.037
55433.0302	-134.8 ± 6.7	187.4 ± 9.4	3.50 ± 0.17	5.84 ± 0.13	0.885 ± 0.049
55434.0157	-148.1 ± 7.4	164.6 ± 8.2	3.82 ± 0.20	6.42 ± 0.09	0.800 ± 0.024
55436.0102	-124.5 ± 6.2	187.4 ± 9.4	4.20 ± 0.10	5.85 ± 0.14	0.916 ± 0.052
55437.0083	-129.4 ± 6.5	187.7 ± 9.4	4.12 ± 0.16	5.93 ± 0.14	0.863 ± 0.017
55439.0018	-150.2 ± 7.5	176.7 ± 8.8	4.58 ± 0.13	5.33 ± 0.12	1.096 ± 0.022
55440.0782	-158.8 ± 7.9	185.0 ± 9.2	4.72 ± 0.15	5.62 ± 0.16	1.132 ± 0.032
55440.0809	-171.1 ± 8.6	140.7 ± 7.0	4.83 ± 0.07	7.78 ± 0.14	0.886 ± 0.033
55440.0835	-156.1 ± 7.8	176.8 ± 8.8	5.38 ± 0.04	6.71 ± 0.12	1.088 ± 0.034
55440.0896	-154.1 ± 7.7	177.5 ± 8.9	5.59 ± 0.11	5.68 ± 0.09	1.185 ± 0.022
55441.0558	-157.1 ± 7.9	185.7 ± 9.3	5.83 ± 0.03	5.97 ± 0.16	1.270 ± 0.030
55442.2185	-157.8 ± 7.9	179.2 ± 9.0	4.58 ± 0.10	6.16 ± 0.15	1.075 ± 0.028
55442.2289	-156.1 ± 7.8	184.7 ± 9.2	5.45 ± 0.09	6.03 ± 0.10	1.080 ± 0.036
55443.1491	-154.2 ± 7.7	184.1 ± 9.2	4.04 ± 0.12	7.05 ± 0.05	0.883 ± 0.039
55444.0295	-152.3 ± 7.6	165.9 ± 8.3	3.41 ± 0.08	7.18 ± 0.12	0.786 ± 0.040
55444.9973	-158.8 ± 7.9	151.5 ± 7.6	4.04 ± 0.11	8.04 ± 0.26	0.688 ± 0.027
55446.1281	-131.5 ± 6.6	172.0 ± 8.6	3.54 ± 0.11	7.07 ± 0.11	0.689 ± 0.044
55447.0302	-138.1 ± 6.9	184.7 ± 9.2	4.41 ± 0.09	7.16 ± 0.09	0.713 ± 0.019
55447.9773	-139.6 ± 7.0	188.8 ± 9.4	4.62 ± 0.11	6.00 ± 0.13	0.825 ± 0.021

Continued on next page

Table B.1 – continued from previous page

MJD	V_{blue}(km. s^{-1})	V_{red}(km. s^{-1})	$-EW_{blue}$ (Å)	$-EW_{red}$ (Å)	V/R
55449.1766	-150.8 ± 7.5	181.1 ± 9.1	4.89 ± 0.06	6.62 ± 0.16	0.852 ± 0.029
55452.0914	-171.1 ± 8.6	167.5 ± 8.4	4.87 ± 0.04	6.73 ± 0.08	0.922 ± 0.043
55459.0563	-118.8 ± 5.9	199.7 ± 10.0	5.25 ± 0.08	7.12 ± 0.07	0.954 ± 0.010
55469.2121	-141.8 ± 7.1	190.4 ± 9.5	5.79 ± 0.09	6.81 ± 0.10	0.906 ± 0.036
55470.0683	-126.9 ± 6.3	205.9 ± 10.2	5.09 ± 0.06	7.01 ± 0.14	0.920 ± 0.038
55470.9906	-139.9 ± 7.0	187.8 ± 9.4	4.20 ± 0.11	7.63 ± 0.14	0.781 ± 0.038
55473.0888	-162.6 ± 8.1	164.6 ± 8.2	4.21 ± 0.08	7.61 ± 0.10	0.694 ± 0.035
55474.0815	-148.1 ± 7.4	186.1 ± 9.3	5.26 ± 0.08	6.92 ± 0.12	0.950 ± 0.037
55474.9457	-159.6 ± 8.0	181.6 ± 9.1	5.02 ± 0.05	6.92 ± 0.11	0.904 ± 0.025
55475.9390	-160.7 ± 8.0	178.2 ± 8.9	5.84 ± 0.11	6.93 ± 0.05	1.025 ± 0.015
55477.1073	-172.6 ± 8.6	165.2 ± 8.3	5.34 ± 0.07	6.00 ± 0.08	1.035 ± 0.029
55478.0549	-178.8 ± 8.9	163.5 ± 8.2	5.12 ± 0.15	6.75 ± 0.13	0.963 ± 0.020
55479.0356	-177.1 ± 8.9	162.6 ± 8.1	5.56 ± 0.08	6.25 ± 0.14	0.912 ± 0.033
55479.9129	-180.8 ± 9.0	165.3 ± 8.3	4.87 ± 0.12	5.92 ± 0.18	0.957 ± 0.026
55482.0367	-151.4 ± 7.6	165.6 ± 8.3	5.46 ± 0.08	5.94 ± 0.11	0.950 ± 0.026
55483.1571	-146.9 ± 7.3	175.9 ± 8.8	5.65 ± 0.14	6.66 ± 0.08	0.944 ± 0.019
55484.0424	-145.2 ± 7.3	184.8 ± 9.2	4.62 ± 0.19	5.90 ± 0.10	0.859 ± 0.013
55497.0991	-154.7 ± 7.7	183.5 ± 9.2	3.92 ± 0.09	6.15 ± 0.12	0.873 ± 0.033
55501.2296	-158.8 ± 7.9	188.1 ± 9.4	4.34 ± 0.11	5.38 ± 0.12	0.869 ± 0.027
55505.1000	-172.6 ± 8.6	163.5 ± 8.2	4.14 ± 0.15	6.67 ± 0.09	0.892 ± 0.020
55513.0206	-142.0 ± 7.1	181.1 ± 9.1	3.85 ± 0.17	7.26 ± 0.11	0.737 ± 0.018
55516.8615	-139.3 ± 7.0	193.3 ± 9.7	4.62 ± 0.16	7.13 ± 0.08	0.771 ± 0.022
55516.9775	-138.8 ± 6.9	201.0 ± 10.8	5.86 ± 0.07	6.54 ± 0.07	0.816 ± 0.018
55520.9526	-156.9 ± 7.8	196.2 ± 9.8	4.32 ± 0.18	6.25 ± 0.11	1.125 ± 0.029
55575.8155	-147.4 ± 7.4	186.0 ± 9.3	5.07 ± 0.17	6.77 ± 0.05	1.025 ± 0.035
55575.8229	-144.3 ± 7.2	167.2 ± 8.4	4.69 ± 0.14	7.32 ± 0.07	0.996 ± 0.042
55578.8468	-140.4 ± 7.0	191.1 ± 9.6	4.03 ± 0.13	7.33 ± 0.05	0.762 ± 0.023
55578.8541	-137.8 ± 6.9	188.0 ± 9.4	4.00 ± 0.13	7.36 ± 0.08	0.758 ± 0.023
55579.8176	-136.8 ± 6.8	185.9 ± 9.3	4.42 ± 0.11	7.28 ± 0.05	0.780 ± 0.037
55579.8250	-135.1 ± 6.8	186.2 ± 9.3	4.55 ± 0.18	7.28 ± 0.06	0.796 ± 0.032
55580.8235	-138.5 ± 6.9	191.0 ± 9.5	4.92 ± 0.12	7.14 ± 0.07	0.781 ± 0.029
55580.8309	-138.7 ± 6.9	192.9 ± 9.6	4.89 ± 0.14	7.05 ± 0.07	0.781 ± 0.031
55595.8731	-132.5 ± 6.6	188.8 ± 9.4	3.36 ± 0.31	6.44 ± 0.13	0.754 ± 0.023
55596.8994	-142.7 ± 7.1	173.9 ± 8.7	3.11 ± 0.23	4.61 ± 0.13	0.901 ± 0.021

Continued on next page

Table B.1 – continued from previous page

MJD	V_{blue}(km. s^{-1})	V_{red}(km. s^{-1})	$-EW_{blue}$ (Å)	$-EW_{red}$ (Å)	V/R
55597.8306	-149.6 ± 7.5	177.2 ± 8.9	3.43 ± 0.21	4.89 ± 0.16	0.957 ± 0.021
55598.9026	-157.0 ± 7.8	173.0 ± 8.6	3.12 ± 0.28	4.66 ± 0.18	0.905 ± 0.021
55608.8368	-156.0 ± 7.8	176.4 ± 8.8	4.22 ± 0.10	4.69 ± 0.24	0.913 ± 0.015
55609.8346	-153.7 ± 7.7	171.2 ± 8.6	4.30 ± 0.17	4.59 ± 0.23	0.957 ± 0.030
55610.8329	-149.1 ± 7.5	171.5 ± 8.6	4.71 ± 0.17	4.52 ± 0.28	0.984 ± 0.033
55611.8750	-153.6 ± 7.7	169.5 ± 8.5	4.72 ± 0.20	4.28 ± 0.22	1.017 ± 0.025
55612.8898	-155.6 ± 7.8	167.5 ± 8.4	5.27 ± 0.16	4.50 ± 0.33	1.072 ± 0.031
55613.8470	-157.0 ± 7.9	156.9 ± 7.8	4.91 ± 0.17	3.90 ± 0.20	1.078 ± 0.018
55614.8486	-158.6 ± 7.9	163.0 ± 8.1	4.11 ± 0.10	4.47 ± 0.19	0.904 ± 0.022
55615.8528	-154.2 ± 7.7	168.0 ± 8.4	4.32 ± 0.15	4.48 ± 0.33	0.927 ± 0.017
55616.8465	-141.6 ± 7.1	164.0 ± 8.2	3.95 ± 0.15	5.16 ± 0.26	0.898 ± 0.014
55617.8366	-145.5 ± 7.3	161.4 ± 8.1	3.89 ± 0.22	5.98 ± 0.18	0.824 ± 0.017
55618.8456	-146.2 ± 7.3	175.2 ± 8.8	3.06 ± 0.16	5.84 ± 0.26	0.704 ± 0.010
55619.8479	-151.0 ± 7.5	173.6 ± 8.7	3.81 ± 0.18	5.17 ± 0.33	0.751 ± 0.033
55620.8580	-151.9 ± 7.6	162.2 ± 8.1	4.00 ± 0.14	5.16 ± 0.31	0.772 ± 0.017
55621.8547	-144.9 ± 7.2	169.4 ± 8.5	3.86 ± 0.17	5.34 ± 0.30	0.685 ± 0.031
55622.8420	-146.2 ± 7.3	174.8 ± 8.7	3.77 ± 0.23	5.36 ± 0.28	0.693 ± 0.015
55834.6150	-133.3 ± 2.0	175.6 ± 2.7	2.02 ± 0.10	4.08 ± 0.20	0.588 ± 0.004
55977.8478	-162.4 ± 8.1	163.4 ± 8.2	3.99 ± 0.09	5.03 ± 0.17	0.875 ± 0.024
55982.8684	-170.1 ± 8.5	153.6 ± 7.7	4.52 ± 0.11	4.68 ± 0.14	1.017 ± 0.044
55988.8519	-111.7 ± 5.6	180.7 ± 9.0	7.03 ± 0.14	2.41 ± 0.20	1.565 ± 0.027
55991.8643	-139.5 ± 7.0	177.9 ± 8.9	3.42 ± 0.15	5.25 ± 0.38	0.669 ± 0.013
55992.8609	-154.3 ± 7.7	176.6 ± 8.8	2.42 ± 0.14	5.51 ± 0.38	0.567 ± 0.020
56110.1915	-165.0 ± 8.3	172.6 ± 8.6	3.16 ± 0.10	5.45 ± 0.22	0.760 ± 0.019
56111.1898	-144.3 ± 7.2	175.0 ± 8.7	3.77 ± 0.07	4.46 ± 0.26	0.782 ± 0.023
56112.1854	-174.2 ± 8.7	164.8 ± 8.2	3.86 ± 0.03	3.61 ± 0.33	0.894 ± 0.045
56114.1784	-177.3 ± 8.9	153.2 ± 7.7	3.98 ± 0.10	3.67 ± 0.27	0.932 ± 0.016
56116.1921	-182.7 ± 9.1	161.1 ± 8.1	4.33 ± 0.08	4.37 ± 0.21	0.897 ± 0.026
56117.1706	-199.4 ± 10.0	146.4 ± 7.3	3.49 ± 0.06	4.05 ± 0.32	0.786 ± 0.023
56120.2140	-141.8 ± 7.1	185.7 ± 9.3	4.16 ± 0.18	3.80 ± 0.21	1.093 ± 0.042
56141.1270	-213.0 ± 10.7	127.0 ± 6.4	4.40 ± 0.05	6.74 ± 0.10	0.734 ± 0.027
56143.0973	-225.5 ± 11.3	119.2 ± 6.0	3.87 ± 0.03	5.85 ± 0.07	0.726 ± 0.018
56144.0936	-239.8 ± 12.0	121.5 ± 6.1	4.07 ± 0.06	6.37 ± 0.10	0.724 ± 0.041
56145.0914	-202.6 ± 10.1	146.3 ± 7.3	5.57 ± 0.02	6.14 ± 0.10	0.902 ± 0.026

Continued on next page

Table B.1 – continued from previous page

MJD	V_{blue}(km. s^{-1})	V_{red}(km. s^{-1})	$-EW_{blue}$ (Å)	$-EW_{red}$ (Å)	V/R
56145.1852	-210.8 ± 10.5	130.0 ± 6.5	5.87 ± 0.03	6.44 ± 0.11	0.859 ± 0.022
56150.1747	-199.5 ± 10.0	143.9 ± 7.2	5.16 ± 0.19	8.69 ± 0.15	0.663 ± 0.029
56152.1471	-200.7 ± 10.0	160.7 ± 8.0	5.24 ± 0.05	8.52 ± 0.12	0.779 ± 0.037
56153.1451	-151.4 ± 7.6	211.9 ± 10.	4.83 ± 0.07	6.98 ± 0.07	0.791 ± 0.036
56154.2262	-201.1 ± 10.1	151.0 ± 7.6	4.58 ± 0.11	8.71 ± 0.07	0.735 ± 0.043
56156.2212	-203.2 ± 10.2	133.6 ± 6.7	4.57 ± 0.11	6.70 ± 0.08	0.912 ± 0.024
56158.1144	-200.9 ± 10.0	138.1 ± 6.9	5.10 ± 0.09	6.12 ± 0.07	1.025 ± 0.030
56159.1895	-210.7 ± 10.5	147.1 ± 7.4	5.74 ± 0.11	6.51 ± 0.04	0.990 ± 0.025
56165.0657	-204.4 ± 10.2	128.8 ± 6.4	4.12 ± 0.08	6.23 ± 0.14	0.842 ± 0.030
56167.2367	-209.1 ± 10.5	117.8 ± 5.9	5.43 ± 0.13	6.58 ± 0.14	0.941 ± 0.027
56169.0288	-204.6 ± 10.2	125.5 ± 6.3	5.37 ± 0.04	6.00 ± 0.18	0.925 ± 0.029
56173.1081	-185.0 ± 9.2	139.5 ± 7.0	5.91 ± 0.07	7.04 ± 0.07	0.923 ± 0.019
56174.0112	-202.3 ± 10.1	125.7 ± 6.3	5.47 ± 0.04	7.08 ± 0.10	0.817 ± 0.012
56176.1403	-190.2 ± 9.5	125.0 ± 6.2	6.15 ± 0.11	9.03 ± 0.05	0.805 ± 0.016
56177.0583	-178.0 ± 8.9	153.1 ± 7.7	7.19 ± 0.08	10.27 ± 0.03	0.685 ± 0.032
56178.2409	-186.6 ± 9.3	173.7 ± 8.7	5.77 ± 0.15	8.53 ± 0.10	0.684 ± 0.037
56179.0971	-196.5 ± 9.8	176.0 ± 8.8	5.40 ± 0.15	8.28 ± 0.17	0.740 ± 0.035
56180.0286	-195.5 ± 9.8	168.4 ± 8.4	4.90 ± 0.15	9.30 ± 0.13	0.750 ± 0.037
56180.1244	-199.6 ± 10.2	164.4 ± 8.2	5.21 ± 0.10	8.62 ± 0.13	0.698 ± 0.034
56182.1035	-199.5 ± 9.2	125.8 ± 6.3	5.00 ± 0.06	7.53 ± 0.13	0.867 ± 0.048
56183.0455	-199.4 ± 10.0	121.3 ± 6.1	4.65 ± 0.09	7.82 ± 0.11	0.882 ± 0.031
56184.0794	-199.0 ± 10.0	130.3 ± 6.5	5.29 ± 0.09	7.52 ± 0.04	0.962 ± 0.016
56185.0439	-195.5 ± 9.8	126.0 ± 6.3	4.55 ± 0.10	7.64 ± 0.10	0.905 ± 0.035
56192.0603	-202.1 ± 10.1	122.7 ± 6.1	5.23 ± 0.09	6.71 ± 0.07	1.019 ± 0.020
56192.9736	-211.4 ± 10.6	130.4 ± 6.5	5.68 ± 0.14	8.67 ± 0.12	0.984 ± 0.030
56194.1607	-214.9 ± 10.7	130.7 ± 6.5	4.75 ± 0.11	6.65 ± 0.08	0.982 ± 0.044
56195.0464	-219.7 ± 11.0	126.7 ± 6.3	4.68 ± 0.09	7.04 ± 0.03	0.977 ± 0.049
56196.0479	-225.0 ± 11.3	114.0 ± 5.7	4.95 ± 0.08	6.80 ± 0.07	0.880 ± 0.039
56198.0364	-202.1 ± 10.1	125.3 ± 6.3	5.54 ± 0.07	6.76 ± 0.01	0.890 ± 0.022
56199.0387	-194.1 ± 9.7	139.8 ± 7.0	4.91 ± 0.10	6.00 ± 0.10	0.838 ± 0.027
56200.0313	-190.0 ± 9.5	127.5 ± 6.4	4.93 ± 0.05	6.38 ± 0.08	0.864 ± 0.014
56202.1048	-188.8 ± 9.4	114.7 ± 5.7	6.68 ± 0.05	8.98 ± 0.05	0.808 ± 0.050
56205.0591	-173.6 ± 8.7	179.9 ± 9.0	6.52 ± 0.07	8.36 ± 0.09	0.856 ± 0.052
56206.1190	-186.8 ± 9.3	152.1 ± 7.6	5.87 ± 0.07	9.37 ± 0.12	0.674 ± 0.068

Continued on next page

Table B.1 – continued from previous page

MJD	V_{blue}(km. s^{-1})	V_{red}(km. s^{-1})	$-EW_{blue}$ (Å)	$-EW_{red}$ (Å)	V/R
56207.1240	-195.5 ± 9.8	159.1 ± 8.0	5.27 ± 0.11	8.35 ± 0.12	0.801 ± 0.060
56208.0251	-201.9 ± 10.1	157.1 ± 7.9	5.33 ± 0.12	8.36 ± 0.17	0.862 ± 0.035
56209.0737	-197.4 ± 9.9	156.5 ± 7.8	5.13 ± 0.07	7.73 ± 0.13	0.914 ± 0.029
56209.9758	-201.6 ± 10.1	146.6 ± 7.3	4.86 ± 0.10	8.26 ± 0.06	0.899 ± 0.081
56212.0010	-203.2 ± 10.2	152.5 ± 7.6	5.23 ± 0.09	7.93 ± 0.07	0.947 ± 0.061
56214.0376	-206.1 ± 10.3	132.2 ± 6.6	4.88 ± 0.02	8.64 ± 0.04	0.823 ± 0.038
56216.0161	-189.0 ± 9.5	133.7 ± 6.7	5.69 ± 0.03	7.41 ± 0.17	0.857 ± 0.027
56220.9475	-215.6 ± 10.8	114.0 ± 5.7	6.11 ± 0.16	7.80 ± 0.12	1.081 ± 0.055
56221.9711	-219.9 ± 11.0	108.6 ± 5.4	7.01 ± 0.08	8.42 ± 0.07	1.011 ± 0.039
56222.0678	-222.5 ± 11.1	112.4 ± 5.6	7.46 ± 0.05	8.25 ± 0.12	1.046 ± 0.037
56222.8916	-225.0 ± 11.2	105.0 ± 5.3	6.32 ± 0.16	7.92 ± 0.08	0.999 ± 0.027
56225.0288	-211.7 ± 10.6	109.6 ± 5.5	4.99 ± 0.06	8.84 ± 0.06	0.686 ± 0.026
56225.8992	-204.5 ± 10.2	119.9 ± 6.0	5.04 ± 0.04	9.00 ± 0.04	0.621 ± 0.030
56226.9616	-150.4 ± 7.5	137.5 ± 6.9	4.87 ± 0.13	8.03 ± 0.08	0.879 ± 0.077
56244.9373	-203.9 ± 10.2	121.9 ± 6.1	6.11 ± 0.07	8.83 ± 0.09	0.968 ± 0.042
56264.9842	-201.7 ± 10.1	136.0 ± 6.8	5.33 ± 0.03	7.11 ± 0.07	0.949 ± 0.023
56265.8974	-200.8 ± 10.0	128.9 ± 6.4	4.56 ± 0.06	7.50 ± 0.06	0.819 ± 0.032
56266.9990	-218.3 ± 10.9	125.4 ± 6.3	4.84 ± 0.14	7.28 ± 0.11	0.839 ± 0.026
56267.9140	-204.9 ± 10.2	129.9 ± 6.5	5.27 ± 0.02	7.83 ± 0.07	0.762 ± 0.036
56268.8559	-204.0 ± 10.2	127.5 ± 6.4	4.34 ± 0.06	7.84 ± 0.03	0.747 ± 0.026
56270.8684	-212.3 ± 10.6	115.3 ± 5.8	5.18 ± 0.05	8.51 ± 0.02	0.786 ± 0.039
56292.8221	-192.1 ± 9.6	139.3 ± 7.0	5.18 ± 0.01	6.47 ± 0.02	1.038 ± 0.021
56293.8536	-200.0 ± 10.0	140.0 ± 7.0	4.51 ± 0.02	7.02 ± 0.01	0.791 ± 0.023
56295.8437	-209.8 ± 10.5	123.5 ± 6.2	3.48 ± 0.08	5.82 ± 0.17	0.785 ± 0.042
56296.8653	-206.7 ± 10.3	127.7 ± 6.4	3.53 ± 0.04	5.56 ± 0.12	0.816 ± 0.041
56297.8581	-209.4 ± 10.5	136.3 ± 6.8	4.01 ± 0.10	6.20 ± 0.14	0.893 ± 0.049
56298.8313	-212.8 ± 10.6	131.9 ± 6.6	4.04 ± 0.08	5.80 ± 0.17	0.848 ± 0.057
56602.8643	-162.5 ± 8.1	190.4 ± 9.5	4.32 ± 0.12	7.57 ± 0.07	0.672 ± 0.014
56603.8543	-171.8 ± 8.6	189.6 ± 9.5	4.48 ± 0.12	8.75 ± 0.09	0.663 ± 0.040
56617.9890	-191.3 ± 9.6	167.4 ± 8.4	4.99 ± 0.04	6.94 ± 0.09	0.894 ± 0.049
56618.9658	-187.4 ± 9.4	158.0 ± 7.9	4.91 ± 0.04	6.88 ± 0.09	0.903 ± 0.039
56619.8891	-187.2 ± 9.4	147.5 ± 7.4	4.46 ± 0.05	6.23 ± 0.08	0.882 ± 0.023
56620.4600	-170.0 ± 1.8	150.8 ± 2.7	4.53 ± 0.23	5.06 ± 0.25	0.901 ± 0.002
56620.8591	-188.0 ± 9.4	150.5 ± 7.5	4.74 ± 0.01	5.28 ± 0.09	0.878 ± 0.011

Continued on next page

Table B.1 – continued from previous page

MJD	V_{blue}(km. s^{-1})	V_{red}(km. s^{-1})	$-EW_{blue}$ (Å)	$-EW_{red}$ (Å)	V/R
56621.3460	-155.3 ± 1.3	147.5 ± 2.5	5.32 ± 0.27	5.01 ± 0.25	0.959 ± 0.003
56621.8790	-169.6 ± 8.5	162.3 ± 8.1	5.64 ± 0.04	5.89 ± 0.05	0.927 ± 0.018
56622.2080	-130.9 ± 1.2	163.4 ± 2.3	4.42 ± 0.22	4.58 ± 0.23	0.893 ± 0.003
56622.8540	-157.8 ± 7.9	169.5 ± 8.5	5.66 ± 0.03	5.70 ± 0.09	0.931 ± 0.018
56624.9133	-163.3 ± 8.2	157.0 ± 7.8	5.62 ± 0.02	7.37 ± 0.02	0.825 ± 0.014
56642.8316	-173.1 ± 8.7	152.7 ± 7.6	5.68 ± 0.04	7.61 ± 0.05	0.930 ± 0.033
56643.8277	-172.6 ± 8.6	153.5 ± 7.7	6.74 ± 0.02	7.58 ± 0.09	0.947 ± 0.024
56644.8159	-181.4 ± 9.1	149.1 ± 7.5	5.74 ± 0.03	7.51 ± 0.08	0.921 ± 0.036
56645.8177	-185.2 ± 9.3	150.5 ± 7.5	5.87 ± 0.09	6.75 ± 0.09	0.940 ± 0.025
56646.8153	-177.9 ± 8.9	145.8 ± 7.3	6.60 ± 0.09	7.41 ± 0.10	0.927 ± 0.022
56647.8212	-156.9 ± 7.8	154.2 ± 7.7	6.10 ± 0.06	7.44 ± 0.07	0.827 ± 0.025
56648.9250	-167.0 ± 8.4	161.1 ± 8.1	5.46 ± 0.02	7.23 ± 0.09	0.717 ± 0.024
56649.8197	-139.2 ± 7.0	167.6 ± 8.4	6.28 ± 0.06	7.08 ± 0.05	0.800 ± 0.013
56650.8233	-131.3 ± 6.6	175.5 ± 8.8	7.12 ± 0.03	7.00 ± 0.08	1.030 ± 0.016
56651.8122	-152.7 ± 7.6	156.7 ± 7.8	6.21 ± 0.03	7.43 ± 0.15	0.833 ± 0.019
56652.8102	-138.9 ± 6.9	173.7 ± 8.7	6.09 ± 0.06	8.05 ± 0.10	0.774 ± 0.016
56655.4490	-143.2 ± 1.8	155.0 ± 1.9	4.79 ± 0.24	6.30 ± 0.32	0.783 ± 0.002
56655.8163	-165.9 ± 8.3	157.2 ± 7.9	6.63 ± 0.08	8.53 ± 0.07	0.823 ± 0.029
56657.8106	-167.4 ± 8.4	199.8 ± 10.	6.07 ± 0.08	11.0 ± 0.17	0.730 ± 0.055
56658.8147	-154.4 ± 7.7	188.0 ± 9.4	5.98 ± 0.06	9.27 ± 0.13	0.833 ± 0.030
56659.4790	-150.9 ± 2.8	149.5 ± 3.5	6.21 ± 0.31	7.81 ± 0.39	0.916 ± 0.010
56659.8145	-163.8 ± 8.2	159.9 ± 8.0	5.78 ± 0.04	9.18 ± 0.13	0.806 ± 0.064
56660.9102	-160.7 ± 8.0	154.9 ± 7.7	5.75 ± 0.04	8.40 ± 0.08	0.885 ± 0.037
56661.9213	-170.3 ± 8.5	141.9 ± 7.1	5.16 ± 0.06	8.39 ± 0.10	0.823 ± 0.043
56662.8565	-160.1 ± 8.0	149.9 ± 7.5	5.16 ± 0.05	8.42 ± 0.11	0.794 ± 0.050
56663.8454	-147.3 ± 7.4	155.6 ± 7.8	5.40 ± 0.05	9.21 ± 0.07	0.828 ± 0.037
56664.8751	-144.4 ± 7.2	165.6 ± 8.3	5.55 ± 0.06	7.45 ± 0.09	0.941 ± 0.007
56668.8490	-168.5 ± 8.4	164.6 ± 8.2	5.92 ± 0.07	8.11 ± 0.06	1.009 ± 0.022
56669.8293	-173.2 ± 8.7	160.6 ± 8.0	6.12 ± 0.06	8.09 ± 0.09	1.025 ± 0.032
56670.8167	-177.5 ± 8.9	156.2 ± 7.8	6.45 ± 0.06	7.65 ± 0.11	1.075 ± 0.042
56671.8226	-182.2 ± 9.1	154.0 ± 7.7	6.30 ± 0.05	7.32 ± 0.06	1.077 ± 0.027
56672.8254	-186.7 ± 9.3	153.4 ± 7.7	6.41 ± 0.04	7.47 ± 0.06	1.017 ± 0.032
56684.8931	-166.0 ± 8.3	166.3 ± 8.3	6.07 ± 0.11	10.9 ± 0.14	0.787 ± 0.064
56999.6370	-148.1 ± 1.6	149.6 ± 1.1	5.21 ± 0.26	5.83 ± 0.29	0.780 ± 0.001

Continued on next page

Table B.1 – continued from previous page

MJD	V_{blue}(km. s^{-1})	V_{red}(km. s^{-1})	$-EW_{blue}$ (Å)	$-EW_{red}$ (Å)	V/R
57003.6320	-151.6 ± 2.6	159.7 ± 1.5	4.50 ± 0.22	5.96 ± 0.30	1.031 ± 0.007
57024.5540	-144.8 ± 7.5	150.8 ± 2.6	3.71 ± 0.19	5.26 ± 0.26	0.706 ± 0.008
57025.5490	-147.4 ± 2.5	150.9 ± 1.4	4.76 ± 0.24	6.12 ± 0.31	0.653 ± 0.001
57318.6230	-143.3 ± 2.3	156.3 ± 3.1	4.37 ± 0.22	6.01 ± 0.30	0.745 ± 0.002
57318.7880	-142.2 ± 5.8	156.7 ± 3.8	4.28 ± 0.21	6.01 ± 0.30	0.732 ± 0.007
57319.4740	-142.6 ± 2.1	153.8 ± 3.6	4.24 ± 0.21	5.84 ± 0.29	0.817 ± 0.003
57319.6160	-147.5 ± 2.2	150.9 ± 2.9	4.85 ± 0.24	6.16 ± 0.31	0.842 ± 0.002
57319.7580	-148.2 ± 2.9	148.1 ± 1.9	4.56 ± 0.23	6.22 ± 0.31	0.847 ± 0.001
57320.4940	-151.9 ± 1.6	143.3 ± 3.8	4.68 ± 0.23	6.57 ± 0.33	0.899 ± 0.003
57320.6530	-151.5 ± 1.6	146.1 ± 4.0	4.43 ± 0.22	6.76 ± 0.34	0.875 ± 0.003
57320.7890	-151.7 ± 1.1	140.3 ± 4.9	4.65 ± 0.23	6.87 ± 0.34	0.903 ± 0.004
57321.7420	-149.0 ± 1.0	154.8 ± 2.9	4.12 ± 0.21	5.75 ± 0.29	0.975 ± 0.011
57323.5420	-142.9 ± 3.0	163.4 ± 1.7	3.99 ± 0.20	5.33 ± 0.27	0.847 ± 0.005
57323.7520	-145.5 ± 1.0	167.4 ± 1.6	4.58 ± 0.23	5.88 ± 0.29	0.860 ± 0.006

Appendix C

Cascade emission

This appendix provides calculations of the cascade emission. A semi-analytical method that does not involve Monte-Carlo simulations and similar to the semi-analytical solution for synchrotron supported cascades described in Böttcher et al. (2013), has been developed. We are only considering the shape of the total, time-integrated spectrum, which can be represented as the equilibrium solution in the case of a constant, continuous injection of primary gamma-rays. Throughout this appendix, we use the formulation as presented by Böttcher et al. (2013). We start out with the injection of first-generation $\gamma-$rays, given by an injection term, $\dot{N}_\epsilon^0$. For the calculations presented here, we use dimensionless energy, $\epsilon \equiv h\nu/m_e c^2$. For linear cascades, we can calculate the opacity for $\gamma - \gamma$ absorption, $\tau_{\gamma\gamma}(\epsilon)$, from the low-energy radiation field as we did in Eq. 4.93 for the simplified case of a mono-energetic stellar photon (E_*).

Under these conditions, the spectrum of escaping (observable) photons can be calculated as

$$\dot{N}_\epsilon^{esc} = \dot{N}_\epsilon^0 e^{-\tau_{\gamma\gamma}(\epsilon)} + \dot{N}_\epsilon^{\rm IC} \left(\frac{1 - e^{-\tau_{\gamma\gamma}[\epsilon]}}{\tau_{\gamma\gamma}[\epsilon]} \right), \tag{C.1}$$

which includes the contributions from the primary high-energy photon spectrum, $\dot{N}_\epsilon^0$, and from inverse-Compton emission from secondaries, $\dot{N}_\epsilon^{\rm IC}$. As the primary $\gamma-$rays are injected only at the boundary, they will be subject to $\gamma-\gamma$ absorption by a factor $e^{-\tau_{\gamma\gamma}}$. The IC photons are produced throughout the emission/cascading volume, for which case the solution to the radiation transfer equation yields the absorption correction factor $(1 - e^{-\tau_{\gamma\gamma}})/\tau_{\gamma\gamma}$.
The emissivity due to Compton scattering of an isotropic external radiation

field is calculated using the result of Jones (1968) - see also Dermer & Menon (2009):

$$\dot{N}_\epsilon^{\rm IC} = \frac{3}{4}\frac{c\sigma_T n_0}{\epsilon_{Ly\alpha}}\int_1^\infty d\gamma \frac{N_e(\gamma)}{\gamma^2}F_c(q,\Gamma_e)H\left(q,\frac{1}{4\gamma^2},1\right), \tag{C.2}$$

where

$$F_c(q,\Gamma_e) = 2q\ln q + (1+2q)(1-q) + \frac{1}{2}\frac{(\Gamma_e q)^2}{(1+\Gamma_e q)}(1-q), \tag{C.3}$$

with

$$\Gamma_e = 4\gamma\epsilon_{Ly\alpha} \text{ and } q = \frac{\epsilon/\gamma}{\Gamma_e(1-\epsilon/\gamma)}. \tag{C.4}$$

The time-integrated electron distribution, $N_e(\gamma)$ will be the equilibrium ($\partial\langle.\rangle/\partial t = 0$) solution to a Fokker-Planck equation which takes the form:

$$\frac{\partial}{\partial\gamma}(\dot{\gamma}N_e[\gamma]) = \dot{N_e}^{\gamma\gamma}(\gamma) + \dot{N}_e(\gamma)^{esc}. \tag{C.5}$$

In the case under consideration here, the electron energy losses will be dominated by inverse-Compton losses. Particle escape is parameterized through an escape timescale, $\dot{N}_e(\gamma)^{esc} = -N_e(\gamma)/t_{esc}$ with $t_{esc} = \eta R_{ext}/c$.
Note that due to the large photon and pair energies, the full Klein-Nishina cross-section has to be used (in acccordance with the evaluaton of the Compton emissivity in Eq. C.3). The resulting energy loss term for an isotropic target photon field has been evaluated by Boettcher, Mause & Schlickeiser (1997):

$$\dot{\gamma}_{\rm IC} = -c\pi r_e^2 n_0 \frac{G(\gamma\epsilon_*)}{\epsilon_*}, \tag{C.6}$$

where

$$G(E) = \ln(1+4E)\left(1+\frac{3}{E}+\frac{3}{4E^2}+\frac{\ln[1+4E]}{2E}-\frac{\ln[4E]}{E}\right)-\frac{5}{2E}$$
$$+\frac{4E}{1+4E}\left(\frac{2}{3}+\frac{1}{2E}+\frac{1}{8E^2}\right)+\frac{8E}{3}\frac{1+5E}{(1+4E)^2}+\frac{1}{E}\sum_{n=1}^{\infty}\frac{(1+4E)^{-n}}{n^2}-\frac{\pi^2}{6E}-2. \tag{C.7}$$

$\dot{N}_e^{\gamma\gamma}(\gamma)$ in Eq. C.6 is the rate of particle injection due to $\gamma-\gamma$ absorption, to be evaluated self-consistently with the radiation field. One of the particles produced in the absorption of a high-energy photon with energy ϵ will assume a major fraction (f_γ) of the photon energy. A value of $f_\gamma = 0.9$ is found to produce a good agreement from comparison with Monte-Carlo simulations and

numerical solutions to the cascade problem. So, an electron/positron pair with energies $\gamma_1 = f_\gamma \epsilon$ and $\gamma_2 = (1 - f_\gamma)\epsilon$ is produced. From Eq. C.2, every photon not escaping will produce an electron/positron pair and so the pair production rate can be written as

$$\dot{N}_e^{\gamma\gamma}(\gamma) = f_{abs}(\epsilon_1)\dot{N}_{\epsilon 1}^{\rm IC} + (1 - e^{-\tau_{\gamma\gamma}(\epsilon 1)})\dot{N}_{\epsilon 1}^{0} + f_{abs}(\epsilon_2)\dot{N}_{\epsilon 2}^{\rm IC} + (1 - e^{-\tau_{\gamma\gamma}(\epsilon 2)})\dot{N}_{\epsilon 2}^{0}, \tag{C.8}$$

where $\epsilon_1 = \gamma/f_\gamma$, $\epsilon_2 = \gamma/(1 - f_\gamma)$ and

$$f_{abs}(\epsilon) \equiv 1 - \frac{1 - e^{-\tau_{\gamma\gamma}(\epsilon)}}{\tau_{\gamma\gamma}(\epsilon)}. \tag{C.9}$$

With this approximation, Eq. C.6 has an implicit solution:

$$N_e(\gamma) = \frac{1}{|\dot{\gamma}_{\rm IC}|} \int_\gamma^\infty d\tilde{\gamma} \{ \dot{N}_e^{\gamma\gamma} - \frac{N_e(\tilde{\gamma})}{t_{esc}} \}. \tag{C.10}$$

The solution in Eq. C.10 is implicit in the sense that the particle spectrum $N_e(\gamma)$ occurs on both sides of the equation as $\dot{N}_e^{\gamma\gamma}$ depends on the Compton emissivity calculated through Eq. C.3, which requires knowledge of $N_e(\gamma')$. However, it is obvious that the electron distribution at $\tilde{\gamma} > \gamma$ depends only on $\gamma - \gamma$ pair production by $\gamma-$rays with energy $\epsilon_{1,2} > \tilde{\gamma}$, which can only have been produced by electrons with energy $\gamma' > \epsilon_{1,2} > \tilde{\gamma} > \gamma$. Thus, for any given electron energy γ, the r.h.s. of Eq. C.10 only depends on the electron distribution at energies $\gamma' > \gamma$. Therefore, Eq. C.10 may be evaluated progressively, starting at the highest pair energies, and then using the solution for $N_e(\gamma)$ for large γ as one progresses towards lower values of γ. Once the equilibrium pair distribution $N_e(\gamma)$ is known, it can be used in Eq. C.3 to evaluate the synchrotron emissivity and hence, using Eq. C.2 the observable photon spectrum.

Bibliography

Abate C., Pols O. R., Izzard R. G., Mohamed S. S., de Mink S. E., 2013, A&A, 552, A26

Abdo A. A. et al., 2009, ApJ, 701, L123

Acciari V. A. et al., 2011, ApJ, 738, 3

Acciari V. A. et al., 2009, ApJ, 700, 1034

Acciari V. A. et al., 2008, ApJ, 679, 1427

Ackermann M. et al., 2013, ApJ, 773, L35

Ahnen M. L. et al., 2016, A&A, 591, A76

Albert J. et al., 2009, ApJ, 693, 303

Albert J. et al., 2006, Science, 312, 1771

Albert J. et al., 2008, ApJ, 684, 1351

Alcock C. et al., 2001, MNRAS, 321, 678

An H. et al., 2015, ApJ, 806, 166

An H., Dufour F., Kaspi V. M., Harrison F. A., 2013, ApJ, 775, 135

An H., Romani R. W., 2017, ApJ, 838, 145

Antoniadis J. et al., 2013, Science, 340, 448

Aragona C., McSwain M. V., Grundstrom E. D., Marsh A. N., Roettenbacher R. M., Hessler K. M., Boyajian T. S., Ray P. S., 2009, ApJ, 698, 514

Axford W. I., Leer E., Skadron G., 1977, International Cosmic Ray Conference, 11, 132

Baade D., 1988, in IAU Symposium, Vol. 132, The Impact of Very High S/N Spectroscopy on Stellar Physics, Cayrel de Strobel G., Spite M., eds., p. 217

Ballester P., 1992, in European Southern Observatory Conference and Workshop Proceedings, Vol. 41, European Southern Observatory Conference and Workshop Proceedings, Grosbøl P. J., de Ruijsscher R. C. E., eds., p. 177

Baring M. G., 1997, in Very High Energy Phenomena in the Universe; Moriond Workshop, Giraud-Heraud Y., Tran Thanh van J., eds., p. 97

Barnes S. I. et al., 2008, in Proc. SPIE, Vol. 7014, Ground-based and Airborne Instrumentation for Astronomy II, p. 70140K

Barnsley R., Smith R., Steele I., 2012, in Astronomical Society of the Pacific Conference Series, Vol. 461, Astronomical Data Analysis Software and Systems XXI, Ballester P., Egret D., Lorente N. P. F., eds., p. 517

Bednarek W., 2007, A&A, 464, 259

Bednarz J., Ostrowski M., 1998, Physical Review Letters, 80, 3911

Begelman M. C., Rudak B., Sikora M., 1990, ApJ, 362, 38

Bell A. R., 1978, MNRAS, 182, 147

Benacquista M., 2013, An Introduction to the Evolution of Single and Binary Stars

Bethe H., Heitler W., 1934, Royal Society of London Proceedings Series A, 146, 83

Bignami G. F., Caraveo P. A., Lamb R. C., Markert T. H., Paul J. A., 1981, ApJ, 247, L85

Bisikalo D. V., Boyarchuk A. A., Harmanec P., Kaigorodov P. V., Kuznetsov O. A., 2006, in Astrophysics and Space Science Library, Vol. 337, Astrophysics and Space Science Library, Fridman A. M., Marov M. Y., Kovalenko I. G., eds., p. 75

Bjorkman J. E., Cassinelli J. P., 1993, ApJ, 409, 429

Blumenthal G. R., Gould R. J., 1970, Reviews of Modern Physics, 42, 237

Boettcher M., Mause H., Schlickeiser R., 1997, A&A, 324, 395

Bosch-Ramon V., Khangulyan D., Aharonian F. A., 2008, A&A, 482, 397

Böttcher M., Dermer C. D., 2005, ApJ, 634, L81

Bramall D. G. et al., 2012, in Proc. SPIE, Vol. 8446, Ground-based and Airborne Instrumentation for Astronomy IV, p. 84460A

Buckley D. A. H., 2005, in Astronomical Society of the Pacific Conference Series, Vol. 329, Nearby Large-Scale Structures and the Zone of Avoidance, Fairall A. P., Woudt P. A., eds., p. Fairall

Buckley D. A. H., Charles P. A., Nordsieck K. H., O'Donoghue D., 2006, in IAU Symposium, Vol. 232, The Scientific Requirements for Extremely Large Telescopes, Whitelock P., Dennefeld M., Leibundgut B., eds., pp. 1–12

Caliandro G. A., Torres D. F., Rea N., 2012, MNRAS, 427, 2251

Carroll B. W., Ostlie D. A., 2006, An introduction to modern astrophysics and cosmology

Casares J., Negueruela I., Ribó M., Ribas I., Paredes J. M., Herrero A., Simón-Díaz S., 2014, Nature, 505, 378

Casares J., Ribas I., Paredes J. M., Martí J., Allende Prieto C., 2005a, MNRAS, 360, 1105

Casares J., Ribó M., Ribas I., Paredes J. M., Martí J., Herrero A., 2005b, MNRAS, 364, 899

Casares J., Ribó M., Ribas I., Paredes J. M., Vilardell F., Negueruela I., 2012, MNRAS, 421, 1103

Cassinelli J. P., Brown J. C., Maheswaran M., Miller N. A., Telfer D. C., 2002, ApJ, 578, 951

Chaisson E., McMillan S., 2005, Astronomy Today

Charles P. A., Coe M. J., 2006, Optical, ultraviolet and infrared observations of X-ray binaries, Lewin W. H. G., van der Klis M., eds., pp. 215–265

Chen A. M., Ng C. W., Takata J., Yu Y. W., Cheng K. S., 2017, ArXiv e-prints

Chernyakova M., Neronov A., Molkov S., Malyshev D., Lutovinov A., Pooley G., 2012, ApJ, 747, L29

Chernyakova M., Neronov A., Walter R., 2006, MNRAS, 372, 1585

Coe M. J., Bartlett E. S., Bird A. J., Haberl F., Kennea J. A., McBride V. A., Townsend L. J., Udalski A., 2015, MNRAS, 447, 2387

Coe M. J., Edge W. R. T., Galache J. L., McBride V. A., 2005, MNRAS, 356, 502

Coleiro A., Chaty S., 2013, ApJ, 764, 185

Conti P. S., 1978, ARA&A, 16, 371

Corbet R. H. D. et al., 2011, The Astronomer's Telegram, 3221

Corbet R. H. D. et al., 2016, ApJ, 829, 105

Cranmer S. R., 2005, ApJ, 634, 585

Cranmer S. R., 2009, ApJ, 701, 396

Crawford S. M., 2015, pyhrs: Spectroscopic data reduction package for SALT. Astrophysics Source Code Library

Dachs J., Wamsteker W., 1982, A&A, 107, 240

Delgado A. J., Thomas H.-C., 1981, A&A, 96, 142

Dermer C. D., Menon G., 2009, High Energy Radiation from Black Holes: Gamma Rays, Cosmic Rays, and Neutrinos

Dewi J. D. M., Pols O. R., Savonije G. J., van den Heuvel E. P. J., 2002, MNRAS, 331, 1027

Dhawan V., Mioduszewski A., Rupen M., 2006, in VI Microquasar Workshop: Microquasars and Beyond, p. 52.1

Dubus G., 2006a, A&A, 451, 9

Dubus G., 2006b, A&A, 456, 801

Dubus G., 2013, A&A Rev., 21, 64

Dubus G., Guillard N., Petrucci P.-O., Martin P., 2017, ArXiv e-prints

Ekström S., Meynet G., Maeder A., Barblan F., 2008, A&A, 478, 467

Fermi LAT Collaboration et al., 2012, Science, 335, 189

Foellmi C., Moffat A. F. J., Guerrero M. A., 2003, MNRAS, 338, 360

Fu W., Lubow S. H., Martin R. G., 2015a, ApJ, 807, 75

Fu W., Lubow S. H., Martin R. G., 2015b, ApJ, 813, 105

Geballe T. R., 2016, in Journal of Physics Conference Series, Vol. 728, Journal of Physics Conference Series, p. 062005

Gehrz R. D., Hackwell J. A., Jones T. W., 1974, ApJ, 191, 675

Gies D. R. et al., 2007, ApJ, 654, 527

Goldoni P., Mereghetti S., 1995, A&A, 299, 751

Gomboc A., Bode M. F., Carter D., Mundell C. G., Newsam A. M., Smith R. J., Steele I. A., 2003, ArXiv Astrophysics e-prints

Gould R. J., Schréder G. P., 1967, Physical Review, 155, 1408

Gregory P. C., 2002, ApJ, 575, 427

Gregory P. C., Peracaula M., Taylor A. R., 1999, ApJ, 520, 376

Gregory P. C., Taylor A. R., 1978, Nature, 272, 704

Gregory P. C., Taylor A. R., 1981, ApJ, 248, 596

Gregory P. C., Xu H.-J., Backhouse C. J., Reid A., 1989, ApJ, 339, 1054

Grundstrom E. D. et al., 2007, ApJ, 656, 437

H. E. S. S. Collaboration et al., 2012, A&A, 541, A5

H. E. S. S. Collaboration et al., 2015, A&A, 577, A131

Haberl F., Sturm R., 2016, A&A, 586, A81

Hadasch D. et al., 2012, ApJ, 749, 54

Hanuschik R. W., 1989, Ap&SS, 161, 61

Hanuschik R. W., 1996, A&A, 308, 170

Harmanec P., Bisikalo D. V., Boyarchuk A. A., Kuznetsov O. A., 2002, A&A, 396, 937

Hellier C., 2001, Cataclysmic Variable Stars

Hilditch R. W., 2001, An Introduction to Close Binary Stars. p. 392

Hobbs G., Lorimer D. R., Lyne A. G., Kramer M., 2005, MNRAS, 360, 974

Horne K., Marsh T. R., 1986, MNRAS, 218, 761

Huang S.-S., 1972, ApJ, 171, 549

Huang W., Gies D. R., McSwain M. V., 2010, ApJ, 722, 605

Hubrig S. et al., 2013, A&A, 551, A33

Hubrig S. et al., 2011, A&A, 528, A151

Hutchings J. B., Crampton D., 1981, PASP, 93, 486

Innanen K. A., Zheng J. Q., Mikkola S., Valtonen M. J., 1997, AJ, 113, 1915

Jauch J. M., Rohrlich F., 1976, The theory of photons and electrons. The relativistic quantum field theory of charged particles with spin one-half

Johnston S., Ball L., Wang N., Manchester R. N., 2005, MNRAS, 358, 1069

Johnston S., Manchester R. N., Lyne A. G., Nicastro L., Spyromilio J., 1994, MNRAS, 268, 430

Jones F. C., 1968, Physical Review, 167, 1159

Kaper L., 2001, in Astrophysics and Space Science Library, Vol. 264, The Influence of Binaries on Stellar Population Studies, Vanbeveren D., ed., p. 125

Kirk J. G., Ball L., Skjæraasen O., 1999, Astroparticle Physics, 10, 31

Kirk J. G., Heavens A. F., 1989, MNRAS, 239, 995

Kiseleva L. G., Eggleton P. P., Mikkola S., 1998, MNRAS, 300, 292

Kniazev A. Y., Gvaramadze V. V., Berdnikov L. N., 2016, MNRAS, 459, 3068

Kozai Y., 1962, AJ, 67, 591

Lanz T., Hubeny I., 2003, ApJS, 146, 417

Lee U., Osaki Y., Saio H., 1991, MNRAS, 250, 432

Lefa E., Kelner S. R., Aharonian F. A., 2012, ApJ, 753, 176

Li J., Torres D. F., Zhang S., Hadasch D., Rea N., Caliandro G. A., Chen Y., Wang J., 2012, ApJ, 744, L13

Lidov M. L., 1962, Planet. Space Sci., 9, 719

Longair M. S., 2011, High Energy Astrophysics

Maeder A., 2009, Physics, Formation and Evolution of Rotating Stars

Manick R., Miszalski B., McBride V., 2015, MNRAS, 448, 1789

Maraschi L., Treves A., Tanzi E. G., 1981, ApJ, 248, 1010

Martin R. G., Nixon C., Armitage P. J., Lubow S. H., Price D. J., 2014a, ApJ, 790, L34

Martin R. G., Nixon C., Lubow S. H., Armitage P. J., Price D. J., Doğan S., King A., 2014b, ApJ, 792, L33

Martin R. G., Tout C. A., Pringle J. E., 2009, MNRAS, 397, 1563

Massi M., 2004, ArXiv Astrophysics e-prints

Massi M., Ribó M., Paredes J. M., Garrington S. T., Peracaula M., Martí J., 2004, A&A, 414, L1

Massi M., Ribó M., Paredes J. M., Peracaula M., Estalella R., 2001, A&A, 376, 217

Massi M., Ros E., Zimmermann L., 2012, A&A, 540, A142

Massi M., Torricelli-Ciamponi G., 2014, A&A, 564, A23

Massi M., Torricelli-Ciamponi G., 2016, A&A, 585, A123

McPhate J. et al., 2011, in Proc. SPIE, Vol. 8145, Society of Photo-Optical Instrumentation Engineers (SPIE) Conference Series, p. 81450I

McSwain M. V., Ray P. S., Ransom S. M., Roberts M. S. E., Dougherty S. M., Pooley G. G., 2011, ApJ, 738, 105

Melatos A., Johnston S., Melrose D. B., 1995, MNRAS, 275, 381

Mirabel I. F., 2006, Science, 312, 1759

Mirzoyan R., Mukherjee R., 2017, The Astronomer's Telegram, 10971

Mohamed S., Podsiadlowski P., 2012, Baltic Astronomy, 21, 88

Moldón J., Johnston S., Ribó M., Paredes J. M., Deller A. T., 2011, ApJ, 732, L10

Monageng I. M., McBride V. A., Coe M. J., Steele I. A., Reig P., 2017a, MNRAS, 464, 572

Monageng I. M., McBride V. A., Townsend L. J., Kniazev A. Y., Mohamed S., Böttcher M., 2017b, ApJ, 847, 68

Morales-Rueda L., Carter D., Steele I. A., Charles P. A., Worswick S., 2004, Astronomische Nachrichten, 325, 215

Moritani Y., Nogami D., Okazaki A. T., Imada A., Kambe E., Honda S., Hashimoto O., Ichikawa K., 2011, PASJ, 63, 25

Naoz S., Fabrycky D. C., 2014, ApJ, 793, 137

Negueruela I., Okazaki A. T., 2001, A&A, 369, 108

Negueruela I., Okazaki A. T., Fabregat J., Coe M. J., Munari U., Tomov T., 2001, A&A, 369, 117

Neto A. D., de Freitas-Pacheco J. A., 1982, MNRAS, 198, 659

O'Donoghue D. et al., 2006, MNRAS, 372, 151

Okazaki A. T., 1991, PASJ, 43, 75

Okazaki A. T., 1997, A&A, 318, 548

Okazaki A. T., Bate M. R., Ogilvie G. I., Pringle J. E., 2002, MNRAS, 337, 967

Okazaki A. T., Hayasaki K., Moritani Y., 2013, PASJ, 65, 41

Okazaki A. T., Negueruela I., 2001, A&A, 377, 161

Ostrowski M., 1991, MNRAS, 249, 551

Owocki S., Ud-Doula A., 2003, in Astronomical Society of the Pacific Conference Series, Vol. 305, Magnetic Fields in O, B and A Stars: Origin and Connection to Pulsation, Rotation and Mass Loss, Balona L. A., Henrichs H. F., Medupe R., eds., p. 350

Papaloizou J. C., Savonije G. J., Henrichs H. F., 1992, A&A, 265, L45

Paredes J. M., Estalella R., Rius A., 1990, A&A, 232, 377

Paredes J. M., Martí J., Ribó M., Massi M., 2000, Science, 288, 2340

Paredes-Fortuny X., Ribó M., Bosch-Ramon V., Casares J., Fors O., Núñez J., 2015, A&A, 575, L6

Porter J. M., 1997, A&A, 324, 597

Porter J. M., Rivinius T., 2003, PASP, 115, 1153

Puls J. et al., 1996, A&A, 305, 171

Rajoelimanana A. F., Charles P. A., Meintjes P. J., Townsend L. J., Schurch M. P. E., Udalski A., 2017, MNRAS, 464, 4133

Rajoelimanana A. F., Charles P. A., Udalski A., 2011, MNRAS, 413, 1600

Rappaport S. A., Joss P. C., 1983, in Accretion-Driven Stellar X-ray Sources, Lewin W. H. G., van den Heuvel E. P. J., eds., p. 13

Reig P., 2011, Ap&SS, 332, 1

Reig P., Fabregat J., Coe M. J., 1997, A&A, 322, 193

Reig P., Larionov V., Negueruela I., Arkharov A. A., Kudryavtseva N. A., 2007, A&A, 462, 1081

Reig P., Nersesian A., Zezas A., Gkouvelis L., Coe M. J., 2016, A&A, 590, A122

Rivinius T., Baade D., Townsend R. H. D., Carciofi A. C., Štefl S., 2013, A&A, 559, L4

Rivinius T., Štefl S., Baade D., 2006, A&A, 459, 137

Romano P. et al., 2016, A&A, 593, A96

Romero G. E., Okazaki A. T., Orellana M., Owocki S. P., 2007, A&A, 474, 15

Rybicki G. B., Lightman A. P., 1986, Radiative Processes in Astrophysics. p. 400

Sarty G. E. et al., 2011, MNRAS, 411, 1293

Savonije G. J., Heemskerk M. H. M., 1993, A&A, 276, 409

Sekhar A., Asher D. J., Werner S. C., Vaubaillon J., Li G., 2017, MNRAS, 468, 1405

Sguera V. et al., 2006, ApJ, 646, 452

Shevchenko I. I., ed., 2017, Astrophysics and Space Science Library, Vol. 441, The Lidov-Kozai Effect ndash; Applications in Exoplanet Research and Dynamical Astronomy

Souami D., Souchay J., 2012, A&A, 543, A133

Stahl O., Kaufer A., Tubbesing S., 1999, in Astronomical Society of the Pacific Conference Series, Vol. 188, Optical and Infrared Spectroscopy of Circumstellar Matter, Guenther E., Stecklum B., Klose S., eds., p. 331

Steele I. A., 2001, Astronomische Nachrichten, 322, 307

Steele I. A., 2004, Astronomische Nachrichten, 325, 519

Stella L., White N. E., Rosner R., 1986, ApJ, 308, 669

Strader J., Chomiuk L., Cheung C. C., Salinas R., Peacock M., 2015, ApJ, 813, L26

Summerlin E. J., Baring M. G., 2012, ApJ, 745, 63

Takeda G., Rasio F. A., 2005, ApJ, 627, 1001

Tanaka T., Odaka H., Enoto T., Nakashima S., 2014, in Suzaku-MAXI 2014: Expanding the Frontiers of the X-ray Universe, Ishida M., Petre R., Mitsuda K., eds., p. 244

Tauris T. M., Konar S., 2003, in Astronomical Society of the Pacific Conference Series, Vol. 308, From X-ray Binaries to Gamma-Ray Bursts: Jan van Paradijs Memorial Symposium, van den Heuvel E. P., Kaper L., Rol E., Wijers R. A. M. J., eds., p. 293

Tauris T. M., van den Heuvel E. P. J., 2006, Formation and evolution of compact stellar X-ray sources, Lewin W. H. G., van der Klis M., eds., pp. 623–665

Tavani M., Arons J., 1997, ApJ, 477, 439

Taylor A. R., Young G., Peracaula M., Kenny H. T., Gregory P. C., 1996, A&A, 305, 817

Telting J. H., Heemskerk M. H. M., Henrichs H. F., Savonije G. J., 1994, A&A, 288, 558

Tonry J., Davis M., 1979, AJ, 84, 1511

Torrejón J. M., Orr A., 2001, A&A, 377, 148

Townsend L. J., Coe M. J., Corbet R. H. D., Hill A. B., 2011, MNRAS, 416, 1556

Townsend R. H. D., Owocki S. P., Howarth I. D., 2004, MNRAS, 350, 189

van den Heuvel E. P. J., 1975, ApJ, 198, L109

Waisberg I. R., Romani R. W., 2015a, ApJ, 805, 18

Waisberg I. R., Romani R. W., 2015b, ApJ, 812, 178

Wang, Sharon X. et al., 2012, ApJ, 761, 46

Waters L. B. F. M., 1986, A&A, 159, L1

Waters L. B. F. M., van Kerkwijk M. H., 1989, A&A, 223, 196

Woolf N. J., Stein W. A., Strittmatter P. A., 1970, A&A, 9, 252

Wright J. T., Howard A. W., 2009, ApJS, 182, 205

Xing Y., Wang Z., Takata J., 2017, ApJ, 851, 92

Yarlagadda R. K. R., 2009, Analog and Digital Signals and Systems, 1st edn. Springer Publishing Company, Incorporated

Zamanov R., Martí J., Stoyanov K., Borissova A., Tomov N. A., 2014, A&A, 561, L2

Zamanov R., Stoyanov K., Martí J., Tomov N. A., Belcheva G., Luque-Escamilla P. L., Latev G., 2013, A&A, 559, A87

Zamanov R. K., Martí J., Paredes J. M., Fabregat J., Ribó M., Tarasov A. E., 1999, A&A, 351, 543

Zamanov R. K., Reig P., Martí J., Coe M. J., Fabregat J., Tomov N. A., Valchev T., 2001, A&A, 367, 884

Zamanov R. K., Stoyanov K. A., Martí J., Latev G. Y., Nikolov Y. M., Bode M. F., Luque-Escamilla P. L., 2016, A&A, 593, A97

Zdziarski A. A., Neronov A., Chernyakova M., 2010, MNRAS, 403, 1873

Zhang S., Torres D. F., Li J., Chen Y. P., Rea N., Wang J. M., 2010, MNRAS, 408, 642